NONLINEAR DISTORTION AND SUPPRESSION IN TRAVELING WAVE TUBES: INSIGHTS AND METHODS

by

John G. Wöhlbier

A dissertation submitted in partial fulfillment of
the requirements for the degree of

Doctor of Philosophy

(Electrical Engineering)

at the

UNIVERSITY OF WISCONSIN–MADISON

2003

To Piper. I am so lucky to have you.

ACKNOWLEDGMENTS

Professor John Booske has provided excellent advising. His zeal for research is infectious, his intuitions are inspiring, and his willingness to take a chance is refreshing.

Professor Ian Dobson has provided excellent advising. His talents for computations and exposition are superior, his genuine and honest nature is welcome, and his willingness to take a chance is refreshing.

Mark Converse, my close graduate colleague for the last four years, provided countless useful discussions that helped to figure out just what it was that we were doing. I also thank him for taking a chance on the code *lmsuite* by using it in his Ph.D. work.

Aarti Singh has provided invaluable feedback in trying to apply my theories. I sincerely hope that her effort to learn how to do some of the calculations pays off. Her babysitting was deeply appreciated by myself, Piper, and especially Evelyn.

I thank my great friend Glen Luckjiff for putting the idea of going back to graduate school into my head, and for his encouragement of the pursuit of Mathematics.

Finally, I am indebted to my lovely wife Piper. Her unselfish nature has allowed me to pour countless hours into completing my Ph.D. The gift of our daughter Evelyn, and hence the creation of our family, has made me one hundred-fold happier than any academic degree ever could. Striking a balance between family time and work has been very difficult for me, and I can only hope that I have done right by my family.

TABLE OF CONTENTS

Page

Page

LIST OF TABLES

LIST OF FIGURES

Figure Page

Figure Page

Figure Page

Figure Page

ABSTRACT

Traveling Wave Tubes (TWTs) are microwave and millimeter wave amplifiers used in radar, satellite communications, and electronic countermeasure applications. On a satellite, the TWT provides the final communications signal boost before transmitting the signal back to earth. In electronic countermeasures, TWTs boost signals that are sent out to deny detection by an enemy radar. The TWT, as with any amplifier, has a less than ideal behavior due to the amplifier nonlinearities. The non-idealities typically result in decreased amplifier efficiencies or reduced bandwidth. Such compromising behavior can be extremely expensive where a 1% increase in efficiency of a TWT could save $\$100,000,000$ over the operating lifetime of a communications satellite.

In this dissertation new advances in nonlinear modeling of TWTs are presented. These advances include new techniques for calculating properties of nonlinear behavior, and new insights into the physical processes responsible for the nonlinear distortions. In particular, the physics of intermodulation distortion, phase distortion, and harmonic injection are studied in detail. The new ideas on intermodulation distortion and phase distortion presented in the thesis revise long-standing assumptions about TWT nonlinearity, and should ultimately play a role in improving TWT designs through improved understanding. The new ideas and explanations of harmonic and signal injection may enable new technologies that would increase efficiency, bandwidth, and linearity, and provide increased functionality and higher data rates with large cost savings for electronic countermeasure and satellite communications markets.

Chapter 1

Introduction and background

1.1 Introduction

Traveling Wave Tubes (TWTs) are microwave and millimeter wave amplifiers that are used extensively in communications, radar, and electronic countermeasure applications. They continue to find wide-spread application due to their inherently wide bandwidths and their high frequency, high power operating points. A compromising feature of the TWT is the device nonlinearity. The nonlinearity manifests as a saturating mechanism and spectral distortion; both of these effects limit TWT efficiency. For electronic countermeasures, power produced in the harmonics of the fundamental limits the output powers obtainable at the fundamental, and this limits the obtainable efficiency at the fundamental. For digital communications applications, the distortions increase bit error rates, and this limits data rates. Reducing nonlinear distortions in TWTs would increase efficiency and bandwidths of electronic countermeasure systems, and would increase data rates and efficiency in digital communications applications.

There are several examples of nonlinear effects that have long plagued TWTs and have been the focus of much research, but are still not completely understood in terms of physical mechanisms. Among these are harmonic injection, cross-modulation, and phase distortion. Moreover, due to increased sophistication of modulation techniques in digital communications, there are new problems associated with TWT nonlinearities which also lack explanations and remedies. For example, there is no general description based on TWT physics for how statistics of the input signal translate to statistics of the output signal. Since improved understanding inevitably leads to improved techniques and designs, wireless communications systems and electronic countermeasure systems certainly stand to benefit from improved explanations and insights into nonlinear TWT physics.

The methods available to study nonlinear TWT physics include experimentation, modeling, simulation, and analysis; this thesis focuses on modeling, simulation, and analysis. The two primary methods for modeling TWT behavior are physics based models and generic input-output models. There are a wide variety of available physics based models. On one end of the spectrum are steady-state models which assume a Fourier series form for the RF input and are usually systems of nonlinear ordinary differential equations. On the other end of the spectrum are electromagnetic particle-in-cell (PIC) models that involve solving electron

beam equations and Maxwell's equations (partial differential equations) in the time-domain. Models in this spectrum can be 1-d, 2-d, 3-d, or some mixture, i.e., different dimensions for the electron beam and electromagnetic fields.

We have developed three new 1-d nonlinear steady-state TWT models, the MUSE model, the S-MUSE model, and LATTE [82]. This "suite" of models provides a foundation for simulation and analysis that has led to a new understanding of many aspects of nonlinear TWT physics. The LATTE model captures the largest amount of nonlinear physics, including RF power saturation, and is ideally suited for simulation. By virtue of its construction, the MUSE model fails to predict the same RF power saturation as LATTE, and is therefore not considered to be as accurate at LATTE. However, the MUSE model has a mathematical structure that allows certain physical aspects of the device physics to be studied which cannot easily be probed in LATTE or any other TWT model past or present. The S-MUSE model is derived from the MUSE model by dropping certain nonlinear terms, and can be considered an approximation to the LATTE solutions applicable prior to power saturation. However, the S-MUSE model is analytically solvable and the structure of the solutions describes much about the underlying nonlinear physics of the TWT. Therefore, although the MUSE and S-MUSE models sacrifice certain physical predictive capabilities and have a more limited range of use, they are advantageous in other respects including speed of computation, analytic tractability, and access to physics not available to other models.

In this thesis we apply LATTE, MUSE, and S-MUSE, derived and compared with the large signal code Christine 1-d [4, 5] in Chapter 2, to some important nonlinear problems in TWT physics. Christine 1-d predictions have been extensively validated with experiments, and are therefore regarded as an acceptable validation benchmark for the new models. In Chapter 3 the analytic solutions to S-MUSE are computed, and technical details are discussed. In Chapter 4 a process for generation of harmonic and intermodulation distortions is given, along with a formula to compute exponential growth rates of the distortions. In Chapter 5 we study phase distortion in the TWT. Using the models we offer a new view of the physical mechanisms of phase distortion that is counter to a decades old view, and apply the new insights to several phase distortion related problems. In Chapter 6 we study the theory and simulation of harmonic injection, and more generally signal injection, for shaping output spectra. The material gives unique insights into many aspects of many different signal injection schemes. Such insights will probably play a role in the development of new linearizer technologies. Finally, in Chapter 7 we give an overview of the entire thesis and describe its impact on the field of vacuum electronics.

1.2 Literature review

In this section we review the TWT literature on the following topics:

1. physical TWT modeling using Eulerian coordinates,

2. physical TWT modeling using Lagrangian coordinates,

3. TWT transfer functions,

4. harmonic injection in TWTs.

Unless otherwise specified the TWT models discussed below are steady-state "frequency domain" models, i.e., inputs may be written as a Fourier series.

1.2.1 TWT modeling using Eulerian coordinates

1.2.1.1 Linear Eulerian theory

The classic linear TWT model was published by J.R. Pierce in 1947 [60]. The analysis uses a one-dimensional transmission line to represent the slow-wave circuit, and models the electron beam as a one dimensional fluid. The fluid equations for the electron beam are a Newton's Law relation and an equation of continuity, both expressed in Eulerian coordinates. The theory, known as "Pierce theory" or "small-signal theory," is widely used and the details have been presented in several text books, for example [7, 39, 41, 48, 54, 61]. The linear theory is a single frequency theory and does not predict saturation of the circuit field.

1.2.1.2 Nonlinear Eulerian theory

Several authors have modeled TWT nonlinearities using the Eulerian electron beam equations that Pierce linearized to get the small-signal theory.

Brillouin [11] develops a single frequency nonlinear TWT theory based on the non-linearized Pierce equations. He first re-derives the small signal results. However, he includes relations for energy density and energy flux, as well as formal inequalities for the limitations of the linear equations. He then considers "large amplitude" regimes of the nonlinear equations. Classes of "stable waves," "shock waves," and "oscillating waves of moderately large amplitude" are considered.

Putz [64] is the first author to attempt an extension of the small signal theory to include multiple frequencies. The following is a summary of [64] from Curtice [19]:

> Putz's method of analysis is to find, to a reasonable approximation, the power-series expansion for the electric field of the slow-wave structure. Starting with an analysis of electron bunching owing to an assumed helical field, the fundamental alternating current can be evaluated and expressed in a power series. This power series, together with the relationship between beam current and electric field on a travelling-wave structure, leads to a power-series expansion for the electric field, the first term of which is merely the usual small-signal result. Several successive approximations are used to obtain a self-consistent solution which, however, ignores space-charge forces in the beam and any transverse motions of the electrons.
>
> The analysis of bunching is done with a single-wave solution (the growing wave) for each signal. This approximation is accurate in tubes of high gain, but will be

> erroneous in cases where the other waves cannot be neglected; e.g. it is not clear how to analyse a t.w.t. with a lumped attenuator. However, if there is at least 20dB gain following the attenuator, the growing wave will adequately describe the circuit field, and [intermodulation] and [cross modulation] effects will result principally from the nonlinear effects after the attenuator. If the gain after the attenuator is insufficient, new effects occur as Ober has shown.

Sobol [73] also attempts a multifrequency analysis. From El-Shandwily [29]:

> Sobol used the same procedure [as DeGrasse] to derive four sets of equations (in addition he neglected the second harmonic that was considered by DeGrasse), and gave numerical solution only for the longitudinal beam parametric amplifier case with the pump frequency at twice the signal frequency.

DeGrasse [26] uses a method similar to Sobol [73]. Again from El-Shandwily [29]:

> DeGrasse gave an analysis of linear O-type amplifiers with two input signals. ... Five sets of equations which describe the operation of the traveling-wave amplifier were derived. One set was for each input signal and one set for the difference, the sum and the second harmonic of one of the input signals. To solve the equations, DeGrasse assumed that both of the input signals propagate independently according to Pierce's linear theory. Knowing the solution for the two input signals the other components could be obtained. Other intermodulation components such as those at $2f_2 - f_1$ and $2f_1 - f_2$ which could be important were not considered.

Curtice [19] extends Putz [64] to include space charge and larger values of the Pierce gain parameter C. A series expansion of the beam current gives a series expansion for the circuit field, the second term of which contains the "first-order nonlinear effects of t.w.t. operation." As in [64] the nonlinear term is normalized into a "normalized distortion factor." This factor is related to the cross-modulation factor, which is then related to output amplitude and phase modulation, and intermodulation power ratio. The normalized distortion factor is computed versus TWT parameters. The analysis however is limited to "the weakly saturated condition."

The group of Datta *et al.* have published a collection of articles using a third order nonlinear model based on Eulerian electron beam equations. Following work by Paschke [57, 58, 59] Datta *et al.* use "successive approximations" to obtain analytic solutions to the nonlinear system. While a 1-d analysis, their model includes all relevant physics, although nonlinearities above the third order are discarded [23]. However, they note that for their results to be "fairly acceptable" [20] the beam plasma frequency must be much below the operating frequency, referring to [59] for justification of this fact. In [20] they introduce the model, solve it for a single frequency, and compare their results to a Lagrangian model for a particular TWT. Interestingly, the Eulerian model demonstrates saturation effects for the TWT parameters presented. In [23] they provide a slightly more detailed derivation and

solution of their model again for a single frequency. In this article they compare their model to a Lagrangian model for two different TWTs and establish a "regime of correctness." In [22] they again study their third-order model, but now consider the generation of harmonics and their control. The effects of dispersion parameters, circuit loss, and harmonic injection on the amount of harmonic content present in the output are studied. For the generation of a harmonic from a drive frequency they consider only the second order nonlinearity, but the third-order nonlinearities are included in the computation of the fundamental frequency. However, in the case of second harmonic injection they include second and third order nonlinearities for both the fundamental and harmonic signals. Reference [24] is similar to [22] although they do not treat harmonic injection. Lastly, in [21] they study harmonic injection to reduce third order intermodulation frequencies using the same formalism as their other papers.

Finally, a paper containing the derivations of the Multifrequency Spectral Eulerian (MUSE) model, S-MUSE model, and a Lagrangian disk model LATTE, all presented in this thesis, appears in [82]. It is worth noting that the MUSE model is the only "exact" steady-state Eulerian model in the literature in that no approximations on the nonlinearities are made. As such, there does not seem to be an analytic solution to the MUSE model and numerical integration must be used to solve it. However, numerical integration of the MUSE model seems to be easier to perform than implementation of the analytic solutions given by Datta *et al.*, especially as the number of frequencies increases.

1.2.2 TWT modeling using Lagrangian coordinates

The impetus for original work using Lagrangian coordinates for the electron beam was that "electrons overtake one another at or even considerably before the point along the tube where the limiting power level is obtained,"[56] in which case Eulerian functions become multi-valued. Codes using such formulations have been quite successful in accurately predicting TWT behavior. Since these models must be numerically integrated, parametric studies of various physical phenomena are more challenging and time consuming than analogous parametric studies of an analytic solution, even if the analytic solution is for an approximate model.

1.2.2.1 Single frequency

The original paper using Lagrangian coordinates to model the electron beam was by Nordsieck [56]. This work ignores space charge effects and circuit loss. Several authors followed Nordsieck with similar Lagrangian models including more physics. From Tien [75]:

> Poulter [62] has extended Nordsieck equations to include space charge, finite C and circuit loss, although he has not perfectly taken into account the space charge and the backward wave. Recently Tien, Walker, and Wolontis [77] have published a small C theory in which "electrons" are considered in the form of

uniformly charged discs and the space charge field is calculated by computing the force exerted on one disc by the others. Results extended to finite C, have been reported by Rowe [66], and also by Tien and Walker [76]. Rowe, using a space charge expression similar to Poulter's, computed the space charge field based on the electron distribution in time instead of the distribution in space. This may lead to appreciable error in his space charge term, although its influence on the final results cannot be easily evaluated.

Tien [75] takes the model by Tien, Walker, and Wolontis [77] and extends it to finite C. Additionally, a method for calculating a backward wave contribution is provided and the effect of the backward wave is studied. This analysis however ignores circuit loss.

For a summary of these papers and those that followed, the reader is referred to the book by Rowe [67]. Multi-dimensionality of the electron beam is also covered in [67].

1.2.2.2 Multiple frequencies

To extend the 1-d single frequency models to handle input signals with multifrequency content, and the associated intermodulation frequencies due to the TWT nonlinearity, models using Fourier series for circuit quantities were developed. Among the original models were El-Shandwily [29] and Giarola [40]. References [71, 78, 27] also develop such models. The papers by Srivastava and Joshi [74] and Datta *et al.* [25] are similar to the earlier papers in how they treat the electron beam, but each handles the circuit and space charge fields differently.

More recently, another collection of such models have appeared in the literature. The models compute the RF quantities using electromagnetic field representations and Maxwell's equations rather than the equivalent circuit models. Antonsen and Levush present a 1-d frequency domain model [4, 5] which is extended to 3-d by Chernin *et al.* [17]. Freund *et al.* formulate 3-d models in both the time domain [37, 36, 34, 35] and the frequency domain [32, 33]. The time domain models are restricted to single or multifrequency sinusoids with a slowly varying envelope.

1.2.3 TWT transfer functions

From the perspective of a system engineer, the TWT can be characterized by input-output transfer functions. Most commonly these include an AM/AM curve relating the output power to the input power, and an AM/PM curve relating the output phase to the input power. The character of these curves captures some of the nonlinearity of the TWT.

Putz [65] considers nonlinear effects in TWTs based on analysis of a physical model, using graphical methods, and using a power series transfer function. In particular, cross-modulation effects are considered with the output of the physical model as well as rules of thumb; harmonic outputs are predicted with graphical methods; intermodulation products

are predicted using a mixture of empirical formulas and graphical methods. Harmonic injection is discussed noting that the harmonic and drive frequencies mix to produce a signal at the drive frequency that adds to the original drive signal. By substituting a multifrequency signal into a power series transfer characteristic, he derives expressions for the nonlinearities present in the output signals at the drive, harmonic, and intermodulation frequencies. Based on these formulas he discusses how the output voltage at intermodulation frequencies depends on products of the input voltages making the intermodulation frequencies. He also discusses the presence of cross-modulation terms and how they indicate a linear proportionality of the change in output voltage (for small input voltages) to interfering signal power. He then compares the power series outputs to the equation derived from the physical model (presumably from [64]) and notes how the forms agree. Lastly, based on the physically derived equation, he claims that nonlinear effects will be least for TWTs with highest values of C and lowest values of circuit loss.

Saleh [69] proposes empirical frequency independent amplitude-phase and quadrature models as well as a frequency dependent quadrature model. For multiple phase modulated carriers he solves the frequency-independent quadrature model for intermodulation frequencies. The two carrier case gives a complete analytic time domain solution while the many carrier solution contains an integral that must be evaluated numerically. He proposes the frequency-dependent quadrature model as an extension to the frequency-independent model, but does no studies using the model. The introductory paragraphs of [69] give a nice summary of amplitude-phase and quadrature models prior to [69]. Abuelma'atti [3] gives a frequency-dependent quadrature model for the TWT basing it on a frequency-independent quadrature model, and gives an example of its use in computing intermodulation products of two frequencies. Guida [42, 43] provides methods for computing intermodulation power for given input signals using specific TWT input-output models. Reference [42] summarizes previous methods for doing such calculations.

Several authors study the physical mechanisms behind the AM/AM and AM/PM transfer curves with large signal codes. The AM/AM mechanism is due to the saturation of the device, while the AM/PM mechanism is "shown" to be related to decrease of electron velocities and the phase of the electron bunch with respect to the voltage wave. Ezura and Kano [30] study the dependence of the AM/PM curves on TWT parameters, amplitudes of circuit waves, and average electron velocities theoretically and experimentally. Hirata and Kanai [46] and Hirata [45] study the relation of AM/PM conversion to the generation of intermodulation products. It is found that the in-phase component of the fundamental charge density modulation with respect to the circuit voltage dominates the generation of intermodulation products.

Carter *et al.* [12] developed a code for predicting intermodulation distortions based on the single carrier transfer characteristics of a TWT. Although details of their input-output model are not given, it is frequency-independent in that it assumes TWT characteristics do not vary appreciably over the band of frequencies under consideration. They compare this model to the output of a multifrequency large signal TWT model for the case of two carriers, three carriers, and eight carriers. To achieve the effect of uncorrelated carriers, several runs of the large signal code with random initial phases are averaged. The results

are generally favorable and all differences are attributed to the frequency-independence of the input-output model.

1.2.4 Harmonic injection in TWTs

By injecting harmonics of drive signals the TWT output spectrum can be advantageously shaped. In the case of single frequency drive, harmonic injection can suppress the output harmonic and boost the fundamental relative to the harmonic. In the case of multifrequency drive, harmonic injection can reduce the intermodulation spectrum.

1.2.4.1 Single drive frequency

Mendel [55] states that enhancement by injecting harmonics

> ... was discovered quite some time ago when it was observed that the wrong type of second-harmonic input would seriously degrade the power output at the fundamental frequency. ... This process is is one of cancellation, whereby the injected second-harmonic signal is such that it is 180° out of phase with the second harmonic signal generated by the nonlinear processes inherent in the interaction mechanism.

Early articles discussing harmonic injection mechanisms and hardware implementations include [65, 44, 38]. We have provided a refinement to the mechanistic picture given in these references. Later, Datta *et al.* [22] give numerical studies of harmonic injection where they compare predictions of Eulerian and Lagrangian models.

1.2.4.2 Multiple drive frequencies

Sauseng *et al.* [70] show that intermodulation distortions can be reduced with harmonic injection by 6 dB to 18 dB below the fundamentals. More recently, Wirth *et al.* [79] have done similar experiments in which they were able to attain 24 dB of suppression. Datta *et al.* [21] have done simulations demonstrating this phenomenon.

Chapter 2

Steady state TWT models

2.1 Introduction

In this chapter we derive a new 1-d nonlinear multifrequency Eulerian TWT model, the MUSE (Multifrequency Spectral Eulerian) model. We also derive a Lagrangian "disk" model LATTE (Lagrangian TWT Equations) from the same initial equations for comparison purposes as well as to demonstrate the theoretical relation between MUSE and a disk model. A simplified MUSE model S-MUSE more suitable for analysis is also derived. These three models are compared to each other and Christine 1-d for a set of TWT parameters which are based on the Hughes (now Boeing) 8537H L-band TWT design. The comparison to Christine 1-d is particularly useful since this code is widely known and used, and it has been validated against experiment for the Hughes TWT [2, 68]. The nonlinearities of MUSE and LATTE are compared, and an example of how MUSE can examine fundamental distortion mechanisms is provided. We also study how the dimensions of the MUSE model and LATTE scale with number of frequencies, an important issue for assessing the use of MUSE as a numerical tool. Results from a simulation with 402 frequencies are provided. Lastly, we discuss the relation of the MUSE model to the "method of collective variables" in free electron laser theory [10].

Section 2.2 presents the models to be considered. We derive the MUSE model and discuss its numerical solution, derive the disk model LATTE, and derive the S-MUSE model. The models are compared to each other and Christine 1-d in Section 2.3. In particular we look at circuit power versus axial distance, a constant of the motion and the issue of electron overtaking. Section 2.4 discusses the nonlinearities in MUSE, the dimensional dependence of MUSE and LATTE on simulation parameters, and the relation of MUSE to the "collective variable" theory of free electron lasers.

2.2 TWT models

2.2.1 MUSE

2.2.1.1 Derivation

For the MUSE model the helix is modeled as a lossless transmission line[1] and Eulerian equations are used for the electron beam. In particular, the time domain model equations are

$$\frac{\partial V}{\partial z} = h_1 * \frac{\partial I}{\partial t} \tag{2.1}$$

$$\frac{\partial I}{\partial z} = h_2 * \frac{\partial V}{\partial t} - A\frac{\partial \rho}{\partial t} \tag{2.2}$$

$$\frac{\partial E}{\partial z} = \frac{\rho}{\epsilon_0} \tag{2.3}$$

$$\frac{\partial v}{\partial t} + v\frac{\partial v}{\partial z} = -\frac{e}{m_e}h_1 * \frac{\partial I}{\partial t} + \frac{e}{m_e}R * E \tag{2.4}$$

$$\frac{\partial \rho}{\partial t} + v\frac{\partial \rho}{\partial z} = -\rho\frac{\partial v}{\partial z}. \tag{2.5}$$

where z is axial distance, t is time, V is transmission line voltage, I is transmission line current, E is the space charge electric field, v is electron beam velocity, and ρ is the volume charge density of an electron beam with cross sectional area A. The $*$ denotes convolution and this allows for frequency dependence of circuit and beam parameters. The functions h_1, h_2 and R are the inverse Fourier transforms

$$h_1(z,t) = \mathcal{F}^{-1}\left\{\frac{\tilde{K}(z, f_\ell\omega_0)}{\tilde{v}_{\rm ph}(z, f_\ell\omega_0)}\right\} \tag{2.6}$$

$$h_2(z,t) = \mathcal{F}^{-1}\left\{\frac{1}{\tilde{K}(z, f_\ell\omega_0)\tilde{v}_{\rm ph}(z, f_\ell\omega_0)}\right\} \tag{2.7}$$

$$R(z,t) = \mathcal{F}^{-1}\left\{\tilde{R}(z, f_\ell\omega_0)\right\} \tag{2.8}$$

where the functions $\tilde{K}(z, f_\ell\omega_0), \tilde{v}_{\rm ph}(z, f_\ell\omega_0)$ and $\tilde{R}(z, f_\ell\omega_0)$ are frequency domain circuit interaction impedance [39], cold circuit phase velocity, and space charge reduction factor [48] respectively. The inverse transforms are aperiodic functions of t and are functions of z to allow for spatial variation of circuit parameters. In the remainder of the thesis notation of the z dependence is suppressed. The constants e, m_e, and ϵ_0 are electron charge, electron mass, and permittivity of free space respectively.

[1] See Appendix A for formulations of the models with circuit loss included.

For reasons that will be made clear later we first make the coordinate transformation

$$\begin{bmatrix} z \\ \psi \end{bmatrix} = \begin{bmatrix} 1 & 0 \\ \frac{\omega_0}{u_0} & -\omega_0 \end{bmatrix} \begin{bmatrix} z \\ t \end{bmatrix}. \tag{2.9}$$

Then

$$\frac{\partial V}{\partial z} = -\frac{\omega_0}{u_0}\frac{\partial V}{\partial \psi} - \omega_0 h_1 * \frac{\partial I}{\partial \psi} \tag{2.10}$$

$$\frac{\partial I}{\partial z} = -\omega_0 h_2 * \frac{\partial V}{\partial \psi} - \frac{\omega_0}{u_0}\frac{\partial I}{\partial \psi} + A\omega_0 \frac{\partial \rho}{\partial \psi} \tag{2.11}$$

$$\frac{\partial E}{\partial z} = -\frac{\omega_0}{u_0}\frac{\partial E}{\partial \psi} + \frac{\rho}{\epsilon_0} \tag{2.12}$$

$$v\frac{\partial v}{\partial z} = \frac{\omega_0 e}{m_e} h_1 * \frac{\partial I}{\partial \psi} + \frac{e}{m_e} R * E + \omega_0 \left(1 - \frac{v}{u_0}\right)\frac{\partial v}{\partial \psi} \tag{2.13}$$

$$v\frac{\partial \rho}{\partial z} = \omega_0 \left(1 - \frac{v}{u_0}\right)\frac{\partial \rho}{\partial \psi} - \rho\left(\frac{\partial v}{\partial z} + \frac{\omega_0}{u_0}\frac{\partial v}{\partial \psi}\right). \tag{2.14}$$

We assume all inputs to the system (signals at $z = 0$) are periodic in t with fundamental frequency ω_0. This implies that solutions as functions of (z, t) are periodic in t with fundamental period $\frac{2\pi}{\omega_0}$ and that solutions as functions of (z, ψ) are periodic in ψ with fundamental period 2π.

For a function $x(z, \psi)$ periodic in ψ we use the Fourier series relations

$$x(z, \psi) = \sum_{\ell=-\infty}^{\infty} \tilde{x}_\ell(z) e^{i f_\ell \psi} \tag{2.15}$$

$$\tilde{x}_\ell(z) = \frac{1}{2\pi}\int_{2\pi} x(z, \psi) e^{-i f_\ell \psi} d\psi \tag{2.16}$$

where the f_ℓ are integers indexed by ℓ. The set of frequencies $\{f_\ell\}$ is chosen to be the frequencies with nonzero Fourier coefficients, thus $\{f_\ell\}$ is the drive frequencies together with the frequencies produced from nonlinear interactions. We index the frequencies so that $f_{-\ell} = -f_\ell$ and $f_m > f_n$ for $m > n$. Since our functions are real valued,

$$\tilde{x}_{-\ell} = \tilde{x}_\ell^*. \tag{2.17}$$

Computing Fourier coefficients of (2.10)–(2.14) gives the MUSE model:

$$\frac{d\tilde{V}_\ell}{dz} = -\frac{i f_\ell \omega_0}{u_0}\tilde{V}_\ell - \frac{i f_\ell \omega_0 \tilde{K}(f_\ell \omega_0)}{\tilde{v}_{\mathrm{ph}}(f_\ell \omega_0)}\tilde{I}_\ell \tag{2.18}$$

$$\frac{d\tilde{I}_\ell}{dz} = -\frac{i f_\ell \omega_0}{\tilde{K}(f_\ell \omega_0)\tilde{v}_{\mathrm{ph}}(f_\ell \omega_0)}\tilde{V}_\ell - \frac{i f_\ell \omega_0}{u_0}\tilde{I}_\ell + i f_\ell \omega_0 A \tilde{\rho}_\ell \tag{2.19}$$

$$\frac{d\tilde{E}_\ell}{dz} = -\frac{i f_\ell \omega_0}{u_0}\tilde{E}_\ell + \frac{\tilde{\rho}_\ell}{\epsilon_0} \tag{2.20}$$

$$\sum_{\substack{m,n \\ f_m+f_n=f_\ell}} \tilde{v}_m \frac{d\tilde{v}_n}{dz} = \frac{if_\ell\omega_0 e\tilde{K}(f_\ell\omega_0)}{m_e\tilde{v}_{\rm ph}(f_\ell\omega_0)}\tilde{I}_\ell + \frac{e}{m_e}\tilde{R}(f_\ell\omega_0)\tilde{E}_\ell + if_\ell\omega_0\tilde{v}_\ell - \sum_{\substack{m,n \\ f_m+f_n=f_\ell}} \frac{if_n\omega_0}{u_0}\tilde{v}_m\tilde{v}_n \quad (2.21)$$

$$\sum_{\substack{m,n \\ f_m+f_n=f_\ell}} \tilde{v}_m \frac{d\tilde{\rho}_n}{dz} = if_\ell\omega_0\tilde{\rho}_\ell - \frac{if_\ell\omega_0}{u_0} \sum_{\substack{m,n \\ f_m+f_n=f_\ell}} \tilde{v}_m\tilde{\rho}_n - \sum_{\substack{m,n \\ f_m+f_n=f_\ell}} \frac{d\tilde{v}_m}{dz}\tilde{\rho}_n \quad (2.22)$$

where $-\infty \le \ell \le \infty$. We have used that for $x(z,\psi)$ and $y(z,\psi)$ periodic, multiplication becomes convolution:

$$x(z,\psi)y(z,\psi) \quad \stackrel{\mathcal{F}}{\longleftrightarrow} \quad \sum_{\substack{m,n \\ f_\ell=f_m+f_n}} \tilde{x}_m(z)\tilde{y}_n(z). \quad (2.23)$$

The summation notation should be read as "*sum over integers m and n such that* $f_m + f_n = f_\ell$."

2.2.1.2 Method of numerical solution

For practical implementation one neglects higher frequencies and limits ℓ to $-M \le \ell \le M$. Then the MUSE model has $5(2M+1)$ complex equations.

During integration of the MUSE model one needs to solve (2.21) and (2.22) for the derivatives $\frac{d\tilde{v}_\ell}{dz}$ and $\frac{d\tilde{\rho}_\ell}{dz}$.[2] Equations (2.21) and (2.22) for $-M \le \ell \le M$ are the linear systems

$$\mathbf{S}\mathbf{w}_v = \mathbf{b}_v \quad (2.24)$$

$$\mathbf{S}\mathbf{w}_\rho = \mathbf{b}_\rho \quad (2.25)$$

where $\mathbf{w}_v, \mathbf{w}_\rho, \mathbf{b}_v$, and $\mathbf{b}_\rho$ are $2M+1$ vectors and $\mathbf{S}$ is a $(2M+1)\times(2M+1)$ matrix. The $\ell^{\rm th}$ entries of $\mathbf{w}_v$ and $\mathbf{w}_\rho$ are $\frac{d\tilde{v}_\ell}{dz}$ and $\frac{d\tilde{\rho}_\ell}{dz}$ respectively, the $\ell^{\rm th}$ entries of $\mathbf{b}_v$ and $\mathbf{b}_\rho$ are equal to the right hand sides of (2.21) and (2.22) respectively, and the $\ell^{\rm th}$ row and $n^{\rm th}$ column entry of $\mathbf{S}$ is $\tilde{v}_m$ where $f_m + f_n = f_\ell$.

We choose the relation between the initial value of the circuit current and the initial value of the circuit voltage as

$$\tilde{I}_\ell(0) = -\frac{\tilde{V}_\ell(0)}{\tilde{K}(f_\ell\omega_0)}. \quad (2.26)$$

[2]For better numerical performance one should solve a normalized system of equations. See Appendix A for normalized versions of the TWT models.

We show in Appendix B that for the linearization of (2.18)–(2.22), (2.26) ensures that only the three forward waves of Pierce theory are excited [41]. If one includes modulations on beam quantities, (2.26) is still the appropriate relation between initial voltage and initial current so that only forward waves are excited.

The circuit power at angular frequency ω is due to both the positive and negative frequencies, so[3]

$$P_\omega(z) \;=\; -\left[\tilde{V}_\ell(z)\tilde{I}^*_\ell(z) + \tilde{V}^*_\ell(z)\tilde{I}_\ell(z)\right]. \tag{2.27}$$

The negative sign in (2.27) is due to the form of the telegrapher equations which are chosen to be consistent with [41]. Given input power $P_\omega(0)$ and phase $\phi_\omega(0)$ at $\omega = f_\ell\omega_0 > 0$, the initial value of circuit voltage is

$$\tilde{V}_\ell(0) \;=\; \sqrt{\frac{P_\omega(0)\tilde{K}(f_\ell\omega_0)}{2}}\, e^{i\phi_\omega(0)} \tag{2.28}$$

$$\tilde{V}_{-\ell}(0) \;=\; \tilde{V}^*_\ell(0). \tag{2.29}$$

If there are (periodic) modulations on any of the quantities at the input, one can calculate the proper initial values using (2.16). Otherwise for $\ell \neq 0$, $\tilde{E}_\ell = \tilde{v}_\ell = \tilde{\rho}_\ell = 0$. Also one has $\tilde{v}_0(0) = u_0$, $\tilde{\rho}_0(0) = \rho_0$, and $\tilde{V}_0 = \tilde{I}_0 = \tilde{E}_0 = 0$.

By treating this problem as an initial value problem with the described initial conditions we are assuming a perfectly matched load and no reflections. When a sever and a mismatched load are included, one must treat the problem as a boundary value problem and use an iterative scheme such as a shooting method [63, Ch. 17]. In the boundary value problem the relation of circuit voltage to circuit current at the input [cf. eqn. (2.26)] will be determined as part of the solution to be consistent with the reflections.

2.2.2 LATTE

2.2.2.1 Derivation

We derive LATTE (Lagrangian TWT Equations) from the Eulerian equations (2.10)–(2.14). The Eulerian independent variables are (z, ψ), where z is axial position and ψ is phase. The Lagrangian independent variables are (z, ψ_0), where z is axial position and ψ_0 is the phase position of a fluid element with respect to the stream wave[4] *when the fluid element is at* $z = 0$. ψ_0 takes values from 0 to -2π.

[3] In Pierce's book [61] he states that the power is $\frac{\tilde{V}_\ell\tilde{V}^*_\ell}{2\tilde{K}(f_\ell\omega_0)}$. Since this result comes from substituting $\tilde{I}_\ell(z) = -\frac{\tilde{V}_\ell(z)}{\tilde{K}(f_\ell\omega_0)}$, which is only valid for source-free transmission line equations, into equation (2.27), it is not valid for the TWT model.

[4] The "stream wave" is a hypothetical wave of frequency ω_0 traveling with speed u_0.

The transformation from Lagrangian to Eulerian coordinates is given by functions Z and Ψ

$$\left[\begin{array}{c} z \\ \psi \end{array} \right] = \left[\begin{array}{c} Z(z,\psi_0) \\ \Psi(z,\psi_0) \end{array} \right]. \tag{2.30}$$

$Z(z,\psi_0)$ is the axial position of fluid element ψ_0 at z so

$$Z(z,\psi_0) = z. \tag{2.31}$$

$\Psi(z,\psi_0)$ is the phase position of fluid element ψ_0 with respect to the stream wave at z.

A function g^{E} of Eulerian variables (z,ψ) is transformed to a function g^{L} of Lagrangian variables (z,ψ_0) using

$$\begin{aligned} g^{\mathrm{L}}(z,\psi_0) &= g^{\mathrm{E}}(Z(z,\psi_0),\Psi(z,\psi_0)) \\ &= g^{\mathrm{E}}(z,\Psi(z,\psi_0)). \end{aligned} \tag{2.32}$$

The linearization of coordinate transformation (2.30) is the matrix

$$\left[\begin{array}{cc} 1 & 0 \\ \frac{\partial \Psi}{\partial z} & \frac{\partial \Psi}{\partial \psi_0} \end{array} \right] \tag{2.33}$$

and its Jacobian J is the determinant of (2.33)

$$J = \frac{\partial \Psi}{\partial \psi_0}. \tag{2.34}$$

Partial derivatives transform via

$$\left[\begin{array}{cc} \frac{\partial}{\partial z} & \frac{\partial}{\partial \psi} \end{array} \right] = \left[\begin{array}{cc} \frac{\partial}{\partial z} & \frac{\partial}{\partial \psi_0} \end{array} \right] \left[\begin{array}{cc} 1 & 0 \\ \frac{\partial \Psi}{\partial z} & \frac{\partial \Psi}{\partial \psi_0} \end{array} \right]^{-1}. \tag{2.35}$$

Consistent with the method of characteristics we take

$$\frac{\partial \Psi}{\partial z} = \frac{\omega_0}{u_0}\left(1 - \frac{u_0}{v^{\mathrm{L}}}\right) \tag{2.36}$$

then the convective derivative [in (z,ψ) coordinates] becomes

$$v^{\mathrm{E}}\frac{\partial v^{\mathrm{E}}}{\partial z} + \omega_0\left(\frac{v^{\mathrm{E}}}{u_0} - 1\right)\frac{\partial v^{\mathrm{E}}}{\partial \psi} = v^{\mathrm{L}}\frac{\partial v^{\mathrm{L}}}{\partial z}. \tag{2.37}$$

Applying the derivative transformations in (2.35) to the continuity equation (2.14) one gets

$$\frac{\partial \Psi}{\partial \psi_0}\frac{\partial \rho^{\mathrm{L}} v^{\mathrm{L}}}{\partial z} = -\omega_0 \frac{\rho^{\mathrm{L}}}{v^{\mathrm{L}}}\frac{\partial v^{\mathrm{L}}}{\partial \psi_0}. \tag{2.38}$$

Taking $\frac{\partial}{\partial\psi_0}$ of (2.36) one gets

$$\frac{\partial}{\partial z}\frac{\partial\Psi}{\partial\psi_0} = \frac{\omega_0}{(v^{\mathrm{L}})^2}\frac{\partial v^{\mathrm{L}}}{\partial\psi_0}. \tag{2.39}$$

Substitute (2.39) into (2.38) and integrate to get

$$\frac{\partial\Psi}{\partial\psi_0}\rho^{\mathrm{L}}v^{\mathrm{L}} = \kappa \tag{2.40}$$

where κ is a constant of integration. We set κ by using the values of $\rho^{\mathrm{L}}v^{\mathrm{L}}$ and $\frac{\partial\Psi}{\partial\psi_0}$ on the ψ_0 axis [by definition $\Psi(0,\psi_0)=\psi_0$ which implies $\frac{\partial\Psi}{\partial\psi_0}(0,\psi_0)=1$] which gives finally

$$\left|\frac{\partial\Psi}{\partial\psi_0}\right|\rho^{\mathrm{L}}v^{\mathrm{L}} = \rho^{\mathrm{L}}(0,\psi_0)v^{\mathrm{L}}(0,\psi_0) \tag{2.41}$$

$$= \frac{I_0(\psi_0)}{A}. \tag{2.42}$$

The absolute value is added to the Jacobian since it would appear in an integral form of conservation of mass.

As a last point regarding the coordinate transformation we change variables in an integral. Pulling the equation for the Fourier coefficient of ρ back to Lagrangian coordinates (for fixed z) one gets

$$\tilde{\rho^{\mathrm{E}}}_\ell = \frac{1}{2\pi}\int_{2\pi}\rho^{\mathrm{E}}e^{-if_\ell\psi}\,d\psi \tag{2.43}$$

$$= \frac{1}{2\pi}\int_{2\pi}\rho^{\mathrm{L}}\left|\frac{\partial\Psi}{\partial\psi_0}\right|e^{-if_\ell\Psi(z,\psi_0)}d\psi_0 \tag{2.44}$$

$$= \frac{1}{2\pi}\int_{2\pi}\frac{I_0(\psi_0)e^{-if_\ell\Psi(z,\psi_0)}}{Av^{\mathrm{L}}(z,\psi_0)}\,d\psi_0 \tag{2.45}$$

where we have used (2.41) to substitute for the Jacobian.

Finally we derive LATTE from (2.10)–(2.14). Equations (2.46)–(2.48) are (2.18)–(2.20) with (2.45) substituted for $\tilde{\rho}_\ell$. Equation (2.14) was used to get (2.45). For (2.13) one writes E and I using the Fourier series synthesis equation (2.15) in Lagrangian coordinates. Equation (2.36) is also included as model equation (2.50). The circuit equations, space

charge equation, Newton's law, and phase relation are (leaving off the superscript L)

$$\frac{d\tilde{V}_\ell}{dz} = -\frac{if_\ell\omega_0}{u_0}\tilde{V}_\ell - \frac{if_\ell\omega_0\tilde{K}(f_\ell\omega_0)}{\tilde{v}_{\rm ph}(f_\ell\omega_0)}\tilde{I}_\ell \tag{2.46}$$

$$\frac{d\tilde{I}_\ell}{dz} = -\frac{if_\ell\omega_0}{\tilde{K}(f_\ell\omega_0)\tilde{v}_{\rm ph}(f_\ell\omega_0)}\tilde{V}_\ell - \frac{if_\ell\omega_0}{u_0}\tilde{I}_\ell + if_\ell\omega_0\frac{1}{2\pi}\int_{2\pi}\frac{I_0(\psi_0)e^{-if_\ell\Psi(z,\psi_0)}}{v(z,\psi_0)}d\psi_0 \tag{2.47}$$

$$\frac{d\tilde{E}_\ell}{dz} = -\frac{if_\ell\omega_0}{u_0}\tilde{E}_\ell + \frac{1}{\epsilon_0 A}\frac{1}{2\pi}\int_{2\pi}\frac{I_0(\psi_0)e^{-if_\ell\Psi(z,\psi_0)}}{v(z,\psi_0)}d\psi_0 \tag{2.48}$$

$$\frac{\partial v}{\partial z} = \frac{1}{v}\sum_{\ell=-\infty}^{\infty}\left\{\frac{if_\ell\omega_0 e\tilde{K}(f_\ell\omega_0)}{m_e\tilde{v}_{\rm ph}(f_\ell\omega_0)}\tilde{I}_\ell + \frac{e}{m_e}\tilde{R}(f_\ell\omega_0)\tilde{E}_\ell\right\}e^{if_\ell\Psi(z,\psi_0)} \tag{2.49}$$

$$\frac{\partial\Psi}{\partial z} = \frac{\omega_0}{u_0}\left(1-\frac{u_0}{v}\right). \tag{2.50}$$

These equations are valid for an arbitrary periodic electron beam modulation. Equations (2.49) and (2.50) are ordinary differential equations parameterized by ψ_0. For calculations one represents the beam as a finite number of "disks" and there are equations (2.49) and (2.50) for each disk. In this case the integration over ψ_0

$$\frac{1}{2\pi}\int_{2\pi}\frac{I_0(\psi_0)e^{-if_\ell\Psi(z,\psi_0)}}{v^{\rm L}(z,\psi_0)}\,d\psi_0 \tag{2.51}$$

becomes the sum

$$\frac{1}{N}\sum_{j=1}^{N}\frac{I_0(\psi_{0j})e^{-if_\ell\Psi(z,\psi_{0j})}}{v^{\rm L}(z,\psi_{0j})}. \tag{2.52}$$

The transformation reveals interesting information about the relation between MUSE and LATTE. For example, the Lagrangian continuity equation (2.41) is often written as (see e.g. [39, pg. 302])

$$Idt = I_0dt_0 \tag{2.53}$$

where I is beam current, t is time, I_0 is initial beam current, and t_0 is the Lagrangian initial time. However, it has not been pointed out in the microwave device literature that

$$\frac{dt}{dt_0} = \frac{I_0}{I} \tag{2.54}$$

is the Jacobian of the transformation from Lagrangian to Eulerian coordinates. We use this fact in Section 2.3.3 to examine when electron overtaking occurs.

2.2.2.2 Constant of the motion

In Lagrangian coordinates the time averaged linear energy density is

$$W = \frac{m_e}{e}\frac{1}{2\pi}\int_{2\pi} I_0(\psi_0)\frac{v}{2}d\psi_0 + \frac{1}{4}\sum_{\ell=-\infty}^{\infty}\left\{\frac{\tilde{K}(f_\ell\omega_0)}{\tilde{v}_{\rm ph}(f_\ell\omega_0)}\tilde{I}_\ell\tilde{I}_\ell^* + \frac{1}{\tilde{v}_{\rm ph}(f_\ell\omega_0)\tilde{K}(f_\ell\omega_0)}\tilde{V}_\ell\tilde{V}_\ell^* - \epsilon_0 A\tilde{R}(f_\ell\omega_0)\tilde{E}_\ell\tilde{E}_\ell^*\right\}. \quad (2.55)$$

The velocity integral is the time average linear beam kinetic energy density. Expressed in Eulerian coordinates this is

$$\frac{m_e}{e}\frac{1}{2\pi}\int_{2\pi} I_0(\psi_0)\frac{v^{\rm L}}{2}d\psi_0 = \frac{m_e A}{e}\frac{1}{2\pi}\int_{2\pi}\frac{\rho^{\rm E}(v^{\rm E})^2}{2}d\psi. \quad (2.56)$$

In the MUSE variables this term is

$$\frac{m_e A}{e}\frac{1}{2\pi}\int_{2\pi}\frac{\rho^{\rm E}(v^{\rm E})^2}{2}d\psi = \frac{m_e A}{2e}\sum_{\substack{\ell,m,n\\ f_\ell+f_m+f_n=0}}\tilde{\rho}_\ell\tilde{v}_m\tilde{v}_n. \quad (2.57)$$

When the circuit parameters $\tilde{K}(f_\ell\omega_0), \tilde{v}_{\rm ph}(f_\ell\omega_0), \tilde{R}(f_\ell\omega_0)$ are not functions of z the energy density W is a constant of the motion. The most convenient way to show this is to compute the derivative in Lagrangian coordinates, then change the result to Eulerian coordinates. Using $v = v^*$,

$$\begin{aligned}
\frac{\partial}{\partial z}4W &= \frac{m_e}{e}\frac{1}{2\pi}\int_{2\pi} I_0(\psi_0)\left[\frac{\partial v}{\partial z} + \left(\frac{\partial v}{\partial z}\right)^*\right]d\psi_0 + \sum_{\ell=-\infty}^{\infty}\left\{\frac{\tilde{K}(f_\ell\omega_0)}{\tilde{v}_{\rm ph}(f_\ell\omega_0)}\left[\frac{d\tilde{I}_\ell}{dz}\tilde{I}_\ell^* + \tilde{I}_\ell\frac{d\tilde{I}_\ell^*}{dz}\right] + \frac{1}{\tilde{v}_{\rm ph}(f_\ell\omega_0)\tilde{K}(f_\ell\omega_0)}\left[\frac{d\tilde{V}_\ell}{dz}\tilde{V}_\ell^* + \tilde{V}_\ell\frac{d\tilde{V}_\ell^*}{dz}\right]\right.\\
&\quad \left. - \epsilon_0 A\tilde{R}(f_\ell\omega_0)\left[\frac{d\tilde{E}_\ell}{dz}\tilde{E}_\ell^* + \tilde{E}_\ell\frac{d\tilde{E}_\ell^*}{dz}\right]\right\}\\
&= \left[\sum_{\ell=-\infty}^{\infty}\left\{\frac{if_\ell\omega_0 A\tilde{K}(f_\ell\omega_0)}{\tilde{v}_{\rm ph}(f_\ell\omega_0)}\tilde{I}_\ell\tilde{\rho}_\ell^* + A\tilde{R}(f_\ell\omega_0)\tilde{E}_\ell\tilde{\rho}_\ell^*\right\}\right.\\
&\quad \left. + \sum_{\ell=-\infty}^{\infty}\left\{-\frac{if_\ell\omega_0 A\tilde{K}(f_\ell\omega_0)}{\tilde{v}_{\rm ph}(f_\ell\omega_0)}\tilde{I}_\ell^*\tilde{\rho}_\ell + A\tilde{R}(f_\ell\omega_0)\tilde{E}_\ell^*\tilde{\rho}_\ell\right\}\right]\\
&\quad + \sum_{\ell=-\infty}^{\infty}\left\{\frac{if_\ell\omega_0 A\tilde{K}(f_\ell\omega_0)}{\tilde{v}_{\rm ph}(f_\ell\omega_0)}\left[\tilde{I}_\ell^*\tilde{\rho}_\ell - \tilde{I}_\ell\tilde{\rho}_\ell^*\right] - A\tilde{R}(f_\ell\omega_0)\left[\tilde{E}_\ell^*\tilde{\rho}_\ell + \tilde{E}_\ell\tilde{\rho}_\ell^*\right]\right\}\\
&= 0. \quad (2.58)
\end{aligned}$$

2.2.3 S-MUSE

2.2.3.1 Derivation

A simplification of MUSE results in the S-MUSE model. S-MUSE is easier to analyze than MUSE while it retains important nonlinear physics. The simplifications are:

1. approximating $\tilde{\rho}_0(z)$ and $\tilde{v}_0(z)$ as constants ρ_0 and u_0
2. neglecting the AC portion of velocity *in the convective derivative*, i.e. letting $v\frac{\partial}{\partial z} \approx u_0\frac{\partial}{\partial z}$
3. ignoring nonlinearities higher than second order in the continuity equation.

Since we have made the transformation $(z,t) \rightarrow (z,\psi)$, some of the nonlinearity of the convective derivative is retained, i.e. the *original* $v\frac{\partial}{\partial z}$ term [as seen in (2.4) and (2.5)] splits into $v\frac{\partial}{\partial z} + v\frac{\omega_0}{u_0}\frac{\partial}{\partial \psi}$ and we only linearize the first of these two nonlinear terms in (2.13) and (2.14). This is the motivation for introducing the (z,ψ) coordinates in (2.9). The S-MUSE model is:

$$\frac{d\tilde{V}_\ell}{dz} = -\frac{if_\ell\omega_0}{u_0}\tilde{V}_\ell - \frac{if_\ell\omega_0\tilde{K}(f_\ell\omega_0)}{\tilde{v}_{\rm ph}(f_\ell\omega_0)}\tilde{I}_\ell \tag{2.59}$$

$$\frac{d\tilde{I}_\ell}{dz} = -\frac{if_\ell\omega_0}{\tilde{K}(f_\ell\omega_0)\tilde{v}_{\rm ph}(f_\ell\omega_0)}\tilde{V}_\ell - \frac{if_\ell\omega_0}{u_0}\tilde{I}_\ell + if_\ell\omega_0 A\tilde{\rho}_\ell \tag{2.60}$$

$$\frac{d\tilde{E}_\ell}{dz} = -\frac{if_\ell\omega_0}{u_0}\tilde{E}_\ell + \frac{\tilde{\rho}_\ell}{\epsilon_0} \tag{2.61}$$

$$\begin{aligned}\frac{d\tilde{v}_\ell}{dz} &= \frac{if_\ell\omega_0 e\tilde{K}(f_\ell\omega_0)}{m_e u_0\tilde{v}_{\rm ph}(f_\ell\omega_0)}\tilde{I}_\ell + \frac{e}{m_e u_0}\tilde{R}(f_\ell\omega_0)\tilde{E}_\ell \\ &\quad - \frac{1}{u_0^2}\sum_{\substack{m\neq 0, n\neq 0\\ f_m+f_n=f_\ell}} if_n\omega_0\tilde{v}_m\tilde{v}_n\end{aligned} \tag{2.62}$$

$$\begin{aligned}\frac{d\tilde{\rho}_\ell}{dz} &= -\frac{if_\ell\omega_0 e\rho_0\tilde{K}(f_\ell\omega_0)}{m_e u_0^2\tilde{v}_{\rm ph}(f_\ell\omega_0)}\tilde{I}_\ell - \frac{e\rho_0}{m_e u_0^2}\tilde{R}(f_\ell\omega_0)\tilde{E}_\ell - \frac{if_\ell\omega_0\rho_0}{u_0^2}\tilde{v}_\ell \\ &\quad - \frac{e}{m_e u_0^2}\sum_{\substack{m\neq 0, n\neq 0\\ f_m+f_n=f_\ell}} \frac{if_m\omega_0\tilde{K}(f_m\omega_0)}{\tilde{v}_{\rm ph}(f_m\omega_0)}\tilde{I}_m\tilde{\rho}_n \\ &\quad - \frac{e}{m_e u_0^2}\sum_{\substack{m\neq 0, n\neq 0\\ f_m+f_n=f_\ell}} \tilde{R}(f_m\omega_0)\tilde{E}_m\tilde{\rho}_n \\ &\quad + \frac{\rho_0}{u_0^3}\sum_{\substack{m\neq 0, n\neq 0\\ f_m+f_n=f_\ell}} if_n\omega_0\tilde{v}_m\tilde{v}_n - \frac{if_\ell\omega_0}{u_0^2}\sum_{\substack{m\neq 0, n\neq 0\\ f_m+f_n=f_\ell}} \tilde{v}_m\tilde{\rho}_n\end{aligned} \tag{2.63}$$

where $-M \leq \ell \leq M, \ell \neq 0$.

2.2.3.2 Vector form

The S-MUSE model (2.59)–(2.63) may be written in the following vector form that is particularly useful for analysis

$$\dot{\mathbf{x}} \;=\; \mathbf{A}\mathbf{x} + \mathbf{H}(\mathbf{x},\mathbf{x}) \tag{2.64}$$

where $\mathbf{x}$ is a $5(2M)$ dimensional complex vector, $\mathbf{A}$ is a $5(2M)\times 5(2M)$ complex matrix, $\mathbf{H}$ is a $5(2M)\times 5(2M)\times 5(2M)$ complex 3-tensor, and overdot represents $\frac{d}{dz}$.

For elements $\mathbf{x}_{\ell_i}$, $\mathbf{A}_{\ell_{ij}}$, and $\mathbf{H}_{\ell_i m_j n_k}$ the subscripts (ℓ, m, n) run from $-M$ to M excluding zero, and the subsubscripts (i, j, k) run from 1 to 5. The subscript ℓ indexes frequencies in the set $\{f_\ell\}$. We index $\mathbf{x}$ with double subscripts such that $\mathbf{x} = [\mathbf{x}_{-M}\ldots\mathbf{x}_{-1}\mathbf{x}_1\ldots\mathbf{x}_M]^{\mathrm{T}}$ and $\mathbf{x}_\ell = [\mathbf{x}_{\ell_1}\mathbf{x}_{\ell_2}\mathbf{x}_{\ell_3}\mathbf{x}_{\ell_4}\mathbf{x}_{\ell_5}]^{\mathrm{T}} = [\tilde{V}_\ell\,\tilde{I}_\ell\,\tilde{E}_\ell\,\tilde{v}_\ell\,\tilde{\rho}_\ell]^{\mathrm{T}}$.

The matrix $\mathbf{A}$ contains the linear parts of (2.59)–(2.63). It is block diagonal with entry $\mathbf{A}_\ell \equiv \mathbf{A}_{\ell\ell}$. The entries $\mathbf{A}_{\ell_{ij}}$ of the block diagonal element $\mathbf{A}_\ell$ are

$$\mathbf{A}_{\ell_{11}} \;=\; -\frac{if_\ell\omega_0}{u_0} \tag{2.65}$$

$$\mathbf{A}_{\ell_{12}} \;=\; -\frac{if_\ell\omega_0\tilde{K}(f_\ell\omega_0)}{\tilde{v}_{\mathrm{ph}}(f_\ell\omega_0)} \tag{2.66}$$

$$\mathbf{A}_{\ell_{21}} \;=\; -\frac{if_\ell\omega_0}{\tilde{K}(f_\ell\omega_0)\tilde{v}_{\mathrm{ph}}(f_\ell\omega_0)} \tag{2.67}$$

$$\mathbf{A}_{\ell_{22}} \;=\; -\frac{if_\ell\omega_0}{u_0} \tag{2.68}$$

$$\mathbf{A}_{\ell_{25}} \;=\; if_\ell\omega_0 A \tag{2.69}$$

$$\mathbf{A}_{\ell_{33}} \;=\; -\frac{if_\ell\omega_0}{u_0} \tag{2.70}$$

$$\mathbf{A}_{\ell_{35}} \;=\; \frac{1}{\epsilon_0} \tag{2.71}$$

$$\mathbf{A}_{\ell_{42}} \;=\; \frac{if_\ell\omega_0 e\tilde{K}(f_\ell\omega_0)}{m_e u_0\tilde{v}_{\mathrm{ph}}(f_\ell\omega_0)} \tag{2.72}$$

$$\mathbf{A}_{\ell_{43}} \;=\; \frac{e\tilde{R}(f_\ell\omega_0)}{m_e u_0} \tag{2.73}$$

$$\mathbf{A}_{\ell_{52}} \;=\; -\frac{if_\ell\omega_0 e\rho_0\tilde{K}(f_\ell\omega_0)}{m_e u_0^2\tilde{v}_{\mathrm{ph}}(f_\ell\omega_0)} \tag{2.74}$$

$$\mathbf{A}_{\ell_{53}} \;=\; -\frac{e\rho_0\tilde{R}(f_\ell\omega_0)}{m_e u_0^2} \tag{2.75}$$

$$\mathbf{A}_{\ell_{54}} \;=\; -\frac{if_\ell\omega_0\rho_0}{u_0^2}. \tag{2.76}$$

Entries $\mathbf{A}_{\ell_{ij}}$ not listed above are zero.

The 3-tensor entries $\mathbf{H}_{\ell_i m_j n_k}$ for (ℓ, m, n) are

Case 1 If ℓ, m, n are such that $f_\ell = f_m + f_n$ then

$$\mathbf{H}_{\ell_4 m_4 n_4} = -\frac{i f_n \omega_0}{u_0^2} \tag{2.77}$$

$$\mathbf{H}_{\ell_5 m_2 n_5} = -\frac{e}{m_e u_0^2} \frac{i f_m \omega_0 \tilde{K}(f_m \omega_0)}{\tilde{v}_{\rm ph}(f_m \omega_0)} \tag{2.78}$$

$$\mathbf{H}_{\ell_5 m_3 n_5} = -\frac{e \tilde{R}(f_m \omega_0)}{m_e u_0^2} \tag{2.79}$$

$$\mathbf{H}_{\ell_5 m_4 n_4} = \frac{\rho_0}{u_0^3} i f_n \omega_0 \tag{2.80}$$

$$\mathbf{H}_{\ell_5 m_4 n_5} = -\frac{i f_\ell \omega_0}{u_0^2}. \tag{2.81}$$

Entries for (i, j, k) not listed are zero.

Case 2 If ℓ, m, n are such that $f_\ell \neq f_m + f_n$ then

$$\mathbf{H}_{\ell_i m_j n_k} = 0 \tag{2.82}$$

for all (i, j, k).

For the $\ell^{\rm th}$ component of $\dot{\mathbf{x}}$ we have

$$\dot{\mathbf{x}}_\ell = \mathbf{A}_\ell \mathbf{x}_\ell + \sum_{\substack{m,n \\ f_m + f_n = f_\ell}} \mathbf{H}_{\ell m n}(\mathbf{x}_m, \mathbf{x}_n) \tag{2.83}$$

where the $i^{\rm th}$ component of the quadratic term is

$$\left(\sum_{\substack{m,n \\ f_m + f_n = f_\ell}} \mathbf{H}_{\ell m n}(\mathbf{x}_m, \mathbf{x}_n) \right)_i = \sum_{\substack{m,n \\ f_\ell = f_m + f_n}} \sum_{j=1}^{5} \sum_{k=1}^{5} \mathbf{H}_{\ell_i m_j n_k} \mathbf{x}_{m_j} \mathbf{x}_{n_k}. \tag{2.84}$$

2.3 Numerical example

In this section we consider a numerical example comparing the models amongst themselves and Christine 1-d. First we look at circuit power as a function of axial distance. We use LATTE as a benchmark and present deviations in dB of the other models from LATTE. For the simulations we also check the constant of the motion (2.55) and compare the terms making up the constant of the motion. For the case of one drive frequency we consider the question of electron overtaking and its correlation to the deviation of MUSE from LATTE. Lastly, we discuss practical issues concerning the choice of frequencies for a simulation comparison with Christine 1-d.

For our numerical study we simulate one constant pitch section of the 8537H TWT with no sever or circuit loss. The parameters for the 8537H are taken from [2] and are shown in Table 2.1. For the frequency dependent parameters $\tilde{v}_{\rm ph}(f_\ell\omega_0)$, $\tilde{K}(f_\ell\omega_0)$, and $\tilde{R}(f_\ell\omega_0)$ we use the outputs of Christine 1-d's tape helix model and space charge reduction factor calculation. These parameter values ensure that MUSE, LATTE, and S-MUSE use the same dispersion parameters as Christine 1-d.

The set of frequencies includes two drive frequencies, the second order products, and the third order intermodulation (3IM) frequencies $2f_1 - f_2$ and $2f_2 - f_1$. Table 2.2 lists the frequencies and dispersion parameters.

The calculations are done using a fixed step $4^{\rm th}$ order Runge-Kutta integrator.

Table 2.1 8537H Parameters (Constant Pitch Section)

Parameter	**Model Value**
Helix mean radius	0.2353 cm
Helix wire width	0.0305 cm
Pitch	0.13 cm
Cathode voltage	-3.1 kV
Beam current	65.5 mA
Min. beam radius	0.0962 cm
BN ($\epsilon_{\rm r} = 5.4$) support rods smeared permittivity	1.21

2.3.1 Circuit power versus axial position

In Fig. 2.1 we plot axial power of the drive, harmonic, and 3IM frequencies for the MUSE model and LATTE. The models agree extremely well for a majority of the TWT length, but there is disagreement between the models at saturation. For a quantitative comparison of all of the models we plot dB difference of the models from LATTE. Figures 2.2–2.4 show the dB difference from LATTE for the drive frequencies, harmonics and sum frequency, and the 3IMs respectively. For each model, the frequency pair having the largest maximum deviation is represented in the figure.

For small z values Figs. 2.3 and 2.4 exhibit large fluctuations in the dB difference from LATTE for the harmonics and 3IMs respectively. However, the numbers being compared are very small and are below the numerical noise floor of the computations. The differences between the harmonics converge before the differences between the 3IMs since the harmonics need to rise above the numerical noise floor before the 3IMs may rise above the numerical noise floor. For $z = 5$cm steady state differences are achieved in both figures.

Inspection of Figs. 2.2–2.4 confirms that the agreement between LATTE and MUSE is very good prior to the onset of saturation (roughly $z \leq 35$cm). Up to $z = 30$cm the

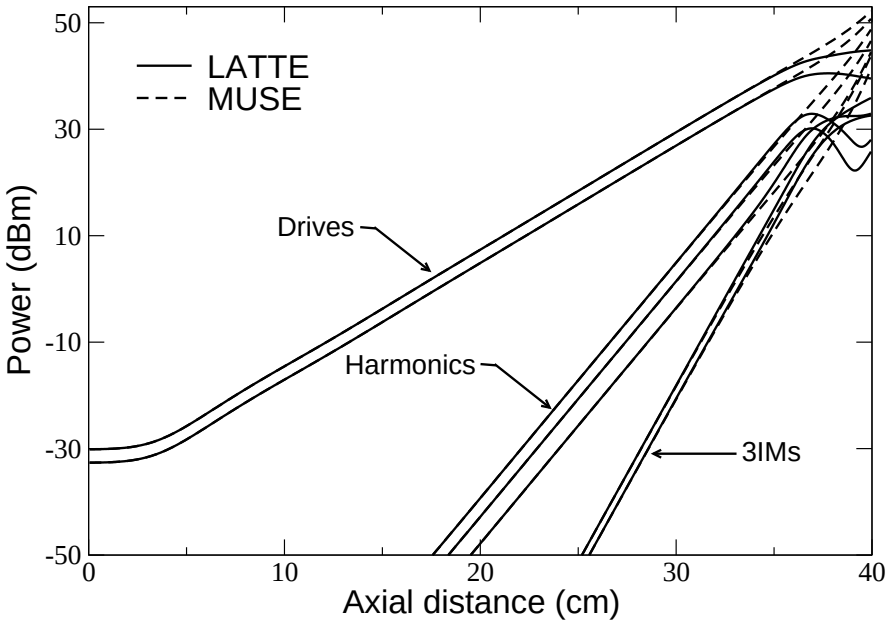

Figure 2.1 Power versus axial distance for LATTE and MUSE.

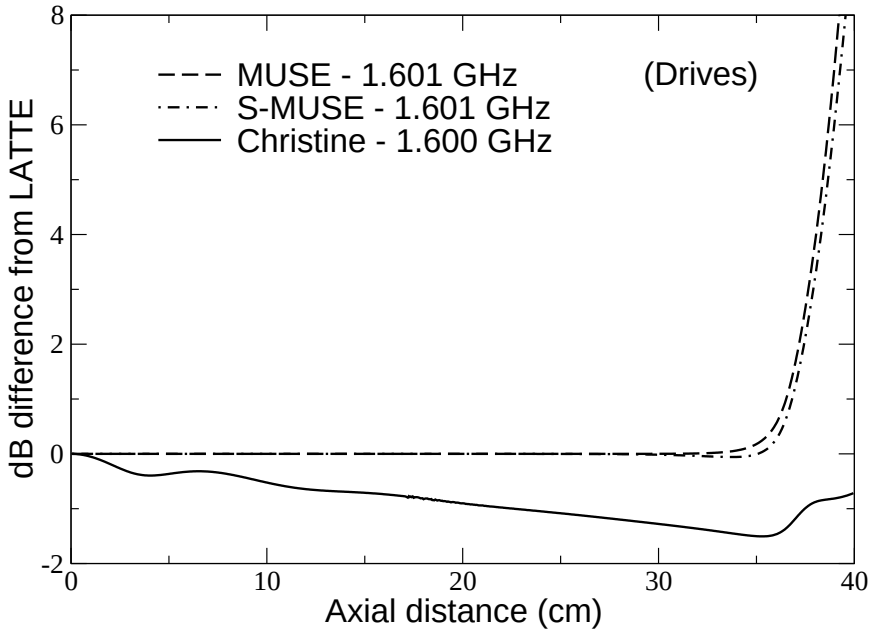

Figure 2.2 dB difference of drive frequencies from LATTE versus axial distance.

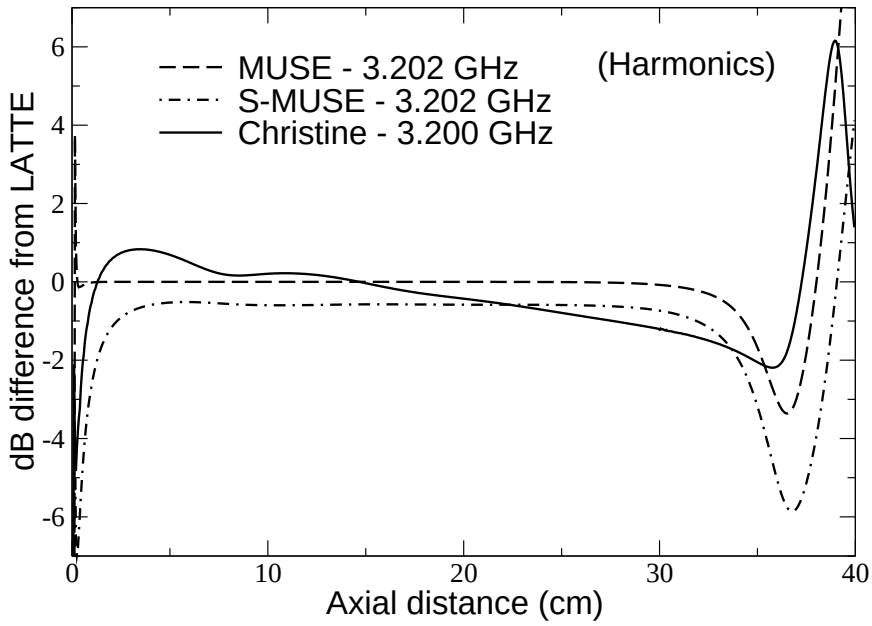

Figure 2.3 dB difference of harmonics and sum frequency from LATTE versus axial distance.

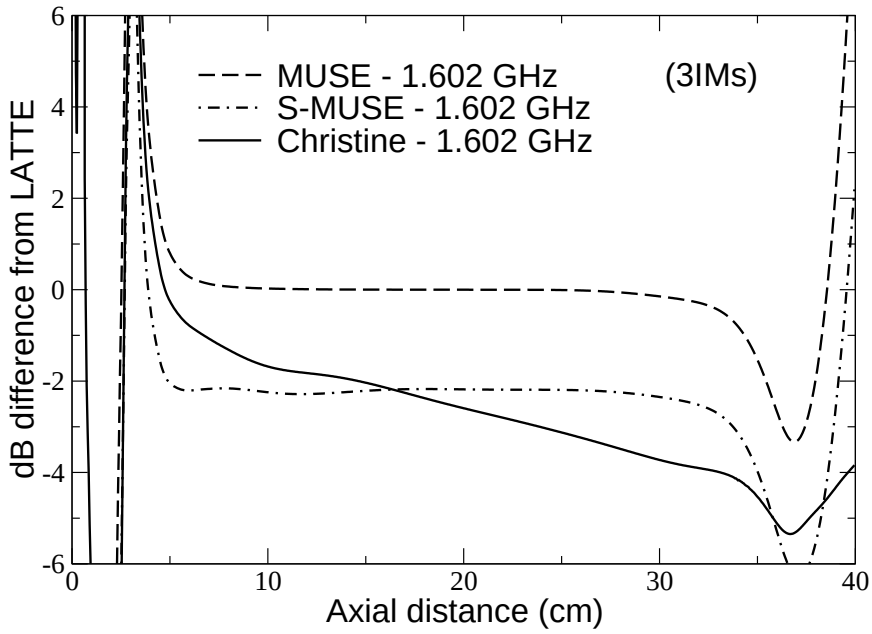

Figure 2.4 dB difference 3IMs from LATTE versus axial distance.

Table 2.2 Simulation Frequencies and Dispersion Parameters

f (GHz)	$\tilde{K}$ (Ω)	$\tilde{v}_{\rm ph}$ ($\times 10^7 m/s$)	$\tilde{R}$
0.001	365.40	3.2845	0.00100
1.599	225.13	2.9983	0.04529
1.600	224.98	2.9980	0.04535
1.601	224.82	2.9977	0.04540
1.602	224.67	2.9974	0.04545
3.200	42.68	2.6460	0.14945
3.201	42.62	2.6459	0.14952
3.202	42.57	2.6458	0.14959

discrepancy is less than 0.1dB. The constant level of the nonlinear products confirms that growth rates of LATTE, MUSE and S-MUSE are the same, even though we see that S-MUSE is less accurate than MUSE, especially for the higher order nonlinear products.

Finally we see the difference between LATTE and Christine 1-d is $<$ 2dB, $\leq$ 3dB, and $\leq$ 5dB in the drives, harmonics, and 3IMs respectively for $z \leq 35$cm. One sees from Fig. 2.2 that the linear growth rates of the drive frequencies are very slightly different for the two models, which results in a disagreement of predicted power between the models which grows with axial distance. The difference in gain predicted by the two models is about 1.5dB out of 72dB. The differences in the nonlinear products are likely due to the nonlinear amplification of the differences in the drive frequencies.

Since Christine 1-d has been validated experimentally [2], the disagreement between LATTE and Christine 1-d raises the question of experimental validation of LATTE and MUSE. To address this question we studied the sensitivity of the output power on certain input parameters. For the present case we found that less than a 1% change in beam voltage can produce a 1dB difference in output power, and a 10% change in "smeared" relative dielectric constant can produce more than a 2 dB difference in output power. In [2] beam voltage and relative dielectric constant were changed by more than 8% from their experimental values. Therefore, we observe that the input parameters to our models could be changed within the same bounds used in [2] to match Christine 1-d results.

2.3.2 Constant of the motion

The total energy density (2.55) is a constant of the motion for MUSE and LATTE when circuit parameters are independent of axial distance. This is confirmed in Fig. 2.5 which also shows the energy density for S-MUSE. Since S-MUSE is an approximation to MUSE one would not expect (2.55) to be a constant of the motion. However, as seen in Fig. 2.5, S-MUSE predicts the value to be constant until $z = 30$ cm.

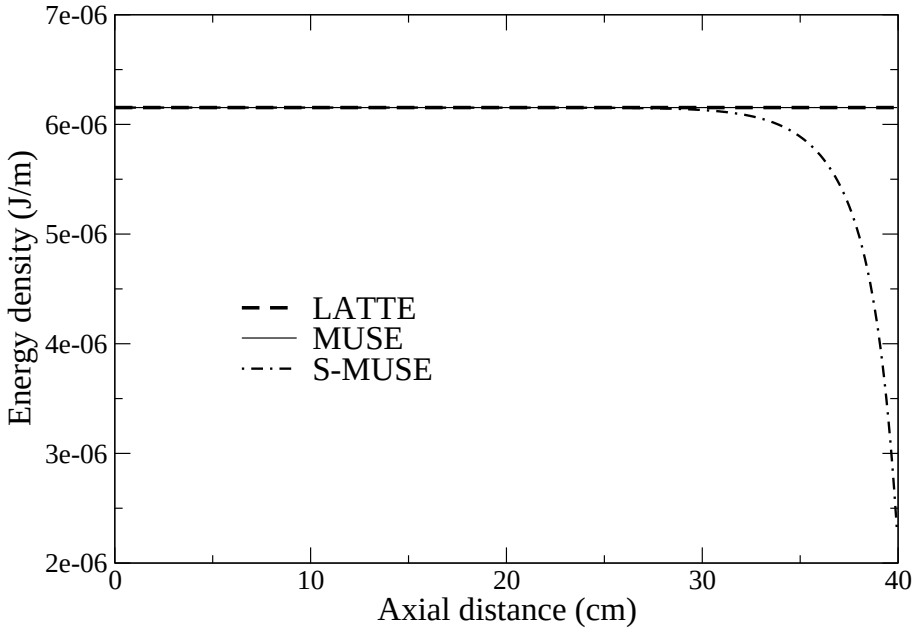

Figure 2.5 Constant of the motion versus axial distance.

Having a constant of the motion can be a useful aid in an investigation of the physics in a model. For example, while LATTE and MUSE predict the constant of the motion, MUSE does not exhibit a saturation (see Fig. 2.1.) This suggests that the partitioning of the energy density is not consistent between the models. In Fig. 2.6 we see that the energy density in the circuit quantities of MUSE continues to rise where that of LATTE saturates. We also see that the beam kinetic energy density continues to decrease in MUSE where in LATTE it reaches a minimum and starts to increase. Additionally there is a difference in the energy density in the space charge field not shown in Fig. 2.6. Thus the energy density terms from the constant of the motion reveal another view of the deviation of the models. Furthermore, the constant of the motion provides a means of checking the error in numerical calculations.

2.3.3 Electron overtaking

Nordsieck's Lagrangian formulation was motivated by the fact that "electrons overtake one another at or even considerably before the point along the tube where the limiting power level is obtained,"[56] in which case Eulerian functions become multi-valued. However, Paschke wanted to "dispel the widespread belief that, because of overtaking, the hydrodynamic model must break down at large levels" [59] with nonlinear Eulerian treatments of electron beams.[5] Since LATTE and MUSE come from the same "hydrodynamic" equations, they are ideally suited to consider overtaking and its role in the deviation of MUSE from LATTE.

The Jacobian of the transformation from Lagrangian to Eulerian coordinates is [equation (2.34)]

$$J \;=\; \frac{\partial \Psi}{\partial \psi_0}.$$

If $J > 0$ for all ψ_0 at some z, then the electron beam, while perhaps bunched, retains the same "disk ordering" (in time) it had at $z = 0$. On the other hand if for some (z, ψ_0) we have $J < 0$, then some disks in the beam have exchanged positions. The z at which electron overtaking occurs is such that $J = 0$ for exactly one value of ψ_0. Beyond this z value $J(z, \psi_0)$ has exactly two zeroes in ψ_0 (for simple overtaking). While overtaking can be observed on a disk trajectory plot such as Fig. 2.7, it may not be possible to establish the exact axial position at which overtaking first occurs. Computing J such as in Fig. 2.8 one can precisely determine the exact axial position where the overtaking starts.

To study if there is a correlation between electron overtaking and the deviation of MUSE from LATTE, we consider a simulation of one drive tone at $f = 1.6$ GHz with the drive level such that saturation occurs at $z = 39.5$ cm. Detailed inspection of Fig. 2.8 reveals that $J = 0$ for one value of ψ_0 at $z = 36.43$ cm. Detailed study of Fig. 2.9, which shows a close-up

[5]The view taken here is that the Eulerian and Lagrangian models are both "hydrodynamic," i.e., they describe the electron beam as a fluid. However, the functions in Lagrangian coordinates allow for the fluid to "fold" over on itself. Only when one seeks approximate numerical solutions to the Lagrangian equations does one get a "disk" model.

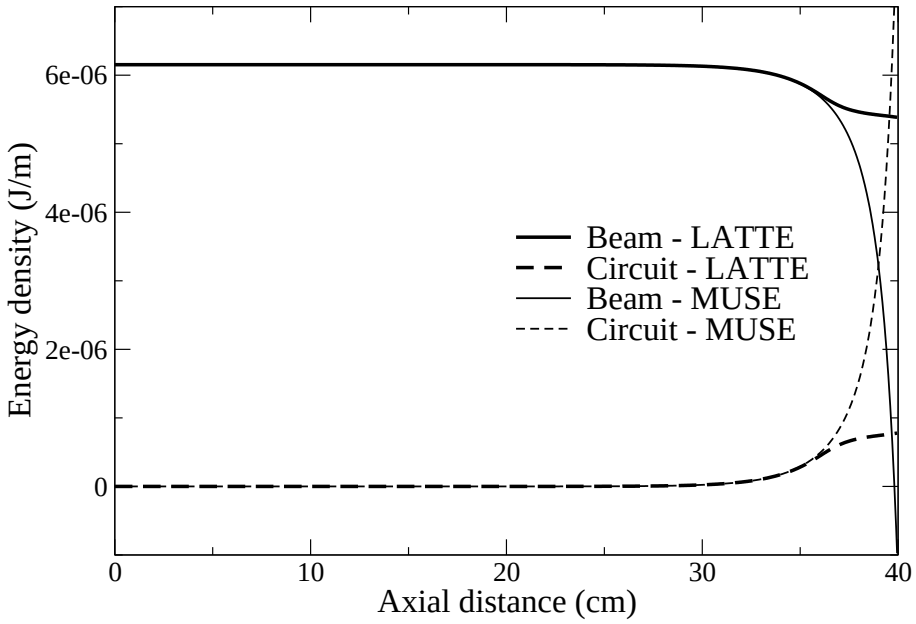

Figure 2.6 Energy densities in circuit and beam versus axial distance for LATTE and MUSE. Energy density in space charge field not shown.

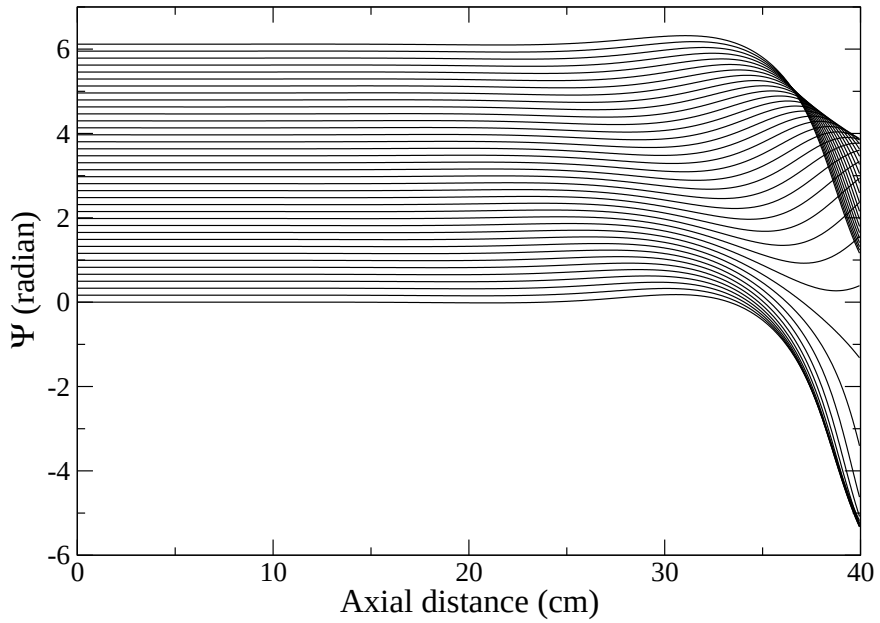

Figure 2.7 Disk orbits versus axial distance.

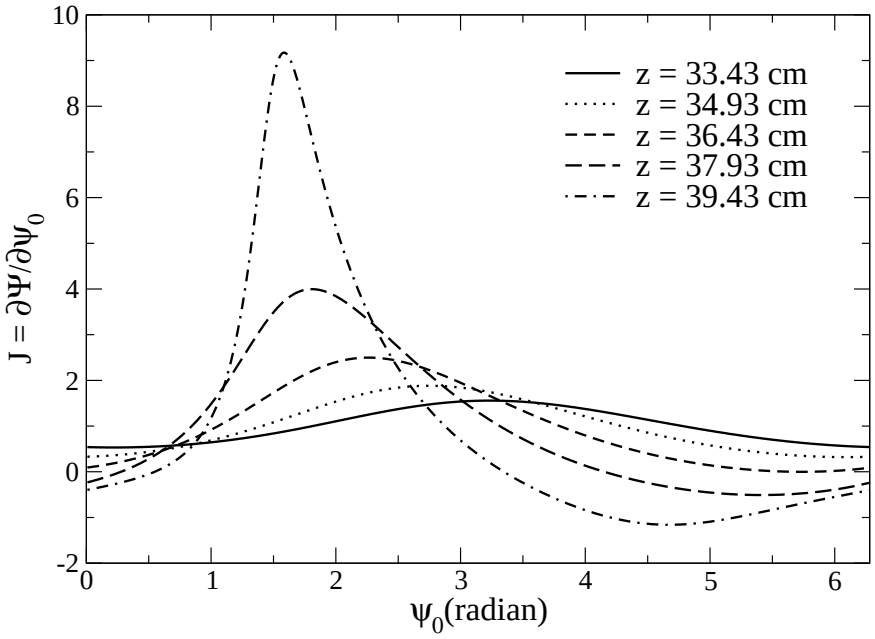

Figure 2.8 Jacobian vs. ψ_0 for several axial positions.

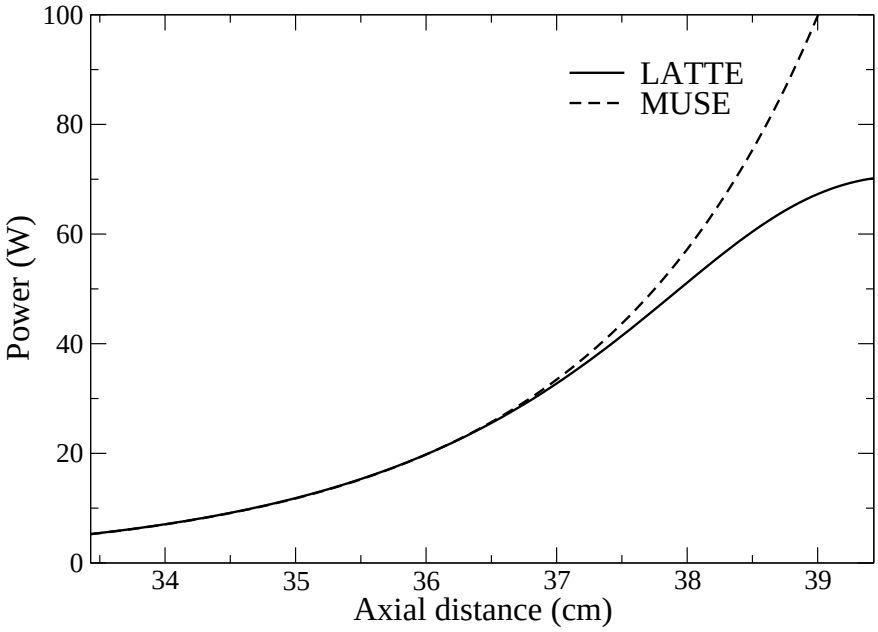

Figure 2.9 Power versus axial distance for LATTE and MUSE.

of the point at which MUSE and LATTE deviate, reveals the position of the deviation to be roughly $z = 36.3$ cm. Therefore, it seems that the deviation of MUSE and LATTE is correlated to electron overtaking.

It is also interesting that the Eulerian model of Datta et al. [20] exhibits saturation for the cases they consider. The discrepancies between the Datta model and MUSE will be a subject of future investigation. Future studies will also attempt to use recent developments in numerical analysis for computing multi-valued solutions of Eulerian functions [53] to enable MUSE to simulate charge overtaking.

2.3.4 Choosing simulation frequencies

Our implementations of MUSE, S-MUSE, and LATTE allow the user to choose any frequency that is an integer multiple of the base frequency. Alternatively, there are two methods of choosing simulation frequencies in the Christine 1-d code. First, one can have the code create an array of frequencies between specified minimum and maximum frequencies spaced by the base frequency. This method alone however would make it impractical to include harmonics of closely spaced drive tones since all frequencies between the drive and the harmonic frequencies that are spaced by the difference frequency would be included. Therefore the Christine 1-d code provides an integer n which allows the user to specify an array for frequencies close to the drive frequencies only, and creates n "harmonic windows" which are frequency arrays containing harmonics of the specified frequency array. The frequencies generated by the use of the harmonic window function may include additional frequencies that are not exactly harmonics of the specified array.

The implications of Christine 1-d's frequency selection method meant that in our Christine 1-d simulations we did not include the difference frequency $f = 1.0$ MHz. Also, due to the use of the harmonic window function we did include a tone at $f = 3.203$ GHz. First we discuss the effect of the difference frequency, then the tone at $f = 3.203$ GHz which is not a nonlinear product of the drive frequencies.

Because of the frequency convolutions in the MUSE model, to predict the evolution of a particular frequency, in principal all frequency pairs adding to the particular frequency need to be accounted for. However, in practice only the dominant contributors are considered. For this example we included the difference frequency $f = 1.0$ MHz since it had a 0.5dB effect on the level of the 3IM in the MUSE simulation.

To estimate the effect of leaving the difference frequency out of the Christine 1-d simulation we ran LATTE simulations including and excluding $f = 1.0$ MHz. For these simulations we observed that the level of the 3IM depends only slightly on the inclusion of the difference frequency (< 0.05dB). Hence, we conclude similar behavior is likely in Christine 1-d. We do not show results for the 1.0 MHz signal since it is so far out of the bandwidth of the TWT.

For $f = 3.203$ GHz we ran LATTE simulations including and excluding this frequency and found that the effect of including $f = 3.203$ GHz is negligible (< 0.02dB difference in 3IMs, less in other tones.) Furthermore, preliminary analytic results from S-MUSE indicate that amplitudes of intermodulation frequencies are determined primarily by the amplitudes

of frequencies mixing to make the product. Therefore, since $f = 3.203$ GHz is not related to the drives or intermodulation frequencies we expect that it will not have a significant effect. For the difference frequency we saw that even though it is a nonlinear product related to the 3IM, it had a small effect on the 3IM in LATTE. An unrelated frequency can be expected to have an even smaller effect.

In sum, we conclude that even though $f = 1.0$ MHz was excluded and $f = 3.203$ GHz was included in the Christine 1-d simulations, it is still appropriate to compare these results to those of MUSE and LATTE.

Finally, we discuss getting dispersion data for $f = 1.0$ MHz since Christine 1-d did not simulate $f = 1.0$ MHz and hence did not generate dispersion data for it. The circuit dispersion parameters at $f = 1.0$ MHz were calculated with an independent tape helix solver and the space charge reduction factor is an estimate based on the values for other frequencies. However, based on MUSE simulations the prediction of the difference frequency does not seem to depend on the dispersion parameters at $f = 1.0$ MHz. This is consistent with preliminary analytic results from S-MUSE which suggest that when a nonlinear product frequency lies out of the linear gain-bandwidth its amplitude and growth rate are primarily determined by the drive frequencies which mix to produce it.

2.4 Discussion

2.4.1 Nonlinearities

The nonlinearities of the MUSE model are different than the nonlinearities of LATTE. The MUSE model has quadratic nonlinearities that arise from the quadratic nonlinearities of the Eulerian electron beam equations. In contrast, LATTE has quadratic nonlinearities, $\frac{1}{v}$ nonlinearities, and complex exponential nonlinearities. As the MUSE predictions agree with LATTE for a majority of the tube length, one can argue that the nonlinear behavior in this region can be described by quadratic nonlinearities. As discussed in Chapter 3, the quadratic nonlinearity is easier to study analytically than the nonlinearities in LATTE.

A quadratic nonlinearity in the time domain becomes a convolution in the frequency domain, as seen in the MUSE model (2.18)–(2.22). This allows one to observe the origin of harmonic and intermodulation frequencies based on the nonlinear combinations of beam velocity and density. As a brief demonstration of the physical insight to be gained from this fact, we consider alternately linearizing v and ρ in the derivation of the MUSE model from (2.1)–(2.5). We use the equations resulting from the "partial linearizations" to examine whether nonlinearities involving v or nonlinearities involving ρ in (2.4) and (2.5) play a larger role in producing distortions.

In both partial linearizations since (2.1)–(2.3) are linear (2.18)–(2.20) are reproduced. If we linearize v in (2.4) and (2.5), make the coordinate transformation (2.9), and compute

Fourier coefficients we get instead of (2.21) and (2.22)

$$\frac{d\tilde{v}_\ell}{dz} = \frac{if_\ell\omega_0 e\tilde{K}(f_\ell\omega_0)}{m_e\tilde{v}_{\rm ph}(f_\ell\omega_0)u_0}\tilde{I}_\ell + \frac{e}{m_e u_0}\tilde{R}(f_\ell\omega_0)\tilde{E}_\ell \tag{2.85}$$

$$\frac{d\tilde{\rho}_\ell}{dz} = -\frac{1}{u_0}\sum_{\substack{m,n\\ f_m+f_n=f_\ell}}\tilde{\rho}_m\left[\frac{d\tilde{v}_n}{dz} + \frac{if_n\omega_0}{u_0}\tilde{v}_n\right]. \tag{2.86}$$

Notice that $\frac{d\tilde{\rho}_0}{dz} \neq 0$.

Similarly linearizing ρ reproduces (2.21) and from (2.5) one gets

$$\sum_{\substack{m,n\\ f_m+f_n=f_\ell}}\tilde{v}_m\frac{d\tilde{\rho}_n}{dz} = if_\ell\omega_0\tilde{\rho}_\ell - \frac{1}{u_0}\sum_{\substack{m,n\\ f_m+f_n=f_\ell}}if_n\omega_0\tilde{v}_m\tilde{\rho}_n - \rho_0\left[\frac{d\tilde{v}_\ell}{dz} + \frac{if_\ell\omega_0}{u_0}\tilde{v}_\ell\right]. \tag{2.87}$$

In (2.87) it is understood that $\frac{d\tilde{\rho}_0}{dz} = 0$.

Figure 2.10 shows the result of integrating the MUSE model (2.18)–(2.22), the v-linearized equations (2.18)–(2.20), (2.85), (2.86), and the ρ-linearized equations (2.18)–(2.21), (2.87) in the 8537H constant pitch section for a drive frequency of $f = 1.6$ GHz. Linearizing the velocity reduces the level of the circuit harmonic more than linearizing the density. Therefore, the velocity has a larger role in producing the harmonic. This observation appears to be valid for many cases.

2.4.2 Dimension scaling of LATTE and MUSE

The computation time of systems of ODEs such as LATTE, MUSE, and Christine 1-d depends on the number of state variables in the simulation, i.e., the *dimension* of the model. (The dimension of the model is equal to the number of coupled ODEs in the system, and hence equal to the number of derivatives that must be calculated at each step of the integration.) The dimension of the MUSE model depends only on the number of frequencies; however, the set of frequencies in a simulation must be chosen with care to assure that all nonlinear product frequencies are accounted for correctly. In a disk model the majority of the dimensions are those accounting for the disks. The number of disks depends on several factors which we will discuss below. To simplify the discussion we consider the dimensions of MUSE and LATTE, noting that other disk models will have similar behavior to LATTE.

LATTE has six complex dimensions per simulation frequency plus $2N$ real dimensions for the disks. MUSE has ten complex dimensions per simulation frequency plus five dimensions for the DC quantities.

To compare dimensions of LATTE to MUSE one needs a formula for the number of disks based on simulation parameters. An estimate for computing the number of disks is given in the Christine 1-d documentation [4]. Depending on simulation parameters, the number of

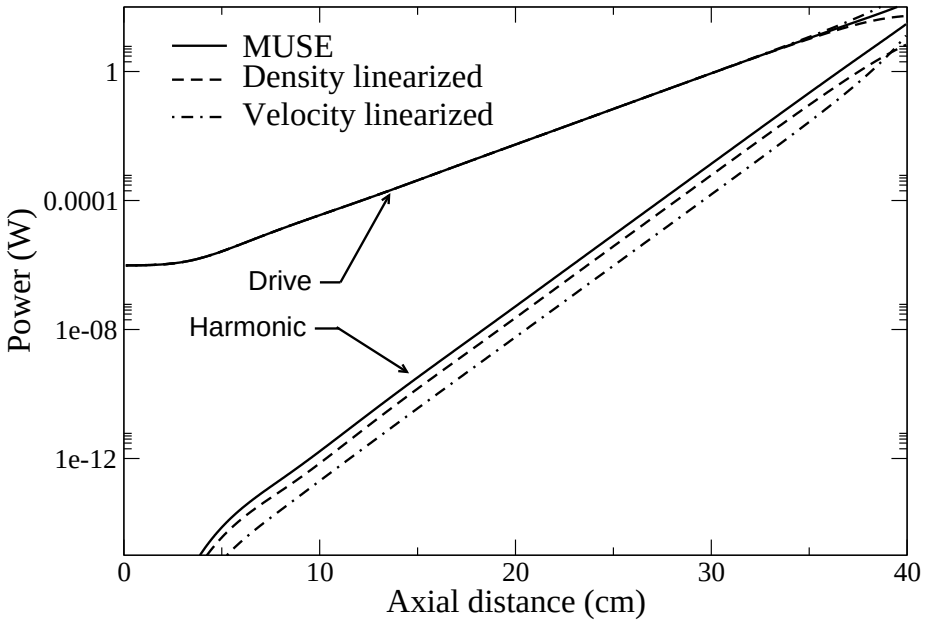

Figure 2.10 Power versus axial distance for partially linearized equations.

disks may need to be increased to obtain convergence of results. We provide a version of this formula applicable to LATTE here. If N_{base} is a "base" number of disks, N_f the number of tones in the simulation, and N_H is the number of harmonics present, then a starting point for the number of disks N in a simulation is given by

$$N = 1.5 N_{\text{base}} N_f N_H. \tag{2.88}$$

It is suggested that N_{base} initially be chosen near 19 and that the choice of N_{base} always be a prime number.

To understand the dimensional dependence on frequency of MUSE, one needs to account for the fact that to simulate a nonlinear product frequency, one may be required to simulate frequencies one is not directly interested in. For example, due to the frequency convolutions in the MUSE model, to simulate 3IMs one needs to track all pairs that sum to these frequencies. Thus to simulate the 3IMs $2f_1 - f_2$ and $2f_2 - f_1$ one needs to account for $2f_1, 2f_2, f_1 - f_2$ and $f_2 - f_1$ in addition to the drive frequencies.

For the example presented we have

$$\begin{aligned} N_{\text{base}} &= 19 \\ N_f &= 8 \\ N_H &= 2 \\ N &= 456. \end{aligned}$$

Thus the dimension of LATTE is 960 (912 real, 48 complex). For MUSE we have 85 complex dimensions.

As an example of using MUSE in cases with many frequencies we include results of a simulation modeled after the noise power ratio simulations in [68], but using the lossless, constant pitch TWT parameters from Section 2.3. The input spectrum consists of 101 evenly spaced frequencies (0.4 MHz spacing) with a 3 MHz notch at the center. The total number of frequencies when accounting for all sum and difference frequencies is 402. The nonzero input amplitudes are assigned randomly between -20 dBm and -30 dBm. The input and output spectra are shown in Fig. 2.11. Not shown in Fig. 2.11 is the spectrum at the sum and difference frequencies. Because the TWT simulation parameters did not include circuit loss or a sever, the output was taken at $z = 26$cm. The simulation ran for 5 hours and 40 minutes on a 1.3 GHz Gnu/Linux PC. As yet there has been no attempt to optimize the speed of the code.

2.4.3 Relation to method of collective variables

In this section we compare MUSE to a collective variable model, and we outline a method for developing a MUSE type model for free electron lasers (FELs). Since the TWT may be described by the same "nonlinear pendulum" equations as the FEL, e.g. [80], we propose that the prescription would result in a useful multifrequency analysis and simulation tool for FELs.

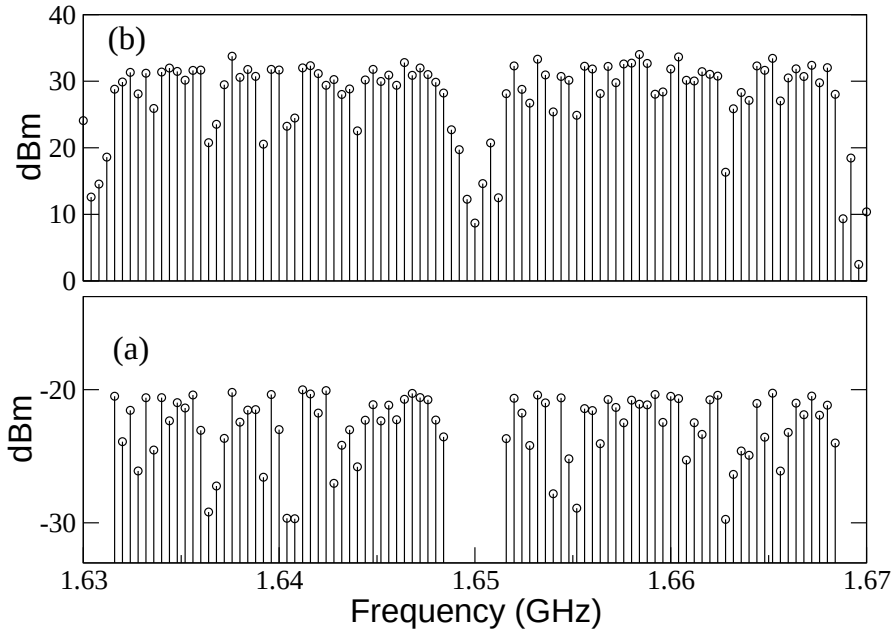

Figure 2.11 Input (a) and output (b) spectra of a simulation with 402 frequencies.

The majority of the initial collective variable work was done for single frequency excitations, where "In the presence of multiple frequencies, it is extremely difficult to obtain a description of FEL dynamics in terms of a reduced set of equations involving collective variables" [9]. With some simplifications and normalizations the MUSE model can be transformed into such a multifrequency collective variable model, applicable at least in the exponential growth region and potentially into the oscillation region.

The method of collective variables [10] involves first defining the "bunching parameter," the first collective variable, as the complex exponential average over particle phases, then differentiating the definition which results in an equation containing a higher "moment." One defines this higher moment as the next collective variable and differentiates this definition to get an equation which contains the next higher moment. At this point a relation is employed to "close" the system of equations.

In contrast, the MUSE model recognizes the first collective variable as the Fourier coefficient of the electron beam charge density, and defines a "second collective variable" as the Fourier coefficient of the electron beam velocity. To get a multifrequency "collective variable model" using the MUSE theory one does a derivation similar to Section 2.2. In particular, one uses the Eulerian electron beam equations, neglecting space charge, and a wave equation for only a forward wave. The result is a system that closely resembles (after normalization) a multifrequency collective variable model that does not need to be "closed."

Using the change of variable equations from Eulerian to Lagrangian coordinates one finds that the second collective variable of [10] is related to beam current. Thus, by taking moments the collective variable method misses having a collective variable for electron beam velocity. This is the primary difference between the approach of [10] and the MUSE approach.

Chapter 3

Analysis of S-MUSE

3.1 Introduction

Much of the work presented in Chapters 4–6 is based on the analysis of the S-MUSE model. The S-MUSE model has a formal analytic solution which allows many insights not obtainable from models which must be numerically solved. For example, analysis of the solution structure of S-MUSE has led to a simple formula for the exponential growth rates of the intermodulation frequencies, a new view of the mechanisms behind nonlinear phase distortion, and a new view of the mechanisms of signal injection for spectrum shaping.

In this chapter we prove that a series solution to the S-MUSE model exists and give a criterion for when the series converges. We also provide the formal analytic solution to the model. Next, we derive formulas which give the vector coefficients of the various modes of the solution. This is particularly important since many of the modes do not contribute substantially to the solution, and using the formulas we can choose and study only the important modes.

3.2 Series solution to S-MUSE

We propose a series solution to the nonlinear equation [see equation (2.64)]

$$\dot{\mathbf{x}} = \mathbf{A}\mathbf{x} + \mathbf{H}(\mathbf{x}, \mathbf{x}) \qquad z \in [0, L],\ \mathbf{x}(0) = \mathbf{w}. \tag{3.1}$$

Write $\mathbf{x}$ as

$$\mathbf{x} = \sum_{\alpha=1}^{\infty} \mathbf{x}^{(\alpha)} \tag{3.2}$$

where superscript (α) is an index not an exponent. This leads to the following differential equations for $\mathbf{x}^{(\alpha)}$

$$\dot{\mathbf{x}}^{(1)} = \mathbf{A}\mathbf{x}^{(1)} \qquad \mathbf{x}^{(1)}(0) = \mathbf{w} \tag{3.3}$$

$$\dot{\mathbf{x}}^{(\alpha)} = \mathbf{A}\mathbf{x}^{(\alpha)} + \sum_{\beta=1}^{\alpha-1} \mathbf{H}\left(\mathbf{x}^{(\beta)}, \mathbf{x}^{(\alpha-\beta)}\right) \tag{3.4}$$

$$\mathbf{x}^{(\alpha)}(0) = \mathbf{0} \qquad \alpha = 2, 3, 4, \ldots.$$

First we show that the series $\sum_\alpha \mathbf{x}^{(\alpha)}$ converges uniformly to $\mathbf{x}$, then we will check that the series solves (3.1). When combinations of α, β appear superscripted without parentheses they are to be taken as powers.

We attempt to find a summable bound on the $|\mathbf{x}^{(\alpha)}|$ so that we may conclude by the Weierstrass test [51, pg. 230] that $\sum_\alpha \mathbf{x}^{(\alpha)}(z)$ converges uniformly to $\mathbf{x}(z)$ on $[0, L]$. To show convergence we use an inductive argument. We propose a bound for $|\mathbf{x}^{(\beta)}|$

$$|\mathbf{x}^{(\beta)}| \leq \frac{|\mathbf{w}|^\beta ||\mathbf{H}||^{\beta-1}}{||\mathbf{A}||^{\beta-1}} e^{||\mathbf{A}||z} \left(e^{||\mathbf{A}||z} - 1\right)^{\beta-1} \tag{3.5}$$

where $||\cdot||$ represents a norm on a matrix or a tensor induced by the vector norm $|\cdot|$ (see Appendix C). Notice

$$|\mathbf{x}^{(1)}| \leq e^{||\mathbf{A}||z} |\mathbf{w}|. \tag{3.6}$$

Then using the induction hypothesis estimate for $\alpha \geq 2$

$$\begin{aligned} |\dot{\mathbf{x}}^{(\alpha)}| &\leq ||\mathbf{A}|||\mathbf{x}^{(\alpha)}| + ||\mathbf{H}|| \sum_{\beta=1}^{\alpha-1} |\mathbf{x}^{(\beta)}||\mathbf{x}^{(\alpha-\beta)}| & (3.7) \\ &\leq ||\mathbf{A}|||\mathbf{x}^{(\alpha)}| + \frac{|\mathbf{w}|^\alpha ||\mathbf{H}||^{\alpha-1}}{||\mathbf{A}||^{\alpha-2}} e^{2||\mathbf{A}||z} (\alpha - 1) \left(e^{||\mathbf{A}||z} - 1\right)^{\alpha-2}. & (3.8) \end{aligned}$$

We use the integrating factor $e^{-||\mathbf{A}||z}$ to integrate with $\mathbf{x}^{(\alpha)}(0) = \mathbf{0}$

$$\begin{aligned} &\int_0^z \left[|\dot{\mathbf{x}}^{(\alpha)}| - ||\mathbf{A}|||\mathbf{x}^{(\alpha)}|\right] e^{-||\mathbf{A}||\tau} \, d\tau \\ &\quad \leq \frac{|\mathbf{w}|^\alpha ||\mathbf{H}||^{\alpha-1}}{||\mathbf{A}||^{\alpha-2}} \int_0^z (\alpha - 1) e^{||\mathbf{A}||\tau} \left(e^{||\mathbf{A}||\tau} - 1\right)^{\alpha-2} \, d\tau & (3.9) \end{aligned}$$

which gives

$$|\mathbf{x}^{(\alpha)}| \leq \frac{|\mathbf{w}|^\alpha ||\mathbf{H}||^{\alpha-1}}{||\mathbf{A}||^{\alpha-1}} e^{||\mathbf{A}||z} \left(e^{||\mathbf{A}||z} - 1\right)^{\alpha-1}. \tag{3.10}$$

Thus for values of z such that

$$\frac{|\mathbf{w}|||\mathbf{H}||}{||\mathbf{A}||} \left(e^{||\mathbf{A}||z} - 1\right) < 1 \tag{3.11}$$

the series converges uniformly to $\mathbf{x}$.

Next we check that the sum solves the original equation. Using equations (3.8) and (3.10) one gets

$$\begin{aligned} |\dot{\mathbf{x}}^{(\alpha)}| &\leq ||\mathbf{A}|||\mathbf{x}^{(\alpha)}| + \frac{|\mathbf{w}|^\alpha ||\mathbf{H}||^{\alpha-1}}{||\mathbf{A}||^{\alpha-2}} e^{2||\mathbf{A}||z} (\alpha - 1) \left(e^{||\mathbf{A}||z} - 1\right)^{\alpha-2} & (3.12) \\ &\leq \frac{|\mathbf{w}|^\alpha ||\mathbf{H}||^{\alpha-1}}{||\mathbf{A}||^{\alpha-2}} e^{||\mathbf{A}||z} \left(e^{||\mathbf{A}||z} - 1\right)^{\alpha-2} \left[\alpha e^{||\mathbf{A}||z} - 1\right]. & (3.13) \end{aligned}$$

The above bound is a convergent sequence when (3.11) holds so $\sum_\alpha \dot{\mathbf{x}}^{(\alpha)}(z)$ converges uniformly to $\dot{\mathbf{x}}(z)$. Therefore due to a theorem from analysis [51, pg. 241] we may differentiate the infinite sum term by term.

First note $\sum_\alpha \mathbf{x}^{(\alpha)}(0) = \mathbf{w}$, then consider

$$\begin{aligned}
\dot{\mathbf{x}} &= \sum_{\alpha=1}^{\infty} \dot{\mathbf{x}}^{(\alpha)} && (3.14)\\
&= \mathbf{A}\sum_{\alpha=1}^{\infty} \mathbf{x}^{(\alpha)} + \sum_{\alpha=2}^{\infty}\sum_{\beta=1}^{\alpha-1} \mathbf{H}\left(\mathbf{x}^{(\beta)}, \mathbf{x}^{(\alpha-\beta)}\right) && (3.15)\\
&= \mathbf{A}\mathbf{x} + \sum_{\alpha=1}^{\infty}\sum_{\beta=1}^{\infty} \mathbf{H}\left(\mathbf{x}^{(\alpha)}, \mathbf{x}^{(\beta)}\right) && (3.16)\\
&= \mathbf{A}\mathbf{x} + \mathbf{H}\left(\mathbf{x}, \mathbf{x}\right). && (3.17)
\end{aligned}$$

We may rearrange the infinite sums above since we have absolute convergence at each $z \in [0, L]$ [51, pg. 226]. Therefore (3.2) solves (3.1) where the differential equations for the terms of (3.2) are given by (3.3) and (3.4).

3.2.1 Practical computation of (3.11)

For the vector form of the S-MUSE equations (2.64), $||\mathbf{A}||$ is of the order of $\frac{1}{\epsilon_0} \sim 10^{11}$ since $||\mathbf{A}||$ is of the order of the largest entry of $\mathbf{A}$. Therefore by (3.11) the values of z for which one gets convergence of the series are much smaller than those of practical interest. To improve on the range of z values for which one gets convergence we consider a diagonalization of (2.64).[1]

Let $\mathbf{P}$ be the modal matrix of $\mathbf{A}$ and consider the transformation

$$\mathbf{y} = \mathbf{P}\mathbf{x}. \tag{3.18}$$

Equation (2.64) in $\mathbf{y}$ coordinates is

$$\dot{\mathbf{y}} = \tilde{\mathbf{A}}\mathbf{y} + \tilde{\mathbf{H}}(\mathbf{y}, \mathbf{y}) \qquad \mathbf{y}(0) = \tilde{\mathbf{w}}. \tag{3.19}$$

If the series solution $\sum_\alpha \mathbf{y}^{(\alpha)}$ is convergent on some interval $0 < z < L$, then since

$$\sum_{\alpha=1}^{\infty} \mathbf{y}^{(\alpha)} = \mathbf{P}\left\{\sum_{\alpha=1}^{\infty} \mathbf{x}^{(\alpha)}\right\} \tag{3.20}$$

we have $\sum_\alpha \mathbf{x}^{(\alpha)}$ convergent on the same interval.

[1] Lemma 5.6.10 of [47, pg. 297] ensures that the magnitude of the largest eigenvalue of $\mathbf{A}$ is a lower bound on matrix norms on $\mathbf{A}$.

In (3.19) we have

$$\tilde{\mathbf{w}} = \mathbf{P}\mathbf{w} \tag{3.21}$$
$$\tilde{\mathbf{A}} = \mathbf{P}\mathbf{A}\mathbf{P}^{-1}. \tag{3.22}$$

To compute $\tilde{\mathbf{H}}$ let $\mathbf{Q} = \mathbf{P}^{-1}$ and note

$$\mathbf{x} = \mathbf{Q}\mathbf{y}. \tag{3.23}$$

The $\ell_i{}^{\text{th}}$ component of $\mathbf{H}(\mathbf{x}, \mathbf{x})$ is[2]

$$[\mathbf{H}(\mathbf{x}, \mathbf{x})]_{\ell_i} = \sum_{\substack{m,n=-M \\ m,n\neq 0}}^{M} \sum_{j,k=1}^{5} \mathbf{H}_{\ell_i m_j n_k} \mathbf{x}_{m_j} \mathbf{x}_{n_k}. \tag{3.24}$$

Transforming the vector $\mathbf{H}(\mathbf{x}, \mathbf{x})$ by $\mathbf{P}$ the $p_a{}^{\text{th}}$ component is

$$\begin{aligned}
&\sum_{\substack{\ell=-M \\ \ell\neq 0}}^{M} \sum_{i=1}^{5} \mathbf{P}_{p_a \ell_i} [\mathbf{H}(\mathbf{x}, \mathbf{x})]_{\ell_i} \\
&\quad = \sum_{\substack{\ell,m,n=-M \\ \ell,m,n\neq 0}}^{M} \sum_{i,j,k=1}^{5} \mathbf{P}_{p_a \ell_i} \mathbf{H}_{\ell_i m_j n_k} \mathbf{x}_{m_j} \mathbf{x}_{n_k} \\
&\quad = \sum_{\substack{\ell,m,n=-M \\ \ell,m,n\neq 0}}^{M} \sum_{\substack{q,r=-M \\ q,r\neq 0}}^{M} \sum_{b,c=1}^{5} \sum_{i,j,k=1}^{5} \mathbf{P}_{p_a \ell_i} \mathbf{H}_{\ell_i m_j n_k} \mathbf{Q}_{m_j q_b} \mathbf{Q}_{n_k r_c} \mathbf{y}_{q_b} \mathbf{y}_{r_c}.
\end{aligned} \tag{3.25}$$

Therefore

$$\tilde{\mathbf{H}}_{p_a q_b r_c} = \sum_{\substack{\ell,m,n=-M \\ \ell,m,n\neq 0}}^{M} \sum_{i,j,k=1}^{5} \mathbf{P}_{p_a \ell_i} \mathbf{H}_{\ell_i m_j n_k} \mathbf{Q}_{m_j q_b} \mathbf{Q}_{n_k r_c}. \tag{3.26}$$

Since $\mathbf{A}$ is block diagonal $\mathbf{P}$ and $\mathbf{Q}$ are also block diagonal. Therefore, for fixed p, q, r the matrix $\mathbf{P}$ has one contributing block and $\mathbf{Q}$ has two contributing blocks, i.e., $\mathbf{P}_{pp} \equiv \mathbf{P}_p$, $\mathbf{Q}_{qq} \equiv \mathbf{Q}_q$, and $\mathbf{Q}_{rr} \equiv \mathbf{Q}_r$. So finally

$$\tilde{\mathbf{H}}_{p_a q_b r_c} = \sum_{i,j,k=1}^{5} \mathbf{P}_{p_{ai}} \mathbf{H}_{p_i q_j r_k} \mathbf{Q}_{q_{jb}} \mathbf{Q}_{r_{kc}}. \tag{3.27}$$

Since $\tilde{\mathbf{A}}$ is diagonal $||\tilde{\mathbf{A}}||_1$ is equal to the largest of the absolute values of the eigenvalues of $\mathbf{A}$ (see Appendix C for a definition of $||\cdot||_1$). In many cases $||\tilde{\mathbf{A}}||$ will be of the order of $10 - 50$ implying much more realistic values of z may satisfy (3.11).

[2]The structure of $\mathbf{H}$ implies that the sum $\sum_{m,n=-M}^{M}$ is equivalent to the sum $\sum_{\substack{m\neq 0, n\neq 0 \\ f_m + f_n = f_\ell}}$.

3.3 Computation of mode amplitudes

The solution to S-MUSE may be written as a sum of complex exponentials, or modes, analogous to the Pierce solution of the linear TWT equations [41]. However, since S-MUSE is a nonlinear system of equations the mode structure of the solutions is much more complicated than the Pierce solution to the linear equations. The number of modes required to represent the solution of a intermodulation frequency grows rapidly as the order intermodulation frequency increases. However, since many of the modes are not "growing modes," or grow more slowly than the fastest growing mode, they do not contribute appreciably to the solution. Therefore, a theory is desired to compute the coefficients of any mode so that the dominant modes may be computed while ignoring modes that do not contribute appreciably to the solution. This theory will be the basis for the work on harmonic injection and phase distortion.

The solution to the ℓ^{th} component of equations (3.3) and (3.4) is

$$\mathbf{x}_\ell^{(1)} = e^{\mathbf{A}_\ell z}\mathbf{w}_\ell \tag{3.28}$$

$$\mathbf{x}_\ell^{(\alpha)} = \int_0^z e^{\mathbf{A}_\ell(z-\tau)} \sum_{\beta=1}^{\alpha-1} \sum_{\substack{m,n \\ f_m+f_n=f_\ell}} \left[\mathbf{x}_m^{(\beta)}(\tau), \mathbf{x}_n^{(\alpha-\beta)}(\tau)\right] \, d\tau$$

$$\alpha = 2, 3, \ldots \tag{3.29}$$

where $e^{\mathbf{A}_\ell z}$ is the matrix exponential [13]. Due to the recursive structure of (3.29), it may be written as

$$\mathbf{x}_\ell^{(\alpha)} = \int_0^z e^{\mathbf{A}_\ell(z-\tau)} \sum_{q=1}^{M} \left(\sum_{r=0}^{N_q} \tau^r \mathbf{c}_q^r \right) e^{\mu_q \tau} d\tau. \tag{3.30}$$

If an exponent of the forcing exponentials in the integral formula for $\mathbf{x}_m^{(\beta)}$, $\beta < \alpha$, $m \neq \ell$, i.e., a μ_q in the integral formula for $\mathbf{x}_m^{(\beta)}$, is equal to an eigenvalue of $\mathbf{A}_m$, then powers of z appear multiplying the exponentials in the result of the integral for $\mathbf{x}_m^{(\beta)}$. The factor τ^r appears in (3.30) to account for the fact that $\mathbf{x}_m^{(\beta)}$ and $\mathbf{x}_n^{(\alpha-\beta)}$ may contain such powers of z. Cases when μ_q is equal to an eigenvalue of $\mathbf{A}_\ell$ will be referred to as "resonant forcing" and the modes that result involving powers of z will be referred to as "secular modes."

Modes are characterized by the arguments of their complex exponentials. The result of the integral in (3.30) has modes characterized by either μ_q or the eigenvalues of $\mathbf{A}_\ell$, λ_{ℓ_i}, $i = 1, \ldots, 5$. Formulas for these modes are given below. The derivation of the formulas is provided in Appendix D.

The λ_{ℓ_k} mode is

$$\sum_{q=1}^{M} \sum_{r=0}^{N_q} \mathbf{P}_\ell \mathbf{R}_\ell(k, r, \mu_q) \mathbf{P}_\ell^{-1} \mathbf{c}_q^r e^{\lambda_{\ell_k} z}, \quad k = 1, \ldots, 5. \tag{3.31}$$

The μ_q modes are:

1. For $\mu_q \neq \lambda_{\ell_i}$, $i = 1, \ldots, 5$

$$\sum_{r=0}^{N_q} \left[\sum_{k=0}^{N_q - r} \mathbf{P}_\ell \mathbf{S}_\ell(\mu_q, r, k) \mathbf{P}_\ell^{-1} \mathbf{c}_q^{r+k} \right] z^r e^{\mu_q z}. \tag{3.32}$$

2. For $\mu_q = \lambda_{\ell_i}$

$$\mathbf{P}_\ell \left\{ \mathbf{T}_\ell(N_q) \mathbf{P}_\ell^{-1} \mathbf{c}_q^{N_q} z^{N_q+1} + \sum_{r=0}^{N_q} \left[H(r) \mathbf{T}_\ell(r-1) \mathbf{P}_\ell^{-1} \mathbf{c}_q^{r-1} + \left(\sum_{k=0}^{N_q - r} \mathbf{S}_\ell(\mu_q, r, k) \mathbf{P}_\ell^{-1} \mathbf{c}_q^{r+k} \right) \right] z^r \right\} e^{\mu_q z}. \tag{3.33}$$

In (3.31)–(3.33) $\mathbf{P}_\ell$ and $\mathbf{P}_\ell^{-1}$ are the modal matrix of $\mathbf{A}_\ell$ and its inverse respectively [13]. The matrices $\mathbf{R}_\ell, \mathbf{S}_\ell$, and $\mathbf{T}_\ell$ are defined by their elements

$$\mathbf{R}_{\ell_{i,j}}(k, r, \mu_q) \equiv \begin{cases} \frac{(-1)^{r+1} r!}{(\mu_q - \lambda_{\ell_k})^{r+1}} & i = j = k \text{ and } \lambda_{\ell_i} \neq \mu_q \\ 0 & \text{otherwise} \end{cases} \tag{3.34}$$

$$\mathbf{S}_{\ell_{i,j}}(\mu_q, r, k) \equiv \begin{cases} (-1)^k \frac{(r+k)!}{r!} \frac{1}{(\mu_q - \lambda_{\ell_j})^{k+1}} & i = j \text{ such that } \lambda_{\ell_i} \neq \mu_q \\ 0 & \text{otherwise} \end{cases} \tag{3.35}$$

$$\mathbf{T}_{\ell_{i,j}}(r) \equiv \begin{cases} \frac{1}{r+1} & i = j \text{ such that } \lambda_{\ell_i} = \mu_q \text{ and } r \neq -1 \\ 0 & \text{otherwise} \end{cases} \tag{3.36}$$

with

$$H(r) = \begin{cases} 1 & r \geq 1 \\ 0 & r = 0. \end{cases} \tag{3.37}$$

A Mathematica implementation of the above theory first determines the integrand in (3.30) using solutions to frequencies combining to make the desired frequency. Modal amplitudes for the desired frequency are then computed from the formulas.

Chapter 4

Generation and growth rates of nonlinear distortions

4.1 Introduction

Figure 2.1 shows circuit power versus axial distance for two drive tones, their second harmonics and sum frequency, and the third order intermodulation products $2f_1 - f_2$ and $2f_2 - f_1$. The simulation data in Fig. 2.1 indicate that the nonlinear product frequencies may be characterized by an exponential growth rate prior to saturation, which suggests that only one of the modes of (3.30) is dominant in the respective solutions. In this Chapter we provide a formula for computing the exponential growth rate of this dominant mode for any desired intermodulation product. During development of the theory a mathematical construct for generation mechanisms of nonlinear distortions is developed, which results in an improved understanding of harmonic and intermodulation distortion generation. The growth rate theory and insights into generation mechanisms turn out to be extremely useful intuition builders for the theories presented in Chapters 5 and 6.

4.2 Theory

The ℓ^{th} component of equation (3.4) which describes the growth of the intermodulation frequencies is

$$\begin{aligned} \dot{\mathbf{x}}_\ell^{(\alpha)} &= \mathbf{A}_\ell \mathbf{x}_\ell^{(\alpha)} + \sum_{\beta=1}^{\alpha-1} \sum_{\substack{m,n \\ f_m+f_n=f_\ell}} \mathbf{H}_{\ell mn}\left(\mathbf{x}_m^{(\beta)}, \mathbf{x}_n^{(\alpha-\beta)}\right) \\ &\qquad \alpha = 2, 3, 4, \ldots \end{aligned} \tag{4.1}$$

The quadratic term in (4.1) governs how frequency components of $\mathbf{x}^{(1)}$, $\mathbf{x}^{(2)}$, $\ldots$, $\mathbf{x}^{(\alpha-1)}$ combine to produce frequency components of $\mathbf{x}^{(\alpha)}$. In particular, the solutions for the drive frequencies produce components in $\mathbf{x}^{(2)}$ for frequencies that are all possible additions of pairs of drive frequencies (and the negatives of the drive frequencies). Then, components of $\mathbf{x}^{(1)}$ and $\mathbf{x}^{(2)}$ produce components in $\mathbf{x}^{(3)}$ for frequencies which are all possible additions of pairs of frequencies from $\mathbf{x}^{(1)}$ and $\mathbf{x}^{(2)}$. Similarly, components of $\mathbf{x}^{(1)}$ and $\mathbf{x}^{(3)}$ and components of $\mathbf{x}^{(2)}$ and $\mathbf{x}^{(2)}$ combine to produce components of $\mathbf{x}^{(4)}$ and so on.

To keep track of the frequencies generated in this process we construct sets $\Omega^{(\alpha)}$ that contain the frequencies generated in the term $\mathbf{x}^{(\alpha)}$. For example, if f_a and f_b are drive frequencies then we define $\Omega^{(1)}$ to contain the drive frequencies and the negative drive frequencies, i.e.,

$$\Omega^{(1)} = \{-f_b, -f_a, f_a, f_b\}. \tag{4.2}$$

From (4.1), the frequencies produced in the second series term are

$$\begin{aligned}\Omega^{(2)} = \{&-2f_b, -f_a - f_b, -2f_a, f_a - f_b,\\ &-f_a + f_b, 2f_a, f_a + f_b, 2f_b\}.\end{aligned} \tag{4.3}$$

Similarly, frequencies in $\mathbf{x}^{(3)}$ are all possible additions of frequency pairs including one from $\Omega^{(1)}$ and one from $\Omega^{(2)}$:

$$\begin{aligned}\Omega^{(3)} = \{&-3f_b, -f_a - 2f_b, -2f_a - f_b, -3f_a,\\ &f_a - 2f_b, -f_b, -f_a, -2f_a + f_b,\\ &2f_a - f_b, f_a, f_b, -f_a + 2f_b,\\ &3f_a, 2f_a + f_b, f_a + 2f_b, 3f_b\}.\end{aligned} \tag{4.4}$$

Notice $\Omega^{(3)}$ contains 3^{rd} harmonics and 3IMs, but also contains the drive frequencies.

In general $\Omega^{(1)}$ contains the positive and negative drive frequencies, and we define $\Omega^{(\alpha)}, \alpha = 2, 3, 4, \ldots$ by

$$\Omega^{(\alpha)} = \{f + g \,|\, f \in \Omega^{(\beta)},\ g \in \Omega^{(\alpha-\beta)}, 1 \le \beta \le \alpha - 1,\ f + g \neq 0\}. \tag{4.5}$$

In applications we truncate the frequency generation process described above. Since the highest order of IMP in $\Omega^{(\alpha)}$ is equal to α, we let S be the highest order IMP of interest and then define Ω to be all of the frequencies in $\Omega^{(1)}, \ldots, \Omega^{(S)}$. Order Ω as

$$\Omega = \{f_{-M}\, f_{-M+1}\, \ldots\, f_{-1}\, f_1\, \ldots\, f_{M-1}\, f_M\} \tag{4.6}$$

where $f_\ell > f_m$ if $\ell > m$ and $f_{-\ell} = -f_\ell$. The indices of Ω are then used to index $\mathbf{x}$.

Based on the integral form of the solution for $\mathbf{x}_\ell^{(\alpha)}$ given in (3.30), and the solutions of the integral computed in Section 3.3 (which were represented as mode contributions), $\mathbf{x}_\ell^{(\alpha)}$ is the linear combination of complex exponentials

$$\mathbf{x}_\ell^{(\alpha)}(z) = \sum_{p=1}^{M_\ell^{(\alpha)}} \sum_{r=0}^{N_\ell^{(\alpha)[p]}} \mathbf{a}_\ell^{(\alpha)[p]\{r\}} z^r \exp\left(\mu_\ell^{(\alpha)[p]} + i\sigma_\ell^{(\alpha)[p]}\right) z \tag{4.7}$$

where $\mathbf{a}_\ell^{(\alpha)[p]\{r\}}$ is a complex vector and $\mu_\ell^{(\alpha)[p]}$, $\sigma_\ell^{(\alpha)[p]}$ are real. Sums such as (4.7) are ordered so that $\mu_\ell^{(\alpha)[1]}$ is the maximum of $\mu_\ell^{(\alpha)[1]}, \mu_\ell^{(\alpha)[2]}, \ldots, \mu_\ell^{(\alpha)[M_\ell^{(\alpha)}]}$. We call $\mu_\ell^{(\alpha)[1]}$ the *maximum growth rate* of $\mathbf{x}_\ell^{(\alpha)}$. The arguments of the complex exponentials in (4.7) are either eigenvalues

of $\mathbf{A}_\ell$ or additions of the arguments of complex exponentials formed in the quadratic term of (4.1). Because of the dispersion and eigenvalue structure in the matrix $\mathbf{A}_\ell$ the dominant mode is never a "secular mode," i.e., $N_\ell^{(\alpha)[1]} = 0$ for all ℓ, α.

Using the form (4.7) and the integral solutions (3.28) and (3.29) of the previous chapter a recursive formula for $\mu_\ell^{(\alpha)[1]}$ in terms of $\mu_\ell^{(1)[1]}, \mu_\ell^{(2)[1]}, \ldots, \mu_\ell^{(\alpha-1)[1]}$ is

$$\mu_\ell^{(\alpha)[1]} = \max_{\substack{m,n,\beta \\ f_m+f_n=f_\ell \\ 1\le\beta\le\alpha-1}} \left\{ \mu_m^{(\beta)[1]} + \mu_n^{(\alpha-\beta)[1]}, \nu_\ell^{[1]} \right\} \tag{4.8}$$

where $\nu_\ell^{[1]}$ is the largest of the real parts of the eigenvalues of $\mathbf{A}_\ell$.

It is important to notice the maximum growth rate is a function of α. A frequency f_ℓ may appear in several of the series terms, and each term in the series in which f_ℓ appears has a maximum growth rate $\mu_\ell^{(\alpha)[1]}$. In many cases the observed growth rate in a simulation will be the maximum growth rate for the first term in the series which the frequency appears, i.e., the smallest value of α for which the frequency appears in $\Omega^{(\alpha)}$. However, as we demonstrate later, this is not always the case.

4.3 Applications

Next we present examples illustrating the IMP generation and the application of formula (4.8). The TWT dispersion and beam parameters are based on a slightly modified XWING wideband TWT [79]. Formula (4.8) is checked against growth rates obtained from Christine 1-d [5].

First we consider two drive frequencies f_a and f_b separated by 1.1 GHz. In the bandwidth between $0.8 - 9.0$ GHz twelve IMPs of order five and lower are generated; all of the IMPs are of the form $mf_a - nf_b$. For the IMP frequencies and dispersion parameters in this example, (4.8) predicts the growth rate as m times the growth rate of f_a plus n times the growth rate of f_b:

$$m\mu_a^{(1)[1]} + n\mu_b^{(1)[1]}. \tag{4.9}$$

That is, for the frequencies that make up these IMPs, the linear growth rates $\nu_\ell^{[1]}$ in (4.8) are always less than the forcing growth rates $\mu_m^{(\beta)[1]} + \mu_n^{(\alpha-\beta)[1]}$. For a large class of TWT dispersion parameters (4.9) is the correct formula for the maximum growth rate of IMPs of the form $mf_a - nf_b$.

In Table 4.1 we compare Christine 1-d data to (4.9) [1]. The agreement is excellent for input power 30 dB below the input power that produces saturation at the output ($-30\,\mathrm{dB_{sat}}$). The agreement is less close for input powers of $-10\,\mathrm{dB_{sat}}$ and $0\,\mathrm{dB_{sat}}$ and this is probably due to the nonlinearities neglected in deriving the S-MUSE model [82]. In all cases the agreement is very good ($< 10\%$ error), indicating that the theory may be used for quantitative and

[1] Since we measure growth rates from power versus axial position data, we actually compare two times equation (4.9) to the data. However, we do not make this distinction in the text of the chapter.

		$-30\,\mathrm{dB_{sat}}$		$-10\,\mathrm{dB_{sat}}$		$0\,\mathrm{dB_{sat}}$	
Order	f (GHz)	μ_{Chr}	% diff.	μ_{Chr}	% diff.	μ_{Chr}	% diff.
1	$f_a = 3.0$	0.744	–	0.764	–	0.770	–
	$f_b = 4.1$	0.696	–	0.728	–	0.733	–
2	$f_b - f_a$	1.443	0.30	1.514	1.44	1.543	2.53
	$2f_a$	1.487	0.03	1.515	0.83	1.555	0.89
	$f_a + f_b$	1.438	0.07	1.443	3.37	1.457	3.23
	$2f_b$	1.387	0.27	1.361	6.99	1.338	9.62
3	$2f_a - f_b$	2.185	0.10	2.239	0.75	2.326	2.21
	$2f_b - f_a$	2.135	0.01	2.170	2.29	2.225	0.57
	$3f_a$	2.227	0.15	2.239	2.38	2.249	2.78
4	$2f_b - 2f_a$	2.885	0.24	2.930	1.86	3.041	1.10
	$3f_a - f_b$	2.923	0.09	2.966	1.80	3.037	0.26
5	$3f_a - 2f_b$	3.625	0.09	3.678	1.91	3.864	2.22
	$3f_b - 2f_a$	3.583	0.27	3.664	1.30	3.833	2.39
	$4f_a - f_b$	3.665	0.12	3.724	1.61	3.807	0.22

Table 4.1 Growth rates for two drive frequencies and nonlinear products up to order five for the bandwidth $0.8 - 9.0\,\mathrm{GHz}$. Results for input powers of $-30\,\mathrm{dB_{sat}}$, $-10\,\mathrm{dB_{sat}}$ and $0\,\mathrm{dB_{sat}}$ are given. μ_{Chr} is growth rate fit to Christine 1-d power versus axial distance data at an axial position in the "small-signal" regime, i.e., after the power curves have reached their asymptotic exponential growth state, but prior to saturation of any of the power curves (see Fig. 4.2). The percent difference columns compare μ_{Chr} to formula (4.9) using % diff. $= |\mu_{\mathrm{Chr}} - \text{Eq. (4.9)}| / \mu_{\mathrm{Chr}}$.

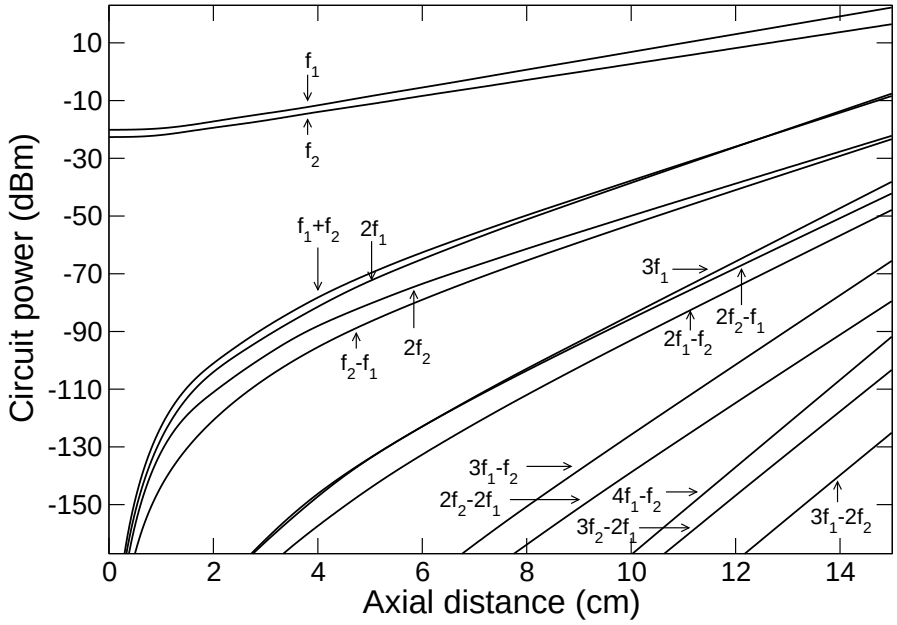

Figure 4.1 Circuit power versus distance for fourteen tones with $P_{\text{in}} = -30\,\text{dB}_{\text{sat}}$.

qualitative studies of IMPs. Figure 4.1 shows power versus axial distance predicted by LATTE for the fourteen tones of the example with $P_{\text{in}} = -30\,\text{dB}_{\text{sat}}$.

Next we consider a particular case with the drive frequency at the low end of the band such that the second and third harmonics are within the linear gain bandwidth. We consider the frequencies $1, 2$, and $3\,\text{GHz}$. In Case 1, the drive frequency is $f_1 = 1\,\text{GHz}$. In Case 2, we also include $f_2 = 2\,\text{GHz}$ and $f_3 = 3\,\text{GHz}$ as drive frequencies as one might when using second and third harmonic injection.

In Case 1, the frequency generation scheme (4.5) gives

$$\Omega^{(1)} = \{-f_1, f_1\} = \{-1, 1\} \tag{4.10}$$

$$\Omega^{(2)} = \{-2, 2\} \tag{4.11}$$

$$\Omega^{(3)} = \{-3, -1, 1, 3\}. \tag{4.12}$$

Formula (4.8) gives the growth rate of the $2\,\text{GHz}$ term as

$$\mu_2^{(2)[1]} = \max\left\{2\mu_1^{(1)[1]}, \nu_2^{[1]}\right\} = \nu_2^{[1]}$$

since the linear growth rate $\nu_2^{[1]}$ for $2\,\text{GHz}$ is greater than two times the linear growth rate $\mu_1^{(1)[1]} = \nu_1^{[1]}$ for $1\,\text{GHz}$. Moreover, the growth rate for $3\,\text{GHz}$ is

$$\mu_3^{(3)[1]} = \max\left\{\mu_1^{(1)[1]} + \mu_2^{(2)[1]}, \nu_3^{[1]}\right\} = \mu_1^{(1)[1]} + \mu_2^{(2)[1]}.$$

That is, the growth rate for the third harmonic is the growth rate for the second harmonic plus the growth rate of the drive. Simulations of this case show that the second and third

harmonics do not achieve their asymptotic growth rates prior to saturation. However, analytic solutions of (2.64) confirm that the growth rates predicted by (4.8) are those of the dominant terms.

In general application of (4.8), it is important to notice that the maximum growth rate $\mu_\ell^{(\alpha)[1]}$ is a function of α. A frequency f_ℓ may appear in several terms of the series, and each of these terms has a maximum growth rate $\mu_\ell^{(\alpha)[1]}$. In many cases the observed growth rate in a simulation will be the maximum growth rate for the first term in the series for which the frequency appears, i.e., corresponding to the smallest α for which the frequency appears in $\Omega^{(\alpha)}$. For example, in Case 1, (4.10) and (4.12) show that $f_1 = 1\,\text{GHz}$ is in both $\Omega^{(1)}$ and $\Omega^{(3)}$ and the corresponding growth rates of these terms are $\mu_1^{(1)[1]}$ and $\mu_1^{(3)[1]}$. Although $\mu_1^{(3)[1]} > \mu_1^{(1)[1]}$, in simulations $\mu_1^{(3)[1]}$ is never observed and $\mu_1^{(1)[1]}$ characterizes the solution. However, a similar conclusion does not hold in Case 2.

In Case 2, the frequency generation scheme (4.5) gives

$$\begin{aligned}\Omega^{(1)} &= \{-f_3, -f_2, -f_1, f_1, f_2, f_3\} = \{-3, -2, -1, 1, 2, 3\}\\ \Omega^{(2)} &= \{-6, -5, -4, -3, -2, -1, 1, 2, 3, 4, 5, 6\}.\end{aligned}$$

Now $f_1 = 1\,\text{GHz}$ is in both $\Omega^{(1)}$ and $\Omega^{(2)}$. Since it is common for second order products to reach the level of drive frequencies before the TWT saturates, in simulations we do see the $\alpha = 2$ term for large enough drive levels of 2 GHz and 3 GHz. This phenomenon is shown in Fig. 4.2 for a Christine 1-d simulation. Both the $\alpha = 1$ and $\alpha = 2$ maximum growth rates are observed and the $\alpha = 2$ maximum growth rate is equal to the theoretically predicted sum of the growth rates driving it to within 1%.

By a mathematical treatment of an approximate nonlinear TWT model, we have yielded a new view of IMP generation and provided estimates for IMP growth rates. In this view, the generation of IMP frequencies is a sequential process wherein higher order IMPs are produced by combining lower order IMPs (and drive frequencies) via a quadratic nonlinearity. The quadratic nonlinearities are the velocity nonlinearity $v\frac{\partial v}{\partial z}$ in Newton's law and the definition of current ρv in the continuity equation [82]. We note that certain models of the klystron and free electron laser can be expressed in the same form (2.64) as S-MUSE, and therefore a similar method for understanding and predicting IMPs could be applied to these devices.

Formula (4.8) indicates that the growth rate of an IMP is the greater of the sum of the growth rates of the frequencies combining to make the IMP and the linear growth rate of the IMP frequency. In most cases the former growth rate applies but there can be exceptions for very wide band TWTs. The analysis refines and gives insight into the conventional rule of thumb [6] of estimating the growth rate of a K^{th} order IMP as K times the growth rate of the drive frequency.

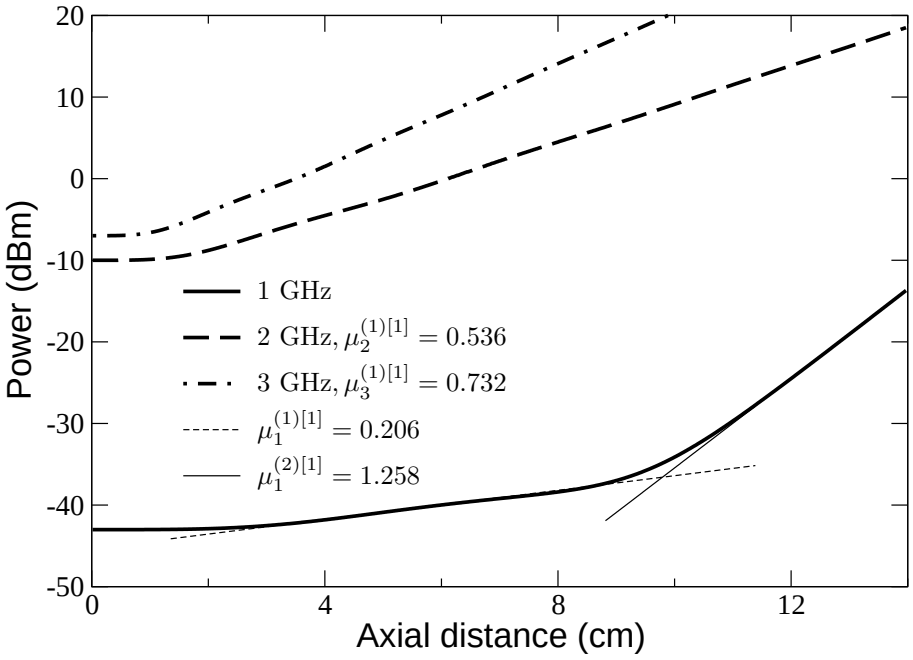

Figure 4.2 Power versus axial distance for 3 harmonically related drive frequencies predicted by Christine 1-d. 1 GHz is a second order product of 2 GHz and 3 GHz and exhibits first its $\alpha = 1$ maximum growth rate, then its $\alpha = 2$ maximum growth rate produced by 2 GHz and 3 GHz.

Chapter 5

On the mechanisms of phase distortion in a TWT

5.1 Introduction

Conventionally, TWT nonlinearity has been quantified via single frequency input-output transfer characteristics. In particular AM/AM (output power vs. input power) curves and AM/PM (the derivative of output phase vs. input power) curves are used (see Fig. 5.1). AM/AM curves exhibit a "linear gain" region, followed by "nonlinear" gain compression and saturation for increasing input powers. In a linear amplifier the AM/PM curve is a flat line, i.e., the difference in phase between the output and the input does not depend on input power. In the TWT, as with any amplifier, the output phase does depend on input power as seen in Fig. 5.1. The physics of this dependence is the subject of this chapter. One sees in Fig. 5.1 that the AM/PM curve deviates from linear behavior for input powers much smaller than those that first produce compression in the AM/AM curve. This shows that phase distortion in TWTs is significant even in the regime defined as the linear gain region based on the AM/AM characteristics.

From a systems perspective the AM/AM and AM/PM nonlinearities are said to "cause" undesirable output spectral content such as intermodulation products [8]. However, since the transfer curves typically come from a measurement they do not contain explicit information about the physics internal to the TWT. In fact, from a physics perspective it is better to say that the transfer curves "capture" aspects of TWT nonlinearity, and thus can be used to predict input-output behavior of the TWT. For example, an input-output model such as an *amplitude-phase model* [69] using the single frequency TWT transfer characteristics predicts intermodulation spectrum around closely spaced carriers [12], but the amplitude-phase model does not predict harmonics of the carrier frequencies. Since it is well established that the carrier harmonics (and sum frequencies) exist in the output spectrum of a TWT, one concludes that the single frequency transfer characteristics capture certain nonlinear physics of the TWT, but fail to capture other nonlinear physics.

The physics behind the AM/AM curve can be understood in terms of power saturation, which is a result of electron bunches falling into accelerating phases of the RF wave and hence taking energy from the RF wave. The physics of phase nonlinearity, we claim, is less well understood. Several authors have claimed that phase distortion is due to the reduction of the average electron beam velocity. For example Gilmour [41] claims that phase distortion

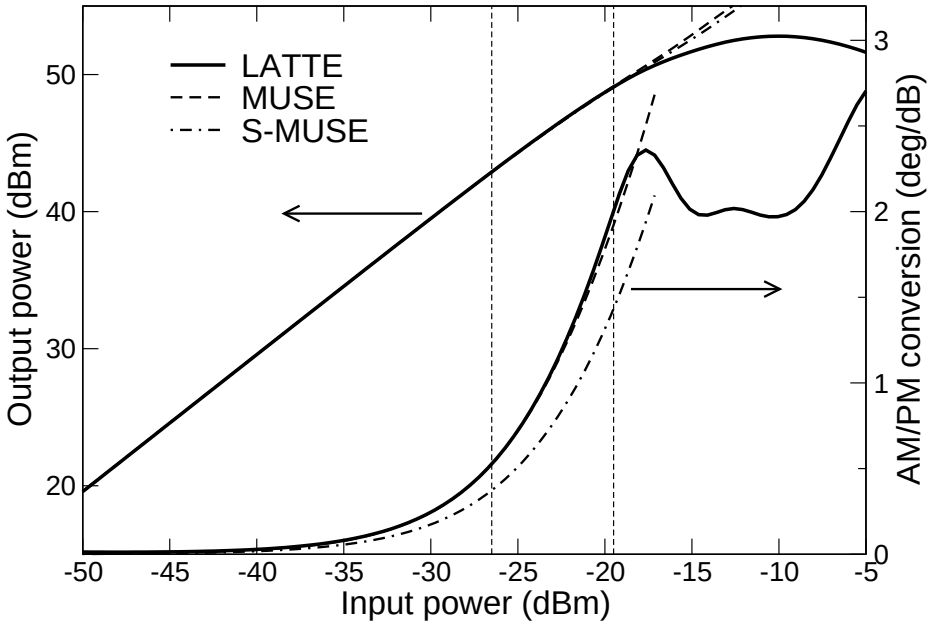

Figure 5.1 AM/AM and AM/PM curves at 14 GHz generated by LATTE, MUSE, and S-MUSE for the TWT parameters in Tables 5.1 and 5.2. The vertical lines at $P_{in} = -19.5$ dBm and $P_{in} = -26.5$ dBm correspond to 1 dB gain compression (3.8 dB backed off from saturation) and 10 dB backed off from saturation respectively, as predicted by LATTE. The simulations to generate the results accounted for circuit frequencies up to the third harmonic and electron beam frequencies up to the tenth harmonic.

"occurs because, as drive level is increased, more power is extracted from the electron beam and the velocity of the beam is reduced. As beam velocity decreases, the velocity of the RF wave on the circuit is reduced and this increases the phase length of the TWT." Furthermore, Ezura and Kano [30] state "in [Refs. [1–5]] where saturation was excluded, one may easily grasp the physical image of the phase distortion due to the decrease of the electron velocities, but not quantitatively." However, in this chapter we show using several arguments that, at least prior to 1 dB of gain compression, that the slowing down of the electron beam is not the dominant mechanism for phase distortion.

In this chapter we offer a new view of phase distortion provided by the new spectral TWT models MUSE and S-MUSE [82]. By artificially suppressing harmonic and dc effects in the electron beam equations of the MUSE model, we show that the beam second harmonic plays a far greater role in the AM/PM distortion prior to gain compression and power saturation than the average slowing down of electrons. Next, using an approximate analytic solution of the output phase for the approximate nonlinear model S-MUSE [82], we conclude that the phase distortion prior to gain compression is mostly a result of the fact that the fundamental frequency is an intermodulation frequency of itself. We also compare the spectrum of an amplitude-phase model using the output phase of the analytic solution to the spectrum predicted by simulation of the S-MUSE model. Furthermore, since it is found that phase distortion depends primarily on the second harmonic existing in the electron beam, we study the dependence of the phase distortion on circuit dispersion and electron beam parameters at the second harmonic. Lastly, using insights developed throughout the chapter, we propose a physical explanation for a new technique of TWT linearization [14] that is counter to that proposed in [14].

In Section 5.2 we present simulation, theory, and physical arguments to support the case that the majority of phase distortion, at least prior to 1 dB of gain compression, is due to beam harmonics and intermodulation distortion of the fundamental with itself, and not due to the slowing down of electrons in the beam. In Section 5.3 we compare S-MUSE simulations of two frequency inputs to results from an amplitude-phase model that uses the analytic solution of output phase for the S-MUSE model. Section 5.4 presents results from parametric studies of phase distortion as a function of circuit dispersion and beam parameters at the second harmonic. We investigate mechanisms for a new technique of TWT linearization [14] in Section 5.5. Sections 5.7 and 5.8 provide theoretical detail to support Section 5.2.

For this work there are two primary benefits of the Eulerian models over Lagrangian models such as LATTE. First, the spectral representation of the electron beam in MUSE allows one to investigate how electron beam frequencies, including "dc" effects such as the reduction of the average electron beam velocity, affect phase distortion. In principle, Lagrangian simulations may also be modified to eliminate spectral components from the electron beam's description by generalizing a method we present in this chapter. However, such modifications are far more cumbersome than the analogous MUSE simulations. Second, S-MUSE possesses an analytic solution which has a direct physical interpretation of phase distortion not afforded by either MUSE or LATTE.

5.2 Phase distortion mechanisms

In this section we study using simulation and analysis the mechanisms of phase distortion. We define $\Phi(P_{\rm in})$ as the phase difference between the TWT output and input of the "hot" circuit voltage wave at frequency $f_\ell\omega_0$, where the "small signal" phase difference is subtracted off. Using this definition, any nonzero value of Φ is considered a "distortion" from the linear behavior. The term "hot" refers to the fact that the spatially dependent local velocity and local wavenumber of the voltage wave at frequency $f_\ell\omega_0$ are in general not equal to the "cold circuit" quantities, i.e., the velocity and wavenumber of a voltage wave with no beam present, nor are they in general equal to the electron beam velocity or effective electron stream wavenumber (i.e. $f_\ell\omega_0/u_0$). Rather, the local velocity and wavenumber of the "hot" wave must be computed from analytic theory or simulation.

If we define $\beta_{\rm lin}$ as the hot wavenumber predicted by linear theory [61], i.e., the wave number corresponding to the exponentially growing mode of the solution, and $\beta_{\rm nl}(P_{\rm in},z)$ as a local hot wavenumber predicted by either analytic theory or simulation, then we have

$$\Phi(P_{\rm in}) \;=\; \int_0^L \left[\beta_{\rm nl}(P_{\rm in},z)-\beta_{\rm lin}\right]\,dz \tag{5.1}$$

where $z=L$ is the TWT output. Notice that $\beta_{\rm lin}$ is independent of input power $P_{\rm in}$ and axial position z. For small input powers $\beta_{\rm nl}$ tends to $\beta_{\rm lin}$.

Rewriting (5.1) in terms of linear and nonlinear hot phase velocities $v_{\rm lin}^{\rm hot}$ and $v_{\rm nl}^{\rm hot}(P_{\rm in},z)$ we get

$$\Phi(P_{\rm in}) \;=\; f_\ell\omega_0\int_0^L\left[\frac{1}{v_{\rm nl}^{\rm hot}(P_{\rm in},z)}-\frac{1}{v_{\rm lin}^{\rm hot}}\right]\,dz. \tag{5.2}$$

Therefore, by definition phase distortion is the result of the nonlinear velocity change of the hot circuit wave. When the cold circuit velocity is less than the dc electron beam velocity (Pierce velocity parameter $b>0$), the hot velocity usually first slows down relative to $v_{\rm lin}^{\rm hot}$, increasing the electrical length of the TWT relative to the linear behavior, and can speed back up in saturation. When the cold circuit velocity is greater than the dc electron beam velocity (Pierce velocity parameter $b<0$), the hot velocity usually first speeds up relative to $v_{\rm lin}^{\rm hot}$, decreasing the electrical length of the TWT relative to the linear behavior, and can slow back down in saturation (see for example Fig. 1 of [30]). In general the factors influencing $v_{\rm nl}^{\rm hot}(P_{\rm in},z)$ are not fully understood for all operating regimes of the TWT.

It will be useful to define hot phase velocity using the model variables we have introduced. For frequency $f_\ell\omega_0$ we write

$$\left|\tilde{V}_\ell(z)\right|e^{i\theta_\ell(z)}e^{if_\ell\omega_0\left(\frac{z}{u_0}-t\right)} \tag{5.3}$$

and from this one can find that

$$v_\ell^{\rm hot}(z) \;=\; \frac{f_\ell\omega_0}{\beta_e+\frac{d\theta_\ell}{dz}} \tag{5.4}$$

where $\beta_e=f_\ell\omega_0/u_0$ is the "stream wavenumber."

5.2.1 Simulation results

For the first set of simulation studies we choose parameters for a representative Ku-band TWT. The electron beam parameters are listed in Table 5.1 and the cold circuit phase velocity $\tilde{v}_{\text{ph}}$, interaction impedance $\tilde{K}$, and space charge reduction factor $\tilde{R}$ [41, 61] are found in Table 5.2. The parameters represent a single lossless, constant pitch section. AM/AM and AM/PM curves at 14 GHz are given in Fig. 5.1. Space charge reduction factors for harmonics higher than the third are computed by (23b) of [5].

Table 5.1 Ku-band TWT electron beam and circuit parameters.

Parameter	**Value**
Cathode voltage	-4.92 kV
Beam current	0.177 A
Beam radius	0.3175 mm
Helix radius	0.60 mm

Table 5.2 Ku-band TWT dispersion parameters.

f (GHz)	$\tilde{v}_{\text{ph}}$ ($\times 10^7$ m/s)	$\tilde{K}$ (Ω)	$\tilde{R}$
14.0	3.858	32.625	0.156
28.0	3.673	1.161	0.389
42.0	3.591	0.061	0.547

Since the Eulerian models apply only prior to electron overtaking, we restrict our attention in this section to input powers smaller than the 1 dB gain compression point. From the AM/AM curve we find that for our TWT design this corresponds to 3.8 dB backed off from saturation. According to [41] the maximum point of AM/PM distortion typically occurs anywhere between 3 and 10 dB backed off from saturation, indicating that the input powers to which we restrict our attention are relevant to real devices.

The spectral structure of the MUSE model allows one to artificially suppress electron beam frequencies as a diagnostic tool to discover where various nonlinearities manifest in TWT behavior. In the following MUSE simulations we include and exclude "dc" effects [time average electron beam velocity $\tilde{v}_0(z)$ and time average electron beam charge density $\tilde{\rho}_0(z)$], second harmonics, and higher order harmonics. A frequency $f_\ell\omega_0$ is excluded from a simulation by forcing derivatives of the TWT state variables at that frequency (e.g. $\tilde{V}_\ell, \tilde{\rho}_\ell$, etc.) to zero in the simulation.

Figure 5.2 shows output phase versus input power curves from MUSE simulations with varying frequencies included. When the fundamental frequency ("f") is the only frequency in the simulation the model reduces to a linear model, and there is no phase distortion. Alternatively including the dc frequency and the second harmonic with the fundamental alone ("dc $+f$" and "$f + 2f$" respectively) indicates that most of the phase distortion is associated with the inclusion of the second harmonic. Furthermore including all frequencies

up to the 10th harmonic ("dc $+f+\cdots+10f$") supports the conclusion that most of the phase distortion is associated with the second harmonic content in the electron beam.

Since the circuit voltage hot phase velocity is the physical quantity internal to the TWT that defines phase distortion [see (5.2)], we look at MUSE predictions of hot phase velocity for $P_{\text{in}} = -19.5\,\text{dBm}$ including and excluding different frequencies. The results shown in Fig. 5.3 confirm that the inclusion of the second harmonic accounts for most of the change in hot phase velocity, which in turn accounts for most of the phase distortion in Fig. 5.2 via (5.2).

Next we provide more evidence that the average velocity reduction in the electron beam is not the primary cause of phase distortion by using MUSE and LATTE simulations as well as a physical argument. First we consider a large signal LATTE simulation that has been modified to remove the average velocity reduction using the approach given in Section 5.8. In Fig. 5.4 we show the phase distortion produced by LATTE simulations with and without the average velocity adjustment. The result confirms that average velocity reduction, at least prior to gain compression, is not the primary cause of the phase distortion.

We limit the maximum power in Fig. 5.4 to $P_{\text{in}} = -23\,\text{dBm}$ for computational reasons. As discussed in Section 5.8, we use (5.49) to compute the evolution of the average disk velocity in a LATTE simulation. For input powers greater than or equal to $P_{\text{in}} = -23\,\text{dBm}$, the number of space charge harmonics required for (5.49) to converge can become quite large. For convergence at $P_{\text{in}} = -23\,\text{dBm}$ one hundred space charge harmonics were required.

To verify that the average velocity computed from the Lagrangian calculation of (5.49) agrees with the MUSE computation of the dc component of the beam velocity $\tilde{v}_0(z)$, we compare the average beam velocities of both models before and after the removal of the spatially evolving average velocity for $P_{\text{in}} = -23\,\text{dBm}$ in Fig. 5.5. For this input power note that the average electron beam velocities predicted by MUSE and LATTE are virtually identical. Furthermore, the average of the modified LATTE velocities given in (5.50) computed by (5.51) verify the removal of the average velocity reduction.

Finally we consider how the reduction of the average beam velocity could not account for the majority of phase distortion. First we consider a comparison of the hot phase velocity predicted by MUSE and LATTE [computed using (5.4)] to the average beam velocity computed by MUSE in Fig. 5.6 for $P_{\text{in}} = -20\,\text{dBm}$. According to Fig. 5.2, the phase distortion for this input power is about 10° which according to Fig. 5.6 corresponds to a change in hot phase velocity of about 1%. As seen in Fig. 5.6 the average velocity for this input power only reduces from its initial value by 0.2%. If the reduction in beam velocity was related to the percent to which the hot phase velocity could change to cause phase distortion, then over the length of $0.5\,\text{cm}$[1] (5.2) indicates that this could only account for about 1.3° of phase

[1]We estimate a constant value of 0.2% reduction, which is the maximum reduction achieved, over half of the entire length for which the reduction takes place.

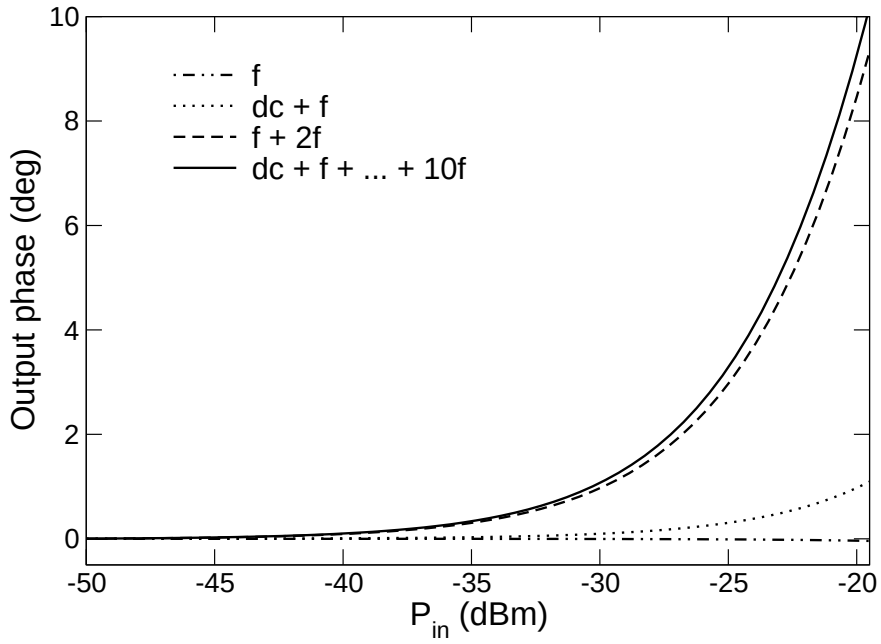

Figure 5.2 Output phase versus input power curves generated by MUSE simulations with varying frequencies included in the simulation. The legend indicates which frequencies were included in the simulation generating the trace. The maximum power represented on the graph corresponds to the 1 dB gain compression point as seen in Fig. 5.1. For the input powers in this figure LATTE and MUSE have nearly identical phase predictions accounting for dc through the tenth harmonic, as seen in Fig. 5.1.

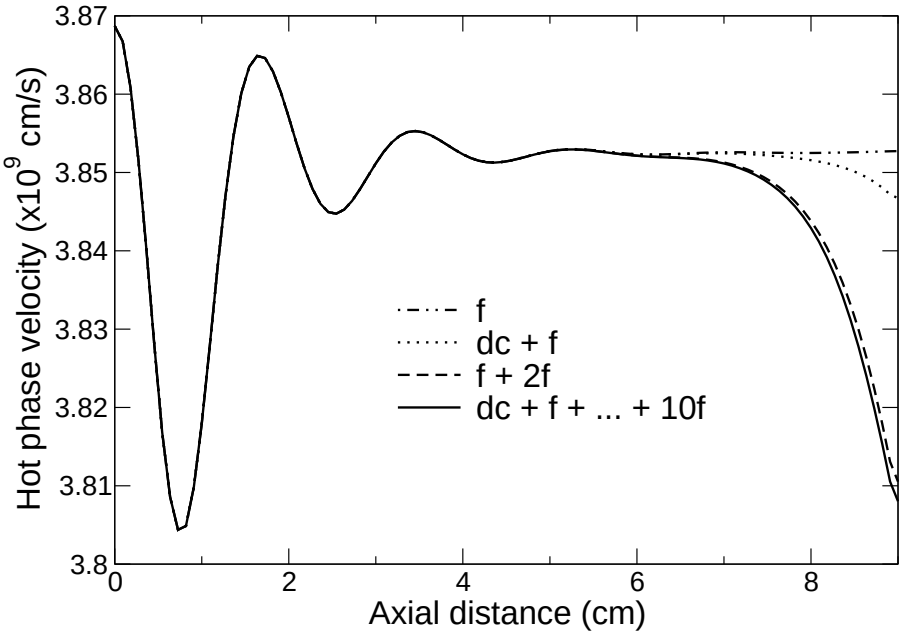

Figure 5.3 MUSE computations of the hot phase velocity (5.4) at the fundamental frequency with varying frequencies included in the simulation. The legend indicates which frequencies were included in the simulation generating the trace. The input power $P_{\text{in}} = -19.5\,\text{dBm}$ corresponds to the 1 dB gain compression point shown in Fig. 5.1. For this input power the phase difference as predicted by LATTE is nearly identical to MUSE when accounting for dc through the tenth harmonic.

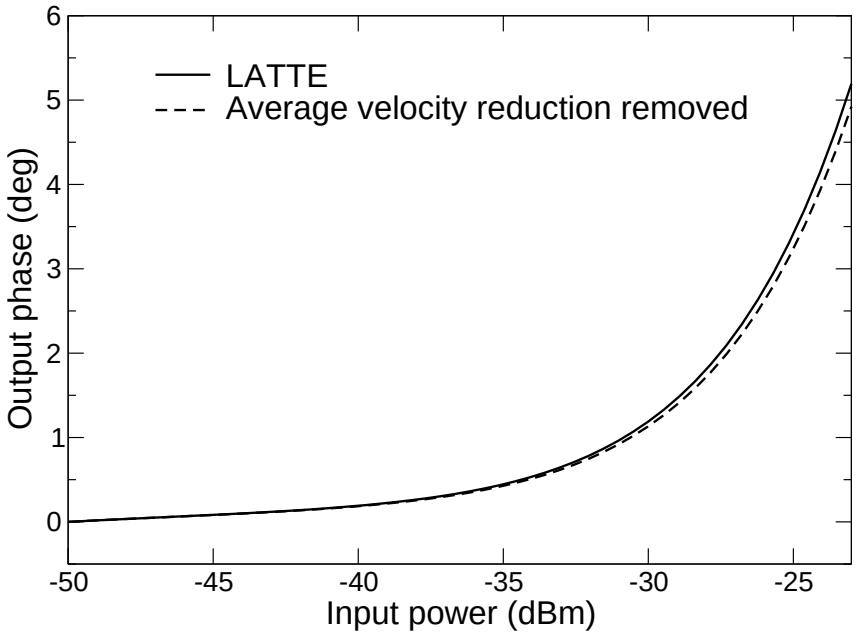

Figure 5.4 Output phase for LATTE simulations with and without removal of the average beam velocity reduction as described in Section 5.8. One hundred space charge harmonics were used to compute $\langle v \rangle_0$ from (5.49).

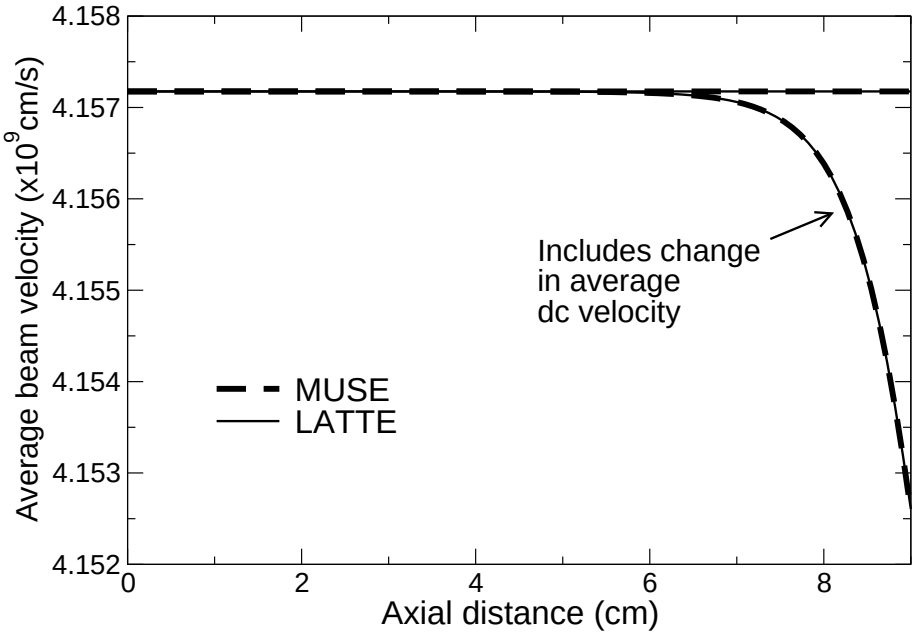

Figure 5.5 Average electron beam velocities computed by LATTE and MUSE. LATTE traces were computed by (5.49), MUSE traces are the dc frequency of the velocity $\tilde{v}_0(z)$. Shown are computations with and without the velocity adjusted to remove the average change in the dc component. The input power used to generate the traces is $P_{\text{in}} = -23\,\text{dBm}$, which is the maximum power appearing in Fig. 5.4.

distortion, far below the 10° seen in Fig. 5.2 and computed thusly

$$\Phi = \omega \int_0^{0.5\text{cm}} \left[\frac{1}{v}\left(1 - \frac{\Delta v}{v}\right) - \frac{1}{v}\right] dz \tag{5.5}$$

$$= \frac{2\pi 14\,\text{GHz}}{3.85 \times 10^7 \text{cm/s}} \times 0.002 \times 0.005 \tag{5.6}$$

$$= 1.3°. \tag{5.7}$$

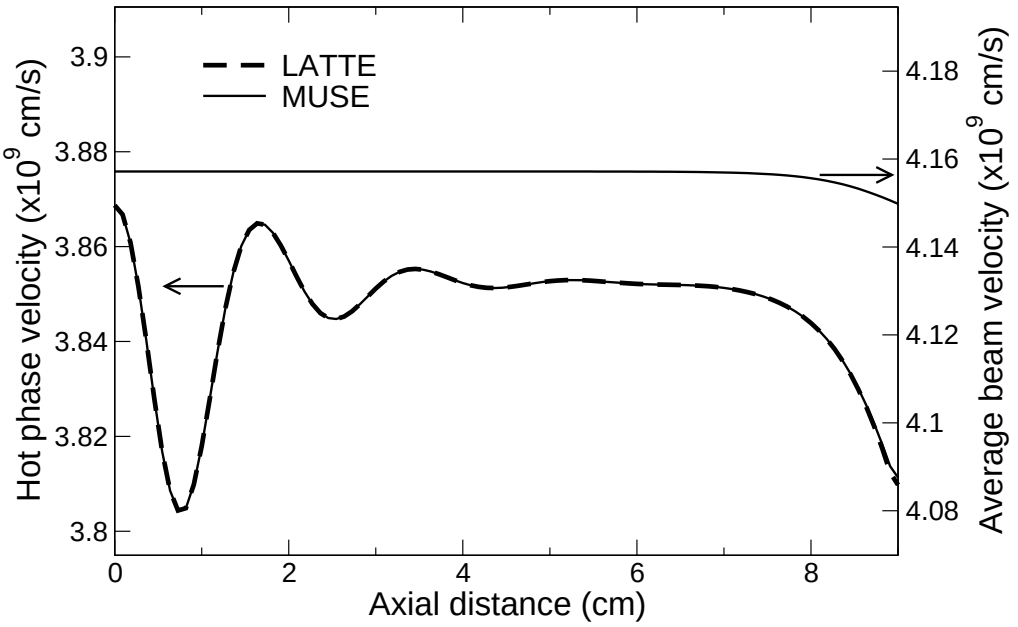

Figure 5.6 Average electron beam velocity computed by MUSE, and hot phase velocity at the fundamental computed by LATTE and MUSE for $P_{\text{in}} = -20\,\text{dBm}$. The ranges of values on both axes are 3% of the value of the respective curve at $z = 5\,\text{cm}$.

5.2.2 Analytic results

We can use the analytic solution of Chapter 3 to probe further into the physical mechanisms of phase distortion. Because of the approximations made in deriving the S-MUSE model, the phase distortion predicted by MUSE, S-MUSE, and LATTE agree qualitatively but not quantitatively. However, we postulate that the physical interpretations made for the S-MUSE model are also true for the MUSE and LATTE models for input powers prior to gain compression.

The structure of the S-MUSE solution for a physical variable at a particular frequency is a linear combination of z dependent complex exponentials [83]. For example, the voltage at

the fundamental may be approximated as

$$\tilde{V}_1(z,t) \;=\; \left\{ A_{\rm dr} \exp\left(\mu_{\rm dr} + i\kappa_{\rm dr}\right) z + \sum_q A^q_{\rm nl} \exp\left(\mu^q_{\rm nl} + i\kappa^q_{\rm nl}\right) z \right\} e^{if_1\omega_0\left(\frac{z}{u_0} - t\right)} \qquad (5.8)$$

where the dr subscript refers to the driven portion of the solution, i.e., the exponentially growing mode due to the fundamental input, and the nl subscript refers to quantities occurring as a result of the nonlinear interactions. The subscript 1 appearing in $\tilde{V}_1$ and f_1 refer to the fundamental frequency. Forms similar to (5.8) apply to the other TWT state variables at the fundamental frequency.

In (5.8) each complex exponential is related to a particular order of intermodulation product, and each successive term in the sum over q accounts for the next higher order odd intermodulation product ($3^{\rm rd}, 5^{\rm th}$, etc.). For example, the fundamental frequency is an odd order intermodulation product of itself, e.g. $2f_1 - f_1 = f_1$, $3f_1 - 2f_1 = f_1$, etc., and we can write (5.8) as

$$\tilde{V}_1(z,t) \;=\; \left\{ A_{\rm dr} e^{\gamma_{\rm dr} z} + A^{\rm 3IM}_{\rm nl} e^{\gamma^{\rm 3IM}_{\rm nl} z} + A^{\rm 5IM}_{\rm nl} e^{\gamma^{\rm 5IM}_{\rm nl} z} + \ldots \right\} e^{if_1\omega_0\left(\frac{z}{u_0} - t\right)} \qquad (5.9)$$

where we have written the growth rates μ and phase angles κ in (5.8) together as complex propagation constants γ.

The complete solution to S-MUSE is made up of an infinite number of complex exponentials (see Chapter 3). In (5.8) and (5.9) we only express the dominant terms and ignore the terms that do not contribute appreciably to the solution near the output of the TWT. Due to the neglect of non-growing or weakly growing modes in (5.8) and (5.9), both from the linear and nonlinear portions of the solution, evaluation of the equations at $z = 0$ does not give the correct value of the input. The equations are therefore only good approximations, both in amplitude and phase, for lengths such that the exponentially growing modes dominate the total solution (for example $z \geq 4\,\text{cm}$ in Fig. 5.6). In Section 5.7 we provide more details for the solution of S-MUSE in order to compute (5.8) and (5.9).

In Fig. 5.7 we compare the output phase computed with (5.8) to the output phase obtained by simulation of the S-MUSE equations [82] for input powers up to the 1 dB compression point. We show the output phase of (5.8) accounting for only the 3IM and also accounting for the 3IM and the 5IM. The analytic prediction accounting for the 5IM matches the simulation almost identically.

Comparing the AM/PM curves (derivatives of the output phase) of S-MUSE and LATTE in Fig. 5.1 we see that S-MUSE predicts most of the phase distortion of the large signal simulation prior to gain compression. Then from Fig. 5.7 we conclude that the majority of the *large signal* TWT phase distortion prior to gain compression is predicted by (5.8). Hence the primary mechanism for the *large signal* phase distortion is that the fundamental frequency is an intermodulation product of itself, which is the view that comes from the analytic solution to the S-MUSE model. We attribute the output phase discrepancies between LATTE and S-MUSE to the nonlinearities that were neglected in deriving S-MUSE, including the

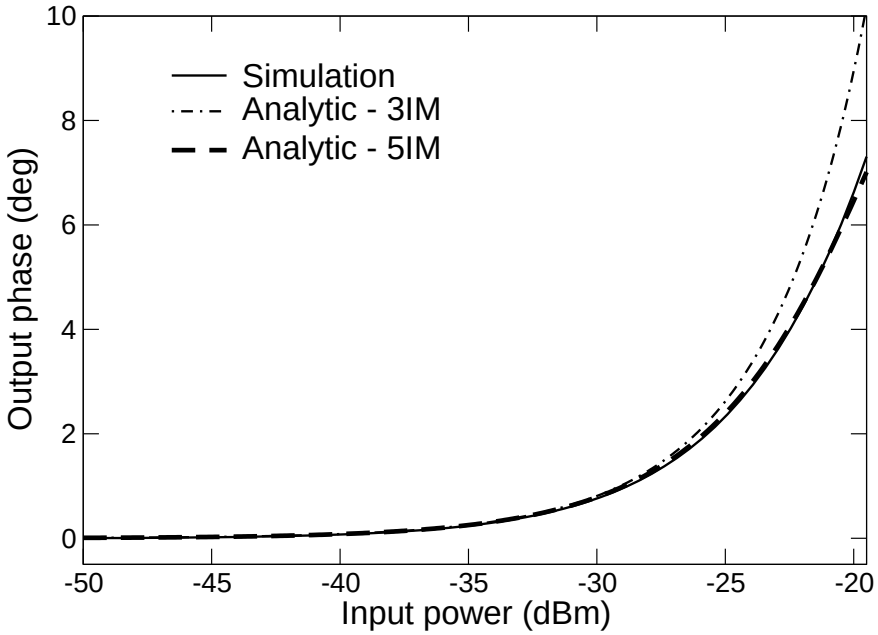

Figure 5.7 Simulation and analytic predictions of S-MUSE output phase. For the analytic formula to match the simulation the contributions from the 5IM term need to be included. The maximum power represented on the graph corresponds to the 1 dB gain compression point as seen in Fig. 5.1. The simulation accounts for circuit frequencies up to the third harmonic and electron beam frequencies up to the tenth harmonic.

approximation of the average beam velocity and the average charge density as constants, and the resulting under predictions of intermodulation spectra by S-MUSE as can be seen in [82].

Based on the above comparison of *large signal* simulations to the analytic solution to S-MUSE, and supported by the simulations of Section 5.2.1, we submit the following view of TWT phase distortion valid prior to gain compression, and speculatively into saturation. The fundamental drive frequency induces harmonic distortions on the electron beam, and these harmonic distortions combine back with the fundamental to produce distortions in the circuit voltage at the fundamental frequency. Furthermore, the third harmonic distortions in the electron beam combine with the second harmonic distortions to produce distortions in the circuit voltage at the fundamental frequency. This process also occurs for higher order harmonics, but to a more limited extent as the order becomes higher. Therefore the fundamental frequency is composed of the driven mode, the 3IM and 5IM distortion modes, as well as higher order odd intermodulation modes. The relative weights of the driven mode and the distortion modes determine the evolving phase of the fundamental circuit voltage, and hence the evolving hot phase velocity of the fundamental circuit voltage. The hot phase velocity then determines the phase distortion as described in the beginning of Section 5.2.

For more insight into the how the hot phase velocity at the fundamental changes to produce phase distortion, we can consider the evolution of the fundamental voltage phase $\theta_1(z)$ as defined in (5.3) and computed from (5.8). For simplicity we consider input powers for which only the 3IM contribution to the analytic solution is required to match the simulation (e.g. P_{in} less than $-28\,\text{dBm}$ in Fig. 5.7). For such inputs we have

$$\theta_1(z) \;=\; \tan^{-1}\left\{\frac{A_{\text{dr}}e^{\mu_{\text{dr}}z}\sin\kappa_{\text{dr}}z + A_{\text{nl}}e^{\mu_{\text{nl}}z}\sin\kappa_{\text{nl}}z}{A_{\text{dr}}e^{\mu_{\text{dr}}z}\cos\kappa_{\text{dr}}z + A_{\text{nl}}e^{\mu_{\text{nl}}z}\cos\kappa_{\text{nl}}z}\right\}. \tag{5.10}$$

Working through the calculations in Section 5.7 one can show that for the input powers under consideration $A_{\text{dr}} \gg A_{\text{nl}}$. However, for large enough values of z the terms $A_{\text{dr}}e^{\mu_{\text{dr}}z}$ and $A_{\text{nl}}e^{\mu_{\text{nl}}z}$ can become comparable since $\mu_{\text{nl}} = 3\mu_{\text{dr}}$. In the limiting cases of small and large z one has $\frac{d\theta_1}{dz} = \kappa_{\text{dr}}$ and $\frac{d\theta_1}{dz} = \kappa_{\text{nl}}$ respectively, implying constant values of hot phase velocity via (5.4). The limiting case of small z is seen, for example, between 4 cm and 7 cm in Fig. 5.6, where the behavior for $z < 4\,\text{cm}$ is due to the complex exponential modes neglected in (5.8). Since 3IMs rarely attain comparable power levels to the fundamental before power saturation, the limiting case of large z is not attained. Therefore the change in hot phase velocity as a function of distance along the TWT, as seen for $z > 7\,\text{cm}$ in Fig. 5.6 for example, is due to the evolution of the relative weights of the modes in (5.8) and (5.10).

In Fig. 5.8 we show S-MUSE simulation and analytic predictions of the evolution of the hot phase velocity for $P_{\text{in}} = -20\,\text{dBm}$. Consistent with Fig. 5.7 the contribution from the 5IM is required for this input power to accurately model the evolution of the hot phase velocity seen in the simulation.

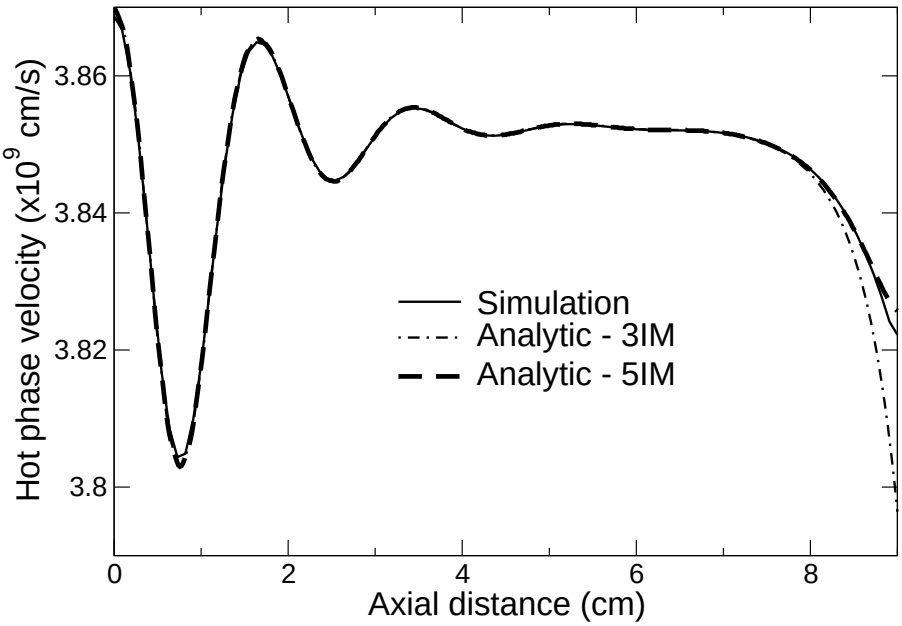

Figure 5.8 Analytic and simulation predictions of S-MUSE hot phase velocity at the fundamental frequency. Inclusion of the 5IM contribution to the analytic solution (5.8) is required to match the simulation result. All of the complex exponentials from the linear portion of the solution are included to get the correct behavior of the hot phase velocity for $z < 4\,\mathrm{cm}$. The simulation includes circuit frequencies up to the third harmonic and electron beam frequencies up to the tenth harmonic.

5.3 Amplitude-phase model & S-MUSE

A popular model for predicting amplifier performance using the nonlinear input-output amplitude and phase transfer characteristics is the so-called amplitude-phase (AP) model [69]. In this section we compare an AP model that uses the analytic prediction of the output phase from (5.8) to S-MUSE simulations with two frequency inputs. While AP models have been proposed and studied, none have used analytic solutions to nonlinear physics based models for the transfer curves. As in Section 5.2, we restrict our attention to input powers to the "linear gain region" of the AM/AM curve.

For an input voltage

$$x(t) \;=\; A(t)\cos(\omega_c t) \tag{5.11}$$

the output voltage in the linear portion of the AM/AM curve for the AP model is

$$y(t) \;=\; \gamma A(t)\cos(\omega_c t + \tilde{\Phi}(A(t))) \tag{5.12}$$

where γ is a constant gain factor, and $\tilde{\Phi}(V_{\rm in})$ is the voltage phase difference between the output and input for an input of $V_{\rm in}\cos\omega_c t$. $\tilde{\Phi}(V_{\rm in})$ is related to $\Phi(P_{\rm in})$ in (5.1) by using [82]

$$P_{\rm in} \;=\; \frac{2V_{\rm in}^2}{\tilde{K}} \tag{5.13}$$

where $\tilde{K}$ is the circuit interaction impedance at ω_c.

If we choose

$$A(t) \;=\; 4V_{\rm in}\cos(\omega_m t) \tag{5.14}$$

then $x(t)$ can be equivalently written

$$x(t) \;=\; 2V_{\rm in}\left\{\cos\left[(\omega_c+\omega_m)t\right] + \cos\left[(\omega_c-\omega_m)t\right]\right\} \tag{5.15}$$

and the output of the AP model is

$$y(t) \;=\; \gamma 4V_{\rm in}\cos(\omega_m t)\cos(\omega_c t + \tilde{\Phi}(4V_{\rm in}\cos(\omega_m t))). \tag{5.16}$$

Using $\tilde{\Phi}$ predicted by (5.8) we compute the output spectrum of (5.16) and compare it to a simulation of the S-MUSE equations with the input given by (5.15). We perform the calculations for two different input powers and two different values of ω_m.

First we fix the input power to $-30\,$dBm and compute the spectra for $\omega_m/2\pi = 1.0\,$MHz and $\omega_m/2\pi = 100.0\,$MHz. The results for the narrow spacing are shown in Fig. 5.9 and the results for the wide spacing are shown in Fig. 5.10. For $\omega_m/2\pi = 1.0\,$MHz the 3IM and 5IM the predictions of the AP model are $2.3\,$dB and $4.2\,$dB below those of the simulation respectively. For $\omega_m/2\pi = 100.0\,$MHz the 3IM and 5IM the predictions of the AP model are $2.9\,$dB and $4.7\,$dB below those of the simulation respectively. Since $\tilde{\Phi}$ is computed at a

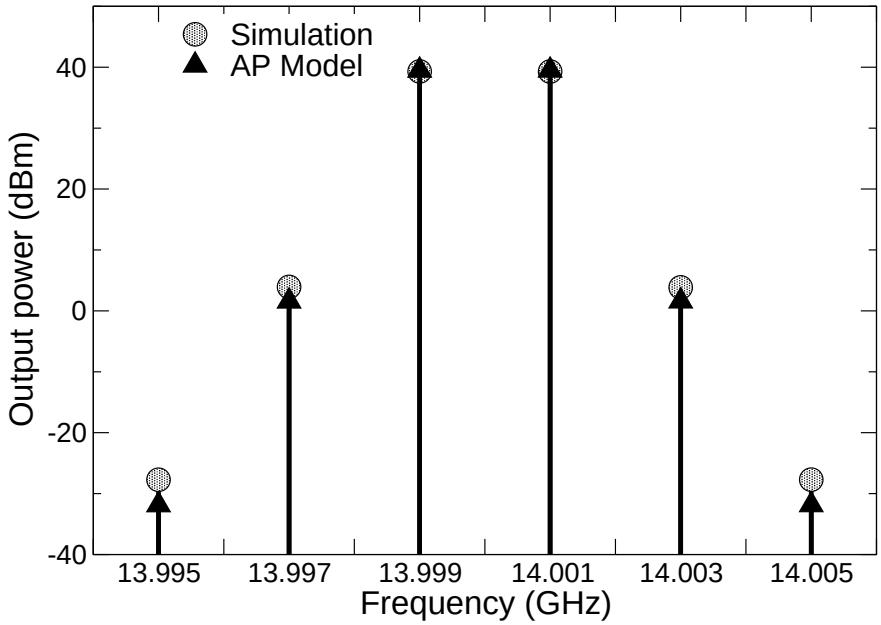

Figure 5.9 Comparison of S-MUSE simulation and the AP model output spectra for two input tones. The input power is $P_{\text{in}} = -30\,\text{dBm}$ and the modulation frequency is $\omega_m/2\pi = 1.0\,\text{MHz}$.

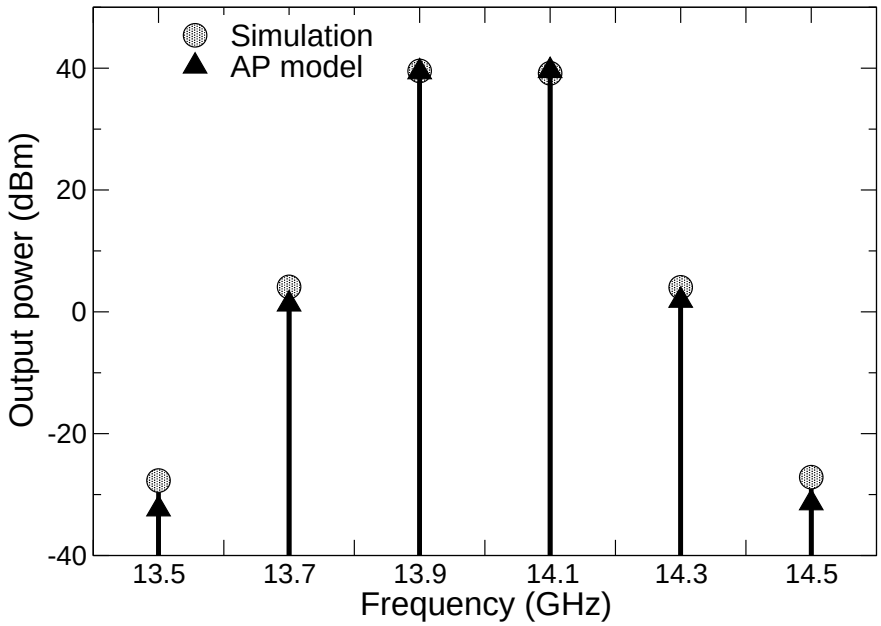

Figure 5.10 Comparison of S-MUSE simulation and the AP model output spectra for two input tones. The input power is $P_{\text{in}} = -30\,\text{dBm}$ and the modulation frequency is $\omega_m/2\pi = 100.0\,\text{MHz}$.

single frequency, namely ω_c, the AP model is expected to apply only over a narrow band of frequencies about ω_c. We see that the AP model with a narrow frequency spacing is in closer agreement with the simulation, but both frequency spacings are similar in their errors.

For the same frequency spacings we repeated the above calculations with an input power $P_{\text{in}} = -23\,\text{dBm}$. The results for the narrow spacing are given in Fig. 5.11 and the results for the wide spacing are given in Fig. 5.12. In both cases the AP model predictions of the 3IM are about 5 dB lower than the simulation results, whereas the 5IM predictions are greater than the simulation results by about 2 dB. While the reason for this discrepancy is not entirely understood, we believe that it might lie in the gain compression that the simulation inherently contains and is ignored in our AP model. Relative to $P_{\text{in}} = -50\,\text{dBm}$ an input of $P_{\text{in}} = -30\,\text{dBm}$ corresponds to 0.11 dB of gain compression, whereas an input of $P_{\text{in}} = -23\,\text{dBm}$ corresponds to 0.5 dB of gain compression predicted by S-MUSE simulations. To test this hypothesis an AP model accounting for the gain compression could be constructed and tested.

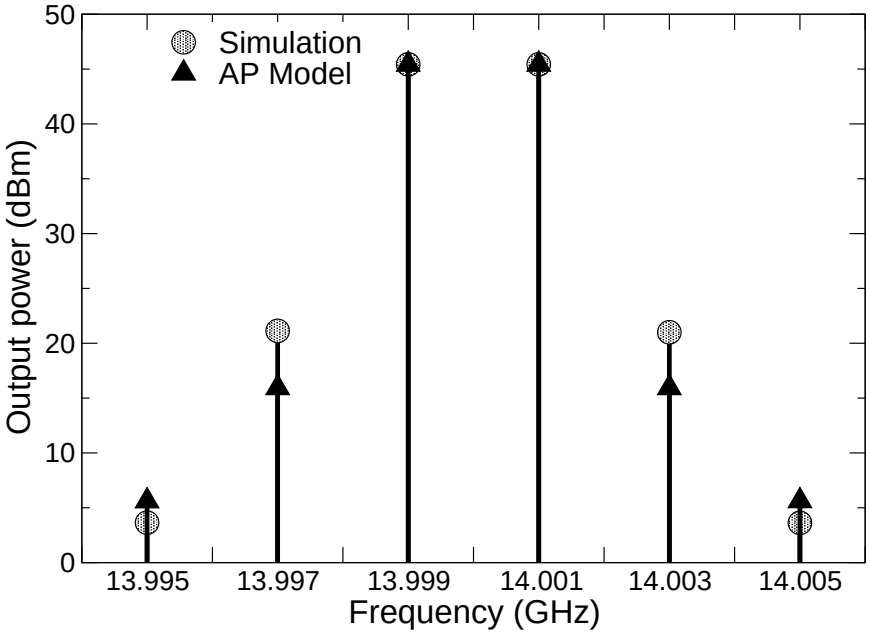

Figure 5.11 Comparison of S-MUSE simulation and the AP model output spectra for two input tones. The input power is $P_{\text{in}} = -23\,\text{dBm}$ and the modulation frequency is $\omega_m/2\pi = 1.0\,\text{MHz}$.

It is instructive to note that the AP model does not predict spectral content at the harmonics of the carrier frequency ω_c, even though it is well known that such spectral distortion exists. This fact is inherent in the construction of the AP model since when transfer curves are measured or simulated, attention is restricted to the TWT behavior at only the fundamental frequency which is observable at the input and output terminals. The relation between the transfer curve distortions to the harmonic spectrum is important if

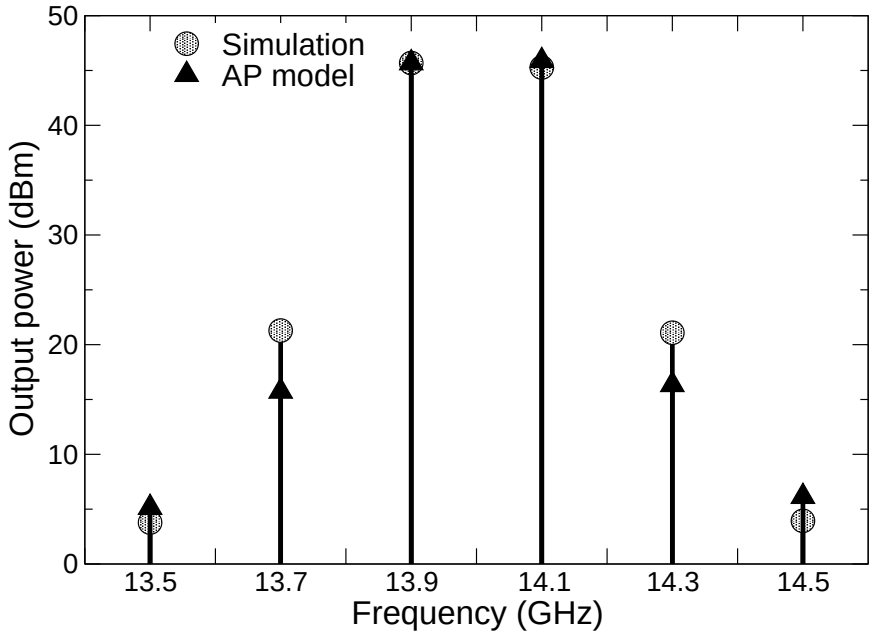

Figure 5.12 Comparison of S-MUSE simulation and the AP model output spectra for two input tones. The input power is $P_{\text{in}} = -23\,\text{dBm}$ and the modulation frequency is $\omega_m/2\pi = 100.0\,\text{MHz}$.

one is designing devices such as linearizers based only on TWT transfer curves, where the temptation might be to restrict one's attention to only the fundamental frequency. In the case of phase distortion Section 5.2 provides what we believe to be the key connections between harmonic distortions and phase distortion at the fundamental.

5.4 Parametric dependence of phase distortion

In Section 5.2 we showed that the second harmonic frequency influences output phase at the fundamental frequency through an intermodulation process. Therefore, it is of interest to know how phase distortion at the fundamental depends on circuit dispersion and electron beam parameters at the second harmonic. Using LATTE we look at the dependence of the AM/PM distortion at the fundamental on the cold circuit phase velocity $\tilde{v}_{\rm ph}$, circuit interaction impedance $\tilde{K}$, and electron beam space charge reduction factor $\tilde{R}$ at the second harmonic. We independently set these parameters to five values and generate AM/AM and AM/PM curves for each parameter value. The values are evenly spaced between the respective parameter value at the fundamental and the parameter value at the third harmonic. The parameter values chosen are not necessarily physically realizable since we are directly changing the parameter, not the circuit dimensions or electron beam dimensions to attain the set of parameters. However, the results give a good indication of the relative role the parameters play in phase distortion.

We expect the phase distortion to behave differently when the second harmonic is in the linear gain bandwidth of the TWT, since the second harmonic will then have a larger amplitude and produce a larger fundamental intermodulation. Therefore we choose two TWT designs for this study, one in which the second harmonic is in the linear gain bandwidth, and one in which the second harmonic is out of the linear gain bandwidth. For the "narrow band" TWT we use the Ku-band design of Section 5.2, and for the "wide band" design we use simulation parameters based on the experimental Wisconsin Northrup Grumman (X-WING) 1.5 octave C-band TWT [79]. The electron beam parameters for X-WING are listed in Table 5.3 and the relevant dispersion parameters for X-WING are listed in Table 5.4.

Table 5.3 XWING TWT electron beam and circuit parameters.

Parameter	**Value**
Cathode voltage	-2.75 kV
Beam current	0.22 A
Beam radius	0.55 mm
Helix radius	1.4 mm

In Figs. 5.13–5.15 we show the simulation results for the Ku-band TWT. From Fig. 5.13 we see that the phase distortion is relatively unaffected by the phase velocity at the second harmonic. We see from Fig. 5.14 that the interaction impedance at the second harmonic

Table 5.4 XWING TWT dispersion parameters.

f (GHz)	$\tilde{v}_{\rm ph}$ ($\times 10^9$ cm/s)	$\tilde{K}$ (Ω)	$\tilde{R}$
2.00	2.487	103.094	2.787×10^{-2}
4.00	2.515	38.132	9.802×10^{-2}
6.00	2.552	15.411	1.846×10^{-1}

can affect the input power at which the maximum AM/PM conversion occurs and the maximum value of AM/PM conversion. Furthermore, larger values of interaction impedance can produce AM/PM conversion coefficients of zero. Finally, from Fig. 5.15 we see that smaller values of space charge reduction factor have a larger maximum AM/PM conversion coefficient, but the input power where the maximum AM/PM conversion is attained is unchanged.

In Figs. 5.16–5.18 we show the simulation results for the C-band TWT. From Fig. 5.16 we see that the phase distortion is relatively unaffected by the phase velocity at the second harmonic as was the case for the narrow band TWT. The interaction impedance at the second harmonic for the wide band TWT displays the clearest trend and has the greatest effect on AM/PM distortion as seen in Fig. 5.17. Larger values of interaction impedance produce the largest AM/PM distortion, most likely because larger interaction impedance produces larger harmonic power which results in larger intermodulation at the fundamental. Finally, from Fig. 5.18 we see that the space charge reduction factor does not have much effect on either the location or value of the maximum AM/PM coefficient.

5.5 Insights into TWT linearization

Chen *et al.* [14] have recently presented a new method of linearizing TWTs. The method involves applying small bias voltages to the helix based on either "direct feed" or feedback processing of the input signal. The bias voltage is a function of the input power "envelope," and has the effect of adjusting the electron beam velocity by changing the potential an electron sees as it enters the helix. The change in electron beam velocity can be equivalently viewed as a change in electron beam voltage. The explanation for how the linearization technique works offered in [14] is based on the view that phase distortion is due to slowing down of electrons in the beam. Our new view of phase distortion led us to doubt their explanation, and attempt to offer our own. The experimental results given in Figs. 4 and 5 of [14] are for TWT input conditions 9 dB backed off from saturation, well within the range of applicability of our theory.

We submit that linearization using the technique of [14] of a two tone input signal as shown in Figs. 4 and 5 of [14], and similar to the input spectra of Section 5.3, should not be explained in terms of phase distortion. Firstly, we claim that a constant voltage applied to the helix to compensate for phase distortion for single frequency sine wave inputs can be explained in terms of linear TWT theory. Secondly, we claim that the linearization of a

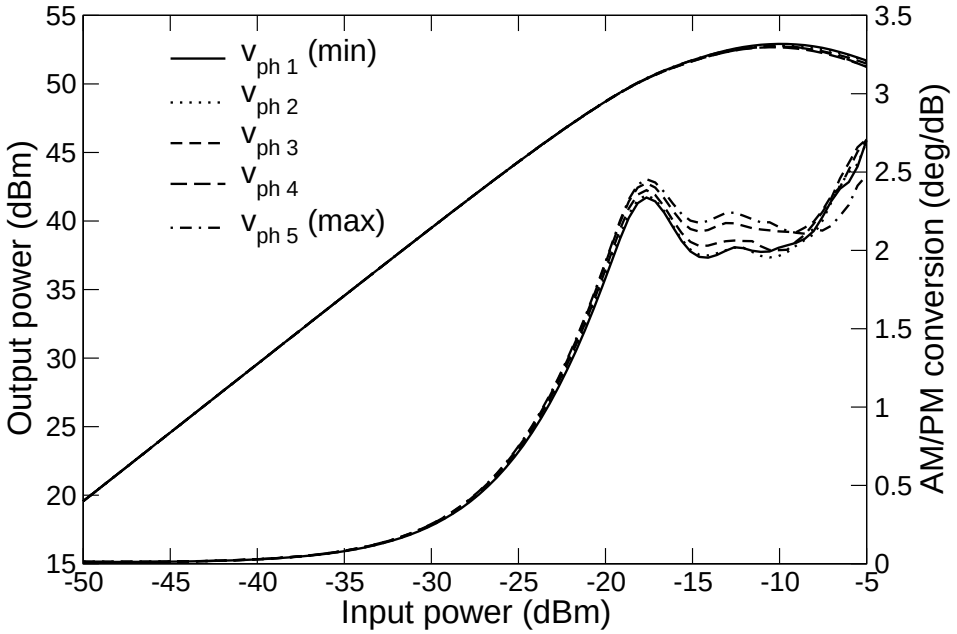

Figure 5.13 AM/AM and AM/PM distortion for the Ku-band design at 14 GHz for five values of cold circuit phase velocity at the second harmonic. The legend represents the five values ranging from the minimum parameter value (min) to the maximum parameter value (max).

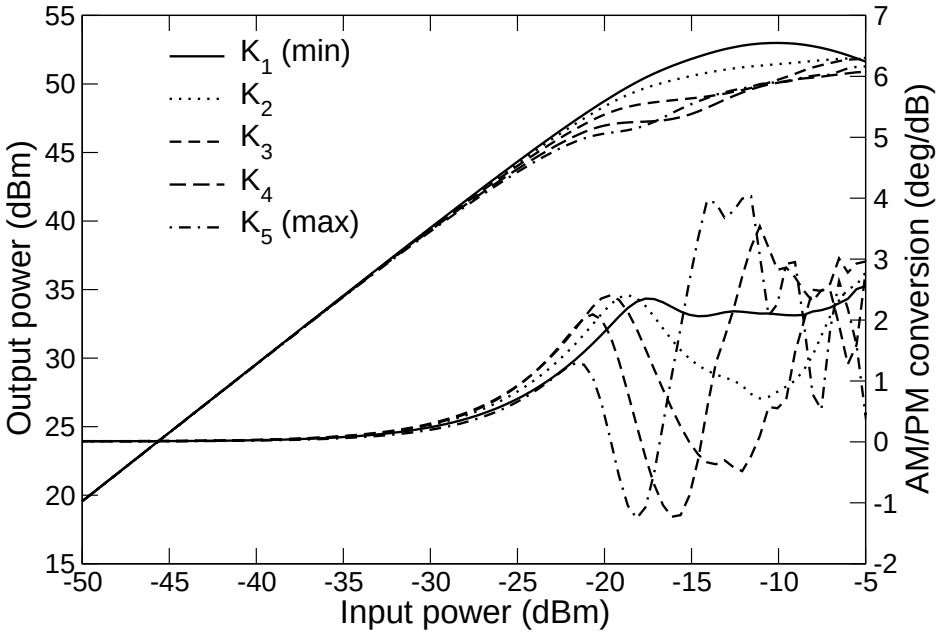

Figure 5.14 AM/AM and AM/PM distortion for the Ku-band design at 14 GHz for five values of cold circuit interaction impedance at the second harmonic. The legend represents the five values ranging from the minimum parameter value (min) to the maximum parameter value (max).

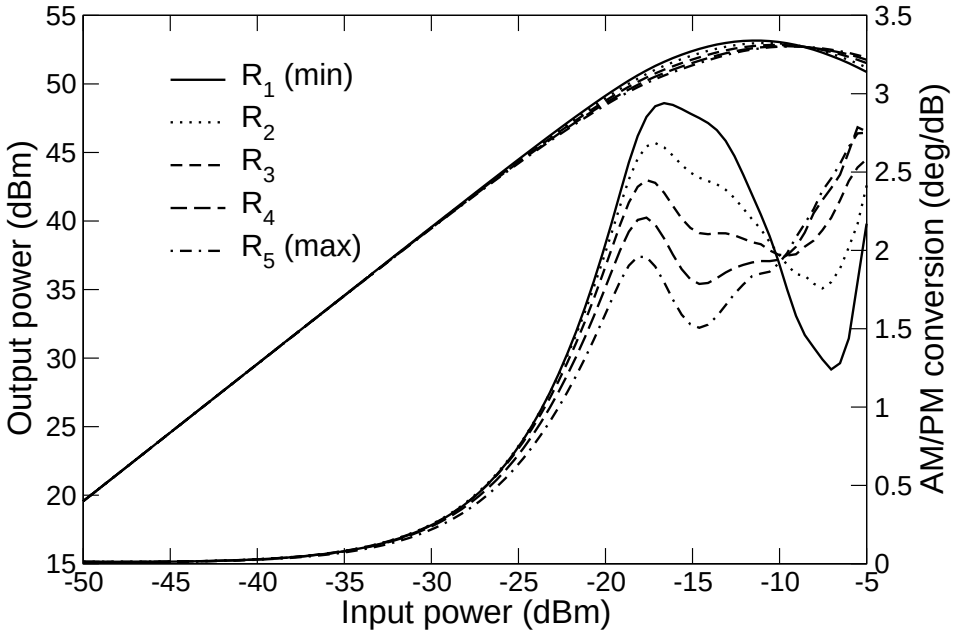

Figure 5.15 AM/AM and AM/PM distortion for the Ku-band design at 14 GHz for five values of space charge reduction factor at the second harmonic. The legend represents the five values ranging from the minimum parameter value (min) to the maximum parameter value (max).

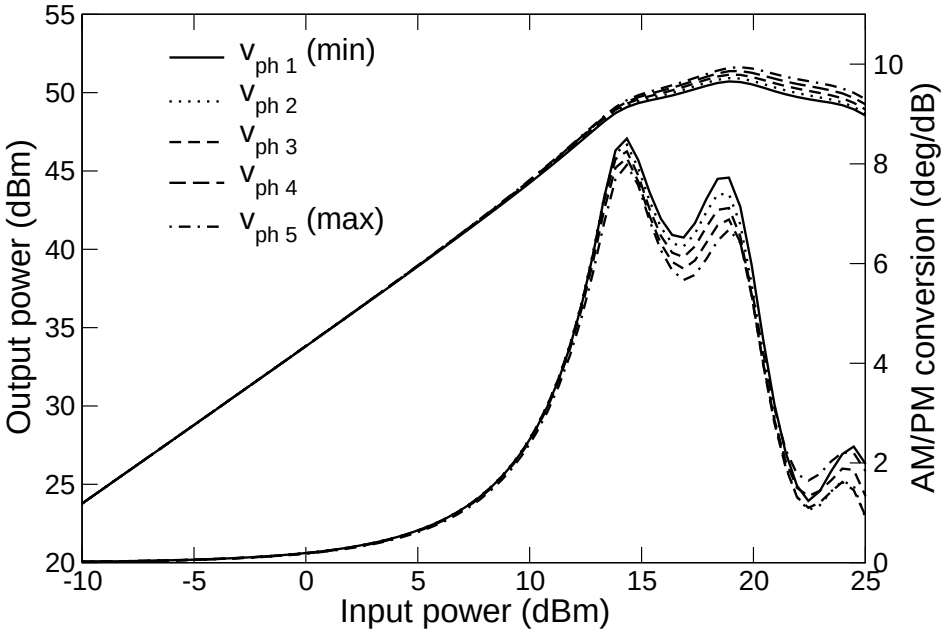

Figure 5.16 AM/AM and AM/PM distortion for the C-band design at 2 GHz for five values of cold circuit phase velocity at the second harmonic. The legend represents the five values ranging from the minimum parameter value (min) to the maximum parameter value (max).

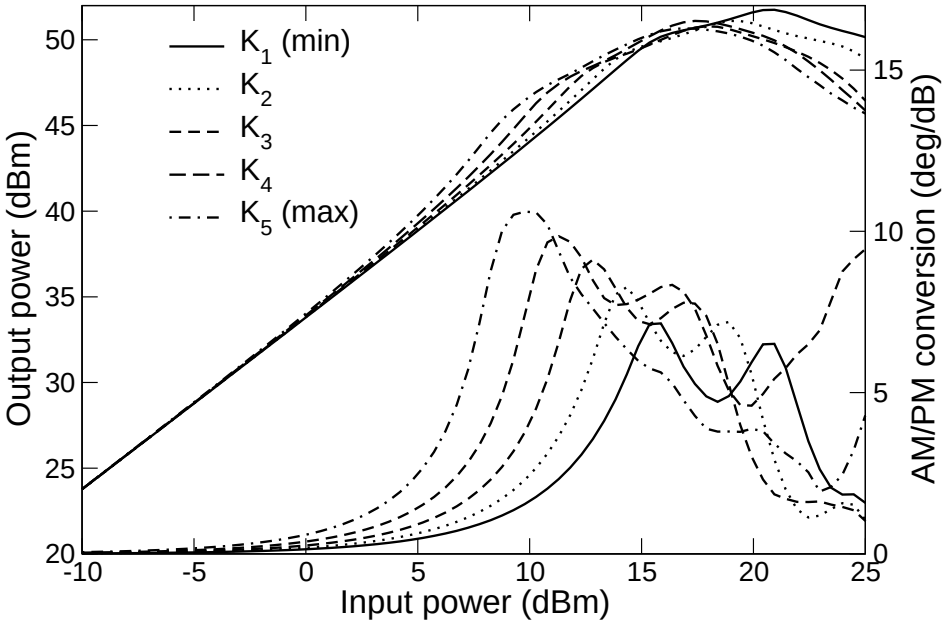

Figure 5.17 AM/AM and AM/PM distortion for the C-band design at 2 GHz for five values of cold circuit interaction impedance at the second harmonic. The legend represents the five values ranging from the minimum parameter value (min) to the maximum parameter value (max).

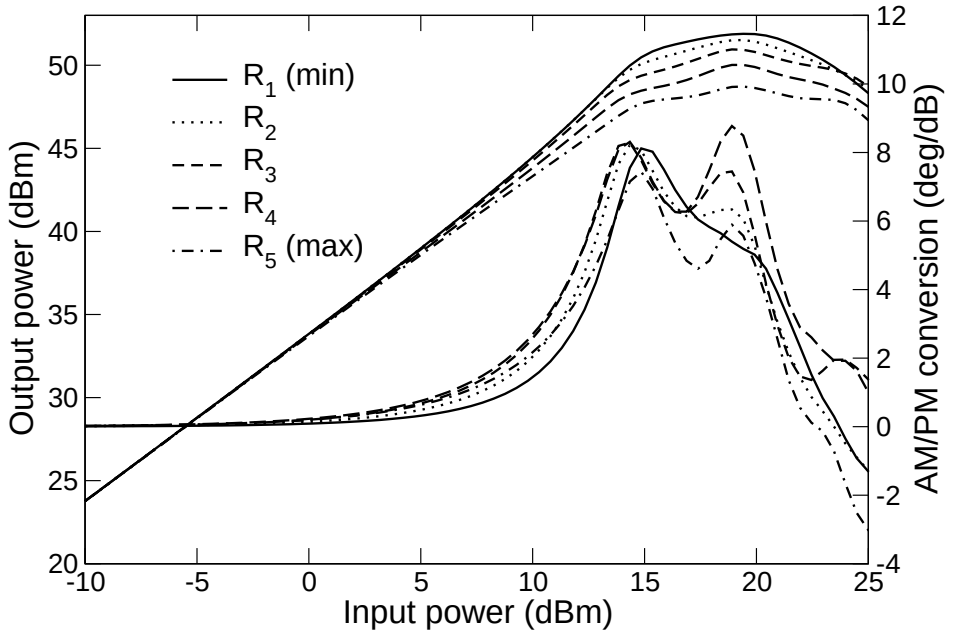

Figure 5.18 AM/AM and AM/PM distortion for the C-band design at 2 GHz for five values of space charge reduction factor at the second harmonic. The legend represents the five values ranging from the minimum parameter value (min) to the maximum parameter value (max).

two tone input signal with the new technique should be viewed as the injection of a beam velocity modulation at the difference frequency of the two input frequencies.

Applying a dc voltage bias to the helix compensates for the nonlinear output phase distortion by changing the electrical length of the TWT, i.e., the number of wavelengths in the TWT, based on the *linear* Pierce theory [61]. That is, the dependence of the linear "hot wavenumber" $\beta_{\rm lin}$ (see Section 5.2) on input voltage is sensitive enough such that a small change in beam voltage can account for a non-negligible phase change at the output of the TWT. Using the driven term of (5.8) one gets

$$\beta_{\rm lin} \;=\; \kappa_{\rm dr}(V_0) + f_1\omega_0\sqrt{\frac{m_e}{2eV_0}} \tag{5.17}$$

where V_0 is beam voltage, m_e is electron mass, and e is electron charge. In (5.17) $\kappa_{\rm dr}(V_0)$ is the imaginary part of the eigenvalue of $\mathbf{A}_1$ (see Section 5.7) corresponding to the exponentially growing solution, and we have used that $eV_0 = (1/2)m_e u_0^2$. One can show that for small changes in V_0 (5.17) is approximately a linear function of V_0 and that the accumulated phase $\beta_{\rm lin}(V_0)L$ can change by as much as 25° for less than a 1% change in V_0.

In Fig. 5.19 we show LATTE calculations of output phase versus input power for five values of beam voltage. The total range of beam voltages spans less than 1% of the design beam voltage, but the phase difference between these values, which to leading order can be predicted by linear theory, is about 25°. To obtain a constant output phase for any value of input power, one can select from the parameterized output phase versus input power curves. One chooses the curve that passes through the desired value of output phase and input power, and sets the bias voltage, by a feedback loop for example, such that the beam voltage is equal to the value labeling the intersecting curve. In this manner the phase distortion, which is a single frequency input measurement, can be compensated for. Note that the input power used for the experiment in [14] would correspond approximately to $P_{\rm in} = -26\,{\rm dBm}$ in Fig. 5.19, i.e., 9 dB backed off from saturation (see Fig. 5.1). To show that the phase offset for different helix voltages is well approximated by linear theory for all input powers, we include input powers up to and beyond saturation.

We saw in Section 5.3 that an input signal consisting of two frequencies with a spacing of $2\omega_m$ centered about ω_c could be written as

$$x(t) \;=\; \cos(\omega_m t)\cos(\omega_c t) \tag{5.18}$$

where typically $\omega_m \ll \omega_c$. If such a signal is passed through a diode for envelope detection, the diode output signal will have a frequency of $2\omega_m$ due to the diode rectification. If this low frequency signal is then used for the helix bias, one effectively has an input modulation on the electron beam voltage at the difference frequency $2\omega_m$. Furthermore, this signal is applied to a "grid compensation circuit" in [14] which would also have the effect of an input modulation on the electron beam voltage at the difference frequency $2\omega_m$. Therefore, we claim that the new technique of linearization put forward by Chen *et al.* [14] is equivalent to injecting a difference frequency modulation on the beam velocity.

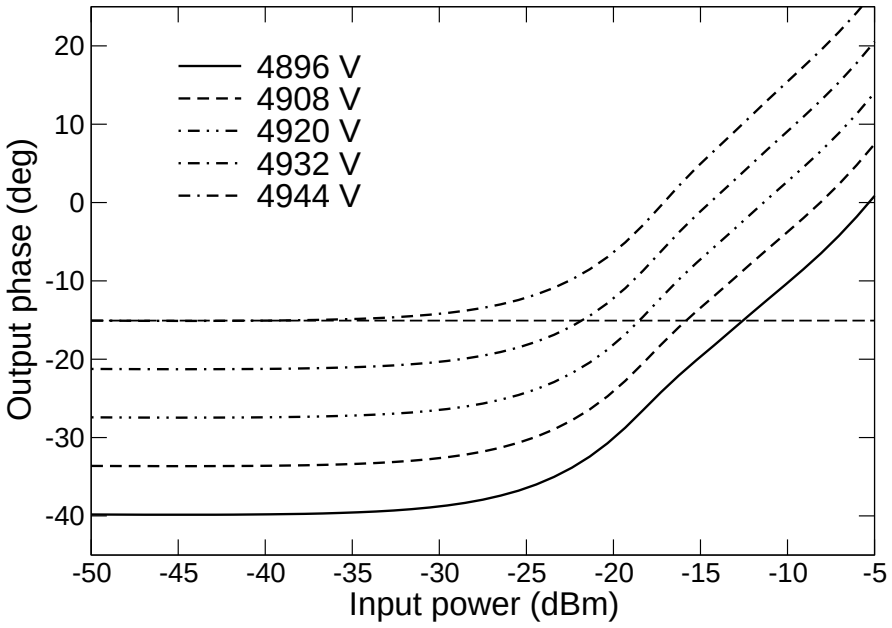

Figure 5.19 Output phase versus input power for several values of dc beam voltage for the Ku-band TWT design. The range of the bias voltages spans 48 V, less than 1% of the design beam voltage.

A recent theory of harmonic injection in a TWT [81] has shown that it is theoretically possible to obtain intermodulation cancellation by injection of the difference frequency in the circuit voltage. However, because the difference frequency is typically outside of the linear gain bandwidth, substantial input powers at the difference frequency are expected to be required. Since the electron beam has no such bandwidth limitations, it is expected that modest difference frequency modulations of the beam velocity, such as with the proposed scheme, may be more effective than difference frequency injection of circuit voltage. This topic will be explored further in a future work.

5.6 Conclusions

Phase distortion has been said to "dominate TWT nonlinearity" [14] in TWTs. In the literature many authors have attributed phase distortion to the slowing down of electrons in the electron beam, i.e., the reduction of the average electron beam velocity (see e.g. [41, 30, 14]). Through simulation and analysis we offer evidence that phase distortion, at least prior to 1 dB gain compression, is not due to slowing down of electrons in the beam. Rather, we attribute phase distortion to harmonic generation in the electron beam and an intermodulation process that results in distortions at the fundamental.

The implications of the new understanding of phase distortion are many. Firstly, provided with a new view of nonlinear TWT physics, one may be led to consider alternative parametric dependencies and explanations for physical phenomenon. We have provided examples of such studies in Sections 5.3–5.5. Furthermore, the new understanding may possibly lead to improved TWT designs, since the notions that a designer has about how a device works inevitably influence how they proceed with a design.

Using the MUSE, S-MUSE, and LATTE TWT models we explore phase distortion in a TWT. The unique ability of the MUSE model to systematically suppress the effects of different frequencies in the nonlinear TWT behavior shows that the second harmonic distortion in the electron beam is the most dominant factor in causing phase distortion, at least prior to gain compression. Furthermore, we show that the average slowing down of electrons is not the primary cause of phase distortion using MUSE simulations in addition to large signal LATTE simulations that were corrected to remove the average velocity reduction.

With the approximate analytic solution to the S-MUSE model we give an insightful picture of the fundamental frequency also being a self-intermodulation product. We show that prior to 1 dB gain compression the analytic solution accounting for the 3IM and 5IM contributions has a phase distortion that closely matches the phase distortion from simulation of the S-MUSE equations. We also show that the change in voltage hot phase velocity which causes phase distortion is due to an evolving balance of the driven and intermodulation modes in the solution.

Leveraging off of our new understanding of phase distortion we consider several applications. First, we compare S-MUSE simulations to an amplitude-phase model that uses the approximate analytic solution to S-MUSE for the output phase versus input power. We se

that there were discrepancies in the intermodulation spectra predicted by the two methods, and that the disagreement is worse for wider frequency spacings and for larger input powers. The study reinforces our view that the amplitude-phase model is an incomplete picture of nonlinear TWT physics, and that measuring single frequency phase distortion characteristics captures only a part of the harmonic and intermodulation physics happening internal to the TWT. Second, we study how phase distortion depends on circuit and electron beam parameters at the second harmonic. We find that circuit interaction impedance at the second harmonic has the greatest effect on AM/PM distortion, especially when the second harmonic is within the linear gain bandwidth of the TWT. Lastly, we consider a new technique of linearization [14] and offer a physical explanation for the linearization mechanism. In this case again we propose that phase distortion was not the proper way of looking at the linearization, and that a view of the intermodulation and difference frequency physics is required.

5.7 Analytic formulas for equation (5.8)

In this section we provide a formalism for solving the S-MUSE model for the components necessary to compute (5.8). We use the vector notation of [82] where $\mathbf{x}_\ell = [\mathbf{x}_{\ell_1} \dots \mathbf{x}_{\ell_5}]^{\mathrm{T}} = \left[\tilde{V}_\ell\, \tilde{I}_\ell\, \tilde{E}_\ell\, \tilde{v}_\ell\, \tilde{\rho}_\ell\right]^{\mathrm{T}}$. The differential equation for $\mathbf{x}_\ell$ is

$$\dot{\mathbf{x}}_\ell \;=\; \mathbf{A}_\ell \mathbf{x}_\ell + \sum_{\substack{m,n \\ f_m + f_n = f_\ell}} \mathbf{H}_{\ell mn}(\mathbf{x}_m, \mathbf{x}_n) \tag{5.19}$$

where matrix and tensor components $\mathbf{A}_{\ell_{ij}}$ and $\mathbf{H}_{\ell_i m_j n_k}$ are listed in Appendix II of [82]. Equation (5.19) may be solved with a series solution

$$\mathbf{x}_\ell \;=\; \sum_{\alpha=1}^{\infty} \mathbf{x}_\ell^{(\alpha)} \tag{5.20}$$

and that this series converges under the appropriate conditions (see Chapter 3). The index α is related to the order of intermodulation product [83]. The formulas for the terms of the series are given by

$$\mathbf{x}_\ell^{(1)} \;=\; e^{\mathbf{A}_\ell z}\mathbf{w}_\ell \qquad\qquad \alpha = 1 \tag{5.21}$$

$$\mathbf{x}_\ell^{(\alpha)} \;=\; \int_0^z e^{\mathbf{A}_\ell (z-\tau)} \sum_{\beta=1}^{\alpha-1} \sum_{\substack{m,n \\ f_m + f_n = f_\ell}} \mathbf{H}_{\ell mn}\left[\mathbf{x}_m^{(\beta)}(\tau), \mathbf{x}_n^{(\alpha-\beta)}(\tau)\right]\, d\tau, \qquad \alpha \geq 2 \tag{5.22}$$

where $\mathbf{w}_\ell$ contains the initial values for frequency $f_\ell \omega_0$ [82] and $e^{\mathbf{A}_\ell z}$ is the matrix exponential of the matrix $\mathbf{A}_\ell z$ [18].

The complex exponential modes of the vector $\mathbf{x}_\ell^{(\alpha)}$ are indexed by p

$$\mathbf{x}_\ell^{(\alpha)}(z) = \sum_{p=1}^{N_\ell^{(\alpha)}} \mathbf{a}_\ell^{(\alpha)[p]} e^{\left(\mu_\ell^{(\alpha)[p]} + i\sigma_\ell^{(\alpha)[p]}\right)z} \tag{5.23}$$

with $\mathbf{a}_\ell^{(\alpha)[p]}$ a complex vector. Sums like (5.23) are ordered so that $\mu_\ell^{(\alpha)[1]}$ is the largest of all the $\mu_\ell^{(\alpha)[p]}$.

For brevity we only provide details to compute the 3IM contribution to (5.8) and refer the reader to Chapter 3 for details on how to compute higher order contributions. To compute the terms of (5.8) and the input-output phase difference Φ we need to compute in order the $p = 1$ modes $\mathbf{x}_1^{(1)[1]}$, $\mathbf{x}_2^{(2)[1]}$, $\mathbf{x}_1^{(3)[1]}$.

5.7.1 Series term $\mathbf{x}_1^{(1)}$

The dominant term in the first order ($\alpha = 1$) drive frequency ($\ell = 1$) solution is

$$\mathbf{x}_1^{(1)[1]} = \mathbf{a}_1^{(1)[1]} e^{\mu_1^{(1)[1]} z} e^{i\sigma_1^{(1)[1]} z} \tag{5.24}$$

where

$$\mathbf{a}_1^{(1)[1]} = \mathbf{P}_1 \mathbf{Q} \mathbf{P}_1^{-1} \mathbf{w}_1 \tag{5.25}$$

$$\mu_1^{(1)[1]} = \mathrm{Re}\{\lambda_{1_1}\}, \tag{5.26}$$

$$\sigma_1^{(1)[1]} = \mathrm{Im}\{\lambda_{1_1}\}, \tag{5.27}$$

and

$$\mathbf{Q}_{i,j} = \begin{cases} 1 & i = j = 1 \\ 0 & \text{otherwise} \end{cases} \tag{5.28}$$

assuming that $\mathbf{P}_1$, the modal matrix of $\mathbf{A}_1$, has the eigenvector associated with λ_{1_1}, the eigenvalue of $\mathbf{A}_1$ with the largest real part, in its first column. Then for (5.8) we have

$$A_{\mathrm{dr}} = \left|\mathbf{a}_{1_1}^{(1)[1]}\right| \tag{5.29}$$

$$\mu_{\mathrm{dr}} = \mu_1^{(1)[1]} \tag{5.30}$$

$$\kappa_{\mathrm{dr}} = \sigma_1^{(1)[1]} + \mathrm{Arg}\left\{\mathbf{a}_{1_1}^{(1)[1]}\right\}. \tag{5.31}$$

5.7.2 Series term $\mathbf{x}_2^{(2)}$

For $\mathbf{x}_2^{(2)[1]}$ we have

$$\mathbf{x}_2^{(2)[1]} = \text{dominant mode of } \left\{\int_0^z e^{\mathbf{A}_2(z-\tau)} \mathbf{H}_{211}\left(\mathbf{x}_1^{(1)[1]}(\tau), \mathbf{x}_1^{(1)[1]}(\tau)\right) d\tau\right\}. \tag{5.32}$$

Let

$$\mathbf{c}_2 = \mathbf{H}_{211}\left(\mathbf{a}_1^{(1)[1]}, \mathbf{a}_1^{(1)[1]}\right) \tag{5.33}$$

then

$$\mathbf{x}_2^{(2)[1]} = \mathbf{P}_2\mathbf{S}_2(2\lambda_{1_1})\mathbf{P}_2^{-1}\mathbf{c}_2 e^{2\lambda_{1_1}z} \tag{5.34}$$

$$= \mathbf{a}_2^{(2)[1]} e^{2\mu_1^{(1)[1]}z} e^{i2\sigma_1^{(1)[1]}z} \tag{5.35}$$

where

$$\mathbf{S}_{\ell_{i,j}}(\gamma) \equiv \begin{cases} \frac{1}{\gamma-\lambda_{\ell_j}} & i=j \\ 0 & \text{otherwise} \end{cases}. \tag{5.36}$$

The eigenvalues λ_{ℓ_j} of $\mathbf{A}_\ell$ have the same order as the eigenvectors of $\mathbf{A}_\ell$ appearing in columns of $\mathbf{P}_\ell$. We have assumed that the real part of $2\lambda_{1_1}$ is larger than the real part of λ_{2_1}, the eigenvalue of $\mathbf{A}_2$ with the largest real part, and that $2\lambda_{1_1} \neq \lambda_{2_j}$ for $j = 1, \ldots, 5$, as is most often the case.

5.7.3 Series term $\mathbf{x}_1^{(3)}$

The third order term at the drive frequency is

$$\mathbf{x}_1^{(3)[1]} = \text{dominant mode of} \left\{ \int_0^z e^{\mathbf{A}_1(z-\tau)} \left[\mathbf{H}_{1,2,-1}\left(\mathbf{x}_2^{(2)[1]}(\tau), \mathbf{x}_{-1}^{(1)[1]}(\tau)\right) \right.\right.$$
$$\left.\left. + \mathbf{H}_{1,-1,2}\left(\mathbf{x}_{-1}^{(1)[1]}(\tau), \mathbf{x}_2^{(2)[1]}(\tau)\right)\right] d\tau \right\}. \tag{5.37}$$

Let

$$\mathbf{c}_1 = \mathbf{H}_{1,2,-1}\left(\mathbf{a}_2^{(2)[1]}, \mathbf{a}_{-1}^{(1)[1]}\right) + \mathbf{H}_{1,-1,2}\left(\mathbf{a}_{-1}^{(1)[1]}, \mathbf{a}_2^{(2)[1]}\right) \tag{5.38}$$

with $\mathbf{a}_{-1} = \mathbf{a}_1^*$ then

$$\mathbf{x}_1^{(3)[1]} = \mathbf{P}_1\mathbf{S}_1(2\lambda_{1_1} + \lambda_{1_1}^*)\mathbf{P}_1^{-1}\mathbf{c}_1 e^{(2\lambda_{1_1}+\lambda_{1_1}^*)z} \tag{5.39}$$

$$= \mathbf{a}_1^{(3)[1]} e^{3\mu_1^{(1)[1]}z} e^{i\sigma_1^{(1)[1]}z}. \tag{5.40}$$

Therefore

$$A_{\text{nl}} = \left|\mathbf{a}_{1_1}^{(3)[1]}\right| \tag{5.41}$$

$$\mu_{\text{nl}} = 3\mu_1^{(1)[1]} \tag{5.42}$$

$$\kappa_{\text{nl}} = \sigma_1^{(1)[1]} + \text{Arg}\left\{\mathbf{a}_{1_1}^{(3)[1]}\right\}. \tag{5.43}$$

Any of the TWT state variables may be computed by choosing the appropriate vector components from $\mathbf{a}_1^{(1)[1]}$ and $\mathbf{a}_1^{(3)[1]}$.

Similarly to compute the 5IM contribution to (5.8) one needs to compute $\alpha = 4$ and $\alpha = 5$ terms.

5.8 Effect of average beam velocity in LATTE

In this section we provide the theory necessary to remove the effect of the reduction of the average beam velocity in the large signal code LATTE. We first need an expression to compute the average velocity from a LATTE simulation, then a way to remove this effect from a subsequent simulation.

In Eulerian coordinates the electron beam average velocity is

$$\langle v(z)\rangle_0 = \frac{1}{2\pi}\int_{2\pi} v^{\mathrm{E}}(z,\psi)\,d\psi \tag{5.44}$$

which in Lagrangian coordinates becomes [82]

$$\langle v(z)\rangle_0 = \frac{1}{2\pi}\int_{2\pi} v^{\mathrm{L}}(z,\psi_0)\left|\frac{\partial\Psi}{\partial\psi_0}\right| d\psi_0 \tag{5.45}$$

$$= \frac{1}{2\pi}\int_{2\pi} \frac{I_0(\psi_0)}{A\rho^L(z,\psi_0)} d\psi_0 \tag{5.46}$$

where $\psi = \omega_0(z/u_0 - t)$ is a phase variable, $I_0(\psi_0)$ is the dc beam current, A is the beam cross sectional area, and the other quantities are defined in Section 2.2.2. We can write ρ^L using the Fourier synthesis equation in Lagrangian coordinates

$$\rho^L(z,\psi_0) = \sum_{\ell=-\infty}^{\infty} \tilde{\rho}_\ell e^{if_\ell\Psi(z,\psi_0)} \tag{5.47}$$

where

$$\tilde{\rho}_\ell = \frac{1}{2\pi}\int_{2\pi} \frac{I_0(\psi_0)}{Av(z,\psi_0)} e^{-if_\ell\Psi(z,\psi_0)}\,d\psi_0. \tag{5.48}$$

For computations the integrals become sums over N "disks," we consider a finite number of positive frequencies M, and we can combine (5.46), (5.47), and (5.48) to get

$$\langle v(z)\rangle_0 = \sum_{i=1}^{N}\left[\sum_{\ell=-M}^{M}\sum_{j=1}^{N}\frac{e^{if_\ell(\Psi_i-\Psi_j)}}{v_j}\right]^{-1} \tag{5.49}$$

where we have assumed $I_0(\psi_0) = I_0$ and used the notation $\Psi(z,\psi_{0i}) = \Psi_i$ and $v(z,\psi_{0i}) = v_i$ where ψ_{0i} is an initial disk phase. For a simulation with small enough input power we can confirm that (5.49) is correct by comparing it to the average electron beam velocity $\tilde{v}_0(z)$ computed by the MUSE model.

To remove the effect of $\langle v(z)\rangle_0$ in a subsequent LATTE simulation, we first compute the adjusted disk velocities

$$\tilde{v}_i = v_i - \langle v\rangle_0 + u_0. \tag{5.50}$$

We confirm by computation that for the power levels we are interested in we have

$$\langle \tilde{v}_i \rangle_0 \quad = \quad u_0, \tag{5.51}$$

then given the adjusted velocities we compute new disk phase trajectories $\tilde{\Psi}_i$ using [82]

$$\frac{\partial \tilde{\Psi}_i}{\partial z} \quad = \quad \frac{\omega_0}{u_0}\left(1 - \frac{u_0}{\tilde{v}_i}\right). \tag{5.52}$$

From the adjusted velocities and phase trajectories we can compute the adjusted electron beam density coefficient given by (5.48) where the integral is replaced by a sum over disks. Finally, one can compute a circuit voltage at the fundamental frequency corresponding to the adjusted beam charge density from the LATTE lossless circuit equations [82]

$$\frac{d\tilde{V}_\ell}{dz} \quad = \quad -\frac{if_\ell\omega_0}{u_0}\tilde{V}_\ell - \frac{if_\ell\omega_0\tilde{K}_\ell}{\tilde{v}_{\mathrm{ph}\ell}}\tilde{I}_\ell \tag{5.53}$$

$$\frac{d\tilde{I}_\ell}{dz} \quad = \quad -\frac{if_\ell\omega_0}{\tilde{K}_\ell\tilde{v}_{\mathrm{ph}\ell}}\tilde{V}_\ell - \frac{if_\ell\omega_0}{u_0}\tilde{I}_\ell + if_\ell\omega_0 A\tilde{\rho}_\ell \tag{5.54}$$

where $\tilde{V}_\ell$ and $\tilde{I}_\ell$ are the complex circuit voltage and circuit current envelopes as defined in (2.15), $\tilde{K}_\ell$ is the circuit interaction impedance at frequency $f_\ell\omega_0$, $\tilde{v}_{\mathrm{ph}\ell}$ is the circuit phase velocity at frequency $f_\ell\omega_0$, and A is the electron beam cross sectional area.

Chapter 6

On the physics of harmonic injection in a TWT

6.1 Introduction

Traveling Wave Tubes (TWTs) are widely used as amplifiers in communications and electronic countermeasure (ECM) systems. Due to the nonlinear nature of the device, spectra amplified by a TWT are distorted, compromising the device performance. In a communications application the distortion may manifest as two channels producing energy in a third channel via third order intermodulation products (3IMs). In this case the channels must operate such that "cross-talk" into other channels is at acceptable levels, which in some applications can be as much as 60 dB below the fundamental signals [49]. In ECM applications, frequency agility is necessary and harmonic generation can limit the usable amplifier bandwidth.

One way to avoid the TWT's nonlinear effects is to reduce the input drive power until the undesired spectral components are at acceptable levels. This method is not an ideal solution because it reduces the overall efficiency of the TWT. Another widely used method for reducing undesired spectral content is harmonic injection. Harmonic injection has been studied experimentally [44, 70, 38, 79] and numerically [28, 22, 21]. It has been shown that for two drive frequencies, injection of second harmonics of the drive frequencies can reduce the 3IM spectra [70, 79, 21]. Since it is typically the 3IM spectra that is responsible for the "cross-talk" between channels, harmonic injection allows one to drive the channel carriers closer to saturation, thus increasing the amplifier efficiency. In ECM applications one can inject the second and higher harmonics to extend the usable bandwidth of the amplifier [44, 38].

Mendel [55] claims that harmonic injection is a process of cancellation, "... whereby the injected second-harmonic signal is such that it is 180° out of phase with the second harmonic signal generated by the nonlinear processes inherent in the interaction mechanism." This view is supported by Garrigus and Glick [38] who went as far providing a speculative drawing of what the waveforms might look like internal to the TWT. However, no quantitative nonlinear theories have been reported that retain the view of the second harmonic signal being made up of an "injected" part and a part "generated by the nonlinear processes inherent in the interaction mechanism." Large signal TWT codes have predicted the phenomenon of

canceling the second harmonic with harmonic injection, however the harmonic frequency in these models was not resolvable into separate components.

In this chapter we develop a general theory of "signal injection" using approximate analytic solutions to the spectral TWT model S-MUSE [82]. The approximate solutions are indeed sums of "injected" terms and terms "generated by the nonlinear processes inherent in the interaction mechanism" as previous authors have speculated. In fact, this is the case in general for various signal injection schemes. Where appropriate we test our insights from the approximate analytic solution in saturated conditions with the large signal code LATTE [82]. LATTE is derived from the same starting equations as S-MUSE and is therefore ideally suited for this purpose. We study in detail two cases of signal injection. First, harmonic injection to suppress the harmonic and enhance the fundamental is considered. Included in this study is the effect of multiple harmonic injection. Secondly we study signal injection to cancel third order intermodulation products. Harmonic injection, difference frequency injection, 3IM injection, and combinations of these schemes are considered.

In Section 6.2 we develop the signal injection theory. The applications are given in Section 6.3, and the chapter is concluded in Section 6.4. Section 6.5 provides the necessary formulas to compute the analytic solutions.

6.2 Theory

6.2.1 Analytic solution structure

S-MUSE can be solved analytically using a series solution (see Chapter 3). Similar to linear Pierce theory [61], the solutions for a state variable at a particular frequency is a sum of complex exponential modes. However, the number of modes required to represent the full solution of an intermodulation product grows rapidly with increasing order of intermodulation product. When possible we consider only the modes that dominate the solution near the output of the TWT, which are typically those modes with the largest growth rates.

In general the solution of the voltage at frequency f_ℓ may be approximated as

$$V_\ell(z,t) \;=\; \left\{ A_\ell^{\mathrm{dr}} \exp\left(\mu_\ell^{\mathrm{dr}} + i\kappa_\ell^{\mathrm{dr}}\right) z + \sum_q A_\ell^{\mathrm{nl}[q]} \exp\left(\mu_\ell^{\mathrm{nl}[q]} + i\kappa_\ell^{\mathrm{nl}[q]}\right) z \right\} e^{if_\ell\omega_0\left(\frac{z}{u_0}-t\right)} \quad (6.1)$$

where the superscript *dr* refers to "driven" quantities and the superscript *nl* refers to quantities generated by nonlinear interactions.

The idea of all of the injection schemes is to adjust the amplitudes and phases of the inputs such that the bracketed term in (6.1) is minimized at $z = L$, where L is the TWT output. This is in contrast to the view put forth in [38] that the undesired signal (the harmonic in their case) is cancelled at all points along the length of the TWT. In the sections of the chapter that describe the different injection schemes, we will identify the structure of the different elements of the solution (6.1). In the appendix, formulas for computing the quantities appearing in (6.1) are provided.

Depending on the injection scheme there may be no "driven" portion of (6.1). For example, in harmonic injection to cancel a 3IM, the naturally generated 3IM cancels with a mode that is a nonlinear product of the injected harmonic and one of the drive frequencies. In this case the only modes present are represented in the sum over q, i.e., $A^{\rm dr} = 0$. For cases when the injected harmonic is out of the linear gain bandwidth the driven portion of (6.1) may also be a sum over modes. To compute the modes in these cases the reader is referred to Chapter 3 for the required formulas.

The solutions to the S-MUSE model of the form (6.1) are approximations that only apply prior to TWT saturation. By using the large signal code LATTE we will argue with simulations that the large signal solutions also have a structure that is composed of modes due to the nonlinearity and modes due to the injected signal.

6.2.2 Electron beam diagnostics

The electron beam current modulation is often considered an important quantity in TWT physics. To study harmonics of the electron beam current during harmonic injection we will need the following quantities. The instantaneous electron beam current in Eulerian coordinates is given by

$$i_{\rm beam} = S\rho v \tag{6.2}$$

where S is the electron beam cross sectional area. The Fourier coefficient of this expression at frequency f_ℓ is

$$\langle i_{\rm beam}(z)\rangle_\ell \;=\; S\frac{1}{2\pi}\int_{2\pi} \rho v e^{-if_\ell\psi}\,d\psi. \tag{6.3}$$

Substituting the Fourier synthesis form of $\rho(z,\psi)$ and $v(z,\psi)$, e.g. $v(z,\psi) = \sum_{\ell=-\infty}^{\infty} \tilde{v}_\ell(z)e^{if_\ell\psi}$, into (6.3) one gets

$$\langle i_{\rm beam}(z)\rangle_\ell \;=\; S\sum_{\substack{m,n\\ f_m+f_n=f_\ell}} \tilde{\rho}_m\tilde{v}_n \tag{6.4}$$

where $\tilde{\rho}_m, \tilde{v}_n$ are MUSE variables, i.e., spatially dependent Fourier coefficients, and the sum is over frequency pairs such that the frequencies add to f_ℓ.

For the Lagrangian model LATTE the beam current harmonics are given by

$$\langle i_{\rm beam}(z)\rangle_\ell \;=\; \frac{1}{2\pi}\int_{2\pi} I_0(\psi_0)e^{-if_\ell\Psi(z,\psi_0)}\,d\psi_0 \tag{6.5}$$

where ψ_0 is the Lagrangian "disk" label and $\Psi(z,\psi_0)$ is the function describing the phase of the disk ψ_0 as a function of axial position. For an unmodulated beam $I_0(\psi_0) = I_0$.

In Section 6.3 we will compute $\langle i_{\rm beam}(z)\rangle_\ell$ for different values of ℓ using the code *lmsuite*.[1]

[1]The code *LATTE/MUSE Numerical Suite* solves the MUSE models and the large signal code LATTE for arbitrary TWT geometries. The code and the input files used in this chapter are available at `http://www.lmsuite.org`.

6.3 Applications

In this section we provide several examples of the harmonic injection theory. The first example is harmonic injection to suppress the harmonic or enhance the fundamental, and the second example is signal injection to suppress an intermodulation product. We study various aspects of the physics that the solutions afford.

For the studies we use TWT parameters based on the X-WING TWT [79]. The electron beam parameters are listed in Table 6.1 and the relevant dispersion parameters are listed in Table 6.2. For frequencies not listed in Table 6.2, dispersion parameters are determined by a linear interpolation between neighboring frequencies. See [82] for a full description of how the dispersion parameters enter into the model equations. The TWT length is $L = 15$ cm. For much of the present study we do not include a circuit sever[2] so that we are considering only the essential physics of signal injection. The small signal gain as a function of frequency for these parameters as computed by S-MUSE is given in Fig. 6.1.

Table 6.1 XWING TWT electron beam and circuit parameters.

Parameter	**Value**
Cathode voltage	-2.75 kV
Beam current	0.22 A
Beam radius	0.55 mm
Helix radius	1.4 mm

Table 6.2 XWING TWT dispersion parameters.

f (GHz)	$\tilde{v}_{\rm ph}$ ($\times 10^7$ m/s)	$\tilde{K}$ (Ω)	$\tilde{R}$
1.00	2.480	139.0	1.55×10^{-2}
2.00	2.486	104.0	4.66×10^{-2}
3.00	2.498	64.0	8.40×10^{-2}
4.00	2.514	38.0	1.24×10^{-1}
5.00	2.533	24.0	1.65×10^{-1}
6.00	2.550	15.0	2.06×10^{-1}
7.00	2.563	10.0	2.45×10^{-1}
8.00	2.577	4.0	2.83×10^{-1}

For sinusoids with frequencies f_a and f_b, we define the phase difference between the signals relative to the sinusoid at f_a. If the phase difference between the sinusoid with frequency f_a and the sinusoid with frequency f_b is said to be $\Delta\theta$ where the phase of the sinusoid with frequency f_a is θ_a, then the phase of the signal at f_b is $(f_b/f_a)(\theta_a + \Delta\theta)$. For example, for harmonically related signals $f_b = 2f_a$, if the input phase is $\theta_a = 10^\circ$ and $\Delta\theta = 30^\circ$, then the

[2]There are a few cases when the effect of a sever is important, and for those cases we do include a sever and discuss its effect.

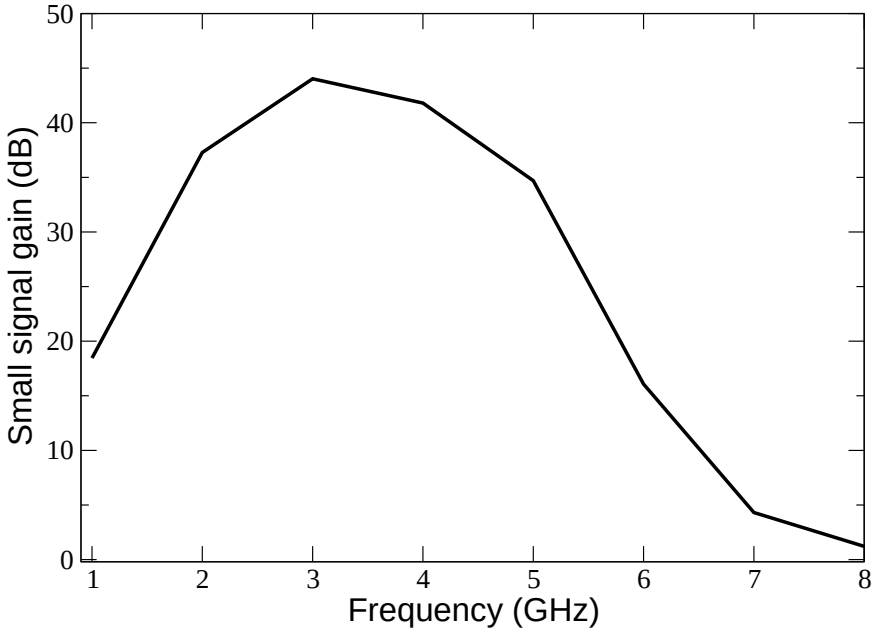

Figure 6.1 Small signal gain of XWING TWT parameters as a function of frequency. Curve was computed with the S-MUSE model.

input phase of the sinusoid at the second harmonic f_b is $\theta_b = 80°$. For harmonically related signals we will always define phase differences at the fundamental frequency. When there are multiple drive frequencies we will specify at which frequency the phase differences are defined.

6.3.1 Fundamental and harmonic frequencies

First we consider second harmonic injection in the presence of one drive frequency. We study the effect of the injected second harmonic on the fundamental and harmonic frequencies in two cases. In the first case the harmonic signal is in the linear gain bandwidth, and in the second case the harmonic is out of the linear gain bandwidth.[3] We then consider injecting the second and third harmonic to cancel the second harmonic.

6.3.1.1 Harmonic in linear gain bandwidth

In the first example we use the fundamental input frequency of 2 GHz and the injected second harmonic at 4 GHz. The voltage solution (6.1) for each of these frequencies has a driven mode and a nonlinear mode. There is a nonlinear mode at 2 GHz because 2 GHz is the difference frequency of 4 GHz and 2 GHz. The nonlinear mode at 4 GHz is because 4 GHz is the second harmonic of 2 GHz. Figure 6.2(a) shows that the output of the fundamental is maximized for an optimum input harmonic phase. At 2 GHz the second term of (6.1) increases monotonically with increasing harmonic input power at fixed phase, therefore the power output at the fundamental increases monotonically for increasing harmonic input power as seen in Fig. 6.2(a). The power enhancement at the fundamental when the harmonic and fundamental have equal input powers (5 dBm) is 1 dB for optimum phase.

Figure 6.2(b) shows that for injected second harmonic powers between -10 dBm and -8 dBm and phases between 85° and 95° the harmonic is suppressed by more than 18 dB. The center of this range corresponds to total cancellation of the second harmonic signal ($-\infty$ dB). It should be noted that experimental realization of this theoretical perfect cancellation is not possible. Line-broadening effects such as phase jitter, shot noise, and voltage supply noise will leave a small, nonzero amplitude at the point of optimal suppression.

From Fig. 6.2(b) and (6.1) we see that the optimum injected harmonic power and phase are independent of each other. That is, for any injected harmonic power a scan in injected harmonic phase may be made to determine the optimum phase. With the injected harmonic phase set to this value the harmonic injected power may be scanned to determine the optimum cancellation point. This method of detecting maximum cancellation has been confirmed experimentally for non-saturated operation [79].

In Fig. 6.3 we show the modes that make up the harmonic solution for the optimum cancellation inputs of Fig. 6.2(b). Shown are the magnitudes of the separate modes, and

[3] We define a frequency to be in the *linear gain bandwidth* if it has an exponentially growing solution predicted by the linear theory [61]. For the parameters provided in Tables 6.1 and 6.2, the frequencies between 1 GHz and 6 GHz are in the linear gain bandwidth.

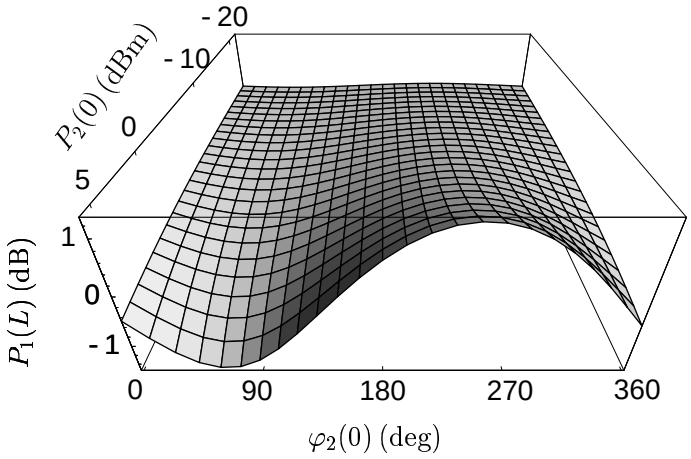

(a) Output power at 2 GHz as a function of injected harmonic power and phase. The optimum second harmonic input phase is $\varphi_2(0) = 244°$. At this input phase the fundamental output power increases monotonically with increasing second harmonic input power until saturation effects set in.

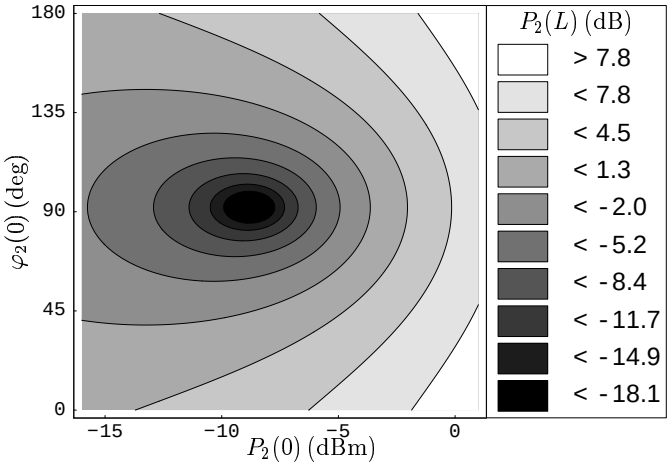

(b) Output power at 4 GHz as a function of injected harmonic power and phase. $P_2(L)$ is in dB with respect to output power at 4 GHz with no harmonic injection. The optimum cancellation harmonic inputs are $P_2(0) = -8.86$ dBm, $\varphi_2(0) = 92.25°$.

Figure 6.2 Output power at (a) fundamental (2 GHz) and (b) second harmonic (4 GHz) as a function of injected harmonic power $P_2(0)$ and injected harmonic phase $\varphi_2(0)$ for second harmonic injection. For both figures the fundamental input power and phase are $P_1(0) = 5$ dBm, $\varphi_1(0) = 0.0°$. With no harmonic injection the harmonic is 9.23 dB below the fundamental at the TWT output.

the magnitude and phase of the total solution (6.1). The figure clearly shows that the axial location of harmonic cancellation (the TWT output) is the point at which the dominant mode of the solution changes from the driven mode to the nonlinear mode. The 180° phase change in the composite solution also illustrates this point.

To test whether the qualitative conclusions about the structure of the solutions during harmonic injection hold more generally, we next consider results of LATTE simulations for input powers that produce power saturation at the fundamental frequency. We find that for saturated operation a single global minimum of harmonic output power versus input power and phase [see Fig. 6.2(b)] ceases to exist. Rather, several local minima form. To determine the global minimum requires an extensive and highly-resolved scan over input power and phase. In Fig. 6.4 we show the second harmonic output power as a function of injected second harmonic input power and phase for a fundamental input power that drives the TWT into saturation. The simulations for saturated operation include the fundamental through fourth harmonic spectral components in the circuit wave and electron beam.

To show that the second harmonic voltage in the TWT has the structure of (6.1) even for saturated operation, we can consider the phase of the voltage predicted by LATTE simulations. Similarly to Fig. 6.3 we expect to see the driven mode character dominate prior to the point of cancellation, and the nonlinearly generated mode character after cancellation. If this is true in the saturated case, then the voltage phase of the harmonic should jump by 180° at the point of cancellation. In Fig. 6.5 we show output powers and voltage phases for the fundamental through fourth harmonic with second harmonic injection to cancel the second harmonic at $z = 15\,\mathrm{cm}$. The fundamental input power is such that without harmonic injection the output power at the fundamental is saturated. With harmonic injection, the fundamental output power at the output ($z = 15\,\mathrm{cm}$) is compressed by about 1 dB as the saturation point has shifted to $z = 13.6\,\mathrm{cm}$. One sees that the output phase at the second harmonic abruptly changes by 180° at the cancellation point, similar to the two-mode analytic solution of the S-MUSE model.

For the same input frequencies we next look at electron beam current modulation magnitude and phase at the fundamental and second harmonic. Equation (6.4) gives the current modulation at frequency $f_\ell\omega_0$ in MUSE variables. The beam charge density $\tilde{\rho}_m$ and beam velocity $\tilde{v}_n$ have the form of (6.1) where the growth rates ($\mu^{\mathrm{dr}}_{m,n}$ and $\mu^{\mathrm{nl}[q]}_{m,n}$) will be the same as those of the voltage, but the magnitudes ($A^{\mathrm{dr}}_{m,n}$ and $A^{\mathrm{nl}[q]}_{m,n}$) and phases ($\kappa^{\mathrm{dr}}_{m,n}$ and $\kappa^{\mathrm{nl}[q]}_{m,n}$) will be different. For the case of second harmonic injection with a single fundamental input, the solutions for the charge density and beam velocity at the fundamental, $\tilde{\rho}_1$ and $\tilde{v}_1$, are composed of a driven mode and a nonlinearly generated mode. Therefore the beam current modulation at the second harmonic $\langle i_{\mathrm{beam}}(z)\rangle_2$, i.e. the product of $\tilde{\rho}_1$ and $\tilde{v}_1$, may be written as a sum of three terms (the cross terms have the same growth rates and may be combined). There is no guarantee that since the inputs are set such that the circuit voltage modes cancel at the TWT output, the modes making up the current modulation will also cancel. In fact, in all of the cases that we have studied, we have found that the current modulation is not cancelled for any point along the length of the TWT. However, the theory predicts that such a cancellation of the beam modulation modes is possible for the proper inputs.

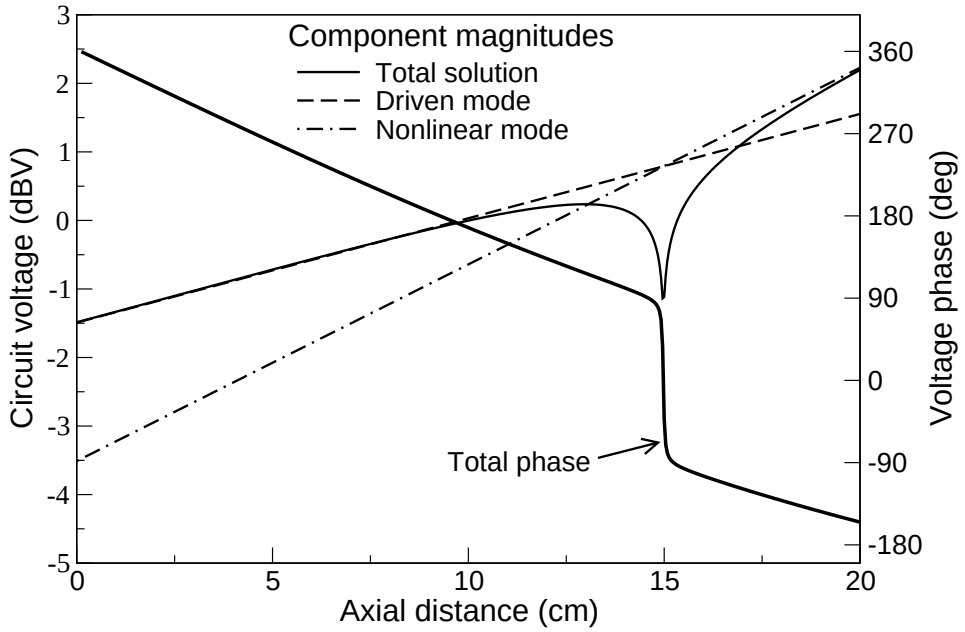

Figure 6.3 Magnitude and phase of (6.1) and component magnitudes of (6.1) for second harmonic 4.0 GHz with second harmonic injection to achieve second harmonic cancellation. The driven mode dominates the solution prior to $z = 15\,\text{cm}$, and the nonlinear mode dominates the solution after $z = 15\,\text{cm}$. This can be seen from the component magnitudes, as well as the 180° phase change of the total solution at $z = 15\,\text{cm}$. Fundamental and second harmonic input powers and phases are $5.0, -8.86\,\text{dBm}$ and $0.0°, 92.25°$ respectively. Voltage phase is with respect to the cold circuit wave at 4 GHz.

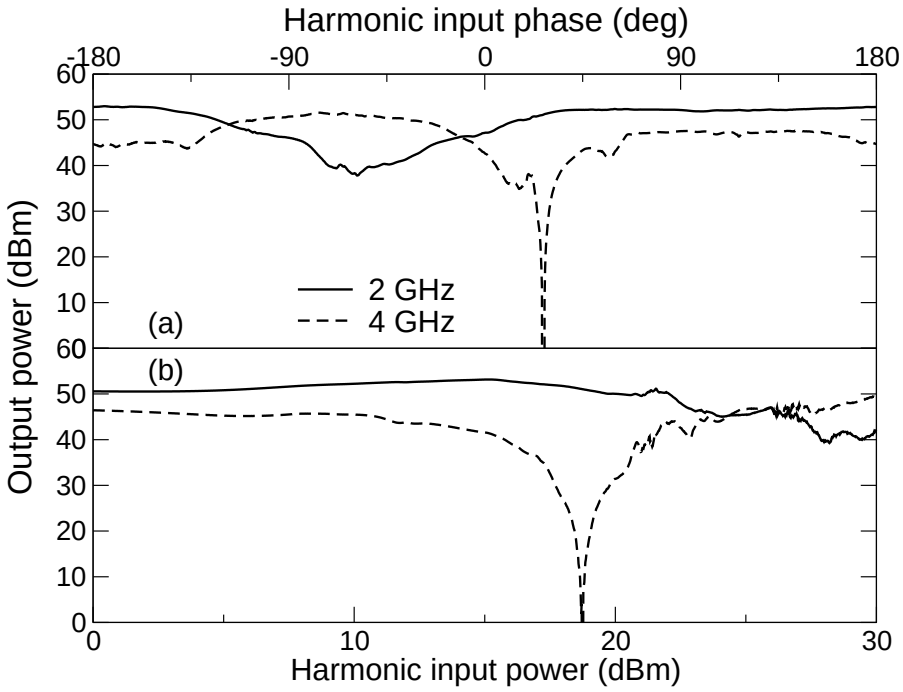

Figure 6.4 Fundamental and harmonic output power versus (a) harmonic input phase and (b) harmonic input power for fundamental input power which produces saturated output with no harmonic injection. Fundamental input power and phase are 20.0 dBm and 0.0° respectively for (a) and (b). In (a) harmonic input power is 18.75 dBm, and in (b) harmonic input phase is 26.475°.

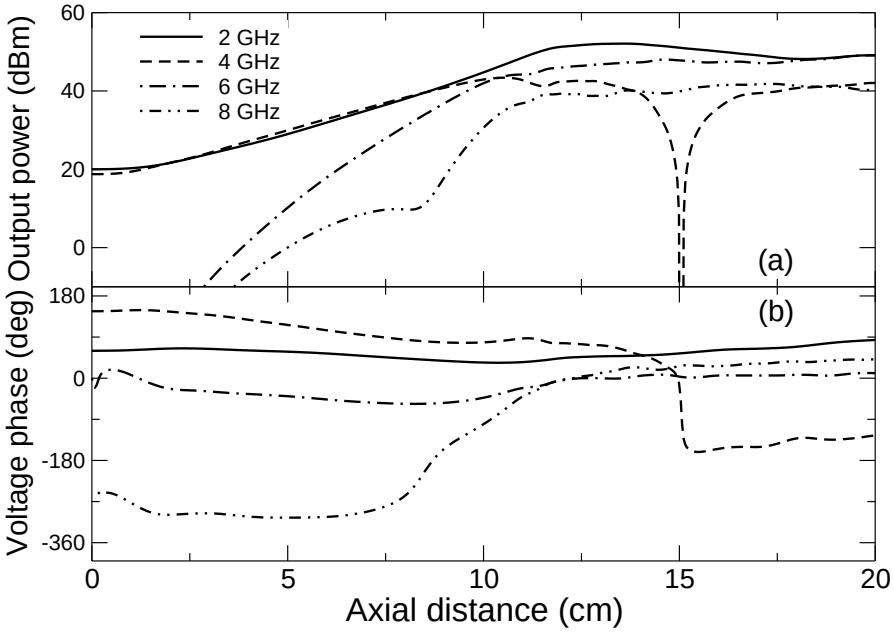

Figure 6.5 Output power (a) and voltage phase (b) for fundamental through fourth harmonic with second harmonic injection to cancel the second harmonic. The abrupt phase change of 180° in the second harmonic is evidence that even for saturated operation the second harmonic solution is comprised of two modes as in the approximate analytic solution (6.1). Fundamental input power and phase of 20.0 dBm and 0.0° produce saturation at $z = 15$ cm in absence of harmonic injection. Second harmonic input power and phase are 18.75 dBm and 26.48° respectively. Voltage phase is with respect to cold circuit wave at the respective frequency.

In Fig. 6.6 we show the beam current modulation magnitude and phase of the fundamental and second harmonic components during harmonic injection to cancel the harmonic voltage at $z = 15\,\text{cm}$, as predicted by LATTE. The fundamental input power is small enough so that no saturation effects are encountered in the simulation region. The second harmonic beam current modulation "changes modes" at about $z = 13\,\text{cm}$ as evidenced by the dip in the magnitude and the phase change. However, this is well before the voltage cancellation which occurs at $z = 15\,\text{cm}$. The relationship between the changing of modes in the beam current and the changing of modes in the circuit voltage is a subject of future study.

6.3.1.2 Harmonic out of linear gain bandwidth: no sever

When the second harmonic is out of the linear gain bandwidth, the component of the analytic solution (6.1) corresponding to the injected harmonic does not have an exponentially growing form, and hence does not *grow* to a level required to cancel the nonlinearly generated harmonic at the output. Thus in most cases modest injected harmonic powers will have a small effect on reducing the second harmonic. To get cancellation of the second harmonic, a large value of injected harmonic power is required. For the analytic solution (6.1) to be a good approximation, additional modes from the full solution should be included to describe the harmonic.

We consider one case of second harmonic injection with the fundamental frequency at 4 GHz and the second harmonic at 8 GHz, where the fundamental input is set to achieve saturation at $z = 15\,\text{cm}$. In Fig. 6.7 we plot fundamental and second harmonic output power versus harmonic input power for two different values of fixed second harmonic input phase. In Fig. 6.7(a) the harmonic input phase is set so that the harmonic output power is minimized for a harmonic input power of 15 dBm. The amount of output harmonic reduction from its value of 40.6 dBm with no harmonic injection is about 4 dB. On the other hand in Fig. 6.7(b) one can see that cancellation of the second harmonic is obtainable in principle. However, the required injected harmonic power to do so is about 1% of the fundamental output power. Comparison of Fig. 6.7 to Fig. 6.4, and their respective relative harmonic to fundamental input powers, illustrates the substantial difference between the case when the second harmonic is in the linear gain bandwidth and when the second harmonic is out of the linear gain bandwidth.

6.3.1.3 Harmonic out of linear gain bandwidth: with sever

Almost all TWTs have circuit severs to control internal reflections. We expect that the presence of the sever will highly attenuate, if not totally eliminate, the non-growing injected harmonic mode. Since the injected mode is the mode that allows for reduction or cancellation of the second harmonic, we expect that when a sever is included reduction of the second harmonic should be possible but a total cancellation is likely not possible for reasonable harmonic injection powers. For simulations including a sever where we restricted the harmonic input to less than 10% of the fundamental output, the maximum amount of harmonic

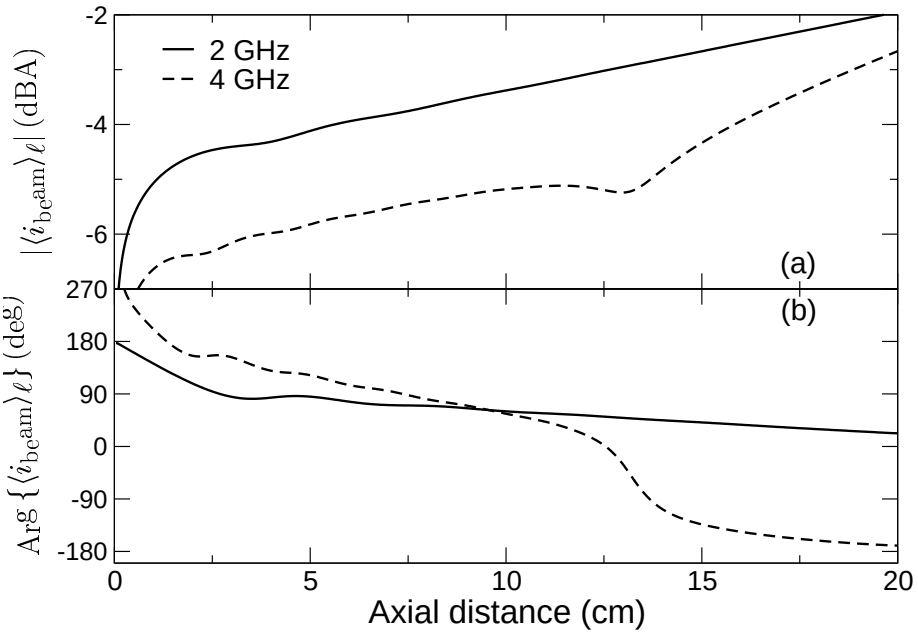

Figure 6.6 Beam current modulation (a) magnitude and (b) phase at fundamental and second harmonic for second harmonic injection to cancel the second harmonic at $z = 15\,\mathrm{cm}$ predicted by LATTE. Harmonic beam current modulation "changes modes" at about $z = 13\,\mathrm{cm}$ as evidenced by magnitude dip and phase change. However, the modes do not cancel to produce zero beam current second harmonic modulation ($-\infty\,\mathrm{dB}$) at any point along the TWT. Fundamental and second harmonic input power and phase are $-20.0, -57.5\,\mathrm{dBm}$ and $0.0°, 91.0°$ respectively, well below powers which produce saturation effects. Beam current modulation magnitudes are in dB with respect to 1 A, and beam current modulation phases are with respect to cold circuit waves at the respective frequencies.

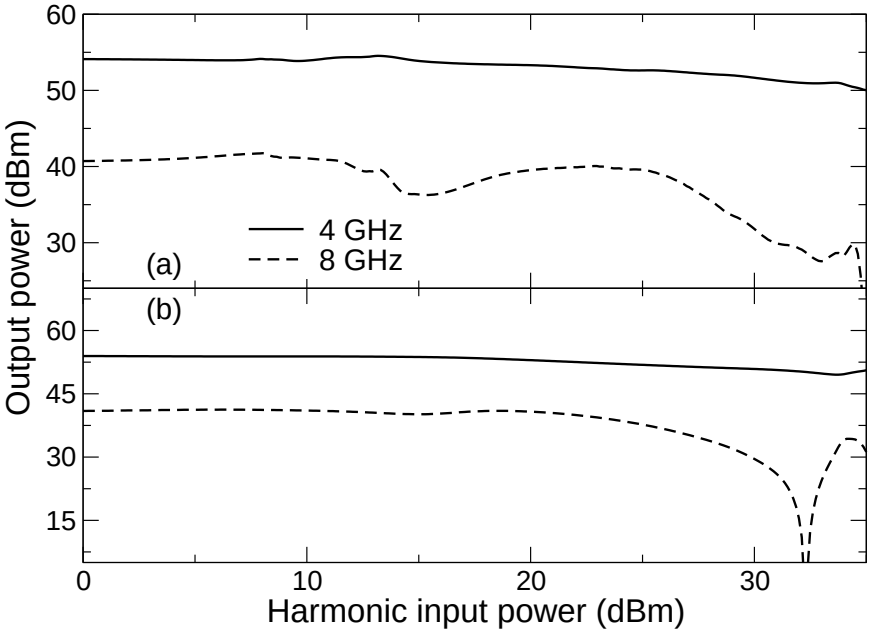

Figure 6.7 Fundamental and second harmonic output power versus second harmonic input power for harmonic input phase equal to (a) 47.9° and (b) 12.5°. In (a) harmonic input phase is set to minimize output harmonic for injected harmonic power of 15 dBm, and in (b) harmonic input phase is set to cancel output harmonic for injected harmonic power of 32.29 dBm. Fundamental input power and phase of 13.0 dBm and 0.0° produce saturated output power of 54.1 dBm at the fundamental and 40.6 dBm at the harmonic with no harmonic injection.

suppression we obtained was 16.4 dB, from 38.8 dBm to 22.4 dBm, for a fundamental input of 27.0 dBm and a harmonic input of 34.5 dBm.

6.3.1.4 Second and third harmonic injection

Next we consider injection of the second and the third harmonic to achieve cancellation of the second harmonic when the second and and third harmonics are both in the linear gain bandwidth. For this injection scheme there are three terms in (6.1) for each of the three frequencies: one driven term and two nonlinear terms. To achieve cancellation for a particular frequency at the output, these three terms should add to zero at $z = L$.

As an example we solve the S-MUSE equations of Section 6.5 for a fundamental frequency of 1.5 GHz, second harmonic of 3.0 GHz, and third harmonic of 4.5 GHz. The respective input powers and phases for the fundamental, second, and third harmonics are $10, -14.2, -10.6$ dBm and $0.0°, 15.0°, -45.0°$. When evaluated at $z = L$ the three terms in (6.1) for the second harmonic frequency may be represented in a phasor diagram as seen in Fig. 6.8. Phasor **A** represents the nonlinear product of the fundamental with itself (the

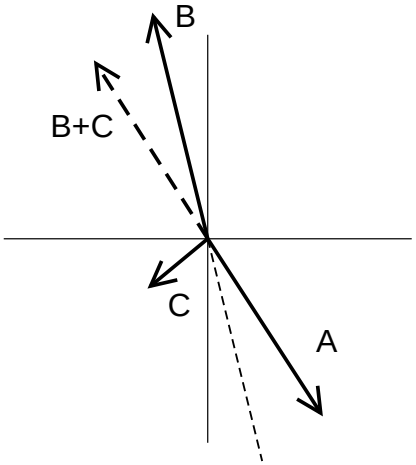

Figure 6.8 Output phasor picture produced by analytic S-MUSE solution for second and third harmonic injection. Phasor **A** represents the second harmonic mode due to nonlinear product of fundamental with itself, phasor **B** represents the injected second harmonic mode, and phasor **C** represents the mode due to the nonlinear product of the third harmonic with the fundamental. Phasor $\mathbf{B} + \mathbf{C}$ cancels phasor **A**.

mode we wish to cancel), phasor **B** represents the driven second harmonic, and phasor **C** represents the nonlinear product of the third harmonic with the fundamental. If a phasor **X** has magnitude $|\mathbf{X}|$ and phase $\theta_{\mathbf{X}} = \text{Arg}\{\mathbf{X}\}$, then note from Fig. 6.8 that for cancellation $|\mathbf{A}| = |\mathbf{B} + \mathbf{C}|$ and that $\theta_{\mathbf{B+C}} - \theta_{\mathbf{A}} = \pi$.

For sufficiently small fixed fundamental input power[4] and fixed fundamental, second, and third harmonic input phases, if $0 < |\theta_{\mathbf{C}} - \theta_{\mathbf{B}}| < \pi$ then the second and third harmonic input powers can be adjusted to achieve second harmonic cancellation. This replaces the necessity of having precise control of the input phase of the injected harmonic in the case of single harmonic injection with the necessity of having precise control of the second and third harmonic input powers. In hardware it is typically easier to precisely control input powers than it is to precisely control input phases.

Using LATTE we found that for input phases identical to the values used to generate Fig. 6.8, and respective input powers for the fundamental, second, and third harmonics of $10, -13.3, -9.6\,\mathrm{dBm}$ the second harmonic is cancelled at $z = 15\,\mathrm{cm}$.

From the phasor diagram in Fig. 6.8 one can see that the relative amounts of injected second and third harmonic power (proportional to the lengths of output phasors **B** and **C**) depend on the relative choice of the input phases of the three injected signals. Judicious choice of the input phases may be used to minimize the amount of injected power. In fact, the minimal injected powers would correspond to inputs such that both phasors **B** and **C** were 180° out of phase with respect to phasor **A**, and the lengths of phasors **B** and **C** were split up such that their magnitudes add to the magnitude of phasor **A**. (This situation however does require precise phase control on the input.) However, a phasor diagram as in Fig. 6.8 is only predicted by the analytic theory we are presenting in this chapter, and is an approximation to the results produced by a large signal code such as LATTE. Therefore, to obtain the minimum input powers with a large signal code such as LATTE detailed input power and phase scans are required.

As in the case of second harmonic injection, one expects that the voltage phase of the solution at the second harmonic will correspond to the mode which dominates the solution. For inputs below those which produce saturation, the dominant modes are growing exponentially and the 180° degree phase change in the solution is clearly seen (e.g. Fig.6.3). For larger inputs the modes are no longer exponentially growing after the point of cancellation, so the abrupt change in phase may not be as evident in the solution. In Fig. 6.9 we show the voltage phase of the second harmonic as a function of axial distance along the TWT for the fundamental input powers of $10.0, 23.0, 28.0\,\mathrm{dBm}$, corresponding to linear behavior, 3 dB compression, and full saturation respectively as predicted by LATTE. In each case the input phases for the fundamental, second, and third harmonic are $0.0°, 15.0°, -45.0°$ and the second and third harmonic input powers have been set to cancel the second harmonic at $z = 15\,\mathrm{cm}$. For linear behavior and saturation the 180° phase change is clearly seen, while for 3 dB compression the phase change is still evident, but not as distinct.

Finally we conjecture about the effect of injecting harmonics higher than third order on canceling an undesired harmonic. The properly phased injection of each additional higher order harmonic will result in one more output phasor (see Fig. 6.8) that can be used to

[4]By "sufficiently small" we mean, for example, that when only the fundamental is injected that neither the fundamental nor the nonlinearly generated second and third harmonic show signs of onset of saturation at $z = L$. In fact, the principle being described may in fact hold for larger input powers, but we have not tried to determine an upper limit on the input powers for which it holds.

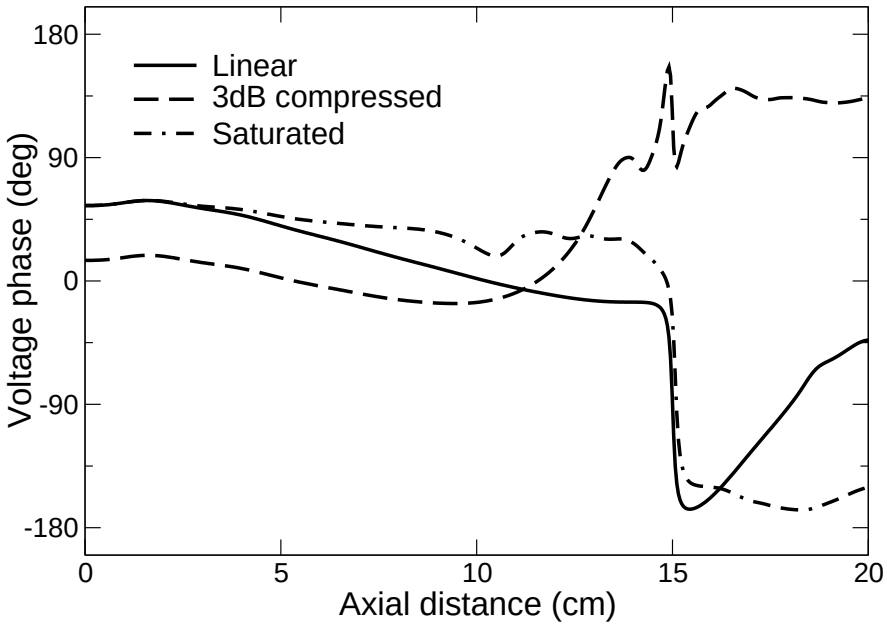

Figure 6.9 Voltage phase of the second harmonic with second and third harmonic injection for fundamental input powers in the linear regime, output 3 dB compressed, and output saturated. Phase is with respect to cold circuit phase velocity at 3.0 GHz. The second harmonic is cancelled at $z = 15$ cm. All traces show change in phase at cancellation point, but characters are different due to different relative inputs. Fundamental, second, and third harmonic power and phase inputs are: linear $10.0, -13.3, -9.6$ dBm, $20.0°, 55.0°, 15.0°$; 3 dB compressed $23.0, 11.086, -1.25$ dBm, $0.0°, 15.0°, -130.0°$; saturated $28.0, 12.345, 12.55$ dBm, $40.0°, 55.0°, 270.0°$.

cancel the undesired phasor. This could result in reducing the power required for each injected signal. However, when the injected harmonics are out of the linear gain bandwidth, their resulting phasors may be too small to have an appreciable affect on canceling the undesired harmonic. This is an area for potential future study.

6.3.2 Intermodulation frequencies

Signal injection can also be used to suppress intermodulation frequencies [70, 79, 21]. Consider two drive frequencies f_a, f_b with $f_a < f_b$, the second order products $2f_a, f_a + f_b, 2f_b, f_b - f_a$, and the third order intermodulation frequencies $2f_a - f_b, 2f_b - f_a$.[5] Then for example, injection of the second harmonic $2f_a$ forms a nonlinear second order product with the fundamental f_b which may be adjusted to cancel the nonlinear third order intermodulation frequency $2f_a - f_b$. Similarly one can inject $2f_b$ to cancel $2f_b - f_a$. Furthermore, in principle, one can inject the difference frequencies and form second order products with the fundamental frequencies to cancel the 3IM frequencies, which has been shown experimentally in solid-state amplifiers [31]. Lastly, one can inject the 3IM frequencies directly with the right amplitudes and phases to achieve cancellation [72].

Similar to the case of multiple harmonic injection, one can use two or more of the above injection frequencies simultaneously to eliminate the need for precise input phase control. The effect of the different injection schemes on the intermodulation frequencies other than those that are being cancelled is a subject of future work.

For the examples of Sections 6.3.2.1 and 6.3.2.4 we choose the drive frequencies to be 1.9 and 2.0GHz with input powers of 0.0 dBm and respective input phases of 0.0° and 30.0°. For the examples of Section 6.3.2.2 we choose the drive frequencies to be 3.9 and 4.0GHz with input powers of −5.0 dBm and respective input phases of 0.0° and 30.0°. These inputs do not produce saturation effects in any of the frequencies at the TWT output. The behavior of the examples considered here with inputs which produce saturation is a subject of future work. In all of the simulations we have accounted for up to the third order products of the input frequencies. In general, signal injection results in additional intermodulation frequencies beyond those which exist in the presence of the fundamental frequencies alone.

6.3.2.1 Injection in linear gain bandwidth

We consider first single signal injection when the injected signal is in the linear gain bandwidth. For second harmonic or difference frequency injection, the form of the solution at the third order intermodulation frequency is given by (6.1) with $A_\ell^{\rm dr} = 0$ and two terms in the sum over q.[6] For 3IM injection, $A_\ell^{\rm dr} \neq 0$ and there is one term in the sum over q. Formulas for $A_\ell^{\rm dr}, A_\ell^{{\rm nl}[q]}$ are given in Section 6.5.

[5] There are other third order intermodulation frequencies that we do not list since they are located near the third harmonics, and may be removed by filtering.

[6] Even though the mode which enables the cancellation for these cases is a nonlinear product mode, we will still refer to it as a "driven mode" as its existence depends on having the signal injected.

In Fig. 6.10 we show the mode amplitudes and composite solution envelope from (6.1) for cancellation with second harmonic injection, and in Fig. 6.11 we show the mode amplitudes and composite solution for cancellation with 3IM injection. Notice that the induced mode which accomplishes the cancellation in the second harmonic injection case is growing much faster than the driven mode which accomplishes the cancellation in the 3IM injection case (the ranges on the vertical axes of the figures are identical). This is because in the former case the mode is a second order mode and has a growth rate equal to the sum of the growth rates of the driving frequencies (2.0 and 3.8 GHz) [83]. In the latter case, the mode is a drive frequency and grows with its linear growth rate.

A subtlety in the case of 3IM injection is that with such an injected signal the solution (6.1) for the 3IM frequency will have more terms in the sum over q. For example, if $f_{3\mathrm{IM}}$ is the injected 3IM and f_a, f_b are the original fundamentals, then $f_{3\mathrm{IM}}$ is equal to the third order products $(f_{3\mathrm{IM}} + f_a) - f_a$ and $(f_{3\mathrm{IM}} + f_b) - f_b$ [the parentheses $(\,\cdot\,)$ indicate the formation of a second order product, and the subtracted off term results in a third order product]. That is, the third order nonlinear solution is now the sum of the original 3IM mode (e.g. $2f_a - f_b$) in addition to the modes produced by the above third order products. However, since the required injected power of the 3IM is so much less than the injected fundamental powers, it was found that the solution was only slightly modified by the inclusion of these additional modes.

6.3.2.2 Injection out of linear gain bandwidth: no sever

Similarly to Section 6.3.1.2, we consider the implications of the injected signals being out of the linear gain bandwidth. For narrow band TWTs it is likely that the second harmonic is out of the linear gain bandwidth. For difference frequency injection the difference frequency would be out of the linear gain bandwidth for most drive frequency spacings; however, for wideband TWTs one could construct pairs of input frequencies such that the difference frequency is in the linear gain bandwidth.

We showed in Section 6.3.1.2 that second harmonic injection to cancel the second harmonic is much less effective when the second harmonic is out of the linear gain bandwidth. This raises the question of the effectiveness of second harmonic injection to cancel an intermodulation product when the second harmonic is out of the linear gain bandwidth. In this case, the injected second harmonic exists in the circuit as a non-growing mode. It combines nonlinearly with one of the drive frequencies resulting in a signal that has a growth rate equal to that of the drive frequency [83]. The growth rate of the 3IM frequency to be cancelled in most cases will be on the order of three times the growth rate of the fundamental frequency [83]. However, the net levels of the signals can be made comparable since the 3IM starts at a much lower amplitude than the second order product (the injected second

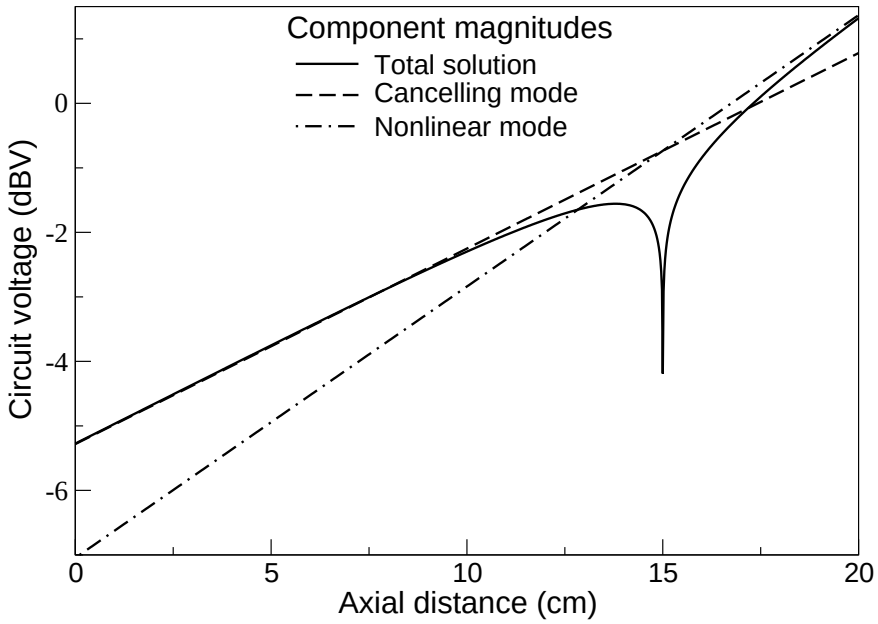

Figure 6.10 Magnitude of (6.1) and component magnitudes of (6.1) for 3IM frequency 1.8 GHz with second harmonic injection to cancel the 3IM frequency. The canceling mode (nonlinear difference product of 3.8 GHz and 2.0 GHz) dominates the solution prior to $z = 15\,\text{cm}$, and the nonlinear mode dominates the solution after $z = 15\,\text{cm}$. Fundamental $(1.9, 2.0\,\text{GHz})$ and second harmonic $(3.8\,\text{GHz})$ input powers and phases are $0.0, 0.0, -18.32\,\text{dBm}$ and $0.0°, 30.0°, 116.24°$ respectively.

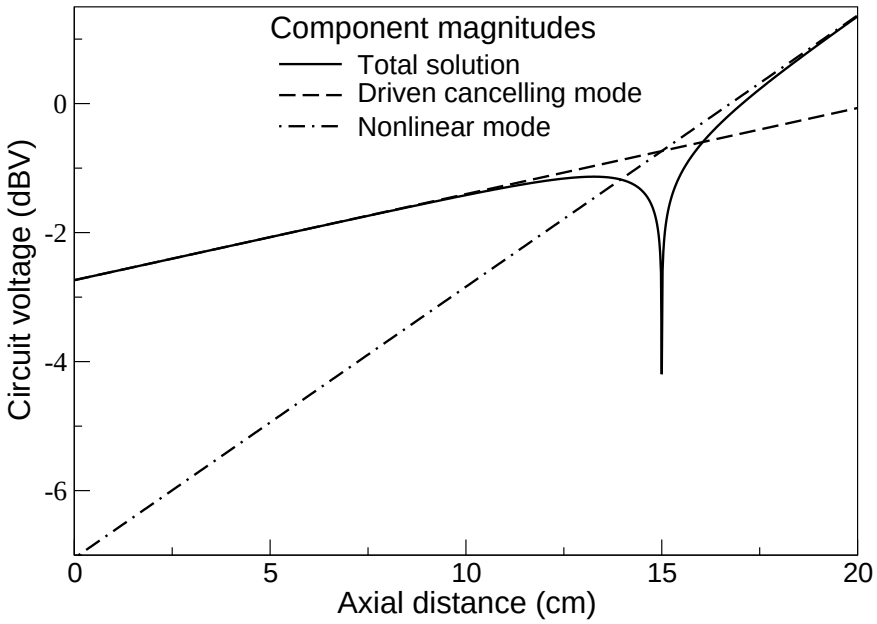

Figure 6.11 Magnitude of (6.1) and component magnitudes of (6.1) for 3IM frequency 1.8 GHz with 3IM injection to cancel the 3IM frequency. The driven mode dominates the solution prior to $z = 15\,\text{cm}$, and the nonlinear mode dominates the solution after $z = 15\,\text{cm}$. Fundamental ($1.9, 2.0\,\text{GHz}$) and 3IM ($1.8\,\text{GHz}$) input powers and phases are $0.0, 0.0, -36.36\,\text{dBm}$ and $0.0°, 30.0°, -146.56°$ respectively.

harmonic combined with the fundamental). Therefore, as shown in Fig. 6.12, harmonic injection to suppress the 3IM when the harmonic is out of the linear gain bandwidth can be effective.[7]

When the injected second harmonic is out of the linear gain bandwidth the level of the injected signal will generally need to be larger relative to the fundamental input powers as compared to when the injected second harmonic is in the linear gain bandwidth. This can be seen by comparing the values of the injected second harmonic powers relative to the fundamental powers for Fig. 6.10 ($-18.32\,\mathrm{dB}$) and Fig. 6.12 ($15.6\,\mathrm{dB}$). The reason is that when the second harmonic is out of the linear gain bandwidth the second order mode used to cancel the 3IM grows at a rate about equal to the drive frequency, whereas when the harmonic is in the gain bandwidth the second order mode used to cancel the 3IM grows at a rate about twice that of the drive frequency [83]. Therefore, to ultimately obtain the same relative power level in the mode, the injected power of the mode with the lower growth rate must be relatively larger. That is, when the second harmonic is out of the linear gain bandwidth, one needs a larger relative harmonic input.

6.3.2.3 Injection out of linear gain bandwidth: with sever

In contrast to harmonic injection to control the second harmonic when the injected harmonic is out of the linear gain bandwidth as in Section 6.3.1.2, we expect from the theory that including a circuit sever will *not* greatly affect the performance of the injection schemes to control the intermodulation spectrum. The reason is that the mode that cancels the 3IM is an exponentially growing mode that has a corresponding modulation in the beam current. When the circuit field of this mode is damped by the sever, the beam modulation re-initiates the circuit field mode after the sever. This is in contrast to the case in Section 6.3.1.2 where the sever heavily damped the mode that performed the harmonic reduction. In fact, in a simulation including a circuit sever with fundamental inputs such that the C3IM ratio (the relative level in dB of the fundamental to the 3IM at the TWT output) without second harmonic injection was the same as those for the simulation that produced Fig. 6.12, we found that the required harmonic injection power relative to the fundamental power was $10.5\,\mathrm{dB}$ as compared to $15.6\,\mathrm{dB}$ for the circuit with no sever.

Next we consider cancellation of a 3IM with injection of the difference frequency. Theoretically this situation is similar to second harmonic injection when the second harmonic is out of the linear gain bandwidth. Even though the difference frequency is out of the linear gain bandwidth, the second order product of the difference frequency and the fundamental will grow at a rate equal to the fundamental frequency growth rate [83]. With sufficiently large difference frequency input power, cancellation of the 3IM can be obtained as shown in Fig. 6.13. Note that the required difference frequency input power relative to the fundamental ($P_{f_2-f_1} - P_{f_1} = 17.4\,\mathrm{dB}$) is similar to the required second harmonic injection power

[7] In general the spectra we present have content near the second, third and/or fourth harmonics of the drive frequencies, but we have chosen only to display the spectra near the fundamentals and second harmonics.

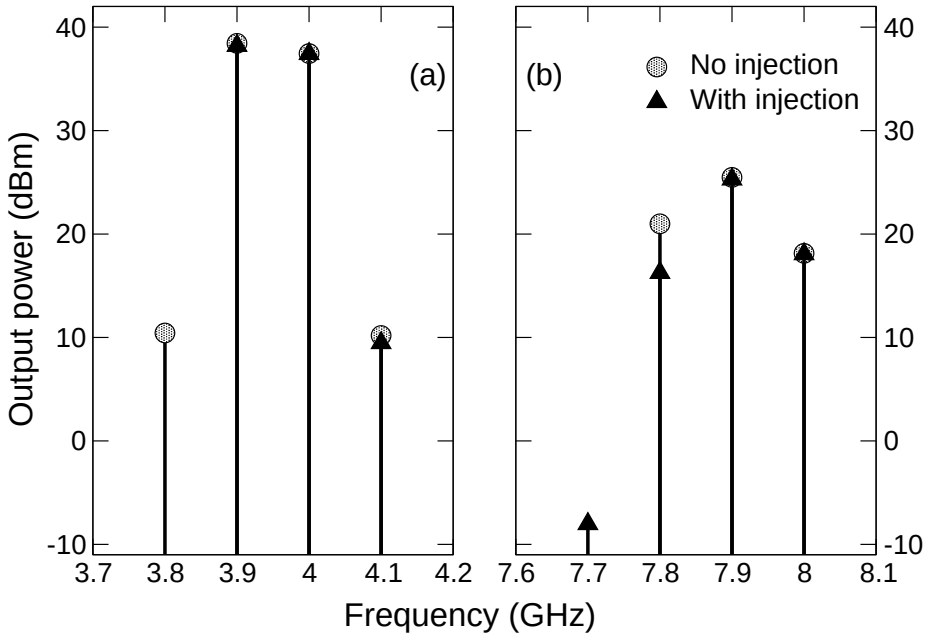

Figure 6.12 Output spectrum (a) near fundamentals and (b) near second harmonics with and without second harmonic injection when second harmonic is out of the linear gain bandwidth. Note additional "intermodulation frequencies" (e.g., at 7.7 GHz) due to injection of the second harmonic. Fundamental inputs 3.9, 4.0 GHz have input power −5.0 dBm and respective phases of 0.0° and 30.0°. Injected harmonic 7.8 GHz has input power and phase of 10.6 dBm and 32.2°. Note that there is also partial suppression of the second harmonic at 7.8 GHz.

relative to the fundamental when the second harmonic is out of the linear gain bandwidth ($P_{2f_1} - P_{f_1} = 15.4\,\text{dB}$). Also note that the difference frequency can be used to cancel either 3IM frequency, but not both 3IMs simultaneously.

There is some question as to whether difference frequency injection will work in practice. Since the wavelength of the difference frequency is much longer than the physical TWT, it is not clear as to whether the mode resulting from the product of the difference frequency and the fundamental frequency will be produced in the device. Ultimately an experimental test of the idea will be needed to determine if it works.

6.3.2.4 Multiple signal injection

Second and third harmonic injection was shown in Section 6.3.1.4 to control the level of the second harmonic while eliminating the need for precise control of the injected signal phases. When using signal injection to control the intermodulation spectrum there are many cases when one might wish to inject multiple signals. For example second harmonic and intermodulation injection or second harmonic and difference frequency injection may be used to control the intermodulation level and eliminate the requirement of precise phase control of the injected signals. Furthermore, one could imagine that for multiple fundamental signals, second harmonic and intermodulation pairs or second harmonic and difference frequency pairs could be used to control the many intermodulation products. However, the effects of injecting many signals on the *other* spectral components, and whether the resulting spectra are improved over the original spectra is not known. While we do not attempt to answer this question here, we give a few examples of multiple signal injection for two fundamental frequencies using LATTE simulations.

In Fig. 6.14 we show the output spectrum with and without injection of a 3IM (2.1 GHz) and second harmonic (4.0 GHz) to cancel the 3IM. The targeted 3IM frequency is totally cancelled while additional spectral components are produced near the fundamentals and second harmonics. Since the new intermodulation products are more than 60 dB below the fundamentals amplitudes, they may not represent a problem as a practical matter. A determination of the importance of these new distortion products would need to be made in the context of linearity requirements for each specific application. As was the case in second and third harmonic injection to control the second harmonic (Section 6.3.1.4), this scheme eliminates the necessity of precise phase control of the injected signals. This is accomplished by producing two output phasors whose lengths can be controlled to cancel the undesired output phasor by adjusting the injected signal input powers (see Fig. 6.8).

Next we consider injecting the second harmonics of both of the fundamental frequencies. In Fig. 6.15 we show the output spectra with and without injection of both second harmonics. The original 3IM frequencies are totally cancelled and there is some cancellation at the second harmonic, as well, while some additional spectral components appear due to the additional input signals. The level of the additional signals near the fundamentals are much lower than the original 3IM frequencies. There are several components generated near the second

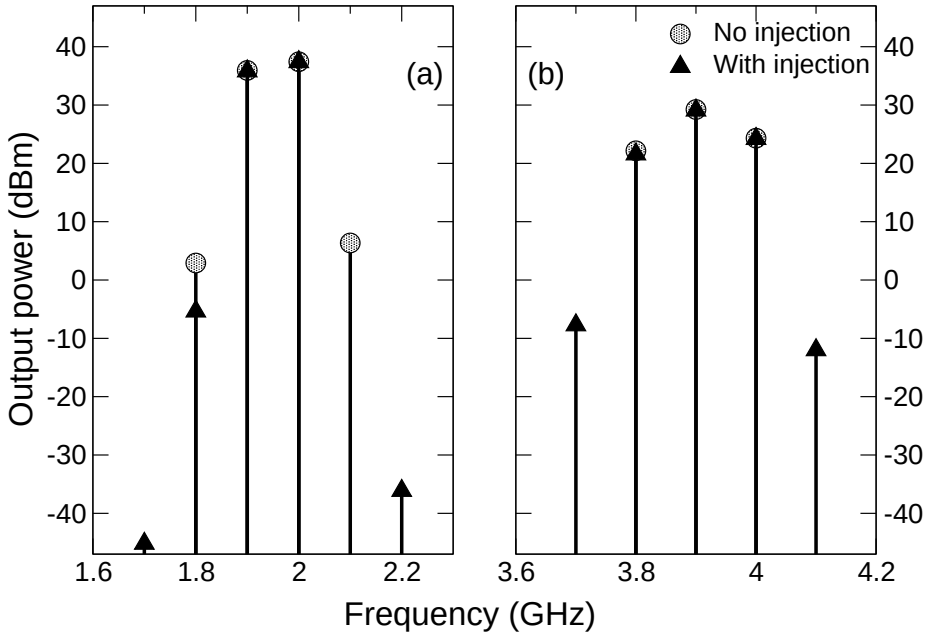

Figure 6.13 Output spectrum (a) near fundamentals and (b) near second harmonics with and without difference frequency injection. Note additional "intermodulation frequencies" due to injection of the difference frequency. Fundamental inputs $1.9, 2.0\,\mathrm{GHz}$ have input power $0.0\,\mathrm{dBm}$ and respective phases of $0.0°$ and $30.0°$. The injected difference frequency $100.0\,\mathrm{MHz}$ has input power and phase of $17.4\,\mathrm{dBm}$ and $134.45°$.

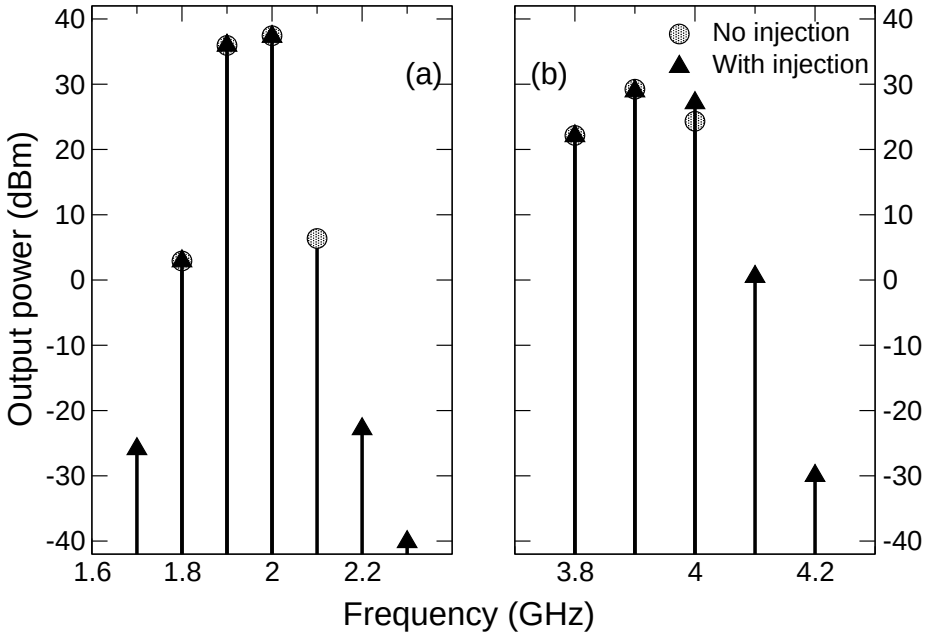

Figure 6.14 Output spectrum (a) near fundamentals and (b) near second harmonics with and without 3IM and second harmonic injection. Note additional "intermodulation frequencies" due to the injection of the signals. Fundamental inputs $1.9, 2.0\,\text{GHz}$ have input power $0.0\,\text{dBm}$ and respective phases of $0.0°$ and $30.0°$. The injected 3IM and second harmonic $2.1, 4.0\,\text{GHz}$ have input powers and phases of $-30.0, -22.0\,\text{dBm}$ and $-13.0°, 35.0°$.

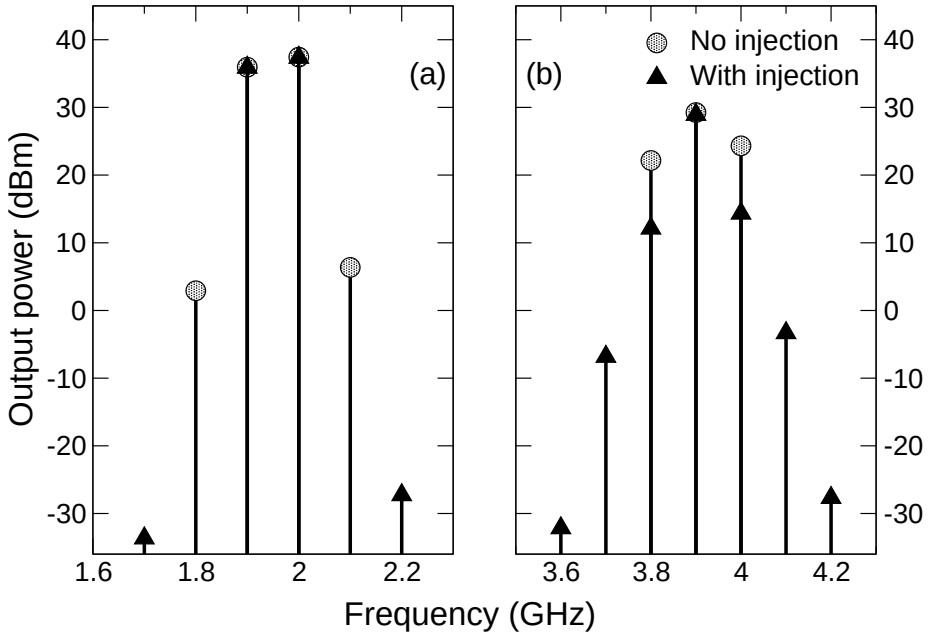

Figure 6.15 Output spectrum (a) near fundamentals and (b) near second harmonics with and without second harmonic injection of both fundamentals. Note additional "intermodulation frequencies" due to the injection of the harmonic signals. Fundamental inputs $1.9, 2.0\,\mathrm{GHz}$ have input power $0.0\,\mathrm{dBm}$ and respective phases of $0.0°$ and $30.0°$. The injected harmonics $3.8, 4.0\,\mathrm{GHz}$ have input powers and phases of $-23.25, -19.4\,\mathrm{dBm}$ and $66.5°, 136.1°$.

harmonics, although it is thought that these could be filtered and would be of less a concern than the spectrum near the fundamental.

Finally, in Fig. 6.16 we show results of injecting the 3IMs and second harmonics of both of the fundamental signals. The 3IM frequencies are cancelled without a requirement of precise input phase control, but the number of additional spectral components becomes quite large. However, all of the signals near the fundamentals are substantially lower than the 3IMs without the injection. If one can tolerate a complicated spectrum near the second harmonics, it is thought that this scheme may be desirable.

We have done some testing of the above multiple signal injection schemes for fundamental inputs of 5 dBm, which start to show the onset of saturation effects in the intermodulation and harmonic signals. For second harmonic injection of both fundamentals simultaneous cancellation of both 3IM frequencies was found to be possible. However, in the case of injecting both 3IMs and both second harmonics we were unable to find, with a coarse search, injection input values to cancel both of the 3IM frequencies simultaneously. The general existence of such inputs is a subject of future study.

6.4 Conclusions

We present an interpretation of harmonic injection, and more generally "signal injection," in a TWT as the cancellation of "driven" and "nonlinear" modes. The interpretations are based on an approximate analytic solution to an approximate nonlinear model. Furthermore, we use "large signal" simulations to test whether the modal solution structure is valid in saturated conditions. In general we find that the large signal simulations indeed show the abrupt phase change signature of the approximate analytic solutions.

The idea has existed for some time that the physical mechanism of harmonic injection is cancellation of such modes [55, 38]. However, we present the first quantitative theory to predict the existence of the modes. Furthermore, the quantitative theory has provided insights into harmonic injection that the intuited notions could not. For example, a phasor picture provided by the theory demonstrates how multiple harmonic injection can eliminate the sensitive dependence of the output signals on the phase of the input signals. Also the analytic solutions elucidate the many effects of the injected signals being outside of the linear gain bandwidth of the TWT. Some experimentation is still required to verify all of the notions put forward in the chapter.

6.5 Formulas for mode amplitudes

In this section we provide formulas required to compute solutions of the dominant modes for the cases discussed in the chapter. We use the vector notation of [82] where $\mathbf{x}_\ell = [\mathbf{x}_{\ell_1} \dots \mathbf{x}_{\ell_5}]^{\mathrm{T}} = \left[\tilde{V}_\ell\, \tilde{I}_\ell\, \tilde{E}_\ell\, \tilde{v}_\ell\, \tilde{\rho}_\ell\right]^{\mathrm{T}}$. Due to the Fourier series used in the model, for each positive frequency f_ℓ there is a corresponding negative frequency indexed by $-\ell$ with $f_{-\ell} = -f_\ell$.

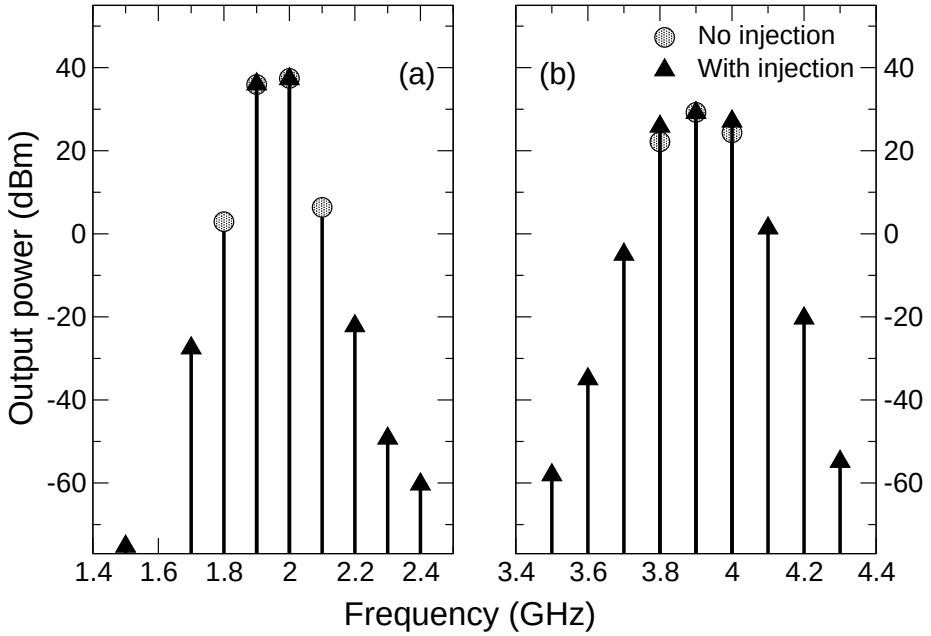

Figure 6.16 Output spectrum (a) near fundamentals and (b) near second harmonics with and without injection of both 3IMs (1.8, 2.1 GHz) and both second harmonics (3.8, 4.0 GHz). Note additional "intermodulation frequencies" due to injection the of the signals. Fundamental inputs 1.9, 2.0 GHz have input power 0.0 dBm and respective phases of 0.0° and 30.0°. The injected 3IM and second harmonics 1.8, 2.1, 3.8, 4.0 GHz have input powers and phases of −26.7, −30.0, −25.0, −22.0 dBm and −150.0°, −13.0°, −140.0°, 35.0°. The large dynamic range of the figure is so that all of the spectral components are shown.

Furthermore $\mathbf{x}_{-\ell} = \mathbf{x}_\ell^*$. The differential equation for $\mathbf{x}_\ell$ is

$$\dot{\mathbf{x}}_\ell = \mathbf{A}_\ell \mathbf{x}_\ell + \sum_{\substack{m,n \\ f_m + f_n = f_\ell}} \mathbf{H}_{\ell mn}(\mathbf{x}_m, \mathbf{x}_n) \tag{6.6}$$

where matrix and tensor components $\mathbf{A}_{\ell_{ij}}$ and $\mathbf{H}_{\ell_i m_j n_k}$ are listed in Appendix II of [82]. One can show that (6.6) may be solved with a series solution

$$\mathbf{x}_\ell = \sum_{\alpha=1}^{\infty} \mathbf{x}_\ell^{(\alpha)} \tag{6.7}$$

and that this series converges under the appropriate conditions. The index α is related to the order of intermodulation product [83]. The formulas for the terms of the series are given by

$$\mathbf{x}_\ell^{(1)} = e^{\mathbf{A}_\ell z} \mathbf{w}_\ell \qquad \alpha = 1 \tag{6.8}$$

$$\mathbf{x}_\ell^{(\alpha)} = \int_0^z e^{\mathbf{A}_\ell (z-\tau)} \sum_{\beta=1}^{\alpha-1} \sum_{\substack{m,n \\ f_m + f_n = f_\ell}} \mathbf{H}_{\ell mn}\left(\mathbf{x}_m^{(\beta)}(\tau), \mathbf{x}_n^{(\alpha-\beta)}(\tau)\right) d\tau, \qquad \alpha \geq 2 \tag{6.9}$$

where $\mathbf{w}_\ell$ contains the initial values for frequency f_ℓ [82] and $e^{\mathbf{A}_\ell z}$ is the matrix exponential of the matrix $\mathbf{A}_\ell z$ [18]. The complex exponential modes of the vector $\mathbf{x}_\ell^{(\alpha)}$ may be indexed by p

$$\mathbf{x}_\ell^{(\alpha)}(z) = \sum_{p=1}^{N_\ell^{(\alpha)}} \mathbf{a}_\ell^{(\alpha)[p]} e^{\left(\mu_\ell^{(\alpha)[p]} + i\sigma_\ell^{(\alpha)[p]}\right) z} \tag{6.10}$$

with $\mathbf{a}_\ell^{(\alpha)[p]}$ a complex vector, and $\mu_\ell^{(\alpha)[p]}$, $\sigma_\ell^{(\alpha)[p]}$ real numbers. Sums like (6.10) are ordered so that $\mu_\ell^{(\alpha)[1]} \geq \mu_\ell^{(\alpha)[2]} \geq \cdots \geq \mu_\ell^{(\alpha)[N_\ell^{(\alpha)}]}$.

To keep the formalism as simple as possible, we provide formulas only for the cases when the injected signals are in the linear gain bandwidth of the TWT. In these cases the solutions for fixed α can be approximated by a single "dominant mode" in the case of single signal injection, or several "dominant modes" in the case of multisignal injection. The total solution (6.1) is a sum of the dominant modes for the different values of α.

When the injected signals are out of the linear gain bandwidth the number of modes required to represent the solutions increases substantially, and the formulas for the solutions involve more caveats and technicalities. A complete formulation accounting for all modes is given in Chapter 3.

We give formulas for first order (linear), second order, and third order products. The formulas may be used to compute all of the cases in the chapter in which the injected signal is in the linear gain bandwidth of the TWT.

6.5.1 First order (linear) solution

The $p = 1$ mode of the first order ($\alpha = 1$) drive frequencies (including injected signals) is given by

$$\mathbf{x}_\ell^{(1)[1]} = \mathbf{a}_\ell^{(1)[1]} e^{\mu_\ell^{(1)[1]} z} e^{i\sigma_\ell^{(1)[1]} z} \tag{6.11}$$

where

$$\mathbf{a}_\ell^{(1)[1]} = \mathbf{P}_\ell \mathbf{Q} \mathbf{P}_\ell^{-1} \mathbf{w}_\ell \tag{6.12}$$
$$\mu_\ell^{(1)[1]} = \mathrm{Re}\{\lambda_{\ell_1}\}, \tag{6.13}$$
$$\sigma_\ell^{(1)[1]} = \mathrm{Im}\{\lambda_{\ell_1}\}, \tag{6.14}$$

and

$$\mathbf{Q}_{i,j} = \begin{cases} 1 & i = j = 1 \\ 0 & \text{otherwise.} \end{cases} \tag{6.15}$$

We assume that $\mathbf{P}_\ell$, the modal matrix of $\mathbf{A}_\ell$, has the eigenvector associated with λ_{ℓ_1}, the eigenvalue of $\mathbf{A}_\ell$ with the largest real part, in its first column. Then for (6.1) we have

$$A_\ell^{\mathrm{dr}} = \left| \mathbf{a}_{\ell_1}^{(1)[1]} \right| \tag{6.16}$$
$$\mu_\ell^{\mathrm{dr}} = \mu_\ell^{(1)[1]} \tag{6.17}$$
$$\kappa_\ell^{\mathrm{dr}} = \sigma_\ell^{(1)[1]} + \mathrm{Arg}\left\{ \mathbf{a}_{\ell_1}^{(1)[1]} \right\}. \tag{6.18}$$

6.5.2 Second order solution

Next we solve for second order products ($\alpha = 2$) of the injected signals. We give formulas for one mode in the sum over q in (6.1) and note that the number of required modes and ordering of the modes is application dependent. A second order product has associated with it a pair of indices m and n such that $f_m + f_n = f_\ell$. We have

$$\mathbf{x}_\ell^{(2)[q]} = \mathbf{a}_\ell^{(2)[q]} e^{\mu_\ell^{(2)[q]} z} e^{i\sigma_\ell^{(2)[q]} z} \tag{6.19}$$

where

$$\mathbf{a}_\ell^{(2)[q]} = \mathbf{P}_\ell \mathbf{S}_\ell \left(\mu_\ell^{(2)[q]} + i\sigma_\ell^{(2)[q]}\right) \mathbf{P}_\ell^{-1} \mathbf{c}_\ell^{(2)[q]} \tag{6.20}$$

$$\mathbf{c}_\ell^{(2)[q]} = \begin{cases} \mathbf{H}_{\ell mn}\left(\mathbf{a}_m^{(1)[1]}, \mathbf{a}_n^{(1)[1]}\right) & \substack{m=n \\ f_m+f_n=f_\ell} \\ \mathbf{H}_{\ell mn}\left(\mathbf{a}_m^{(1)[1]}, \mathbf{a}_n^{(1)[1]}\right) & \substack{m\neq n \\ f_m+f_n=f_\ell} \\ \quad + \mathbf{H}_{\ell nm}\left(\mathbf{a}_n^{(1)[1]}, \mathbf{a}_m^{(1)[1]}\right) & \end{cases} \tag{6.21}$$

$$\mu_\ell^{(2)[q]} = \mu_m^{(1)[1]} + \mu_n^{(1)[1]} \tag{6.22}$$

$$\sigma_\ell^{(2)[q]} = \sigma_m^{(1)[1]} + \sigma_n^{(1)[1]} \tag{6.23}$$

$$\mathbf{S}_{\ell_{i,j}}(\gamma) \equiv \begin{cases} \frac{1}{\gamma - \lambda_{\ell_j}} & i = j \\ 0 & \text{otherwise} \end{cases} \tag{6.24}$$

and we have assumed that $\mu_m^{(1)[1]} + \mu_n^{(1)[1]} > \mathrm{Re}\{\lambda_{\ell_1}\}$. The eigenvalues λ_{ℓ_j} of $\mathbf{A}_\ell$ have the same ordering as the eigenvectors of $\mathbf{A}_\ell$ appearing in columns of $\mathbf{P}_\ell$.

Then for a mode of (6.1) we have

$$A_\ell^{\mathrm{nl}[q]} = \left|\mathbf{a}_{\ell_1}^{(2)[q]}\right| \tag{6.25}$$

$$\mu_\ell^{\mathrm{nl}[q]} = \mu_\ell^{(2)[q]} \tag{6.26}$$

$$\kappa_\ell^{\mathrm{nl}[q]} = \sigma_\ell^{(2)[q]} + \mathrm{Arg}\left\{\mathbf{a}_{\ell_1}^{(2)[q]}\right\}. \tag{6.27}$$

This mode can describe sum and difference frequencies of the injected signals.

6.5.3 Third order solution

Lastly we solve for third order products ($\alpha = 3$) of the injected signals. Given the dominant mode of the injected signal $\mathbf{x}_m^{(1)[1]}$ from (6.11) and a dominant mode of a second order product $\mathbf{x}_n^{(2)[1]}$ from (6.19) one has[8]

$$\mathbf{x}_\ell^{(3)[1]} = \mathbf{a}_\ell^{(3)[1]} e^{\mu_\ell^{(3)[1]} z} e^{i\sigma_\ell^{(3)[1]} z} \tag{6.28}$$

where

$$\mathbf{a}_\ell^{(3)[1]} = \mathbf{P}_\ell \mathbf{S}_\ell \left(\mu_\ell^{(3)[1]} + i\sigma_\ell^{(3)[1]}\right) \mathbf{P}_\ell^{-1} \mathbf{c}_\ell^{(3)[1]} \tag{6.29}$$

$$\mathbf{c}_\ell^{(3)[1]} = \mathbf{H}_{\ell mn}\left(\mathbf{a}_m^{(1)[1]}, \mathbf{a}_n^{(2)[1]}\right) + \mathbf{H}_{\ell nm}\left(\mathbf{a}_n^{(2)[1]}, \mathbf{a}_m^{(1)[1]}\right) \tag{6.30}$$

$$\mu_\ell^{(3)[1]} = \mu_m^{(1)[1]} + \mu_n^{(2)[1]} \tag{6.31}$$

$$\sigma_\ell^{(3)[1]} = \sigma_m^{(1)[1]} + \sigma_n^{(2)[1]}. \tag{6.32}$$

[8]Unlike the $\alpha = 2$ case we allow for only one third order mode in the total solution (6.1). Although a more general formalism is possible the examples provided in this chapter do not require it.

Therefore for (6.1) we have for the dominant mode of the third order product

$$A_\ell^{\mathrm{nl}[1]} = \left|\mathbf{a}_{\ell_1}^{(3)[1]}\right| \tag{6.33}$$

$$\mu_\ell^{\mathrm{nl}[1]} = \mu_\ell^{(3)[1]} \tag{6.34}$$

$$\kappa_\ell^{\mathrm{nl}[1]} = \sigma_\ell^{(3)[1]} + \mathrm{Arg}\left\{\mathbf{a}_{\ell_1}^{(3)[1]}\right\}. \tag{6.35}$$

Chapter 7

Conclusions

This thesis provides a fresh view of nonlinear TWT modeling and analysis. We present major theoretical advances on several important nonlinear problems whose solutions have remained elusive for many years. This work comes during a time when the focus of the research in the TWT community is largely on producing advanced design codes, and using these codes to improve TWT performance and reduce the time and cost of development. While the latter activities are essential to the progress of the field, one cannot discount the importance of new theoretical notions of the physical mechanisms at play in the device. One could argue that such notions are *as important* as a design code since it is the designer's ideas and intuitions that guide their use of codes.

A major theme emerging from this thesis is that in pursuing nonlinear problems one should think twice before discarding a nonlinear model that is not "exact." In fact, the thesis makes a clear case for using several nonlinear models on the same problem, even if some of the models are "limited." In this work useful models are produced by trading off model accuracy for desirable model "structure" as well as analytic tractability. Having several models is critical because often a nonlinear problem does not have a clear "answer," and instead one must resort to presenting evidence to support a hypothesis. The more varied the sources of evidence the better.

The modeling in Chapter 2 presents a comprehensive, pedagogical view of 1-d nonlinear steady-state TWT modeling. The mathematical connection between models using Eulerian and Lagrangian electron beam descriptions is clearly outlined in terms of a coordinate transformation using the method of characteristics. An extensive comparison of the new models to each other and to the well known TWT code Christine 1-d is given. This comparison of the Eulerian models to the "correct" Lagrangian models serves to establish the limitations of the Eulerian models. The advantages of the Eulerian models are also indicated. However, these advantages are increasingly clear throughout the remaining chapters of the thesis.

The models of Chapter 2 have been incorporated into a code named *LATTE/MUSE Numerical Suite*, or *lmsuite* [1]. This code represents a first in TWT design codes in that it is totally open[1] and available to the broader research community. TWT codes in the past have largely been either proprietary, or simply not made available. The existence of

[1]By "open" we mean that the source code is available for users to modify as they choose.

such a code could benefit both education and research. For education of undergraduate and graduate students, *lmsuite* provides a tool for learning TWT physics that is very similar to the tools they would find in an industrial setting. This benefits both the students and employers since it would reduce the training time required in a new job setting. The code has been designed with education in mind and includes such features as the ability to animate results. In the research community *lmsuite* could potentially provide a common platform on which researchers can compare their ideas and designs.

In Chapter 3 we give the formal details of the analytic solution to the S-MUSE model. These mathematical details form an important foundation for the remainder of the thesis work. However, what is more important is how these calculations are used in the subsequent chapters to arrive at new physical understanding.

In Chapter 4 we use the structure of the S-MUSE analytic solutions to develop a new view of the generation of intermodulation distortion. For subsequent work we have relied extensively on the intuitions built by this theory. In the theory second order products are produced by mixing of input frequencies, third order products are produced from mixing second order products with drive frequencies, fourth order products are produced by mixing third order products with drive frequencies and mixing second order products with second order products, and so on. The generation process is compactly summarized in an equation for intermodulation frequency generation [equation (4.5)]. A subtle insight coming from this generating structure is that an input frequency is also an intermodulation product of itself. This fact proves to be very important when considering TWT phase distortion.

Furthermore, the structure of the S-MUSE solutions yields a formula for growth rates of intermodulation products [equation (4.8)]. To test the universality of this result, we compare the predicted growth rate formulas to Christine 1-d data. We show that even though the quantitative values of the growth rates predicted by our theory and the Christine 1-d code do not agree, the structures of the growth rate formulas are manifest in the Christine 1-d data. Formula (4.8) indicates that the growth rate of an IMP is the greater of the sum of the growth rates of the frequencies combining to make the IMP and the linear growth rate of the IMP frequency. In most cases the former growth rate applies but there can be exceptions for very wide band TWTs. The analysis refines and gives insight into the conventional rule of thumb [6] of estimating the growth rate of a K^{th} order IMP as K times the growth rate of the drive frequency. The structure of the solutions given in this chapter, and their associated growth rates, turn out to be very important when one considers signal injection where the injected frequencies are out of the linear gain bandwidth.

In Chapter 5 we study the physical mechanisms for phase distortion in a TWT. Phase distortion has been said to "dominate TWT nonlinearity" [14] in TWTs. In the literature, many authors have attributed phase distortion to the slowing down of electrons in the electron beam, i.e., the reduction of the average electron beam velocity (see e.g. [41, 30, 14]). Through simulation and analysis we offer evidence that phase distortion, at least prior to 1 dB gain compression, is not due to slowing down of electrons in the beam. Rather, we attribute phase distortion to harmonic generation in the electron beam and an intermodulation process that results in distortions at the fundamental.

The implications of the new understanding of phase distortion are many. Firstly, provided with a new view of nonlinear TWT physics, one may be led to consider alternative parametric dependencies and explanations for physical phenomenon. We have provided examples of such studies in Sections 5.3–5.5. Furthermore, the new understanding may possibly lead to improved TWT designs, since the notions that a designer has about how a device works inevitably influence how they proceed with a design.

Using the MUSE, S-MUSE, and LATTE TWT models we explore phase distortion in a TWT. The unique ability of the MUSE model to systematically suppress the effects of different frequencies in the nonlinear TWT behavior shows that the second harmonic distortion in the electron beam is the most dominant factor in causing phase distortion, at least prior to gain compression. Furthermore, we show that the average slowing down of electrons is not the primary cause of phase distortion using MUSE simulations and large signal LATTE simulations that were corrected to remove the average velocity reduction.

With the approximate analytic solution to the S-MUSE model we give an insightful picture of the fundamental frequency also being a self-intermodulation product. We show that prior to 1 dB gain compression the analytic solution accounting for the 3IM and 5IM contributions has a phase distortion that matches almost identically to the phase distortion from simulation of the S-MUSE equations. We also show that the change in voltage hot phase velocity which causes phase distortion is due to an evolving balance of the driven and intermodulation modes in the solution.

Leveraging off of our new understanding of phase distortion we consider several applications of the theory. First, we compare S-MUSE simulations to an amplitude-phase model that uses the approximate analytic solution to S-MUSE for the output phase versus input power. We see that there are discrepancies in the intermodulation spectra predicted by the two methods, and that the disagreement is worse for wider frequency spacings and for larger input powers. The study reinforces our view that the amplitude-phase model is an incomplete picture of nonlinear TWT physics, and that measuring single frequency phase distortion characteristics captures only a part of the harmonic and intermodulation physics happening internal to the TWT. Second, we study how phase distortion depends on circuit and electron beam parameters at the second harmonic. We find that circuit interaction impedance at the second harmonic has the greatest effect on AM/PM distortion, especially when the second harmonic is within the linear gain bandwidth of the TWT. Lastly, we consider a new technique of linearization [14] and offer a physical explanation for the linearization mechanism. In this case again we propose that phase distortion is not the proper way of looking at the linearization, and that a view of the intermodulation and difference frequency physics is required.

In Chapter 6 we study signal injection to shape TWT output spectra. Harmonic injection is used in ECM TWTs to extend usable device bandwidths. In such a setting extended bandwidths have implications in terms of cost savings, e.g., replacing two or three transmitters by one ultra-wideband transmitter, and improved functionality in small systems such as Unmanned Aerial Vehicles where only one transmitter is permitted. We show theoretically, and it has been shown experimentally, that harmonic and signal injection can be used to

reduce intermodulation spectrum. The incorporation of such ideas into TWT linearizer technologies will allow devices to be run closer to saturation. This could have a major impact on the TWT marketplace since it has been said that 1% increase in TWT amplifier efficiency can result in a savings of $\$100,000,000$ over the life of a satellite [50]. In this sense we are viewing our contribution to the understanding of harmonic and signal injection as "enabling theory" to achieve increased efficiencies and dollar savings.

We present an interpretation of harmonic injection, and more generally "signal injection," in a TWT as the cancellation of "driven" and "nonlinear" modes. The interpretations are based on an approximate analytic solution to an approximate nonlinear model. Furthermore, the insights provided by the analytic solutions suggest methods of inquiry into "large signal" simulations to test whether the modal solution structure is valid in saturated conditions. In general we find that the large signal simulations indeed show the abrupt phase change signature of the approximate analytic solutions.

The idea has existed for some time that the physical mechanism of harmonic injection is cancellation of such modes [55, 38]. However, we present the first quantitative theory to predict the existence of the modes. Furthermore, the quantitative theory provides insights into harmonic injection that the intuited notions could not. For example, a phasor picture provided by the theory demonstrates how multiple harmonic injection can eliminate the sensitive dependence of the output signals on the phase of the input signals. Also the analytic solutions elucidate the many effects of the injected signals being outside of the linear gain bandwidth of the TWT. Some experimentation is still required to verify all of the notions that we have put forward.

Appendix A: Normalization, attenuation, and slowly varying envelopes in MUSE, S-MUSE, and LATTE

In this appendix we introduce the terms necessary to model circuit loss in the starting model equations (2.10)–(2.14), and re-derive the models MUSE, S-MUSE, and LATTE from these equations. Simultaneously we introduce a variable normalization scheme that is desirable for computing solutions numerically. Lastly, to avoid dealing with reflections in TWTs with severs, we re-derive the models using a slowly varying envelope approximation. The model equations found in this appendix are those that are used in the code *LATTE/MUSE Numerical Suite*, or *lmsuite* [1].

To incorporate circuit loss into the models of Chapter 2, we modify starting equations (2.1), (2.2), and (2.4), and perform analogous derivations. For a transmission line with series inductance L, series resistance $\mathbf{R}$[1], shunt capacitance C, and shunt conductance G we have [15][2]

$$\frac{\partial V}{\partial z} = \mathbf{R}I + L\frac{\partial I}{\partial t} \tag{A.1}$$

$$\frac{\partial I}{\partial z} = GV + C\frac{\partial V}{\partial t}. \tag{A.2}$$

In general we assume that $L, \mathbf{R}, C$, and G are frequency dependent as well as functions of axial position z.[3] We proceed with writing the TWT models in terms of $L, \mathbf{R}, C$, and G, and provide relationships between these parameters and the more familiar parameters loss, phase velocity, and interaction impedance in Section A.2.

[1] We will use bold $\mathbf{R}$ to denote resistance as unbolded R is being used for space charge reduction factor.

[2] Equations (A.1) and (A.2) differ from (9-31) and (9-32) of [15] by a factor of -1 on the left hand side. We have chosen (A.1) and (A.2) to remain consistent with the model equations in Chapter 2.

[3] We have forgone the convolution notation found in equations (2.1), (2.2), and (2.4).

A.1 TWT models

Equations (2.10)–(2.14) with the loss terms added become (again forgoing the convolution notation)

$$\frac{\partial V}{\partial z} = \mathbf{R}I - \frac{\omega_0}{u_0}\frac{\partial V}{\partial \psi} - \omega_0 L\frac{\partial I}{\partial \psi} \tag{A.3}$$

$$\frac{\partial I}{\partial z} = GV - \omega_0 C\frac{\partial V}{\partial \psi} - \frac{\omega_0}{u_0}\frac{\partial I}{\partial \psi} + A\omega_0\frac{\partial \rho}{\partial \psi} \tag{A.4}$$

$$\frac{\partial E}{\partial z} = -\frac{\omega_0}{u_0}\frac{\partial E}{\partial \psi} + \frac{\rho}{\epsilon_0} \tag{A.5}$$

$$v\frac{\partial v}{\partial z} = \frac{e}{m_e}\left(\omega_0 L\frac{\partial I}{\partial \psi} - \mathbf{R}I\right) + \frac{e}{m_e}RE + \omega_0\left(1 - \frac{v}{u_0}\right)\frac{\partial v}{\partial \psi} \tag{A.6}$$

$$v\frac{\partial \rho}{\partial z} = \omega_0\left(1 - \frac{v}{u_0}\right)\frac{\partial \rho}{\partial \psi} - \rho\left(\frac{\partial v}{\partial z} + \frac{\omega_0}{u_0}\frac{\partial v}{\partial \psi}\right). \tag{A.7}$$

A.1.1 Normalization

For normalization we define the following characteristic quantities for the independent coordinates

$$Z = L \tag{A.8}$$

$$U = u_0 \tag{A.9}$$

$$T = \frac{Z}{U} \tag{A.10}$$

where L is the TWT circuit length, u_0 is the DC beam velocity, and hence T is a characteristic time. If we define normalized space and time variables

$$\hat{z} = \frac{z}{Z} \tag{A.11}$$

$$\hat{t} = \frac{t}{T} \tag{A.12}$$

this implies a normalized phase variable via (2.9)

$$\hat{\psi} = \frac{1}{\omega_0 T}\psi = (\hat{z} - \hat{t}). \tag{A.13}$$

Derivatives with respect to z and ψ then become

$$\frac{\partial}{\partial z} = \frac{1}{Z}\frac{\partial}{\partial \hat{z}} \tag{A.14}$$

$$\frac{\partial}{\partial \psi} = \frac{1}{\omega_0 T}\frac{\partial}{\partial \hat{\psi}}. \tag{A.15}$$

For dependent variables we define

$$D = \rho_0 \tag{A.16}$$

and choose the following normalizations

$$\hat{V} = \frac{\mathbf{C}}{KI_0}V \tag{A.17}$$

$$\hat{I} = \frac{\mathbf{C}}{I_0}I \tag{A.18}$$

$$\hat{E} = \frac{\epsilon_0}{ZD}E \tag{A.19}$$

$$\hat{v} = \frac{v}{U} \tag{A.20}$$

$$\hat{\rho} = \frac{\rho}{D} \tag{A.21}$$

where ρ_0 is the DC linear charge density, I_0 is the DC beam current ($I_0 = \rho_0 u_0 A$), V_0 is the DC beam voltage, and $\mathbf{C}$ is the Pierce gain parameter defined by[4]

$$\mathbf{C}^3 = \frac{KI_0}{4V_0}. \tag{A.22}$$

Since the parameters K and $\mathbf{C}$ are frequency dependent, the normalizations of V and I are frequency dependent. Furthermore, since K and $\mathbf{C}$ are spatially dependent we choose to normalize V and I with the values of K and $\mathbf{C}$ at the input of the TWT, $z = 0$. The normalizations for V and I in (A.17) and (A.18) follow historical choices (e.g. [56, 40]) and account for the frequency dependent TWT gain.

Substitution of (A.14), (A.15), and (A.17)–(A.21) into (A.3)–(A.7) result in the following set of normalized equations

$$\frac{\partial \hat{V}}{\partial \hat{z}} = \hat{\mathbf{R}}\hat{I} - \frac{\partial \hat{V}}{\partial \hat{\psi}} - \hat{L}\frac{\partial \hat{I}}{\partial \hat{\psi}} \tag{A.23}$$

$$\frac{\partial \hat{I}}{\partial \hat{z}} = \hat{G}\hat{V} - \hat{C}\frac{\partial \hat{V}}{\partial \hat{\psi}} - \frac{\partial \hat{I}}{\partial \hat{\psi}} + \mathbf{C}\frac{\partial \hat{\rho}}{\partial \hat{\psi}} \tag{A.24}$$

$$\frac{\partial \hat{E}}{\partial \hat{z}} = -\frac{\partial \hat{E}}{\partial \hat{\psi}} + \hat{\rho} \tag{A.25}$$

$$\hat{v}\frac{\partial \hat{v}}{\partial \hat{z}} = 2\mathbf{C}^2\left(\hat{L}\frac{\partial \hat{I}}{\partial \hat{\psi}} - \hat{\mathbf{R}}\hat{I}\right) + \hat{R}\hat{E} + (1-\hat{v})\frac{\partial \hat{v}}{\partial \hat{\psi}} \tag{A.26}$$

$$\hat{v}\frac{\partial \hat{\rho}}{\partial \hat{z}} = (1-\hat{v})\frac{\partial \hat{\rho}}{\partial \hat{\psi}} - \hat{\rho}\left(\frac{\partial \hat{v}}{\partial \hat{z}} + \frac{\partial \hat{v}}{\partial \hat{\psi}}\right) \tag{A.27}$$

[4]Bold faced $\mathbf{C}$ is used for the Pierce parameter to distinguish from capacitance C.

where we have defined the normalized quantities

$$\hat{\mathbf{R}} = \mathbf{R}\frac{Z}{K} \tag{A.28}$$

$$\hat{L} = L\frac{U}{K} \tag{A.29}$$

$$\hat{G} = G(ZK) \tag{A.30}$$

$$\hat{C} = C(UK) \tag{A.31}$$

$$\hat{R} = \frac{eDT^2}{m_e\epsilon_0}R = \omega_p^2 T^2 R \tag{A.32}$$

In the remainder of the appendix we omit the hat (ˆ) from normalized variables when one can deduce from the equations whether or not the variables are normalized [e.g. compare (A.3)–(A.7) to (A.23)–(A.27)].

A.1.2 MUSE

To derive MUSE we compute the Fourier coefficient formulas for (A.23)–(A.27). The Fourier series (2.15) in normalized variables is

$$\hat{x}(\hat{z},\hat{\psi}) = \sum_{\ell=-\infty}^{\infty} \hat{\tilde{x}}_\ell(\hat{z}) e^{if_\ell \hat{\omega}_0 \hat{\psi}}. \tag{A.33}$$

where

$$\hat{\omega}_0 = \omega_0 T. \tag{A.34}$$

The normalized fundamental frequency $\hat{\omega}_0$ is the result of the time scaling $\hat{t} = t/T$. From (A.33) one sees that $\frac{\partial}{\partial\hat{\psi}} \to if_\ell\hat{\omega}_0$. Quantities with tildes (˜) are considered to be in the frequency domain and have a frequency subscript ℓ, e.g., $\tilde{\mathbf{R}}(z, f_\ell\omega_0)$ will be written as $\tilde{\mathbf{R}}_\ell$.

The normalized MUSE model with circuit loss is

$$\frac{d\tilde{V}_\ell}{dz} = -if_\ell\omega_0\tilde{V}_\ell + \left(\tilde{\mathbf{R}}_\ell - if_\ell\omega_0\tilde{L}_\ell\right)\tilde{I}_\ell \tag{A.35}$$

$$\frac{d\tilde{I}_\ell}{dz} = \left(\tilde{G}_\ell - if_\ell\omega_0\tilde{C}_\ell\right)\tilde{V}_\ell - if_\ell\omega_0\tilde{I}_\ell + if_\ell\omega_0\tilde{\mathbf{C}}_\ell\tilde{\rho}_\ell \tag{A.36}$$

$$\frac{d\tilde{E}_\ell}{dz} = -if_\ell\omega_0\tilde{E}_\ell + \tilde{\rho}_\ell \tag{A.37}$$

$$\sum_{\substack{m,n\\ f_m+f_n=f_\ell}} \tilde{v}_m\frac{d\tilde{v}_n}{dz} = 2\tilde{\mathbf{C}}_\ell^2\left(if_\ell\omega_0\tilde{L}_\ell - \tilde{\mathbf{R}}_\ell\right)\tilde{I}_\ell + \tilde{R}_\ell\tilde{E}_\ell + if_\ell\omega_0\tilde{v}_\ell - \sum_{\substack{m,n\\ f_m+f_n=f_\ell}} if_n\omega_0\tilde{v}_m\tilde{v}_n \tag{A.38}$$

$$\sum_{\substack{m,n\\ f_m+f_n=f_\ell}} \tilde{v}_m\frac{d\tilde{\rho}_n}{dz} = if_\ell\omega_0\tilde{\rho}_\ell - if_\ell\omega_0\sum_{\substack{m,n\\ f_m+f_n=f_\ell}}\tilde{v}_m\tilde{\rho}_n - \sum_{\substack{m,n\\ f_m+f_n=f_\ell}}\frac{d\tilde{v}_m}{dz}\tilde{\rho}_n \tag{A.39}$$

where $-\infty \le \ell \le \infty$.

For computing solutions to MUSE we use the following vector form. Equations (A.35)–(A.37) are linear and can be represented by a linear system of the form $\dot{\mathbf{y}} = \mathbf{A}\mathbf{y}$.[5] Equations (A.38) and (A.39) are written as

$$\mathbf{V}\dot{\mathbf{w}} = \mathbf{M}\mathbf{w} + \mathbf{S}(\mathbf{w},\mathbf{w}) \tag{A.40}$$

so

$$\dot{\mathbf{w}} = \mathbf{V}^{-1}\mathbf{M}\mathbf{w} + \mathbf{V}^{-1}\mathbf{S}(\mathbf{w},\mathbf{w}). \tag{A.41}$$

We have

$$\mathbf{w} = \left[\mathbf{w}_{\tilde{v}}\ \mathbf{w}_{\tilde{\rho}}\right]^{\mathrm{T}} \tag{A.42}$$

and

$$\mathbf{w}_{\tilde{v}} = \left[\tilde{v}_{-M}\ \ldots\ \tilde{v}_{-2}\ \tilde{v}_{-1}\ \tilde{v}_0\ \tilde{v}_1\ \tilde{v}_2\ \ldots\ \tilde{v}_M\right]^{\mathrm{T}} \tag{A.43}$$

$$\mathbf{w}_{\tilde{\rho}} = \left[\tilde{\rho}_{-M}\ \ldots\ \tilde{\rho}_{-2}\ \tilde{\rho}_{-1}\ \tilde{\rho}_0\ \tilde{\rho}_1\ \tilde{\rho}_2\ \ldots\ \tilde{\rho}_M\right]^{\mathrm{T}}. \tag{A.44}$$

For purposes of indexing the vector $\mathbf{w}$ and the matrix $\mathbf{V}$ we note that $\mathbf{w}$ has $2(2M+1)$ elements. The entries $\tilde{v}_\ell$, $\ell = -M \ldots M$ correspond to entries $\mathbf{w}_\ell$, $\ell = 1 \ldots 2M+1$; the entries $\tilde{\rho}_\ell$, $\ell = -M \ldots M$ correspond to entries $\mathbf{w}_{\ell+3M+2}$, $\ell = 1 \ldots 2M+1$.

[5]The vector, matrix, and tensor notation used in this appendix does not match that used in Chapter 2.

The matrix $\mathbf{V}$ has the block structure

$$\mathbf{V} = \begin{bmatrix} \mathrm{I} & 0 \\ \mathrm{II} & \mathrm{III} \end{bmatrix} \tag{A.45}$$

where the blocks are of size $(2M+1) \times (2M+1)$. The indices of the blocks follow.

- Block I:

i^{th} row	j^{th} column	entry
$i = 1 \ldots 2M+1$	$j = 1 \ldots 2M+1$	let $\ell = i - M - 1$, $n = j - M - 1$, for m such that $f_n + f_m = f_\ell$: if $m > 0$ then $\tilde{v}_m$, if $m < 0$ then $\tilde{v}^*_{\lvert m \rvert}$, if $m = 0$ $(\ell = n)$ then $\tilde{v}_0$

- Block II:

$i + (2M+1)^{\text{th}}$ row	j^{th} column	entry
$i = 1 \ldots 2M+1$	$j = 1 \ldots 2M+1$	let $\ell = i - M - 1$, $n = j - M - 1$, for m such that $f_n + f_m = f_\ell$: if $m > 0$ then $\tilde{\rho}_m$, if $m < 0$ then $\tilde{\rho}^*_{\lvert m \rvert}$, if $m = 0$ $(\ell = n)$ then $\tilde{\rho}_0$

- Block III:

$i + (2M+1)^{\text{th}}$ row	$j + (2M+1)^{\text{th}}$ column	entry
$i = 1 \ldots 2M+1$	$j = 1 \ldots 2M+1$	let $\ell = i - M - 1$, $n = j - M - 1$, for m such that $f_n + f_m = f_\ell$: if $m > 0$ then $\tilde{v}_m$, if $m < 0$ then $\tilde{v}^*_{\lvert m \rvert}$, if $m = 0$ $(\ell = n)$ then $\tilde{v}_0$.

In the coding of MUSE (as found in *lmsuite*) the linear and nonlinear terms on the right hand side of (A.40) are formed explicitly rather than via the matrix $\mathbf{M}$ and tensor $\mathbf{S}$. Therefore in this appendix we do not define the elements of $\mathbf{M}$ and $\mathbf{S}$.

A.1.3 S-MUSE

The S-MUSE model is derived similarly to Section 2.2.3. The assumptions accounting for normalizations are:

1. approximating $\tilde{\rho}_0(z)$ and $\tilde{v}_0(z)$ as equal to 1
2. neglecting the AC portion of velocity *in the convective* derivative, i.e., letting $\hat{v}\frac{\partial}{\partial \hat{z}} \approx \frac{\partial}{\partial \hat{z}}$
3. ignoring nonlinearities higher than second order in the continuity equation.

The normalized S-MUSE model with circuit loss is

$$\frac{d\tilde{V}_\ell}{dz} = -if_\ell\omega_0\tilde{V}_\ell + \left(\tilde{\mathbf{R}}_\ell - if_\ell\omega_0\tilde{L}_\ell\right)\tilde{I}_\ell \tag{A.46}$$

$$\frac{d\tilde{I}_\ell}{dz} = \left(\tilde{G}_\ell - if_\ell\omega_0\tilde{C}_\ell\right)\tilde{V}_\ell - if_\ell\omega_0\tilde{I}_\ell + if_\ell\omega_0\tilde{\mathbf{C}}_\ell\tilde{\rho}_\ell \tag{A.47}$$

$$\frac{d\tilde{E}_\ell}{dz} = -if_\ell\omega_0\tilde{E}_\ell + \tilde{\rho}_\ell \tag{A.48}$$

$$\frac{d\tilde{v}_\ell}{dz} = 2\tilde{\mathbf{C}}_\ell^2\left(if_\ell\omega_0\tilde{L}_\ell - \tilde{\mathbf{R}}_\ell\right)\tilde{I}_\ell + \tilde{R}_\ell\tilde{E}_\ell - \sum_{\substack{m\neq 0, n\neq 0\\ f_m+f_n=f_\ell}} if_n\omega_0\tilde{v}_m\tilde{v}_n \tag{A.49}$$

$$\begin{aligned}\frac{d\tilde{\rho}_\ell}{dz} &= 2\tilde{\mathbf{C}}_\ell^2\left(\tilde{\mathbf{R}}_\ell - if_\ell\omega_0\tilde{L}_\ell\right)\tilde{I}_\ell - \tilde{R}_\ell\tilde{E}_\ell - if_\ell\omega_0\tilde{v}_\ell \\ &\quad + 2\sum_{\substack{m\neq 0, n\neq 0\\ f_m+f_n=f_\ell}} \tilde{\mathbf{C}}_m^2\left(\tilde{\mathbf{R}}_m - if_m\omega_0\tilde{L}_m\right)\tilde{I}_m\tilde{\rho}_n - \sum_{\substack{m\neq 0, n\neq 0\\ f_m+f_n=f_\ell}} \tilde{R}_m\tilde{E}_m\tilde{\rho}_n \\ &\quad + \sum_{\substack{m\neq 0, n\neq 0\\ f_m+f_n=f_\ell}} if_n\omega_0\tilde{v}_m\tilde{v}_n - if_\ell\omega_0\sum_{\substack{m\neq 0, n\neq 0\\ f_m+f_n=f_\ell}} \tilde{v}_m\tilde{\rho}_n\end{aligned} \tag{A.50}$$

where $-\infty \leq \ell \leq \infty, \ell \neq 0$.

A.1.4 LATTE

This derivation follows closely Section 2.2.2 differing in that the starting equations are the normalized equations (A.23)–(A.27). We define the transformation

$$\begin{bmatrix} \hat{z} \\ \hat{\psi} \end{bmatrix} = \begin{bmatrix} \hat{Z}(\hat{z}, \hat{\psi}_0) \\ \hat{\Psi}(\hat{z}, \hat{\psi}_0) \end{bmatrix} \tag{A.51}$$

with

$$\hat{Z}(\hat{z}, \hat{\psi}_0) = \hat{z}. \tag{A.52}$$

The linearization of coordinate transformation (A.51) is the matrix

$$\begin{bmatrix} 1 & 0 \\ \frac{\partial\hat{\Psi}}{\partial\hat{z}} & \frac{\partial\hat{\Psi}}{\partial\hat{\psi}_0} \end{bmatrix} \tag{A.53}$$

and its Jacobian $\hat{J}$ is the determinant of (A.53)

$$\hat{J} = \frac{\partial\hat{\Psi}}{\partial\hat{\psi}_0}. \tag{A.54}$$

Partial derivatives transform via

$$\left[\begin{array}{cc} \frac{\partial}{\partial \hat{z}} & \frac{\partial}{\partial \hat{\psi}} \end{array} \right] = \left[\begin{array}{cc} \frac{\partial}{\partial \hat{z}} & \frac{\partial}{\partial \hat{\psi}_0} \end{array} \right] \left[\begin{array}{cc} 1 & 0 \\ \frac{\partial \hat{\Psi}}{\partial \hat{z}} & \frac{\partial \hat{\Psi}}{\partial \hat{\psi}_0} \end{array} \right]^{-1}. \tag{A.55}$$

Consistent with the method of characteristics we take

$$\frac{\partial \hat{\Psi}}{\partial \hat{z}} = 1 - \frac{1}{v^{\hat{\mathrm{L}}}} \tag{A.56}$$

then the convective derivative [in $(\hat{z}, \hat{\psi})$ coordinates] becomes

$$v^{\hat{\mathrm{E}}} \frac{\partial v^{\hat{\mathrm{E}}}}{\partial \hat{z}} + \left(v^{\hat{\mathrm{E}}} - 1 \right) \frac{\partial v^{\hat{\mathrm{E}}}}{\partial \hat{\psi}} = v^{\hat{\mathrm{L}}} \frac{\partial v^{\hat{\mathrm{L}}}}{\partial \hat{z}} \tag{A.57}$$

where a superscript E refers to a function in Eulerian coordinates and a superscript L refers to a function in Lagrangian coordinates.

Applying the derivative transformations in (A.55) to the continuity equation (A.27) one gets

$$\frac{\partial \hat{\Psi}}{\partial \hat{\psi}_0} \frac{\partial \rho^{\hat{\mathrm{L}}} v^{\hat{\mathrm{L}}}}{\partial \hat{z}} = -\frac{\rho^{\hat{\mathrm{L}}}}{v^{\hat{\mathrm{L}}}} \frac{\partial v^{\hat{\mathrm{L}}}}{\partial \hat{\psi}_0}. \tag{A.58}$$

Taking $\frac{\partial}{\partial \hat{\psi}_0}$ of (A.56) one gets

$$\frac{\partial}{\partial \hat{z}} \frac{\partial \hat{\Psi}}{\partial \hat{\psi}_0} = \frac{1}{(v^{\hat{\mathrm{L}}})^2} \frac{\partial v^{\hat{\mathrm{L}}}}{\partial \hat{\psi}_0}. \tag{A.59}$$

Substitute (A.59) into (A.58) and integrate to get

$$\left| \frac{\partial \hat{\Psi}}{\partial \hat{\psi}_0} \right| \rho^{\hat{\mathrm{L}}} v^{\hat{\mathrm{L}}} = \kappa \tag{A.60}$$

where κ is a constant of integration. We set κ by using the values of $\rho^{\hat{\mathrm{L}}} v^{\hat{\mathrm{L}}}$ and $\frac{\partial \hat{\Psi}}{\partial \hat{\psi}_0}$ on the $\hat{\psi}_0$ axis [by definition $\hat{\Psi}(0, \hat{\psi}_0) = \hat{\psi}_0$ which implies $\frac{\partial \hat{\Psi}}{\partial \hat{\psi}_0}(0, \hat{\psi}_0) = 1$] which gives finally

$$\left| \frac{\partial \hat{\Psi}}{\partial \hat{\psi}_0} \right| \rho^{\hat{\mathrm{L}}} v^{\hat{\mathrm{L}}} = \rho^{\hat{\mathrm{L}}}(0, \hat{\psi}_0) v^{\hat{\mathrm{L}}}(0, \hat{\psi}_0) \tag{A.61}$$

$$= \frac{I_0(\hat{\psi}_0)}{I_0}. \tag{A.62}$$

If there is a modulated beam current $I_0(\hat{\psi}_0)$ the constant I_0 is chosen to be the DC component for example. For no beam modulation the right hand side of (A.62) is equal to one.

The change of variable equation for the Fourier coefficient integral is (having changed from ψ to $\hat{\psi}$ which accounts for a factor of $\hat{\omega}_0$ in several places)

$$\tilde{\hat{\rho}}_\ell^E = \frac{\hat{\omega}_0}{2\pi}\int_{\frac{2\pi}{\hat{\omega}_0}} \hat{\rho}^{\mathrm{E}} e^{-if_\ell\hat{\omega}_0\hat{\psi}}\, d\hat{\psi} \tag{A.63}$$

$$= \frac{\hat{\omega}_0}{2\pi}\int_{\frac{2\pi}{\hat{\omega}_0}} \hat{\rho}^{\mathrm{L}} \left|\frac{\partial\hat{\Psi}}{\partial\hat{\psi}_0}\right| e^{-if_\ell\hat{\omega}_0\hat{\Psi}(\hat{z},\hat{\psi}_0)} d\hat{\psi}_0 \tag{A.64}$$

$$= \frac{\hat{\omega}_0}{2\pi}\int_{\frac{2\pi}{\hat{\omega}_0}} \frac{I_0(\hat{\psi}_0)e^{-if_\ell\hat{\omega}_0\hat{\Psi}(\hat{z},\hat{\psi}_0)}}{I_0\hat{v^{\mathrm{L}}}(\hat{z},\hat{\psi}_0)}\, d\hat{\psi}_0 \tag{A.65}$$

where we have used (A.62) to substitute for the Jacobian.

Finally we derive LATTE from (A.23)–(A.27). Equations (A.66)–(A.68) are (A.35)–(A.37) with (A.65) substituted for $\tilde{\rho}_\ell$. Equation (A.27) was used to get (A.65). For (A.26) one writes E and I using a normalized Fourier series synthesis equation in Lagrangian coordinates and gets (A.69). Equation (A.56) is also included as model equation (A.70). The circuit equations, space charge equation, Newton's law, and phase relation are [leaving off the superscript L and normalization hats (ˆ)]

$$\frac{d\tilde{V}_\ell}{dz} = -if_\ell\omega_0\tilde{V}_\ell + \left(\tilde{\mathbf{R}}_\ell - if_\ell\omega_0\tilde{L}_\ell\right)\tilde{I}_\ell \tag{A.66}$$

$$\frac{d\tilde{I}_\ell}{dz} = \left(\tilde{G}_\ell - if_\ell\omega_0\tilde{C}_\ell\right)\tilde{V}_\ell - if_\ell\omega_0\tilde{I}_\ell + if_\ell\omega_0\tilde{\mathbf{C}}_\ell\frac{\omega_0}{2\pi}\int_{\frac{2\pi}{\omega_0}} \frac{I_0(\psi_0)e^{-if_\ell\omega_0\Psi(z,\psi_0)}}{I_0 v(z,\psi_0)} d\psi_0 \tag{A.67}$$

$$\frac{d\tilde{E}_\ell}{dz} = -if_\ell\omega_0\tilde{E}_\ell + \frac{\omega_0}{2\pi}\int_{\frac{2\pi}{\omega_0}} \frac{I_0(\psi_0)e^{-if_\ell\omega_0\Psi(z,\psi_0)}}{I_0 v(z,\psi_0)} d\psi_0 \tag{A.68}$$

$$\frac{\partial v}{\partial z} = \frac{1}{v}\sum_{\ell=-\infty}^{\infty}\left\{2\tilde{\mathbf{C}}_\ell^2\left(if_\ell\omega_0\tilde{L}_\ell - \tilde{\mathbf{R}}_\ell\right)\tilde{I}_\ell + \tilde{R}_\ell\tilde{E}_\ell\right\} e^{if_\ell\omega_0\Psi(z,\psi_0)} \tag{A.69}$$

$$\frac{\partial\Psi}{\partial z} = 1 - \frac{1}{v}. \tag{A.70}$$

As discussed in Section 2.2.2 for numerical implementation the integrals become sums over disk phases, and the factor in front of the Fourier integral transforms to one over the number of disk phases. Notice however that where the unnormalized initial disk phases ψ_0 were distributed over 2π, the normalized initial disk phases $\hat{\psi}_0$ are distributed over $\frac{2\pi}{\hat{\omega}_0}$.[6]

[6]This only applies to a beam with initially uniform density. For a modulated current that is comprised of a density and velocity modulation, one would have to compute the corresponding initial phase distribution.

A.2 Relation of $L, \mathbf{R}, C$, and G to $v_{\rm ph}, K$, and α.

In this section we develop relationships between unnormalized model circuit parameters $L, \mathbf{R}, C$, and G and commonly supplied cold TWT parameters phase velocity, interaction impedance, and loss. It is important to note that the relations developed in this section only strictly apply to a transmission line circuit with *uniform* parameters and *no electron beam, i.e., a cold circuit*. An analogous theory for a *non-uniform* cold circuit based on the present theory is not thought to exist, since the present analysis is based on *autonomous* linear system theory [18], and with non-uniform parameters the system becomes non-autonomous. Therefore, the following equations are to be considered approximations. In this section quantities with a tilde ($\tilde{}$) depend on frequency and axial distance z; frequency and distance notation will be suppressed.

Equations (A.1) and (A.2) in (z, ψ) coordinates [see (2.9)] are

$$\frac{\partial V}{\partial z} = \mathbf{R}I - \frac{\omega_0}{u_0}\frac{\partial V}{\partial \psi} - \omega_0 L \frac{\partial I}{\partial \psi} \tag{A.71}$$

$$\frac{\partial I}{\partial z} = GV - \frac{\omega_0}{u_0}\frac{\partial I}{\partial \psi} - \omega_0 C \frac{\partial V}{\partial \psi}. \tag{A.72}$$

Using the frequency domain relations

$$V = \tilde{V} e^{i f_\ell \psi} \tag{A.73}$$

$$I = \tilde{I} e^{i f_\ell \psi} \tag{A.74}$$

in (A.71) and (A.72) and letting $f_\ell \omega_0 = \omega$ one gets the ordinary differential equations

$$\frac{d}{dz}\begin{bmatrix} \tilde{V} \\ \tilde{I} \end{bmatrix} = \begin{bmatrix} -i\frac{\omega}{u_0} & \tilde{\mathbf{R}} - i\omega\tilde{L} \\ \tilde{G} - i\omega\tilde{C} & -i\frac{\omega}{u_0} \end{bmatrix} \begin{bmatrix} \tilde{V} \\ \tilde{I} \end{bmatrix}. \tag{A.75}$$

The eigenvalues of the matrix in (A.75) give the "propagation constants." The eigenvalues $\gamma^\pm$ are given by

$$\gamma^+ = -i\frac{\omega}{u_0} + \sqrt{\left(\tilde{\mathbf{R}} - i\omega\tilde{L}\right)\left(\tilde{G} - i\omega\tilde{C}\right)} \tag{A.76}$$

$$\gamma^- = -i\frac{\omega}{u_0} - \sqrt{\left(\tilde{\mathbf{R}} - i\omega\tilde{L}\right)\left(\tilde{G} - i\omega\tilde{C}\right)} \tag{A.77}$$

where γ^+ corresponds to a "forward wave."

To find the interaction impedance we assume a forward voltage wave of the form $V_0^+ e^{\gamma^+ z}$ and a forward current wave of the form $I_0^+ e^{\gamma^+ z}$ and compute their relation via (A.75). One finds that

$$\tilde{Z} = \sqrt{\frac{\tilde{\mathbf{R}} - i\omega\tilde{L}}{\tilde{G} - i\omega\tilde{C}}}. \tag{A.78}$$

We will relate the impedance $\tilde{Z}$ to the impedance $\tilde{K}$ shortly.

Lastly we would like to compute $\tilde{L}, \tilde{\mathbf{R}}, \tilde{C}$, and $\tilde{G}$ in terms of supplied parameters $\tilde{v}_{\rm ph}, \tilde{K}$, and $\tilde{\alpha}$ where $\tilde{\alpha}$ is loss in Np/m. Although $\tilde{K}$ is usually defined as a real quantity (e.g. [16, Eq. (46)]) we allow for it to be complex as does Pierce [61, pp. 110–111]. To return to (z,t) coordinates from (z,ψ) coordinates one forms the quantity $e^{\gamma^+ z}e^{if_\ell \psi}$ and inserts the definition of ψ from (2.9). Looking at the argument of this expression one can identify the propagation constant $\sqrt{\left(\tilde{\mathbf{R}} - i\omega\tilde{L}\right)\left(\tilde{G} - i\omega\tilde{C}\right)}$. One can check that due to the choice of $e^{-i\omega t}$ (implicit in the definition of ψ) rather than $e^{i\omega t}$, the interaction impedance and propagation constant in the present theory are conjugates of the conventional definitions [15]. We assume that the *conventional* propagation constant $\gamma = \alpha + i\beta$ is given where $\alpha = \tilde{\alpha}$ and $\beta = \frac{\omega}{\tilde{v}_{\rm ph}}$. If we let

$$\mathbf{X} = \tilde{\mathbf{R}} - i\omega\tilde{L} \tag{A.79}$$
$$\mathbf{Y} = \tilde{G} - i\omega\tilde{C} \tag{A.80}$$

then one has

$$\gamma^* = \sqrt{\mathbf{XY}} \tag{A.81}$$
$$\tilde{Z} = \tilde{K}^* \tag{A.82}$$
$$= \sqrt{\frac{\mathbf{X}}{\mathbf{Y}}} \tag{A.83}$$

or

$$\mathbf{X} = \gamma^*\tilde{K}^* \tag{A.84}$$
$$\mathbf{Y} = \frac{\gamma^*}{\tilde{K}^*}. \tag{A.85}$$

Finally the quantities we desire in terms of given data are

$$\tilde{\mathbf{R}} = \mathrm{Re}\left\{\gamma^*\tilde{K}^*\right\} \tag{A.86}$$
$$\tilde{L} = -\frac{1}{\omega}\mathrm{Im}\left\{\gamma^*\tilde{K}^*\right\} \tag{A.87}$$
$$\tilde{G} = \mathrm{Re}\left\{\frac{\gamma^*}{\tilde{K}^*}\right\} \tag{A.88}$$
$$\tilde{C} = -\frac{1}{\omega}\mathrm{Im}\left\{\frac{\gamma^*}{\tilde{K}^*}\right\}. \tag{A.89}$$

A.3 Slowly varying envelope models

The models of Sections A.1.2, A.1.3, and A.1.4 implicitly include backward waves since there are two circuit wave equations, one for voltage and one for current. When a sever is

included in the TWT circuit, the presence of the backward wave can complicate computations since small values of the backward wave at the input correspond to large values of the backward wave at the output (for no backward wave interaction). In cases when the total sever loss is larger than the forward gain, the backward wave can become larger than the forward wave at the TWT output. In principle one can choose the phasing of the input voltage and current such that the backward wave is minimized resulting in only the desired forward wave solution. However, since the proper phasing is not known a priori, an iterative numerical method is required to find the desired phase relation. An example of a method one might use is a "shooting method" [63, Ch. 17].

Unfortunately, shooting can become very computationally expensive for large numbers of input frequencies. Each "shooting iteration" amounts to integrating the differential equations a certain number of times using "guesses" for what the unknown inputs should be, and subsequently modifying those guesses so that the outputs tend towards the desired output boundary conditions (e.g. no reflections on the output end). More specifically for N unknown input parameters the differential equations must be integrated $N+1$ times per shooting iteration. If one had 100 input frequencies with nonzero inputs for which the forward wave solutions were desired, and for example it took ten shooting iterations to converge to the desired solution, one would need to solve the differential equations roughly 1000 times! Even at several minutes per integration the computational times become prohibitive.

As an alternative to solving the equations with shooting, we develop yet another set of model equations that do not include a backward wave. We use the "slowly varying envelope" approximation which assumes that for a function $A(z,t)$ of the form

$$A(z,t) \;=\; a(z)e^{i(\omega t-\beta z)} \tag{A.90}$$

one has

$$\left|\frac{da}{dz}\right| \;\ll\; |\beta a|\,. \tag{A.91}$$

That is, the envelope $a(z)$ changes on a length scale which is much less than the wavelength of the perturbation. The following inequality for the rate of change of the growth rate

$$\left|\frac{d^2a}{dz^2}\right| \;\ll\; \left|\beta^2 a\right| \tag{A.92}$$

is also often used when making the slowly varying envelope approximation. The use of these inequalities eliminates the backward wave while having only a minor affect on the linear growth rates and predicted amplitudes of the resulting models.

To proceed with the modeling we start with the circuit equations

$$\frac{\partial V}{\partial z} \;=\; \mathbf{R}I + L\frac{\partial I}{\partial t} \tag{A.93}$$

$$\frac{\partial I}{\partial z} \;=\; GV + C\frac{\partial V}{\partial t} - A\frac{\partial \rho}{\partial t}. \tag{A.94}$$

Taking $\frac{\partial}{\partial z}$ of (A.93) and $\frac{\partial}{\partial t}$ of (A.94) gives

$$\frac{\partial^2 V}{\partial z^2} = \frac{d\mathbf{R}}{dz} I + \frac{dL}{dz}\frac{\partial I}{\partial t} + \mathbf{R}GV + \mathbf{R}C\frac{\partial V}{\partial t} - \mathbf{R}A\frac{\partial \rho}{\partial t} + L\frac{\partial^2 I}{\partial z \partial t} \tag{A.95}$$

$$\frac{\partial^2 I}{\partial z \partial t} = G\frac{\partial V}{\partial t} + C\frac{\partial^2 V}{\partial t^2} - A\frac{\partial^2 \rho}{\partial t^2}. \tag{A.96}$$

We combine (A.95) and (A.96) to get

$$\begin{aligned}\frac{\partial^2 V}{\partial z^2} = {} & \frac{d\mathbf{R}}{dz} I + \frac{dL}{dz}\frac{\partial I}{\partial t} \\ & + \mathbf{R}GV + (\mathbf{R}C + GL)\frac{\partial V}{\partial t} + LC\frac{\partial^2 V}{\partial t^2} \\ & - \mathbf{R}A\frac{\partial \rho}{\partial t} - LA\frac{\partial^2 \rho}{\partial t^2}.\end{aligned} \tag{A.97}$$

The appearance of I in (A.97) is a complication that has to be dealt with [67, pg. 66][7]. In portions of the TWT with uniform parameters the terms involving I are zero. However, the terms are nonzero when parameters are changing, such as in a sever region. As a first approximation we simply ignore the terms. As a next order approximation one could let $I = -\frac{V}{K}$.

We assume a solution structure of the form

$$A(z,t) = \tilde{A}_\ell(z) e^{i(\beta_{c\ell} z - f_\ell \omega_0 t)} \tag{A.98}$$

$$= \tilde{A}_\ell(z) e^{i\Delta\beta_\ell z} e^{i f_\ell(\beta_{e0} z - \omega_0 t)} \tag{A.99}$$

where

$$\beta_{c\ell} = \frac{f_\ell \omega_0}{\tilde{v}_{\mathrm{ph}\ell}} \tag{A.100}$$

$$\beta_{e0} = \frac{\omega_0}{u_0} \tag{A.101}$$

$$\Delta\beta_\ell = \beta_{c\ell} - f_\ell \beta_{e0}. \tag{A.102}$$

The relationship to the phase factor $e^{i f_\ell(\beta_{e0} z - \omega_0 t)}$ via $\Delta\beta_\ell$ is given so that we can connect the electron beam equations in this description to those of the previous description. Using the

[7] While Rowe discusses this complication, the setting is slightly different in that he does not use a conductance in his circuit equations.

definitions we have

$$\frac{\partial A}{\partial t} = -if_\ell\omega_0\tilde{A}_\ell e^{i(\beta_{c\ell}z-f_\ell\omega_0 t)} \tag{A.103}$$

$$\frac{\partial^2 A}{\partial t^2} = -(f_\ell\omega_0)^2\tilde{A}_\ell e^{i(\beta_{c\ell}z-f_\ell\omega_0 t)} \tag{A.104}$$

$$\frac{\partial A}{\partial z} = \left(\frac{d\tilde{A}_\ell}{dz}+i\beta_{c\ell}\tilde{A}_\ell\right)e^{i(\beta_{c\ell}z-f_\ell\omega_0 t)} \tag{A.105}$$

$$\frac{\partial^2 A}{\partial z^2} = \left(\frac{d^2\tilde{A}_\ell}{dz^2}+i2\beta_{c\ell}\frac{d\tilde{A}_\ell}{dz}-\beta_{c\ell}^2\tilde{A}_\ell\right)e^{i(\beta_{c\ell}z-f_\ell\omega_0 t)}. \tag{A.106}$$

Substituting these derivatives into (A.97) one gets

$$\begin{aligned}\frac{d^2\tilde{V}_\ell}{dz^2}+i2\beta_{c\ell}\frac{d\tilde{V}_\ell}{dz} = \\ \left[\tilde{\mathbf{R}}_\ell\tilde{G}_\ell-if_\ell\omega_0\left(\tilde{\mathbf{R}}_\ell\tilde{C}_\ell+\tilde{G}_\ell\tilde{L}_\ell\right)+\beta_{c\ell}^2-(f_\ell\omega_0)^2\tilde{L}_\ell\tilde{C}_\ell\right]\tilde{V}_\ell \\ +\left[if_\ell\omega_0\tilde{\mathbf{R}}_\ell A+(f_\ell\omega_0)^2\tilde{L}_\ell A\right]\tilde{\rho}_\ell.\end{aligned} \tag{A.107}$$

Making the slowly varying envelope approximation (A.107) becomes

$$\begin{aligned}\frac{d\tilde{V}_\ell}{dz} = \\ -\frac{i}{2f_\ell\omega_0}\tilde{v}_{\mathrm{ph}\ell}\left[\tilde{\mathbf{R}}_\ell\tilde{G}_\ell-if_\ell\omega_0\left(\tilde{\mathbf{R}}_\ell\tilde{C}_\ell+\tilde{G}_\ell\tilde{L}_\ell\right)+\left(\frac{f_\ell\omega_0}{\tilde{v}_{\mathrm{ph}\ell}}\right)^2-(f_\ell\omega_0)^2\tilde{L}_\ell\tilde{C}_\ell\right]\tilde{V}_\ell \\ -\frac{i}{2f_\ell\omega_0}\tilde{v}_{\mathrm{ph}\ell}\left[if_\ell\omega_0\tilde{\mathbf{R}}_\ell A+(f_\ell\omega_0)^2\tilde{L}_\ell A\right]\tilde{\rho}_\ell.\end{aligned} \tag{A.108}$$

To normalize (A.108) we use

$$\frac{d}{dz} = \frac{1}{Z}\frac{d}{d\hat{z}} \tag{A.109}$$

and

$$\tilde{V}_\ell = \frac{\tilde{K}_\ell I_0}{\tilde{\mathbf{C}}_\ell}\hat{\tilde{V}}_\ell \tag{A.110}$$

$$\tilde{\rho}_\ell = D\hat{\tilde{\rho}}_\ell. \tag{A.111}$$

The expression for cold circuit phase velocity is

$$\tilde{v}_{\mathrm{ph}\ell} = \frac{f_\ell\omega_0}{\mathrm{Im}\left\{\sqrt{\left(\tilde{\mathbf{R}}_\ell-if_\ell\omega_0\tilde{L}_\ell\right)\left(\tilde{G}_\ell-if_\ell\omega_0\tilde{C}_\ell\right)}\right\}}. \tag{A.112}$$

Substituting normalized variables gives

$$\frac{\tilde{v}_{\mathrm{ph}\ell}}{U} = \frac{f_\ell \hat{\omega}_0}{\mathrm{Im}\left\{\sqrt{\left(\hat{\tilde{\mathbf{R}}}_\ell - i f_\ell \hat{\omega}_0 \hat{\tilde{L}}_\ell\right)\left(\hat{\tilde{G}}_\ell - i f_\ell \hat{\omega}_0 \hat{\tilde{C}}_\ell\right)}\right\}}. \tag{A.113}$$

Thus we define the normalized phase velocity to be $\hat{\tilde{v}}_{\mathrm{ph}\ell} = \tilde{v}_{\mathrm{ph}\ell}/U$ and compute it from the normalized circuit parameters using (A.113).

Equation (A.108) becomes [leaving hats (ˆ) off normalized quantities, including $\hat{\omega}_0 = \omega_0 T$]

$$\begin{aligned}\frac{d\tilde{V}_\ell}{dz} &= \frac{\tilde{v}_{\mathrm{ph}\ell}}{2}\left[i f_\ell \omega_0 \left(\tilde{L}_\ell \tilde{C}_\ell - \frac{1}{\tilde{v}_{\mathrm{ph}\ell}^2}\right) - i\frac{\tilde{\mathbf{R}}_\ell \tilde{G}_\ell}{f_\ell \omega_0} - \left(\tilde{\mathbf{R}}_\ell \tilde{C}_\ell + \tilde{G}_\ell \tilde{L}_\ell\right)\right]\tilde{V}_\ell \\ &\quad + \frac{\tilde{v}_{\mathrm{ph}\ell}}{2}\left[\tilde{\mathbf{R}}_\ell - i f_\ell \omega_0 \tilde{L}_\ell\right]\tilde{\mathbf{C}}_\ell \tilde{\rho}_\ell. \end{aligned} \tag{A.114}$$

The Fourier coefficients of ρ need to be related to those used in previous formulations so that minimal changes may be made to previous electron beam equations. We relate the present case to previous cases in the following steps

$$\tilde{\rho}_{c\ell} = \frac{\omega_0}{2\pi}\int_0^{\frac{2\pi}{\omega_0}} \rho e^{-i(\beta_{c\ell} - f_\ell \omega_0 t)}\, dt \tag{A.115}$$

$$= \frac{\omega_0}{2\pi}\int_0^{\frac{2\pi}{\omega_0}} \rho e^{i(\beta_e - \beta_{c\ell})z} e^{-i f_\ell \omega_0 (\frac{z}{u_0} - t)}\, dt \tag{A.116}$$

$$= e^{-i\Delta\beta_\ell z}\tilde{\rho}_{b\ell} \tag{A.117}$$

where the c and b subscripts on $\tilde{\rho}_{c\ell}$ and $\tilde{\rho}_{b\ell}$ represent "circuit" and "beam" respectively. Equation (A.114) implicitly uses $\tilde{\rho}_{c\ell}$ where previous formulations use $\tilde{\rho}_{b\ell}$. In normalized variables (A.117) becomes

$$\hat{\tilde{\rho}}_{c\ell} = e^{i f_\ell \hat{\omega}_0 \left(1 - \frac{1}{\tilde{v}_{\mathrm{ph}\ell}}\right) z}\hat{\tilde{\rho}}_{b\ell} \tag{A.118}$$

$$= \tilde{Z}_\ell(z)\hat{\tilde{\rho}}_{b\ell} \tag{A.119}$$

where we have defined the phase factor $\tilde{Z}_\ell(z)$

$$\tilde{Z}_\ell(z) = e^{i f_\ell \hat{\omega}_0 \left(1 - \frac{1}{\tilde{v}_{\mathrm{ph}\ell}}\right) z}. \tag{A.120}$$

In Newton's equation we will need the circuit field

$$\frac{\partial V}{\partial z} = \sum_{\ell=-\infty}^{\infty}\left(\frac{d\tilde{V}_\ell}{dz} + i\beta_{c\ell}\tilde{V}_\ell\right)e^{i(\beta_{c\ell} z - f_\ell \omega_0 t)}. \tag{A.121}$$

Using the slowly varying envelope approximation we can ignore the $\frac{d\tilde{V}_\ell}{dz}$ term in (A.121). Alternatively this term may be kept to establish the extent to which this portion of the approximation affects results. Again we relate this expression to the previous formulation via the phase factor $\tilde{Z}_\ell(z)$

$$\frac{\partial V}{\partial z} = \sum_{\ell=-\infty}^{\infty} \left(\frac{d\tilde{V}_\ell}{dz} + i\frac{f_\ell \omega_0}{\tilde{v}_{\mathrm{ph}\ell}} \tilde{V}_\ell \right) \tilde{Z}_\ell^*(z) e^{if_\ell \psi}. \tag{A.122}$$

Note that the phase information contained in the complex Fourier amplitudes of the voltage is with respect to the cold circuit wave for this slowly varying envelope formulation. In contrast, the phase information in the complex Fourier amplitudes of the space charge field is with respect to the frequency dependent stream wave, i.e., the wave with the complex phase factor $e^{if_\ell \omega_0 (z/u_0 - t)}$. This must be considered when one interprets results or reconstructs waveforms. The following model equations are solved in the code *lmsuite* when the input variable `svea` is set equal to `true`.

A.3.1 MUSE

The MUSE model using the slowly varying envelope approximation becomes

$$\begin{aligned}
\frac{d\tilde{V}_\ell}{dz} &= \frac{\tilde{v}_{\mathrm{ph}\ell}}{2} \left[if_\ell \omega_0 \left(\tilde{L}_\ell \tilde{C}_\ell - \frac{1}{\tilde{v}_{\mathrm{ph}\ell}^2} \right) - i\frac{\tilde{\mathbf{R}}_\ell \tilde{G}_\ell}{f_\ell \omega_0} - \left(\tilde{\mathbf{R}}_\ell \tilde{C}_\ell + \tilde{G}_\ell \tilde{L}_\ell \right) \right] \tilde{V}_\ell \\
&\quad + \frac{\tilde{v}_{\mathrm{ph}\ell}}{2} \left[\tilde{\mathbf{R}}_\ell - if_\ell \omega_0 \tilde{L}_\ell \right] \tilde{\mathbf{C}}_\ell \tilde{Z}_\ell(z) \tilde{\rho}_\ell \qquad \text{(A.123)} \\
\frac{d\tilde{E}_\ell}{dz} &= -if_\ell \omega_0 \tilde{E}_\ell + \tilde{\rho}_\ell \qquad \text{(A.124)} \\
\sum_{\substack{m,n \\ f_m + f_n = f_\ell}} \tilde{v}_m \frac{d\tilde{v}_n}{dz} &= -2\tilde{\mathbf{C}}_\ell^2 \frac{if_\ell \omega_0}{\tilde{v}_{\mathrm{ph}\ell}} \tilde{Z}_\ell^*(z) \tilde{V}_\ell + \tilde{R}_\ell \tilde{E}_\ell \\
&\quad + if_\ell \omega_0 \tilde{v}_\ell - \sum_{\substack{m,n \\ f_m + f_n = f_\ell}} if_n \omega_0 \tilde{v}_m \tilde{v}_n \qquad \text{(A.125)} \\
\sum_{\substack{m,n \\ f_m + f_n = f_\ell}} \tilde{v}_m \frac{d\tilde{\rho}_n}{dz} &= if_\ell \omega_0 \tilde{\rho}_\ell - if_\ell \omega_0 \sum_{\substack{m,n \\ f_m + f_n = f_\ell}} \tilde{v}_m \tilde{\rho}_n \\
&\quad - \sum_{\substack{m,n \\ f_m + f_n = f_\ell}} \frac{d\tilde{v}_m}{dz} \tilde{\rho}_n \qquad \text{(A.126)}
\end{aligned}$$

where $-\infty \leq \ell \leq \infty$. The matrix $\mathbf{V}$ is the same as for the original MUSE model. We do not state the model with retention of the $\frac{d\tilde{V}_\ell}{dz}$ term in (A.125).

A.3.2 S-MUSE

The S-MUSE model using the slowly varying envelope approximation becomes

$$\begin{aligned}
\frac{d\tilde{V}_\ell}{dz} &= \frac{\tilde{v}_{\mathrm{ph}\ell}}{2}\left[if_\ell\omega_0\left(\tilde{L}_\ell\tilde{C}_\ell - \frac{1}{\tilde{v}_{\mathrm{ph}\ell}^2}\right) - i\frac{\tilde{\mathbf{R}}_\ell\tilde{G}_\ell}{f_\ell\omega_0} - \left(\tilde{\mathbf{R}}_\ell\tilde{C}_\ell + \tilde{G}_\ell\tilde{L}_\ell\right)\right]\tilde{V}_\ell \\
&\quad + \frac{\tilde{v}_{\mathrm{ph}\ell}}{2}\left[\tilde{\mathbf{R}}_\ell - if_\ell\omega_0\tilde{L}_\ell\right]\tilde{\mathbf{C}}_\ell\tilde{Z}_\ell(z)\tilde{\rho}_\ell \qquad \text{(A.127)} \\
\frac{d\tilde{E}_\ell}{dz} &= -if_\ell\omega_0\tilde{E}_\ell + \tilde{\rho}_\ell \qquad \text{(A.128)} \\
\frac{d\tilde{v}_\ell}{dz} &= -2\tilde{\mathbf{C}}_\ell^2\frac{if_\ell\omega_0}{\tilde{v}_{\mathrm{ph}\ell}}\tilde{Z}_\ell^*(z)\tilde{V}_\ell + \tilde{R}_\ell\tilde{E}_\ell - \sum_{\substack{m\neq 0, n\neq 0\\ f_m+f_n=f_\ell}} if_n\omega_0\tilde{v}_m\tilde{v}_n \qquad \text{(A.129)} \\
\frac{d\tilde{\rho}_\ell}{dz} &= 2\tilde{\mathbf{C}}_\ell^2\frac{if_\ell\omega_0}{\tilde{v}_{\mathrm{ph}\ell}}\tilde{Z}_\ell^*(z)\tilde{V}_\ell - \tilde{R}_\ell\tilde{E}_\ell - if_\ell\omega_0\tilde{v}_\ell \\
&\quad + 2\sum_{\substack{m\neq 0, n\neq 0\\ f_m+f_n=f_\ell}}\tilde{\mathbf{C}}_m^2\frac{if_m\omega_0}{\tilde{v}_{\mathrm{ph}m}}\tilde{Z}_m^*(z)\tilde{V}_m\tilde{\rho}_n - \sum_{\substack{m\neq 0, n\neq 0\\ f_m+f_n=f_\ell}}\tilde{R}_m\tilde{E}_m\tilde{\rho}_n \\
&\quad + \sum_{\substack{m\neq 0, n\neq 0\\ f_m+f_n=f_\ell}} if_n\omega_0\tilde{v}_m\tilde{v}_n - if_\ell\omega_0\sum_{\substack{m\neq 0, n\neq 0\\ f_m+f_n=f_\ell}}\tilde{v}_m\tilde{\rho}_n \qquad \text{(A.130)}
\end{aligned}$$

where $-\infty \leq \ell \leq \infty, \ell \neq 0$. We do not state the model with retention of the $\frac{d\tilde{V}_\ell}{dz}$ term in (A.129) and hence (A.130).

A.3.3 LATTE

The LATTE model using the slowly varying envelope approximation becomes

$$\begin{aligned}
\frac{d\tilde{V}_\ell}{dz} &= \frac{\tilde{v}_{\mathrm{ph}\ell}}{2}\left[if_\ell\omega_0\left(\tilde{L}_\ell\tilde{C}_\ell - \frac{1}{\tilde{v}_{\mathrm{ph}\ell}^2}\right) - i\frac{\tilde{\mathbf{R}}_\ell\tilde{G}_\ell}{f_\ell\omega_0} - \left(\tilde{\mathbf{R}}_\ell\tilde{C}_\ell + \tilde{G}_\ell\tilde{L}_\ell\right)\right]\tilde{V}_\ell \\
&\quad + \frac{\tilde{v}_{\mathrm{ph}\ell}}{2}\left[\tilde{\mathbf{R}}_\ell - if_\ell\omega_0\tilde{L}_\ell\right]\tilde{\mathbf{C}}_\ell\tilde{Z}_\ell(z)\frac{\omega_0}{2\pi}\int_{\frac{2\pi}{\omega_0}}\frac{I_0(\psi_0)e^{-if_\ell\omega_0\Psi(z,\psi_0)}}{I_0 v(z,\psi_0)}d\psi_0 \qquad \text{(A.131)} \\
\frac{d\tilde{E}_\ell}{dz} &= -if_\ell\omega_0\tilde{E}_\ell + \frac{\omega_0}{2\pi}\int_{\frac{2\pi}{\omega_0}}\frac{I_0(\psi_0)e^{-if_\ell\omega_0\Psi(z,\psi_0)}}{I_0 v(z,\psi_0)}d\psi_0 \qquad \text{(A.132)} \\
\frac{\partial v}{\partial z} &= \frac{1}{v}\sum_{\ell=-\infty}^{\infty}\left\{-2\tilde{\mathbf{C}}_\ell^2\frac{if_\ell\omega_0}{\tilde{v}_{\mathrm{ph}\ell}}\tilde{Z}_\ell^*(z)\tilde{V}_\ell + \tilde{R}_\ell\tilde{E}_\ell\right\}e^{if_\ell\omega_0\Psi(z,\psi_0)} \qquad \text{(A.133)} \\
\frac{\partial\Psi}{\partial z} &= 1 - \frac{1}{v}. \qquad \text{(A.134)}
\end{aligned}$$

Retaining the $\frac{d\tilde{V}_\ell}{dz}$ term in (A.133) gives alternatively

$$\frac{\partial v}{\partial z} = \frac{1}{v}\sum_{\ell=-\infty}^{\infty}\left\{-2\tilde{\mathbf{C}}_\ell^2\left(\frac{d\tilde{V}_\ell}{dz}+\frac{if_\ell\omega_0}{\tilde{v}_{\mathrm{ph}\ell}}\tilde{V}_\ell\right)\tilde{Z}_\ell^*(z)+\tilde{R}_\ell\tilde{E}_\ell\right\}e^{if_\ell\omega_0\Psi(z,\psi_0)}. \tag{A.135}$$

Appendix B: Matched input impedance

In this appendix we provide a method for deriving the ratio of the input transmission line voltage to the input transmission line current such that the backward wave is suppressed. The calculation is only strictly applicable if the circuit parameters are uniform. If the circuit has non-uniform parameters, such as a sever, the calculation may be used to estimate the input impedance, and the impedance would then be modified by the differential equation solver so that the output boundary conditions are satisfied.

Let $\mathbf{v}^1, \ldots, \mathbf{v}^5$ be the eigenvectors of $\mathbf{A}_\ell$ with $\mathbf{v}^5$ associated with the backward wave eigenvalue. The linear systems view of the problem is to find, for a given input voltage $\tilde{V}_\ell(0)$, the input current $\tilde{I}_\ell(0)$ such that the input vector $[\tilde{V}_\ell(0)\ \tilde{I}_\ell(0)\ 0\ 0\ 0]^{\mathrm{T}}$ is in the subspace spanned by $\mathbf{v}^1, \mathbf{v}^2, \mathbf{v}^3, \mathbf{v}^4$. Relating voltage to current by $\tilde{V}_\ell = Z\tilde{I}_\ell$ this may be written as

$$\begin{bmatrix} \mathbf{v}^1 & \mathbf{v}^2 & \mathbf{v}^3 & \mathbf{v}^4 \end{bmatrix} \begin{bmatrix} a_1 \\ a_2 \\ a_3 \\ a_4 \end{bmatrix} = \begin{bmatrix} 1 \\ Z^{-1} \\ 0 \\ 0 \\ 0 \end{bmatrix} \tag{B.1}$$

where the $\mathbf{v}^i$ are 5-dimensional column vectors and we wish to solve for Z. Write this as

$$\begin{bmatrix} \mathbf{v}^1 & \mathbf{v}^2 & \mathbf{v}^3 & \mathbf{v}^4 & 0 \\ & & & & -1 \\ & & & & 0 \\ & & & & 0 \\ & & & & 0 \end{bmatrix} \begin{bmatrix} a_1 \\ a_2 \\ a_3 \\ a_4 \\ Z^{-1} \end{bmatrix} = \begin{bmatrix} 1 \\ 0 \\ 0 \\ 0 \\ 0 \end{bmatrix}. \tag{B.2}$$

Define the matrix on the left hand side of (B.2) to be $\mathbf{V}$, then the lower left entry of $\mathbf{V}^{-1}$ is Z^{-1}.

If there are nonzero modulations on beam quantities the problem is solved similarly. In this case the problem is over determined and the pseudo-inverse must be used rather than the inverse. The pseudo-inverse minimizes the projection of the initial vector onto the $\mathbf{v}^5$ vector.

Appendix C: Induced norms

C.1 Matrix norm

The following results come from Horn and Johnson [47]. Given a vector norm $|\cdot|$, an induced norm on the matrix $\mathbf{A}$ is

$$||\mathbf{A}|| \equiv \sup_{\mathbf{x}\neq 0} \frac{|\mathbf{A}\mathbf{x}|}{|\mathbf{x}|} \tag{C.1}$$

$$= \sup_{|\mathbf{x}|=1} |\mathbf{A}\mathbf{x}|. \tag{C.2}$$

For the vector norms $|\cdot|_1$, $|\cdot|_2$, and $|\cdot|_\infty$ we have the following formulas for the induced matrix norms.

1. The 1 norm for vectors is defined as $|\mathbf{x}|_1 = \sum_{i=1}^n |\mathbf{x}_i|$ where $|\cdot|$ of a scalar is absolute value. For the matrix $\mathbf{A}$

$$||\mathbf{A}||_1 = \max_j \sum_{i=1}^n |a_{ij}|. \tag{C.3}$$

2. The 2 norm for vectors is defined as $|\mathbf{x}|_2 = \sqrt{\sum_{i=1}^n \mathbf{x}_i^2}$. For the matrix $\mathbf{A}$

$$||\mathbf{A}||_2 = \sqrt{\lambda_{\max}\left(\mathbf{A}^*\mathbf{A}\right)} \tag{C.4}$$

   where $\mathbf{A}^*$ is the complex conjugate transpose of $\mathbf{A}$ and $\lambda_{\max}\left(\mathbf{A}^*\mathbf{A}\right)$ denotes the largest eigenvalue of $\mathbf{A}^*\mathbf{A}$.

3. The ∞ norm for vectors is defined as $|\mathbf{x}|_\infty = \max_i |\mathbf{x}_i|$ where $|\cdot|$ of a scalar is absolute value. For the matrix $\mathbf{A}$

$$||\mathbf{A}||_\infty = \sup_{|\mathbf{x}|_\infty=1} \max_i \sum_{j=1}^n |a_{ij}|\,|\mathbf{x}_j| \tag{C.5}$$

$$= \max_i \sum_{j=1}^n |a_{ij}|. \tag{C.6}$$

C.2 Tensor norm

We define the tensor norm as

$$||\mathbf{H}|| \equiv \sup_{\mathbf{x},\mathbf{y}\neq 0} \frac{|\mathbf{H}(\mathbf{x},\mathbf{y})|}{|\mathbf{x}|\,|\mathbf{y}|} \tag{C.7}$$

$$= \sup_{|\mathbf{x}|,|\mathbf{y}|=1} |\mathbf{H}(\mathbf{x},\mathbf{y})|. \tag{C.8}$$

To see that (C.8) follows from (C.7) let $p = \sup_{\mathbf{x},\mathbf{y}\neq 0} \frac{|\mathbf{H}(\mathbf{x},\mathbf{y})|}{|\mathbf{x}||\mathbf{y}|}$ and $q = \sup_{|\mathbf{x}|,|\mathbf{y}|=1} |\mathbf{H}(\mathbf{x},\mathbf{y})|$. Since $|\mathbf{x}|, |\mathbf{y}| = 1$ is a subset of $\mathbf{x}, \mathbf{y} \neq 0$ and when $|\mathbf{x}|, |\mathbf{y}| = 1$ we have $\frac{|\mathbf{H}(\mathbf{x},\mathbf{y})|}{|\mathbf{x}||\mathbf{y}|} = |\mathbf{H}(\mathbf{x},\mathbf{y})|$ it follows that $q \leq p$. Conversely for each $\mathbf{x}, \mathbf{y} \neq 0$ with supremum p, there are vectors $\hat{\mathbf{x}} = \frac{\mathbf{x}}{|\mathbf{x}|}$, $\hat{\mathbf{y}} = \frac{\mathbf{y}}{|\mathbf{y}|}$ with $|\hat{\mathbf{x}}| = |\hat{\mathbf{y}}| = 1$ and $\frac{|\mathbf{H}(\mathbf{x},\mathbf{y})|}{|\mathbf{x}||\mathbf{y}|} = |\mathbf{H}(\hat{\mathbf{x}},\hat{\mathbf{y}})|$, following from the multilinear nature of $\mathbf{H}$. Since $\hat{\mathbf{x}}, \hat{\mathbf{y}}$ might not be the vectors at which the supremum is obtained $p \leq q$.

To be a norm (C.7), (C.8) must satisfy 1.–3. on pg. 57 of [13].

1. $||\mathbf{H}|| \geq 0$ follows since $|\cdot| \geq 0$. ($\Leftarrow$) $\mathbf{H} = 0$ implies $\mathbf{H}(\mathbf{x},\mathbf{y}) = 0$ for all $\mathbf{x}, \mathbf{y}$. ($\Rightarrow$, by contrapositive) $\mathbf{H} \neq 0$ implies for some i, j, k that $\mathbf{H}_{ijk} \neq 0$. Then there are $\mathbf{x}, \mathbf{y}$ with $\mathbf{x}_{j,k} \neq 0$ and $\mathbf{y}_{j,k} \neq 0$, all other components zero, such that $(\mathbf{H}(\mathbf{x},\mathbf{y}))_i = \mathbf{H}_{ijk}\mathbf{x}_j\mathbf{y}_k + \mathbf{H}_{ikj}\mathbf{x}_k\mathbf{y}_j \neq 0$.[1]

2. $||\alpha\mathbf{H}|| = \sup_{|\mathbf{x}|,|\mathbf{y}|=1} |\alpha\mathbf{H}(\mathbf{x},\mathbf{y})| = |\alpha|\,||\mathbf{H}||$ following from the vector norm $|\cdot|$.

3. For this we need $|\mathbf{H}(\mathbf{x},\mathbf{y})| \leq ||\mathbf{H}||\,|\mathbf{x}|\,|\mathbf{y}|$ which follows from the definition (C.7) (and 1. for $\mathbf{H} = 0$). Then for $||\mathbf{H}_1 + \mathbf{H}_2||$, from the vector norm $|(\mathbf{H}_1 + \mathbf{H}_2)(\mathbf{x},\mathbf{y})| \leq |\mathbf{H}_1(\mathbf{x},\mathbf{y})| + |\mathbf{H}_2(\mathbf{x},\mathbf{y})| \leq (||\mathbf{H}_1|| + ||\mathbf{H}_2||)|\mathbf{x}|\,|\mathbf{y}|$. Taking the supremum of this inequality on the balls $|\mathbf{x}|, |\mathbf{y}| = 1$ gives the desired result.

Now calculate the norm for the three vector norms.

1. The 1 norm for vectors is defined as $|\mathbf{x}|_1 = \sum_{i=1}^n |\mathbf{x}_i|$ where $|\cdot|$ of a scalar is absolute value. Compute

$$||\mathbf{H}||_1 = \sup_{|\mathbf{x}|_1,|\mathbf{y}|_1=1} \sum_{i=1}^n \left| \sum_{j=1}^n \sum_{k=1}^n \mathbf{H}_{ijk}\mathbf{x}_j\mathbf{y}_k \right|. \tag{C.9}$$

   For fixed i the sum over j, k is maximized when one chooses the largest $\mathbf{H}_{ijk}$, i.e. lets $\mathbf{x}, \mathbf{y}$ have ones in the j^{th} and k^{th} positions and zeros in the other positions. Then take a maximum over j, k to maximize the sum over i, so

$$||\mathbf{H}||_1 = \max_{j,k} \sum_{i=1}^n |\mathbf{H}_{ijk}|. \tag{C.10}$$

2. No formula for $||\mathbf{H}||_2$ was found by the author. Using the representation $\mathbf{H}(\mathbf{x},\mathbf{y}) = \mathbf{x}^{\mathrm{T}}\mathbf{H}\mathbf{y}$ and trying to follow the matrix result leaves the matrix $\mathbf{x}^{\mathrm{T}*}\mathbf{x}^{\mathrm{T}}$ between $\mathbf{H}^*$ and $\mathbf{H}$. Even though this matrix is hermitian, it seems to change (in a simple example) the eigenvalues of $\mathbf{H}^*\mathbf{H}$.

[1] If one tries to define the tensor norm with just one vector $\mathbf{x}$ rather than two vectors $\mathbf{x}, \mathbf{y}$ then this condition fails as one can construct a nonzero tensor that gives $||\mathbf{H}|| = 0$.

3. The ∞ norm for vectors is defined as $|\mathbf{x}|_\infty = \max_i |\mathbf{x}_i|$ where $|\cdot|$ of a scalar is absolute value. Compute

$$||\mathbf{H}||_\infty = \sup_{|\mathbf{x}|_\infty,|\mathbf{y}|_\infty=1} \max_i \left| \sum_{j=1}^{n} \sum_{k=1}^{n} \mathbf{H}_{ijk}\mathbf{x}_j\mathbf{y}_k \right|. \tag{C.11}$$

For each i choose $\mathbf{x}_j, \mathbf{y}_k = \pm 1$ such that $\mathbf{H}_{ijk}\mathbf{x}_j\mathbf{y}_k > 0$, then

$$||\mathbf{H}||_\infty = \sup_{|\mathbf{x}|_\infty,|\mathbf{y}|_\infty=1} \max_i \sum_{j=1}^{n} \sum_{k=1}^{n} |\mathbf{H}_{ijk}| \, |\mathbf{x}_j| \, |\mathbf{y}_k| \tag{C.12}$$

$$= \max_i \sum_{j=1}^{n} \sum_{k=1}^{n} |\mathbf{H}_{ijk}|. \tag{C.13}$$

C.3 Results for double indices

The vector formulation of the S-MUSE model in Section 2.2.3 uses a double index notation, e.g. $\mathbf{x}_{\ell_i}, \mathbf{A}_{\ell_{ij}}, \mathbf{H}_{\ell_i m_j n_k}$. For the case of the 1-norm we modify the above results to reflect this notation. The vector 1-norm becomes

$$|\mathbf{x}|_1 = \sum_{\substack{\ell=-M \\ \ell\neq 0}}^{M} \sum_{i=1}^{5} |\mathbf{x}_{\ell_i}| \tag{C.14}$$

where $|\cdot|$ of a scalar is absolute value. Using this one gets for the matrix and tensor 1-norms

$$||\mathbf{A}||_1 = \max_{\ell,j} \sum_{i=1}^{5} |\mathbf{A}_{\ell_{ij}}| \tag{C.15}$$

$$||\mathbf{H}||_1 = \max_{m,n,j,k} \sum_{\substack{\ell=-M \\ \ell\neq 0}}^{M} \sum_{i=1}^{5} |\mathbf{H}_{\ell_i m_j n_k}|. \tag{C.16}$$

Appendix D: Derivation of modal amplitudes

In this appendix we derive the formulas given in Section 3.3 for the modes of the integral

$$\int_0^z e^{\mathbf{A}_\ell(z-\tau)} \sum_{q=1}^{M} \left(\sum_{r=0}^{N_q} \tau^r \mathbf{c}_q^r \right) e^{\mu_q \tau} \, d\tau. \tag{D.1}$$

We assume that $\mathbf{A}_\ell$ is diagonalizable with eigenvalues λ_{ℓ_j}. First we compute one term of the sum in the integrand, then we compute the sum.

D.1 One term of equation (D.1)

One term of (D.1) is

$$\int_0^z e^{\mathbf{A}_\ell(z-\tau)} \tau^p \mathbf{c}_q^p e^{\mu_q \tau} \, d\tau \tag{D.2}$$

where we have changed indexing from r to p for convenience at a later point in the calculation. In general the integral may be written as

$$\mathbf{P}_\ell \left\{ \int_0^z \begin{bmatrix} e^{\lambda_{\ell_1} z} e^{(\mu_q - \lambda_{\ell_1})\tau} \tau^p & 0 & \dots & 0 \\ 0 & e^{\lambda_{\ell_2} z} e^{(\mu_q - \lambda_{\ell_2})\tau} \tau^p & \dots & 0 \\ \vdots & \vdots & \ddots & 0 \\ 0 & 0 & \dots & e^{\lambda_{\ell_5} z} e^{(\mu_q - \lambda_{\ell_5})\tau} \tau^p \end{bmatrix} d\tau \right\} \mathbf{P}_\ell^{-1} \mathbf{c}_q^p. \tag{D.3}$$

We consider an entry of the diagonal matrix in the integrand. When $\mu_q \neq \lambda_{\ell_j}$

$$\begin{aligned} &\int_0^z e^{\lambda_{\ell_j} z} e^{(\mu_q - \lambda_{\ell_j})\tau} \tau^p d\tau = \\ &\qquad e^{\mu_q z} \sum_{n=0}^{p} (-1)^n \frac{p!}{(p-n)!} \frac{z^{p-n}}{(\mu_q - \lambda_{\ell_j})^{n+1}} + e^{\lambda_{\ell_j} z} \frac{(-1)^{p+1} p!}{(\mu_q - \lambda_{\ell_j})^{p+1}} \end{aligned} \tag{D.4}$$

If $\lambda_{\ell_j} = \mu_q$ for some j, then

$$\begin{aligned} \int_0^z e^{\lambda_{\ell_j} z} e^{(\mu_q - \lambda_{\ell_j})\tau} \tau^p d\tau &= \int_0^z e^{\lambda_{\ell_j} z} \tau^p d\tau \\ &= e^{\mu_q z} \frac{z^{p+1}}{p+1}. \end{aligned} \tag{D.5}$$

To keep track of the modal contributions we define the matrices

$$\mathbf{R}_{\ell_{i,j}}(k,p,\mu_q) \equiv \begin{cases} \frac{(-1)^{p+1}p!}{(\mu_q-\lambda_{\ell_k})^{p+1}} & i=j=k \text{ and } \lambda_{\ell_i}\neq\mu_q \\ 0 & \text{otherwise} \end{cases} \tag{D.6}$$

$$\tilde{\mathbf{S}}_{\ell_{i,j}}(\mu_q,p,n) \equiv \begin{cases} (-1)^n\frac{p!}{(p-n)!}\frac{1}{(\mu_q-\lambda_{\ell_j})^{n+1}} & i=j \text{ such that } \lambda_{\ell_i}\neq\mu_q \\ 0 & \text{otherwise} \end{cases} \tag{D.7}$$

$$\mathbf{T}_{\ell_{i,j}}(p) \equiv \begin{cases} \frac{1}{p+1} & i=j \text{ such that } \lambda_{\ell_i}=\mu_q \text{ and } p\neq -1 \\ 0 & \text{otherwise.} \end{cases} \tag{D.8}$$

Next we compute the coefficients for the different modes of (D.2). The λ_{ℓ_k} mode is

$$\mathbf{P}_\ell\mathbf{R}_\ell(k,p,\mu_q)\mathbf{P}_\ell^{-1}\mathbf{c}_q^p e^{\lambda_{\ell_k}z}, \quad k=1\ldots 5. \tag{D.9}$$

The μ_q mode is

1. If $\mu_q\neq\lambda_{\ell_j}$, $j=1,\ldots,5$

$$\sum_{n=0}^{p}\mathbf{P}_\ell\tilde{\mathbf{S}}_\ell(\mu_q,p,n)\mathbf{P}_\ell^{-1}\mathbf{c}_q^p z^{p-n}e^{\mu_q z}. \tag{D.10}$$

2. If $\mu_q=\lambda_{\ell_i}$ for some i, then

$$\mathbf{P}_\ell\left[\mathbf{T}_\ell(p)z^{p+1}+\sum_{n=0}^{p}\tilde{\mathbf{S}}_\ell(\mu_q,p,n)z^{p-n}\right]\mathbf{P}_\ell^{-1}\mathbf{c}_q^p e^{\mu_q z}. \tag{D.11}$$

The matrix $\mathbf{R}_\ell$ has been constructed so that if $\lambda_{\ell_k}=\mu_q$ equation (D.9) is zero; if $\lambda_{\ell_k}=\mu_q$ the λ_{ℓ_k} mode is given by (D.11). One can check that the matrix $\tilde{\mathbf{S}}_\ell(\mu_q,p,n)$ is different in (D.10) and (D.11); in (D.10) it is a diagonal matrix, and in (D.11) one of the diagonal entries is zero.

D.2 Equation (D.1)

We now compute the entire integral (D.1), repeated here

$$\int_0^z e^{\mathbf{A}_\ell(z-\tau)}\sum_{q=1}^{M}\left(\sum_{p=0}^{N_q}\tau^p\mathbf{c}_q^p\right)e^{\mu_q\tau}\,d\tau.$$

By linearity this is

$$\sum_{q=1}^{M}\sum_{p=0}^{N_q}\int_0^z e^{\mathbf{A}_\ell(z-\tau)}\tau^p\mathbf{c}_q^p e^{\mu_q\tau}\,d\tau. \tag{D.12}$$

From (D.9) the λ_{ℓ_k} mode is

$$\sum_{q=1}^{M}\sum_{r=0}^{N_q}\mathbf{P}_\ell\mathbf{R}_\ell(k,r,\mu_q)\mathbf{P}_\ell^{-1}\mathbf{c}_q^r e^{\lambda_{\ell_k}z}, \qquad k=1,\ldots,5. \tag{D.13}$$

If $\lambda_{\ell_k}=\mu_q$ for some q, the sum from $r=0$ to $r=N_q$ is zero due to the matrix $\mathbf{R}_\ell$. For the μ_q modes we compute the sum over p

1. If $\mu_q\neq\lambda_{\ell_j}$, $j=1,\ldots,5$, from (D.10) we have

$$\sum_{p=0}^{N_q}\sum_{n=0}^{p}\mathbf{P}_\ell\tilde{\mathbf{S}}_\ell(\mu_q,p,n)\mathbf{P}_\ell^{-1}\mathbf{c}_q^p z^{p-n}e^{\mu_q z}. \tag{D.14}$$

2. If $\mu_q=\lambda_{\ell_i}$ for some i, from (D.11) we have

$$\sum_{p=0}^{N_q}\mathbf{P}_\ell\left[\mathbf{T}_\ell(p)z^{p+1}+\sum_{n=0}^{p}\tilde{\mathbf{S}}_\ell(\mu_q,p,n)z^{p-n}\right]\mathbf{P}_\ell^{-1}\mathbf{c}_q^p e^{\mu_q z}. \tag{D.15}$$

In (D.14) and (D.15) the power of z depends on p and n. For convenience we reindex to collect terms multiplying similar powers of z. Let

$$r = p-n \tag{D.16}$$
$$k = n \tag{D.17}$$

and

$$\begin{aligned}\mathbf{S}_{\ell_{i,j}}(\mu_q,r,k) &\equiv \tilde{\mathbf{S}}_{\ell_{i,j}}(\mu_q,r+k,k)\\ &= \begin{cases}(-1)^k\frac{(r+k)!}{r!}\frac{1}{(\mu_q-\lambda_{\ell_j})^{k+1}} & i=j \text{ such that } \lambda_{\ell_i}\neq\mu_q\\ 0 & \text{otherwise.}\end{cases}\end{aligned} \tag{D.18}$$

Then (D.14) and (D.15) become

1. If $\mu_q\neq\lambda_{\ell_j}$, $j=1,\ldots,5$,

$$\sum_{r=0}^{N_q}\left[\sum_{k=0}^{N_q-r}\mathbf{P}_\ell\mathbf{S}_\ell(\mu_q,r,k)\mathbf{P}_\ell^{-1}\mathbf{c}_q^{r+k}\right]z^r e^{\mu_q z} \tag{D.19}$$

2. If $\mu_q=\lambda_{\ell_i}$ for some i,

$$\begin{aligned}\mathbf{P}_\ell\Bigg\{\mathbf{T}_\ell(N_q)\mathbf{P}_\ell^{-1}\mathbf{c}_q^{N_q}z^{N_q+1}+\sum_{r=0}^{N_q}\Bigg[H(r)\mathbf{T}_\ell(r-1)\mathbf{P}_\ell^{-1}\mathbf{c}_q^{r-1}\\ +\left(\sum_{k=0}^{N_q-r}\mathbf{S}_\ell(\mu_q,r,k)\mathbf{P}_\ell^{-1}\mathbf{c}_q^{r+k}\right)\Bigg]z^r\Bigg\}e^{\mu_q z}\end{aligned} \tag{D.20}$$

where

$$H(r) = \begin{cases} 1 & r \geq 1 \\ 0 & r = 0. \end{cases} \tag{D.21}$$

Appendix E: Application of MUSE and LATTE methods to klystron modeling

In this appendix we apply the methodology of Chapter 2 to a simple klystron model. In fact the scope of the present work will be restricted to a modulated electron beam, leaving an extension of the treatment to include intermediate and output cavities as the subject of future work. The cavity modeling would follow [52].

We present the equations for the electron beam, derive the MUSE, S-MUSE and LAKE (Lagrangian Klystron Equations) models, and finally present the analytic solution of the S-MUSE klystron model.

E.1 Modulated electron beam models

E.1.1 Equations

We choose to write the electron beam equations in (z, ψ) coordinates as opposed to (z, t) coordinates for the same reason we did in the TWT model; (z, ψ) coordinates allow the derivation of S-MUSE and hence analytic solutions which provide physical insights. The electron beam equations in (z, ψ) coordinates are[1]

$$\frac{\partial E}{\partial z} = -\frac{\omega_0}{u_0}\frac{\partial E}{\partial \psi} + \frac{\rho}{\epsilon_0} \tag{E.1}$$

$$v\frac{\partial v}{\partial z} = \frac{e}{m_e}RE + \omega_0\left(1 - \frac{v}{u_0}\right)\frac{\partial v}{\partial \psi} \tag{E.2}$$

$$v\frac{\partial \rho}{\partial z} = \omega_0\left(1 - \frac{v}{u_0}\right)\frac{\partial \rho}{\partial \psi} - \rho\left(\frac{\partial v}{\partial z} + \frac{\omega_0}{u_0}\frac{\partial v}{\partial \psi}\right). \tag{E.3}$$

Gauss' law (E.1) predicts the space charge field based on the electron beam charge density, Newton's law (E.2) gives the force on the electrons due to the space charge field, and the continuity equation (E.3) ensures conservation of charge. The factor R in (E.2) is the space charge reduction factor which accounts for the finite beam radius by reducing the force applied to an electron.

For the case of an initially unmodulated electron beam it is assumed that the first cavity imparts a velocity modulation [52]

$$v(0, t) = u_0\left(1 + \frac{\epsilon(t)}{2}\right) \tag{E.4}$$

so

$$v(0, \psi) = u_0\left(1 + \frac{\epsilon\left(-\frac{\psi}{\omega_0}\right)}{2}\right). \tag{E.5}$$

[1]The convolution notation of Chapter 2, which is strictly required in the time domain, is forgone here.

Furthermore we have

$$E(0,\psi) = 0 \tag{E.6}$$
$$\rho(0,\psi) = \rho_0. \tag{E.7}$$

It is often the case of interest that $\epsilon(t)$ is periodic and given as a Fourier series.

E.1.2 Normalization

For normalization purposes we define the following characteristic quantities for the independent coordinates

$$Z = L \tag{E.8}$$
$$U = u_0 \tag{E.9}$$
$$T = \frac{Z}{U} \tag{E.10}$$

where L is the klystron length (e.g. $\lambda_q/4$), u_0 is the DC beam velocity, and hence T is a characteristic time. If we define normalized space and time variables

$$\hat{z} = \frac{z}{Z} \tag{E.11}$$
$$\hat{t} = \frac{t}{T} \tag{E.12}$$

this implies a normalized phase variable via (2.9)

$$\hat{\psi} = \frac{1}{\omega_0 T}\psi = (\hat{z} - \hat{t}). \tag{E.13}$$

Derivatives with respect to z and ψ then become

$$\frac{\partial}{\partial z} = \frac{1}{Z}\frac{\partial}{\partial \hat{z}} \tag{E.14}$$
$$\frac{\partial}{\partial \psi} = \frac{1}{\omega_0 T}\frac{\partial}{\partial \hat{\psi}}. \tag{E.15}$$

For dependent variables we define

$$D = \rho_0 \tag{E.16}$$

and choose the following normalizations

$$\hat{E} = \frac{\epsilon_0}{ZD}E \tag{E.17}$$
$$\hat{v} = \frac{v}{U} \tag{E.18}$$
$$\hat{\rho} = \frac{\rho}{D} \tag{E.19}$$

where ρ_0 is the DC linear charge density, I_0 is the DC beam current ($I_0 = \rho_0 u_0 A$), and V_0 is the DC beam voltage.

Substitution of (E.14), (E.15), and (E.17)–(E.19) into (E.1)–(E.3) result in the following set of normalized equations

$$\frac{\partial \hat{E}}{\partial \hat{z}} = -\frac{\partial \hat{E}}{\partial \hat{\psi}} + \hat{\rho} \tag{E.20}$$

$$\hat{v}\frac{\partial \hat{v}}{\partial \hat{z}} = \hat{R}\hat{E} + (1-\hat{v})\,\frac{\partial \hat{v}}{\partial \hat{\psi}} \tag{E.21}$$

$$\hat{v}\frac{\partial \hat{\rho}}{\partial \hat{z}} = (1-\hat{v})\,\frac{\partial \hat{\rho}}{\partial \hat{\psi}} - \hat{\rho}\left(\frac{\partial \hat{v}}{\partial \hat{z}} + \frac{\partial \hat{v}}{\partial \hat{\psi}}\right) \tag{E.22}$$

where we have defined

$$\hat{R} = \frac{eDT^2}{m_e \epsilon_0} R = \omega_p^2 T^2 R. \tag{E.23}$$

For boundary data one has

$$\hat{E}(0,\psi) = 0 \tag{E.24}$$

$$\hat{v}(0,\psi) = \frac{v(z,\psi)}{U} \tag{E.25}$$

$$\hat{\rho}(0,\psi) = 1. \tag{E.26}$$

In the remainder of the appendix we omit the hat (ˆ) from normalized variables when one can deduce from the equations whether or not the variables are normalized [e.g. compare (E.1)–(E.3) to (E.20)–(E.22)].

E.1.3 MUSE

To derive MUSE we compute the Fourier coefficient formulas for (E.20)–(E.22). The Fourier series (2.15) in normalized variables is

$$\hat{x}(\hat{z},\hat{\psi}) = \sum_{\ell=-\infty}^{\infty} \hat{\tilde{x}}_\ell(\hat{z}) e^{i f_\ell \hat{\omega}_0 \hat{\psi}}. \tag{E.27}$$

where

$$\hat{\omega}_0 = \omega_0 T. \tag{E.28}$$

The normalized fundamental frequency $\hat{\omega}_0$ is the result of the time scaling $\hat{t} = t/T$. From (E.27) one sees that $\frac{\partial}{\partial \hat{\psi}} \to i f_\ell \hat{\omega}_0$. Quantities with tildes (˜) are considered to be in the frequency domain and have a frequency subscript ℓ, e.g., $\tilde{R}(z, f_\ell \omega_0)$ will be written as $\tilde{R}_\ell$.

The normalized MUSE model for a modulated electron beam is

$$\frac{d\tilde{E}_\ell}{dz} = -if_\ell\omega_0\tilde{E}_\ell + \tilde{\rho}_\ell \tag{E.29}$$

$$\sum_{\substack{m,n\\ f_m+f_n=f_\ell}} \tilde{v}_m\frac{d\tilde{v}_n}{dz} = \tilde{R}_\ell\tilde{E}_\ell + if_\ell\omega_0\tilde{v}_\ell - \sum_{\substack{m,n\\ f_m+f_n=f_\ell}} if_n\omega_0\tilde{v}_m\tilde{v}_n \tag{E.30}$$

$$\begin{aligned}\sum_{\substack{m,n\\ f_m+f_n=f_\ell}} \tilde{v}_m\frac{d\tilde{\rho}_n}{dz} &= if_\ell\omega_0\tilde{\rho}_\ell - if_\ell\omega_0 \sum_{\substack{m,n\\ f_m+f_n=f_\ell}} \tilde{v}_m\tilde{\rho}_n \\ &\quad - \sum_{\substack{m,n\\ f_m+f_n=f_\ell}} \frac{d\tilde{v}_m}{dz}\tilde{\rho}_n\end{aligned} \tag{E.31}$$

where $-\infty \le \ell \le \infty$.

E.1.4 S-MUSE

The S-MUSE model is derived similarly to Section 2.2.3. The assumptions accounting for normalizations are:

1. approximating $\tilde{\rho}_0(z)$ and $\tilde{v}_0(z)$ as equal to 1
2. neglecting the AC portion of velocity *in the convective* derivative, i.e., letting $\hat{v}\frac{\partial}{\partial\hat{z}} \approx \frac{\partial}{\partial\hat{z}}$
3. ignoring nonlinearities higher than second order in the continuity equation.

The normalized S-MUSE klystron model is

$$\frac{d\tilde{E}_\ell}{dz} = -if_\ell\omega_0\tilde{E}_\ell + \tilde{\rho}_\ell \tag{E.32}$$

$$\frac{d\tilde{v}_\ell}{dz} = \tilde{R}_\ell\tilde{E}_\ell - \sum_{\substack{m\neq0,n\neq0\\ f_m+f_n=f_\ell}} if_n\omega_0\tilde{v}_m\tilde{v}_n \tag{E.33}$$

$$\begin{aligned}\frac{d\tilde{\rho}_\ell}{dz} &= -\tilde{R}_\ell\tilde{E}_\ell - if_\ell\omega_0\tilde{v}_\ell - \sum_{\substack{m\neq0,n\neq0\\ f_m+f_n=f_\ell}} \tilde{R}_m\tilde{E}_m\tilde{\rho}_n \\ &\quad + \sum_{\substack{m\neq0,n\neq0\\ f_m+f_n=f_\ell}} if_n\omega_0\tilde{v}_m\tilde{v}_n - if_\ell\omega_0 \sum_{\substack{m\neq0,n\neq0\\ f_m+f_n=f_\ell}} \tilde{v}_m\tilde{\rho}_n\end{aligned} \tag{E.34}$$

where $-\infty \le \ell \le \infty, \ell \neq 0$.

E.1.5 LAKE (Lagrangian Klystron Equations)

For the derivation of the required elements of the Lagrangian coordinate theory, accounting for normalizations, we refer to Section A.1.4. We derive LAKE from (E.17)–(E.19).

Equation (E.35) is (E.29) with (A.65) substituted for $\tilde{\rho}_\ell$. For (E.2) one writes E using a normalized Fourier series synthesis equation in Lagrangian coordinates and gets (E.36). Equation (A.56) is also included as model equation (E.37). The space charge equation, Newton's law, and phase relation are [leaving off the superscript L and normalization hats (ˆ)]

$$\frac{d\tilde{E}_\ell}{dz} = -if_\ell\omega_0\tilde{E}_\ell + \frac{\hat{\omega}_0}{2\pi}\int_{\frac{2\pi}{\hat{\omega}_0}} \frac{e^{-if_\ell\omega_0\Psi(z,\psi_0)}}{v(z,\psi_0)}d\psi_0 \tag{E.35}$$

$$\frac{\partial v}{\partial z} = \frac{1}{v}\sum_{\ell=-\infty}^{\infty} \tilde{R}_\ell\tilde{E}_\ell e^{if_\ell\omega_0\Psi(z,\psi_0)} \tag{E.36}$$

$$\frac{\partial \Psi}{\partial z} = 1 - \frac{1}{v}. \tag{E.37}$$

As discussed in Section 2.2.2 for numerical implementation the integrals become sums over disk phases, and the factor in front of the Fourier integral transforms to one over the number of disk phases. Notice however that where the unnormalized initial disk phases ψ_0 were distributed over 2π, the normalized initial disk phases $\hat{\psi}_0$ are distributed over $\frac{2\pi}{\hat{\omega}_0}$. The velocity boundary data is given by

$$v(0,\psi_0) = 1 + \frac{\epsilon(-T\hat{\psi}_0)}{2} \tag{E.38}$$

where ϵ is the function given with the original time t as the independent coordinate.

E.2 Analysis of S-MUSE

As in the case of the TWT we can compute analytically the solution to the klystron S-MUSE equations. A substantial difference however is that the klystron "action" is not an exponential growth of an electron beam modulation, rather a "ballistic" current bunching due to the velocity modulation. The intensity of current bunching is ultimately limited by the repulsive space charge forces. Based on this difference it may not be easy to pick out "dominant modes" of nonlinear product frequencies as it was in the S-MUSE TWT theory.

E.2.1 Vector form

We write the S-MUSE model (E.32)–(E.34) in the following vector form that is particularly useful for analysis

$$\dot{\mathbf{x}} = \mathbf{A}\mathbf{x} + \mathbf{H}(\mathbf{x},\mathbf{x}) \tag{E.39}$$

where $\mathbf{x}$ is a $3(2M)$ dimensional complex vector, $\mathbf{A}$ is a $3(2M)\times 3(2M)$ complex matrix, $\mathbf{H}$ is a $3(2M)\times 3(2M)\times 3(2M)$ complex 3-tensor, and overdot represents $\frac{d}{dz}$.

For elements $\mathbf{x}_{\ell_i}$, $\mathbf{A}_{\ell_{ij}}$, and $\mathbf{H}_{\ell_i m_j n_k}$ the subscripts (ℓ, m, n) run from $-M$ to M excluding zero, and the subsubscripts (i, j, k) run from 1 to 3. The subscript ℓ indexes frequencies in the set $\{f_\ell\}$. We index $\mathbf{x}$ with double subscripts such that $\mathbf{x} = [\mathbf{x}_{-M} \ldots \mathbf{x}_{-1}\mathbf{x}_1 \ldots \mathbf{x}_M]^{\mathrm{T}}$ and $\mathbf{x}_\ell = [\mathbf{x}_{\ell_1}\mathbf{x}_{\ell_2}\mathbf{x}_{\ell_3}]^{\mathrm{T}} = [\tilde{E}_\ell\, \tilde{v}_\ell\, \tilde{\rho}_\ell]^{\mathrm{T}}$.

The matrix $\mathbf{A}$ contains the linear parts of (E.32)–(E.34). It is block diagonal with entry $\mathbf{A}_\ell \equiv \mathbf{A}_{\ell\ell}$. The entries $\mathbf{A}_{\ell_{ij}}$ of the block diagonal element $\mathbf{A}_\ell$ are

$$\begin{aligned}
\mathbf{A}_{\ell_{11}} &= -if_\ell\omega_0 && \text{(E.40)}\\
\mathbf{A}_{\ell_{13}} &= 1 && \text{(E.41)}\\
\mathbf{A}_{\ell_{21}} &= \tilde{R}_\ell && \text{(E.42)}\\
\mathbf{A}_{\ell_{31}} &= -\tilde{R}_\ell && \text{(E.43)}\\
\mathbf{A}_{\ell_{32}} &= -if_\ell\omega_0 && \text{(E.44)}
\end{aligned}$$

Entries $\mathbf{A}_{\ell_{ij}}$ not listed above are zero. All parameters represent their normalized values.

The 3-tensor entries $\mathbf{H}_{\ell_i m_j n_k}$ for (ℓ, m, n) are

Case 1 If ℓ, m, n are such that $f_\ell = f_m + f_n$ then

$$\begin{aligned}
\mathbf{H}_{\ell_2 m_2 n_2} &= -if_n\omega_0 && \text{(E.45)}\\
\mathbf{H}_{\ell_3 m_1 n_3} &= -\tilde{R}_m && \text{(E.46)}\\
\mathbf{H}_{\ell_3 m_2 n_2} &= if_n\omega_0 && \text{(E.47)}\\
\mathbf{H}_{\ell_3 m_2 n_3} &= -if_\ell\omega_0. && \text{(E.48)}
\end{aligned}$$

Entries for (i, j, k) not listed are zero.

Case 2 If ℓ, m, n are such that $f_\ell \neq f_m + f_n$ then

$$\mathbf{H}_{\ell_i m_j n_k} = 0 \qquad \text{(E.49)}$$

for all (i, j, k).

For the ℓ^{th} component of $\dot{\mathbf{x}}$ we have

$$\dot{\mathbf{x}}_\ell = \mathbf{A}_\ell\mathbf{x}_\ell + \sum_{\substack{m,n \\ f_m+f_n=f_\ell}} \mathbf{H}_{\ell mn}(\mathbf{x}_m, \mathbf{x}_n) \qquad \text{(E.50)}$$

where the i^{th} component of the quadratic term is

$$\left(\sum_{\substack{m,n \\ f_m+f_n=f_\ell}} \mathbf{H}_{\ell mn}(\mathbf{x}_m, \mathbf{x}_n) \right)_i = \sum_{\substack{m,n \\ f_\ell=f_m+f_n}} \sum_{j=1}^{3}\sum_{k=1}^{3} \mathbf{H}_{\ell_i m_j n_k}\mathbf{x}_{m_j}\mathbf{x}_{n_k}. \qquad \text{(E.51)}$$

LIST OF REFERENCES

[1] The code can be downloaded from `http://www.lmsuite.org`.

[2] D.K. Abe, M.T. Ngô, B. Levush, T.M. Antonsen, Jr., and D.P. Chernin. A comparison of L-band helix TWT experiments with CHRISTINE, a 1-D multifrequency helix TWT code. *IEEE Trans. Plasma Sci.*, 28(3):576–587, June 2000.

[3] M.T. Abuelma'atti. Frequency-dependent nonlinear quadrature model for TWT amplifiers. *IEEE Trans. Commun.*, COM-32(8):982–986, August 1984.

[4] T.M. Antonsen, Jr. and B. Levush. CHRISTINE: A multifrequency parametric simulation code for traveling wave tube amplifiers. *NRL Memo report NRL/FR/6840-97-9845*, 1997.

[5] T.M. Antonsen, Jr. and B. Levush. Traveling-wave tube devices with nonlinear dielectric elements. *IEEE Trans. Plasma Sci.*, 26(3):774–786, 1998.

[6] C.M. Armstrong. (private communication).

[7] B.N. Basu. *Electromagnetic Theory and Applications in Beam-Wave Electronics*. World Scientific Publishing Co. Pte. Ltd., Singapore, 1996.

[8] A.L. Berman and C.E. Mahle. Nonlinear phase shift in traveling-wave tubes as applied to multiple access communications satellites. *IEEE Trans. Communications Technology*, 18:37–48, 1970.

[9] A. Bhattacharjee, S.Y. Cai, J.W. Dodd, and T.C. Marshall. Optical spikes in a free electron laser: Theory and experiment. *Nucl. Instr. and Meth. A*, 304:99–103, 1991.

[10] R. Bonifacio, F. Casagrande, and L. De Salvo Souza. Collective variable description of a free-electron laser. *Phys. Rev. A*, 33(4):2836–2839, 1986.

[11] L. Brillouin. The traveling-wave tube (discussion of waves for large amplitudes). *J. Appl. Phys.*, 20(12):1196–1206, 1949.

[12] R.G. Carter, W. Bösch, V. Srivastava, and G. Gatti. Computer simulation of intermodulation distortion in traveling wave tube amplifiers. *IEEE Trans. Electron Devices*, 48(1):178–180, January 2001.

[13] C.T. Chen. *Linear System Theory and Design*. The Oxford Series in Electrical and Computer Engineering. Oxford University Press, New York, second edition, 1984.

[14] T. Chen, Y. Goren, C. Jensen, P. Lally, and D. Gagne. A novel technology for linearizing traveling wave tube amplifiers. In *2002 IEEE-MTT-S International Microwave Symposium Digest*, volume 2, pages 773–776, 2002.

[15] David K. Cheng. *Field and Wave Electromagnetics*. Addison-Wesley Publishing Co., Reading, Massachusetts, second edition, 1989.

[16] D. Chernin, T.M. Antonsen, Jr., and B. Levush. Exact treatment of the dispersion and beam interaction impedance of a thin tape helix surrounded by a radially stratified dielectric. *IEEE Trans. Electron Devices*, 46(7):1472–1483, July 1999.

[17] D. Chernin, T.M. Antonsen, Jr., B. Levush, and D.R. Whaley. A three-dimensional multifrequency large signal model for helix traveling wave tubes. *IEEE Trans. Electron Devices*, 48(1):3–11, January 2001.

[18] E.A. Coddington and N. Levinson. *Theory of Ordinary Differential Equations*. McGraw-Hill, New York, 1955.

[19] W.R. Curtice. First-order nonlinear effects in travelling-wave tubes. *Proc. IEE*, 114(8):1048–1050, August 1967.

[20] S.K. Datta, P.K. Jain, and B.N. Basu. Third-order saturation effects in a helix traveling-wave tube under Eulerian approximations. *Microwave and Optical Technology Letters*, 16(6):345–349, 1997.

[21] S.K. Datta, P.K. Jain, and B.N. Basu. Control of IM3 distortion in helix TWTs by harmonic injection – an Eulerian hydrodynamical study. *IEEE Trans. Electron Devices*, 48(1):62–66, 2001.

[22] S.K. Datta, P.K. Jain, M.D. Raj Narayan, and B.N. Basu. Eulerian analysis for harmonic generation and its control in a helix travelling-wave tube. *Int. J. Electron.*, 85(3):377–395, 1998.

[23] S.K. Datta, P.K. Jain, M.D. Raj Narayan, and B.N. Basu. Nonlinear Eulerian hydrodynamical analysis of helix traveling-wave tubes. *IEEE Trans. Electron Devices*, 45(9):2055–2062, 1998.

[24] S.K. Datta, P.K. Jain, M.D. Raj Narayan, and B.N. Basu. Nonlinear Eulerian hydrodynamical analysis of helix traveling-wave tubes for harmonic generation and its control. *IEEE Trans. Electron Devices*, 46(2):420–426, 1999.

[25] S.K. Datta, S.U.M. Reddy, B.N. Basu, and K.U. Limaye. A novel Lagrangian simulation technique for helix traveling-wave tubes. *Microwave and Optical Technology Letters*, 18(4):308–310, 1998.

[26] R. W. DeGrasse. Frequency mixing in microwave beam-type devices. Technical Report 386-2, Stanford University, Electron Devices Laboratory, Stanford Electronics Laboratories, July 1958.

[27] N. J. Dionne, R. Harper, and H. J. Krahn. Sector beam multisignal TWT analysis. *Int. Electron Devices Meet. Tech. Dig.*, pages 362–365, 1988.

[28] N.J. Dionne. Harmonic generation in octave bandwidth traveling-wave tubes. *IEEE Trans. Electron Devices*, ED-17(4):365–372, 1970.

[29] M.E. El-Shandwily. Analysis of multi-signal traveling-wave amplifier operation. Technical Report 85, Electron Physics Lab., University of Michigan, Ann Arbor, June 1965.

[30] E. Ezura and T. Kano. Measured and theoretical nonlinear phase distortion in traveling-wave tubes. *IEEE Trans. Electron Devices*, ED-22(10):890–897, October 1975.

[31] C. Fan and K.M. Cheng. Amplifier linearization using simultaneous harmonic and baseband injection. *IEEE Microwave Wireless Components Lett.*, 11(10):404–406, October 2001.

[32] H.P. Freund. Nonlinear theory of helix traveling wave tubes in the frequency domain. *Phys. Plasmas*, 6(9):3633–3646, 1999.

[33] H.P. Freund. Three-dimensional nonlinear theory of helix traveling-wave tubes. *IEEE Trans. Plasma Sci.*, 28(3):748–759, June 2000.

[34] H.P. Freund and E.G. Zaidman. Nonlinear theory of collective effects in helix traveling wave tubes. *Phys. Plasmas*, 4(6):2292–2301, 1997.

[35] H.P. Freund and E.G. Zaidman. Time-dependent simulation of helix traveling wave tubes. *Phys. Plasmas*, 7(12):5182–5194, December 2000.

[36] H.P. Freund, E.G. Zaidman, and T.M. Antonsen, Jr. Theory of helix traveling wave tubes with dielectric and vane loading. *Phys. Plasmas*, 3(8):3145–3161, August 1996.

[37] H.P. Freund, E.G. Zaidman, A. Mankofsky, N.R. Vanderplaats, and M.A. Kodis. Nonlinear analysis of helix traveling wave tubes. *Phys. Plasmas*, 2(10):3871–3879, October 1995.

[38] W.E. Garrigus and M.L. Glick. Multi-octave high-power TWT operation. *Microwave Journal*, 18:35–40, 1975.

[39] J.W. Gewartowski and H.A. Watson. *Principles of Electron Tubes*. D. Van Nostrand Co., Inc., Princeton, 1965.

[40] A.J. Giarola. A theoretical description for the multiple-signal operation of a TWT. *IEEE Trans. Electron Devices*, ED-15(6):381–395, June 1968.

[41] A.S. Gilmour, Jr. *Principles of Traveling Wave Tubes*. Artech House, Boston, 1994.

[42] A.A. Guida. TWT equal carrier intermodulation calculations. *IEEE Trans. Commun.*, COM-34(10):1024–1030, October 1986.

[43] A.A. Guida. Accurate calculation of TWT intermodulation in the many-carrier case. *IEEE Trans. Commun.*, COM-35(6):685–687, June 1987.

[44] J.J. Hamilton and D. Zavadil. Harmonically-enhanced two-octave TWTA. *Microwave Journal*, 15:24–25, 1972.

[45] H. Hirata. Analysis of phase and intermodulation distortion of a traveling-wave tube. *Int. J. Electron.*, 83(2):249–269, 1997.

[46] H. Hirata and H. Kanai. Generation mechanism of intermodulation products in a traveling wave tube. *Electronics and Communications in Japan*, 77(11):89–98, 1994.

[47] R.A. Horn and C.R. Johnson. *Matrix Analysis*. Cambridge University Press, Cambridge, 1990.

[48] R.G.E. Hutter. *Beam and Wave Electronics in Microwave Tubes*. D. Van Nostrand Company, Inc., Princeton, 1960.

[49] D.J. Jennings, A. Bateman, and J.P. McGeehan. Adjacent channel power and error-vector magnitude performance of reduced complexity CALLUM systems. *IEE Proc.-Commun.*, 146(5):297–302, October 1999.

[50] D.S. Komm, R.T. Benton, H.C. Limburg, W.L. Menninger, and X. Zhai. Advances in space TWT efficiencies. In *International Vacuum Electronics Conference*, page 6.2, 2000.

[51] S. Lang. *Undergraduate Analysis*. Springer-Verlag, New York, 2$^{\text{nd}}$ edition, 1997.

[52] Y.Y. Lau, D.P. Chernin, C. Wilsen, and R.M. Gilgenbach. Theory of intermodulation in a klystron. *IEEE Trans. Plasma Sci.*, 28(3):959–970, June 2000.

[53] X. Li, J.G. Wöhlbier, S. Jin, and J.H. Booske. An Eulerian method for computing multi-valued solutions of the Euler-Poisson equations and application to wave breaking in klystrons. *Phys. Rev. E*, 2003. (To be submitted).

[54] S. Liao. *Microwave Electron-Tube Devices*. Prentice Hall, Englewood Cliffs, 1988.

[55] J.T. Mendel. Helix and coupled-cavity travelling-wave tubes. *Proc. IEEE*, 61:280–288, 1973.

[56] A. Nordsieck. Theory of the large signal behavior of traveling-wave amplifiers. *Proc. IRE*, 41:630–637, May 1953.

[57] F. Paschke. On the nonlinear behavior of electron-beam devices. *RCA Rev.*, 18:221–242, 1957.

[58] F. Paschke. Generation of second harmonic in a velocity-modulated electron beam of finite diameter. *RCA Rev.*, 19:617–627, 1958.

[59] F. Paschke. Nonlinear theory of a velocity-modulated electron beam with finite diameter. *RCA Rev.*, 21:53–74, 1960.

[60] J.R. Pierce. Theory of the beam-type traveling-wave tube. *Proc. IRE*, 35:111–123, 1947.

[61] J.R. Pierce. *Traveling Wave Tubes*. Van Nostrand, Princeton, N.J., 1950.

[62] A. C. Poulter. Large signal theory of the traveling wave tube. Technical Report 73, Electronics Research Laboratory, Stanford University, January 1954. ONR Contract NG ONR 251(07).

[63] W.H. Press, S.A. Teukolsky, W.T. Vetterling, and B.P. Flannery. *Numerical Recipes in C: The Art of Scientific Computing*. Cambridge University Press, Cambridge, 1997.

[64] J. L. Putz. Nonlinear phenomena in traveling-wave amplifiers. Technical Report 37, Electronics Research Laboratory, Stanford University, October 1951.

[65] J.L. Putz. Predicting nonlinear effects in TWTs. *Microwaves*, 4:32–39, June 1965.

[66] J. E. Rowe. A large signal analysis of the traveling-wave amplifier. Technical Report 19, Electron Tube Laboratory, University of Michigan, Ann Arbor, April 1955.

[67] J.E. Rowe. *Nonlinear Electron-Wave Interaction Phenomena*. Academic Press, New York, 1965.

[68] P.N. Safier, D.K. Abe, T.M. Antonsen, Jr., B.G. Danly, and B. Levush. Simulation of noise-power ratio with the large-signal code CHRISTINE. *IEEE Trans. Electron Devices*, 48(1):32–37, Jan. 2001.

[69] A.A.M. Saleh. Frequency-independent and frequency-dependent nonlinear models of TWT amplifiers. *IEEE Trans. Commun.*, COM-29(11):1715–1720, November 1981.

[70] O. Sauseng, M.A. Huisjen, and W.E. Garrigus. Reduction of intermodulation distortion with harmonic injection for wideband travelling-wave tubes. *IEDM Technical Digest*, pages 411–414, 1975.

[71] M.K. Scherba and J.E. Rowe. Characteristics of multisignal and noise-modulated high-power microwave amplifiers. *IEEE Trans. Electron Devices*, ED-18(1):11–34, 1971.

[72] A. Singh, J.G. Wöhlbier, J.E. Scharer, and J.H. Booske. Injection schemes for TWT linearization. In *IVEC 2003 Conference Proceedings*.

[73] H. Sobol. Modulation characteristics of O-type electron stream devices. Technical report, Electron Physics Laboratory, The University of Michigan, Ann Arbor, October 1957.

[74] V. Srivastava and S.N. Joshi. Improved nonlinear model for multisignal analysis of helix TWTs. *IEE Proceedings-H*, 139(2):129–134, 1992.

[75] P.K. Tien. A large signal theory of traveling wave amplifiers. *The Bell System Technical Journal*, pages 349–374, March 1956.

[76] P.K. Tien and L.R. Walker. *Proc. IRE*, page 1007, August 1955. Correspondence Section.

[77] P.K. Tien, L.R. Walker, and V.M. Wolontis. A large signal theory of traveling-wave amplifiers. *Proc. IRE*, pages 260–277, March 1955.

[78] S. Wallander. Nonlinear multisignal TWT theory. *Int. J. Electron.*, 29:201–216, 1970.

[79] M.A. Wirth, A. Singh, J.E. Scharer, and J.H. Booske. Third-order intermodulation reduction by harmonic injection in a TWT amplifier. *IEEE Trans. Electron Devices*, 49(6):1082–1084, 2002.

[80] J.G. Wöhlbier. Modeling and analysis of a traveling wave tube under multitone excitation. Master's thesis, University of Wisconsin–Madison, 2000.

[81] J.G. Wöhlbier, J.H. Booske, and I. Dobson. On the physics of harmonic injection in a traveling wave tube. To be submitted.

[82] J.G. Wöhlbier, J.H. Booske, and I. Dobson. The Multifrequency Spectral Eulerian (MUSE) model of a traveling wave tube. *IEEE Trans. Plasma Sci.*, 30(3):1063–1075, 2002.

[83] J.G. Wöhlbier, I. Dobson, and J.H. Booske. Generation and growth rates of nonlinear distortions in a traveling wave tube. *Phys. Rev. E*, 66, 2002. Article 56504.